

KIEL UNIVERSITY

DOCTORAL THESIS

**Design and Diagnostic of a Microdischarge
for *in situ* TEM Investigation of Plasma
Surface Processes**

LUKA HANSEN

*A thesis submitted in fulfillment of the requirements
for the degree of*

Doctor of Science

in the

Plasma Technology Group
Institute of Experimental and Applied Physics
Faculty of Mathematics and Natural Sciences

Kiel, January 2023

Supervisor and 1. Examiner:
Prof. Dr. Holger Kersten

2. Examiner:
Prof. Dr. Lorenz Kienle

3. Examiner:
Prof. Dr. J. Gary Eden

Oral examination date: 19.12.2022

Print approval date: 19.12.2022

Declaration of Authorship

I, Luka Hansen, declare that this thesis titled, "Design and Diagnostic of a Microdischarge for *in situ* TEM Investigation of Plasma Surface Processes" fulfills the following conditions:

Ich, Luka Hansen, versichere an Eides Statt, dass die vorliegende Dissertation mit dem Titel „Design and Diagnostic of a Microdischarge for *in situ* TEM Investigation of Plasma Surface Processes“ folgende Bedingungen erfüllt:

EN: This work is - expect for advice given by the supervisors - written independently in terms of content and form, using only the indicated resources.

DE: Die Abhandlung ist abgesehen von der Beratung durch die Betreuer nach Inhalt und Form eigenständig und nur mit den angegebenen Hilfsmitteln verfasst.

EN: This thesis was not fully or partially submitted, published, or submitted for publication at another place within an examination procedure. Apart from examination procedures published or for publication submitted parts are clearly labeled.

DE: Die Arbeit wurde weder ganz noch zum Teil an einer anderen Stelle im Rahmen eines Prüfungsverfahrens vorgelegt, veröffentlicht oder zur Veröffentlichung eingereicht. Außerhalb eines Prüfungsverfahrens veröffentlichte Teile sind gekennzeichnet.

EN: The work has been produced in compliance with the rules of good scientific practice of the German Research Foundation.

DE: Die Arbeit ist unter Einhaltung der Regeln guter wissenschaftlicher Praxis der Deutschen Forschungsgemeinschaft entstanden.

EN: I have never been deprived of an academic degree.

DE: Mir wurde niemals ein akademischer Grad entzogen.

Signed: / Unterzeichnet:

Place and date: / Ort und Datum:

“Remember to look up at the stars and not down at your feet. Try to make sense of what you see and wonder about what makes the universe exist. Be curious. And however difficult life may seem, there is always something you can do and succeed at. It matters that you don’t just give up.”

Stephen Hawking

Abstract

The plasma surface interaction is one of the most discussed topics in the field of plasma physics. Novel *in situ* techniques are necessary to obtain a better understanding of the plasma surface interaction during the plasma treatment. This thesis aims to overcome the present barrier between plasma treatment and material analysis by developing a microplasma cell intended for *in situ* transmission electron microscopy (TEM) investigations.

A parallel plate atmospheric pressure DC normal glow microplasma discharge was designed according to the necessary requirements given by the TEM and extensively diagnosed using conventional and non-conventional diagnostics. Different electrode materials (Au, Cu, ITO, Mg), electrode distances (50 μm , 100 μm , 150 μm), working gases (Ar, He), and electric potentials (positive vs ground or negative vs ground) have been investigated. The current-voltage characteristics showed glow like behavior in the current range of ± 0.5 mA to 3 mA with electrode potentials of ± 140 V to 190 V for most experimental conditions. Constant current densities of 16 mA mm^{-2} for He or 28 mA mm^{-2} for Ar working gases could be determined by optical imaging of the discharge. Sheath thicknesses in the range of a few μm were calculated based on the collision-dominated Child-Langmuir law and their trends agree with optical imaging measurements.

A cathode-favored asymmetric energy flux was measured probably caused by the ions. Ion effects were also visible in the measurement process itself and in the electrode surface modifications studied *ex situ*. The combination of electrical and energy flux measurements allowed to determine high efficiencies of the discharge in the 90 % region and effective secondary electron coefficients ranging from 1 to 1.6. Further, the combination allowed to postulate an energy balance at the cathode and investigate the power transfer from the plasma to the surface caused by ion effects. The power balance revealed significant differences in the power transfer mechanisms depending on the working gas. These differences could be observed in the different plasma-induced changes of an Au thin film coated onto an SiN_x TEM grid. Ar as working gas results in uniform surface modifications, as the power is transferred mainly in many small doses via the kinetic energy of ions and fast neutrals. He results in desorption hot spots in the thin film, as the power is mainly transferred in a few large doses via recombination of He ions on the surface.

Tetrapodal ZnO (t-ZnO) was etched in a capacitively coupled low-pressure $\text{H}_2\text{-C}_2\text{H}_2$ plasma to create t-ZnO nanobrushes. The nanobrushes showed excellent H_2 gas sensing properties due to their large surface-to-volume ratio. Still, in context of the *in situ* microplasma cell, the etching process itself is of great interest, as the structural changes of the t-ZnO could be observed very well *in situ*. The t-ZnO was also used as example for highly porous ceramic framework materials to investigate the plasma permeability into these highly porous materials. A novel approach using polymers as marker materials was successfully demonstrated. Penetration depths in the range of 1.6 mm to 4 mm were found, depending on the experimental conditions.

A vacuum-proof housing for the microplasma was developed from two aluminum shells and sealed by O-rings and epoxy. The *in situ* microplasma cell was successfully assembled and introduced into the TEM. No microplasma could be ignited inside of the TEM, as the conductive shells in combination with the doped Si based TEM grids resulted in an avalanche diode circuit. The next generation of the *in situ* microplasma cell will be built from ceramic shells to overcome this issue. Still, first images have been taken in the TEM, proofing the capability of resolving 30 nm large structures, despite the TEM electron beam passing through two 50 nm Au films on top of 35 nm

SiN_x films and a 100 μm He gas column. Furthermore, it was possible to obtain selected area electron diffraction (SAED) patterns and energy dispersive X-ray (EDX) spectra.

Kurzfassung

Die Plasma-Oberflächen Wechselwirkung ist eines der am meisten diskutierten Themen im Bereich der Plasmaphysik. Neuartige *in situ* Techniken sind notwendig um ein besseres Verständnis der Plasma-Oberflächen Wechselwirkung während der Plasmabehandlung zu bekommen. Diese Dissertation zielt darauf die präsenste Barriere zwischen Plasmabehandlung und Materialanalyse zu überwinden, indem eine Mikroplasmazelle entwickelt wird, welche für *in situ* Transmissionselektronenmikroskopie (TEM) gedacht ist.

Eine Parallelplatten Atmosphärendruck DC Glimmentladung wurde designet in Einklang mit den Einschränkungen, die vom TEM vorgegeben waren und mittels konventionellen und nicht-konventionellen Diagnostiken intensiv untersucht. Verschiedene Elektrodenmaterialien (Au, Cu, ITO, Mg), Elektrodenabstände (50 μm , 100 μm , 150 μm), Arbeitsgase (Ar, He), und elektrische Potentiale (Positiv gegen Erdung oder Negativ gegen Erdung) wurden untersucht. Die Strom-Spannungs-Kennlinien zeigten das Verhalten einer Glimmentladung im Strombereich von $\pm 0.5 \text{ mA}$ bis 3 mA bei Elektrodenpotentialen von $\pm 140 \text{ V}$ bis 190 V während der meisten Experimente. Konstante Stromdichten im Bereich von 16 mA mm^{-2} für He oder 28 mA mm^{-2} für Ar als Arbeitsgas wurden mittels optischer Bildgebung ermittelt. Randschichtdicken von einigen μm wurden auf Grundlage des stoßbestimmten Child-Langmuir Gesetzes ermittelt und mit optischen Messungen verglichen.

Ein asymmetrischer, vermutlich aufgrund der Ionen die Kathode bevorzugender, Energiestrom wurde gemessen. Weiter waren Ioneneffekte im Messprozess selber sichtbar und ebenfalls in *ex situ* durchgeführten Modifikationen der Elektrodenoberflächen. Aus der Kombination von elektrischen und Energiestrommessungen konnten hohe Effizienzen im Bereich von 90 % und effektive sekundär Elektronen Koeffizienten von 1 bis 1,6 reichend bestimmt werden. Weiter erlaubte die Kombination eine Energiebilanz für die Kathode aufzustellen und die durch Plasmaionen an die Oberfläche übertragene Leistung zu untersuchen. Die Energiebilanz zeigte signifikante Unterschiede bei den Leistungsübertragungsmechanismen der beiden Arbeitsgase. Diese Unterschiede waren ebenfalls in der unterschiedlichen Plasmamodifikation von Au Dünnschichten sichtbar, welche auf SiN_x TEM Substraten abgeschieden wurden. Mit Ar als Arbeitsgas wurde eine gleichmäßige Oberflächenveränderung erzielt, da die Leistung hauptsächlich in vielen kleinen Paketen durch die kinetische Energie von Ionen und schnellen Neutralen übertragen wird. Im Gegensatz dazu werden bei He als Arbeitsgas Desorptionsbrennpunkte im Dünnschicht erzeugt, da die Leistung hauptsächlich in wenigen großen Paketen durch Rekombination von He Ionen an der Oberfläche übertragen wird.

Tetrapodales ZnO (t-ZnO) wurde in einer kapazitiv gekoppelten $\text{H}_2\text{-C}_2\text{H}_2$ Niederdruckentladung geätzt, um t-ZnO Nanobürsten zu erzeugen. Die t-ZnO Nanobürsten zeigten exzellente H_2 Gassensor Eigenschaften aufgrund ihres großen Oberfläche-zu-Volumen Verhältnisses. Dennoch, im Kontext der *in situ* Mikroplasmazelle, ist der Ätzprozess selbst von großem Interesse, da die strukturellen Veränderungen des t-ZnO gut *in situ* beobachtbar sein sollten. Weiter wurde das t-ZnO noch als Beispiel für extrem poröse, keramische Gerüstmaterialien genutzt, um die Plasma Permeabilität in diese extrem porösen Materialien zu untersuchen. Ein neuartiger Ansatz mittels Polymeren als Indikatormaterial wurde erfolgreich demonstriert. Eindringtiefen im Bereich von 1.6 mm bis 4 mm wurden bestimmt, abhängig von den experimentellen Bedingungen.

Ein vakuumfestes Gehäuse für die Mikroentladung wurde aus zwei Aluminiumschalen entwickelt und mittels O-Ringen und Epoxy-Kleber abgedichtet. Die *in situ* Mikroplasmazelle wurde erfolgreich zusammen gebaut und ins TEM eingebracht. Keine Mikroentladung konnte innerhalb des TEMs gezündet werden, da die leitfähigen Schalen zusammen mit den dotierten Si-basierten TEM Substraten einen Avalanche-Dioden Schaltkreis gebildet haben. Die nächste Generation von *in situ* Mikroplasmazellen wird aus keramischen Schalen aufgebaut werden, um dieses Problem zu lösen. Dennoch, erste TEM Bilder wurden aufgenommen, welche die Möglichkeit beweisen 30 nm große Strukturen aufzulösen, obwohl der TEM Elektronenstrahl zwei 50 nm dicke Au Filme aufgetragen auf 35 nm SiN_x Filme und 100 µm He Gas Säule durchdringen muss. Weiter konnte ebenfalls die Möglichkeit der Feinbereichsbeugung (SAED) und der energiedispersiven Röntgenspektroskopie (EDX) demonstriert werden.

Contents

Declaration of Authorship	v
Abstract	ix
Kurzfassung	xi
1 Introduction	1
2 Plasma Basics	5
2.1 Plasma - the fourth State of Matter	5
2.1.1 Quasineutrality and Collective Behavior	5
2.1.2 Debye-Shielding	6
2.2 Plasma Generation	7
2.2.1 Gas Breakdown	7
2.2.2 Paschen Law	9
2.2.3 Direct Current (DC) Plasma	10
2.2.4 Plasma Sheath	13
Child-Langmuir Law	14
Collisional Sheath	15
2.2.5 High Frequency (HF) Plasma	16
2.3 Microplasma	19
2.4 Plasma Surface Interaction	23
2.4.1 Secondary Electron Emission	23
2.4.2 Adsorption and Desorption	24
2.4.3 Surface Reactions	26
2.4.4 Sputtering	27
2.4.5 Thin Film Growth	28
2.4.6 Plasma Etching	28
3 Plasma and Surface Diagnostics	31
3.1 Plasma Diagnostics	31
3.1.1 Electrical Measurements	31
3.1.2 Optical Emission Spectroscopy	35
3.1.3 Optical Imaging	37
3.1.4 Calorimetric Measurements	38
Publication I: The Use of Passive Thermal Probes for the Determination of Energy Fluxes in Atmospheric Pressure Plasmas	38
3.2 Electron Microscopy	51
3.2.1 Transmissions Electron Microscopy (TEM)	51
<i>In situ</i> TEM	54
3.2.2 Scanning Electron Microscopy (SEM)	54
3.2.3 Energy dispersive X-ray spectroscopy (EDX)	55
3.3 Additional Surface Diagnostics	55

3.3.1	X-ray Photoelectron Spectroscopy (XPS)	56
3.3.2	Water Contact Angle (WCA)	56
4	Atmospheric Pressure DC Microplasma	57
	Publication II: Conventional and non-conventional diagnostics of a stable atmospheric pressure DC normal glow microplasma discharge intended for <i>in situ</i> TEM studies	57
5	Ex situ Polycrystalline Au Thin Film Modifications	75
	Publication III: Correlations between energy flux and thin film modifications in an atmospheric pressure direct current microplasma	75
6	Low-Pressure Plasma Treatment of Highly Porous Framework Materials	89
	Publication IV: Fabrication of ZnO Nanobrushes by H ₂ -C ₂ H ₂ Plasma Etching for H ₂ Sensing Applications	89
	Publication V: On the plasma permeability of highly porous ceramic framework materials using polymers as marker materials	103
7	In situ Microplasma Cell Development	115
7.1	Restrictions given by the TEM	115
7.2	Microplasma Setup and Geometry	116
7.3	3 mm Cell	118
7.3.1	Dimensions	118
7.3.2	Reducing the TEM Grid Size	120
	Ultrasonic Cutting	120
	Laser Cutting	120
	Chemical Etching	121
7.3.3	Assembly of the 3 mm Microplasma Cell	121
7.3.4	State of the Art	123
7.4	4 mm Cell	124
7.4.1	Dimensions	124
7.4.2	Assembly of the 4 mm Microplasma Cell	125
7.4.3	Electrical Testing	127
7.4.4	Vacuum Testing	128
7.4.5	State of the Art	129
7.5	Ceramic Cell	131
8	In situ Microplasma Cell TEM Imaging	135
8.1	Mounting of the Cell into the Custom Holder	135
8.2	Image Quality and Accessible Imaging Modes	136
8.2.1	Bright Field Imaging	136
8.2.2	Selected Area Electron Diffraction (SAED)	138
8.2.3	Energy Dispersive X-ray Spectroscopy (EDX)	139
9	Summary and Outlook	141
	Bibliography	147
	Acknowledgements	167
A	Technical Drawings	171

B	Additional Electrical Data from <i>in situ</i> Cell Testing	181
B.1	Vacuum Testing	181
B.2	Ceramic Cell Testing	181
C	Peer-reviewed Publications and selected Conference Contributions	185
C.1	List of Peer-reviewed Publications	185
C.2	Selected Conference Contributions	186

List of Figures

2.1	Schematic of the electrical breakdown process of a gas by an electron avalanche. Neutral gas atoms are drawn as circles, becoming ions (pathway marked with + and solid lines) after an ionizing electron collision. Pathways of electrons are marked with - and dashed lines. An electron emitted from the cathode can start the process or already present free electrons in the gas created by e.g. cosmic radiation.	8
2.2	The Paschen curves exemplarily given for air, argon and helium to highlight the solely dependence of the breakdown voltage U_{bd} on the product of pressure and electrode distance pd	10
2.3	The current dependent discharge regimes of a direct current plasma. Adapted from [68], Fig. 4.12.	11
2.4	Typical luminous regions of a DC glow discharge and other characteristic values. Adapted from [68], Fig. 9.4.	12
2.5	Schematic of a plasma surface boundary layer. The quasineutrality is broken in a region with the thickness d_s ; the so-called sheath. An again quasineutral presheath with a comparable size to the ion mean free path $\lambda_{mfp,i}$ connects the plasma bulk with the sheath. Adapted from [11], Fig. 7.1.	14
2.6	Schematic sketches of different possibilities to generate a capacitively coupled HF plasma (CCP) in a grounded vacuum chamber. A matchbox uses variable capacitors and inductors to match the plasmas impedance to the typically $50\ \Omega$ output impedance of the HF generator. a) A symmetric CCP setup as both electrodes have the same area. b) An asymmetric CCP setup with a larger grounded electrode. c) Again an asymmetric CCP utilizing the vacuum chamber walls as electrodes.	17
2.7	Paschen curves for air, Ar and He at a fixed pressure of 101 325 Pa (1 atm) and γ value of 0.1. The fixed pressure results in a solely dependence of the breakdown voltage U_{bd} on the electrode distance d	19
2.8	Schematic sketch of different MHCD setups where A denotes the anode and C the cathode. Adapted from [64], Fig. 2.	20
2.9	Structure zone diagram showcasing typical thin film features during energetic deposition. The film thickness t^* and structure depends on the generalized temperature T^* and energy flux E^* . The given numbers on the axes are only for orientation as actual numbers depend on the material and other conditions. Reprinted from Publication [225] with permission from Elsevier.	29
3.1	The basic electrical circuit used for the generation of the microplasma. a) DC power source with adjustable polarity; b,c,d) (high) voltage probes; e,h) resistors, f) inductance; g) connections to electrodes & i) ground. . .	32

3.2	Typical electric measurement of a microplasma ignition. Voltages, shown in blue and corresponding to the left y-axis, were measured directly at the power supply and at the microplasma electrodes. Discharge current, shown in red and corresponding to the right y-axis, was measured utilizing the $10\ \Omega$ shunt resistor. The discharge was ignited for roughly 10 s as visible in the center image. Voltage set at the power supply was 900 V and resulted in an electrode voltage of roughly 170 V and a current of 1.9 mA. The microplasma was operated in He with an Au electrode distance of 100 μm . The left figure is a zoom into the breakdown region. The voltage ramp up of the power supply is visible. The right figure shows the switch off region, where the voltage and current ramps down.	34
3.3	Two exemplary optical emission spectra of the microplasma operated in Ar (a) or He (b) with Au electrodes and an electrode distance of 100 μm . The normalized intensities turned out to be current and voltage independent, thus, the spectra are averaged over multiple currents. Additionally, potentially relevant atomic lines from the NIST database [255] normalized to their given maximum intensity in the region of interest are shown for the identification of the found spectral lines originating from the microplasma.	36
3.4	Illustrating one of the spatial calibration methods. A ruler with defined distances is imaged instead of the plasma. The intensity profiles along horizontal and vertical cuts through the images are analyzed. Distances between maxima correspond to the 100 μm distances between thick lines on the ruler.	38
	Schematic drawing of the PTP (Publication I)	39
	Schematic of the calibration experiment (Publication I)	39
3.6	Schematic drawings of a transmission electron microscope (TEM) and a scanning electron microscope (SEM) to showcase the different imaging mechanisms (transmission or surface signal generation) and complexity of the electrostatic lens systems, especially for the TEM.	52
	Electrical circuit of the microplasma (Publication II)	57
	Schematic sketch of the microplasma setup (Publication II)	57
	Sketch of the PTP setup (Publication III)	75
	Sketch of the Au coated TEM grid setup (Publication III)	75
	Sketch of the plasma etching setup (Publication IV)	89
	SEM image of the microsensor device (Publication IV)	89
	Sketch of the experimental setup (Publication V)	103
	Sketch of the permeability measurement technique (Publication V)	103
7.1	Illustrations of the split pole piece and the custom TEM holder for a better understanding of the given requirements.	116
7.2	a) Sketch of a cut through the TEM grid electrode to illustrate the thin film layers. b) Light microscope image of a TEM grid electrode. The 1 nm Ti film is below the 50 nm Au film.	117
7.3	Long distance microscope pictures of the Kapton spacer either produced by laser cutting or via stamping. The nominal dimensions are illustrated to showcase both manufacturing methods produce a well-suited spacer.	118

7.4	Half section view of the microplasma electrode setup.	118
7.5	CAD drawing of the 3 mm <i>in situ</i> microplasma cell shells. Technical drawings with dimensions can be found in the appendix A.	119
7.6	a) The TEM grid holder designed for the laser cut process. The centering ring is slid down after the vacuum is created and the height clamp is removed. b) The outer diameter of the TEM grid was successfully reduced with a clear edge. The heat introduced to the TEM grid during the cutting resulted in modifications of the SiN _x film at the edge visible in the reflection pattern. The window in the center was destroyed during the process.	120
7.7	a) Sketch of the TEM grid clamp made from PTFE for the chemical etching process. The diameter of the O-rings or Viton® washers can control the area to be etched. b) A chemical etched TEM grid with an intact window. The red circle indicates the target diameter of 2.3 mm. The edge got thinned due to the etching.	121
7.8	Photograph of the custom-built glove box setup. The long distance microscope images are displayed on the monitor on the left and enable a closer look during the cell assembly.	122
7.9	Photographs during the assembly of the 3 mm cell. a) The bottom O-ring, electrode and Kapton spacer are already placed inside of the bottom shell. The silver conductive paint (SCP) for this prototype was applied too close to the center of the electrode. b) The second Kapton spacer and top electrode were placed to complete the electrode stack. c) Side-view onto the electrode stack.	123
7.10	Photographs of the assembled 3 mm cell prototype. Obvious imperfections are visible as a result of errors during the assembly.	123
7.11	CAD drawing of the 4 mm <i>in situ</i> microplasma shells. Technical drawings with dimensions can be found in the appendix A.	124
7.12	Three quarter section view of the designed 4 mm <i>in situ</i> microplasma cell.	125
7.13	Long distance microscope images during the assembly of the 4 mm cell. The scale is valid for all images. a) Prepared for gluing. b) Application of epoxy. c) Conduct omitted from epoxy. d) Placement of top electrode with wire in conduct. e) Sealing the conduct with epoxy. g) Ready for closing the centering tool.	126
7.14	Pictures of the 4 mm <i>in situ</i> microplasma cell. a) Taken with the long distance microscope while still clamped in the centering tool. b) Upside down on mm paper with focus on the intact TEM window.	126
7.15	a) The applied voltage (source), the voltage present at the electrodes (cell), and the current through the microplasma (cell, red, right y-axis) over time of a glued microplasma cell. b) I-V characteristics of a glued microplasma cell ignited on several days.	127
7.16	View onto the microplasma cell inside of a low-pressure chamber connected via two contact pads on an isolating glass dish for electrical testing.	128
7.17	The applied voltage (source), the voltage present at the electrodes (cell), and the current through the microplasma (cell, red, right y-axis) over time of an <i>in situ</i> microplasma cell for the first ignition a) or the second ignition b).	129

7.18	Three quarter section view of the designed 4 mm <i>in situ</i> microplasma cell to illustrate the current path through the avalanche diode. 1) Incoming current via the wire, breakthrough of the 35 nm SiN _x insulation layer to enter the doped Si wafer. 2) Direct contact to the aluminum cell housing. 3) In the closed state a direct contact between the shells is present. 4) Again, a direct contact between the aluminum cell and the doped Si wafer is present. 5) Breakthrough of the second isolating SiN _x layer to establish contact to the second electrode, and, thus leave the cell via the second wire.	130
7.19	Long distance microscope images of the current ceramic cell design. a) The 3D printed ceramic shells on mm paper. b) The bottom electrode and both Kapton spacers stacked into the bottom cell prepared for gluing. c) Glued ceramic <i>in situ</i> microplasma cell.	132
8.1	a) Top view of the <i>in situ</i> microplasma cell connected to the adapter chip and mounted into the custom TEM holder. b) Side view of the custom TEM holder with the mounted <i>in situ</i> microplasma cell.	136
8.2	Different TEM bright field images partly overshadowed by diffraction patterns (a, f)) of two <i>in situ</i> microplasma cells. In a)-c) images of a He filled cell is shown. For the cell used for the images d)-f) the He atmosphere is expected, but could not be guaranteed.	137
8.3	Comparison of the achieved resolution at the entrance (a) and exit (b) window of the <i>in situ</i> microplasma cell. Please note, that no He atmosphere was present inside of the cell.	138
8.4	Comparison of SAED patterns of the with He filled <i>in situ</i> microplasma cell and a single electrode.	139
8.5	Comparison of EDX spectra obtained either measuring an He filled <i>in situ</i> microplasma cell or a single electrode.	139
B.1	Voltages and currents of a 4 mm <i>in situ</i> microplasma cell placed inside of a vacuum chamber at different pressures and time steps.	182
B.2	Voltages and currents of the ceramic cell to demonstrate the avalanche diode like behavior with a higher breakdown voltage compared to the cells assembled with aluminum shells.	183

List of Tables

2.1	Gas characteristic constants for Townsends empirical law and the Paschen law [83].	9
2.2	Characteristic values of microplasmas and how they were determined. For details regarding the microplasma setups or more information on the different diagnostics the interested reader is referred to the respective literature.	21
7.1	Summary of the requirements on the <i>in situ</i> microplasma cell.	116

List of Abbreviations

ATP	Active Thermal Probe
DBD	Dielectric Barrier Discharge
DCSBD	Dielectric Coplanar Surface Barrier Discharge
CAP	Cold Atmospheric Pressure
CCD	Charge-Coupled Device
CCP	Capacitively Coupled Plasma
CVD	Chemical Vapor Deposition
DBD	Dielectric Barrier Discharge
DC	Direct Current
DRIE	Deep Reactive Ion Etching
EEDF	Electron Energy Distribution Function
EF	Energy Flux
EI	Electrode
EPDM	Ethylene Propylene Diene Monomere Rubber
EU	European Union
FFT	Fast Fourier Transformation
FIB	Focused Ion Beam
HAADF-STEM	High Angle Annular Dark Field Scanning Transmission Electron Microscopy
HF	High Frequency
HR	High Resolution
HRTEM	High-Resolution Transmission Electron Microscopy
HVDC	High-Voltage Direct Current
ICCD	Intensified Charge-Coupled Device
ICP	Inductively Coupled Plasma
IR	Infrared
ITO	Indium Tin Oxide
LED	Light Emitting Diode
Mat	Material
MEMS	Microelectromechanical Systems
MHCD	Micro Hollow Cathode Discharge
NW	Nano Wire
OES	Optical Emission Spectroscopy
PECVD	Plasma Enhanced Chemical Vapor Deposition
PMMA	Poly(methyl methacrylate)
PP	Polypropylene
PTP	Passive Thermal Probe
R&D	Research & Development
REF	Rescaled Energy Flux
RF	Radio Frequency
SAED	Selected Area Electron Diffraction
SDBD	Surface Dielectric Barrier Discharge

SEDR	Surface Electron Depletion Region
SEE	Secondary Electron Emission
SEM	Scanning Electron Microscopy
S.-S.	Stainless-Steel
STEM	Scanning Transmission Electron Microscopy
SCP	Silver Conductive Paint
SZD	Structure Zone Diagramm
Tef	Teflon
TEM	Transmission Electron Microscopy
t-ZnO	Tetrapodal-ZnO
US	United States
UV	Ultraviolet
USD	United States Dollar
WCA	Water Contact Angle
VOC	Volatile Organic Compounds
XPS	X-ray Photoelectron Spectroscopy
ZA	Zone Axis

Physical Constants

Boltzmann constant	$k_{\text{B}} = 1.380\,649 \times 10^{-23} \text{ J K}^{-1}$
Elementary charge	$e_0 = 1.602\,176\,634 \times 10^{-19} \text{ C}$
Planck constant	$h = 6.626\,070\,15 \times 10^{-34} \text{ J Hz}^{-1}$
Speed of light	$c_0 = 2.997\,924\,58 \times 10^8 \text{ m s}^{-1}$
Universal constant	$A_0 = 1.201\,73 \times 10^6 \text{ A m}^{-2} \text{ K}^{-2}$
Vacuum permittivity	$\epsilon_0 = 8.854\,187\,812\,8 \times 10^{-12} \text{ F m}^{-1}$

List of Symbols

A	(surface) area	m^2
A	gas characteristic constant (Paschen law)	$\text{Pa}^{-1} \text{m}^{-1}$
A	Richardson constant	$\text{A m}^{-2} \text{K}^{-2}$
B	gas characteristic constant (Paschen law)	$\text{V Pa}^{-1} \text{m}^{-1}$
a	acceleration	m s^{-2}
C	heat capacity	J K^{-1}
C	electrical capacitance	F
c	specific heat capacity	$\text{J K}^{-1} \text{kg}^{-1}$
c_{eff}	conversion efficiency	
D	interelectrode distance	m
d	sheath thickness	m
d_f	minimum feature size	m
E	electric field strength	V m^{-1}
E_{bond}	bond potential	eV
E_{kin}	kinetic energy	eV
E_{photon}	photon energy	eV
E_{rec}	recombination energy	eV
E^*	normalized energy flux	
F	force	N
H	enthalpy	W
I	current	A
J	energy flux	W cm^{-2}
j	current density	A m^{-2}
j_A	flux of species A	$\text{m}^{-2} \text{s}^{-1}$
K_0	number of desorption escape attempts	s^{-1}
K_{desor}	desorption rate	s^{-1}
L	electrical inductance	H
M	mass	kg
m	mass	kg
N_0	total number of surface sites	
n	density	m^{-3}
n_{ref}	refractive index	
n_a	adsorbat density	m^{-2}
NA	numerical aperture	
P	power	W
p	impulse	Ns
p	pressure	N m^{-3}
Q	extra charge	C
q	charge	C
R	electrical resistance	Ω
r	distance	m
r_{reaction}	reaction rate	s^{-1}

S	gas response	
s	sticking coefficient	
s_0	initial sticking coefficient	
T	temperature	K
T_S	substrate temperature	K
T^*	generalized temperature	
t	time	s
t^*	film thickness	nm
U	voltage	V
u	velocity	m s^{-1}
V	voltage	V
V	volume	m^3
W	work function	eV
Z	atomic number	
α	cooling coefficient	$\text{J K}^{-1} \text{s}^{-1}$
α	Townsend coefficient	m^{-1}
ϵ_r	relative permittivity	
γ	secondary electron emission coefficient	
$\gamma_{\text{SV,SL,LV}}$	interfacial energy (solid-vapor, solid-liquid, liquid-vapor)	J m^{-2}
Γ_p	particle flux	$\text{cm}^{-3} \text{s}^{-1}$
$\mu_{\text{e,i}}$	electron or ion mobility	$\text{cm}^2 \text{V}^{-1} \text{s}^{-1}$
ν_{mi}	ion-neutral momentum transfer frequency	s^{-1}
ν_{iz}	ionization frequency	s^{-1}
λ	mean free path	m
λ	(light) wavelength	m
λ_D	Debye length	m
λ_I	mean free path of ionisation	m
λ_R	material-specific correction factor of the Richardson constant	
Φ	(electric) potential	V
σ	collision cross section	m^2
σ_{reaction}	reaction cross section	m^2
Θ	surface coverage	
Θ_C	contact angle	rad
Θ_h	half-angle of converging spot	rad
τ	response time	s
ω	plasma frequency	s^{-1}
ξ	damping factor	

*Dedicated to my father,
who made me believe in wonders and second chances.
Who thought me to never give up and continue fighting no
matter how bad the odds are.
But also helped me to understand, that the inevitable has to be
accepted ...*

*... and to my mother,
who showed me that even a journey without a happy end can be
wonderful, if one is surrounded by beloved people.
Who showed unbelievable strengths and never stopped being
supportive to all people around her despite sometimes being
tired and exhausted.*

*Gewidmet meinem Vater,
der mich an Wunder und zweite Chancen glauben ließ.
Der mich gelehrt hat niemals aufzugeben und zu kämpfen, egal
wie schlecht die Chancen stehen.
Aber mir auch geholfen hat zu verstehen, dass das
Unausweichliche akzeptiert werden muss ...*

*... und meiner Mutter,
die mir gezeigt hat, dass eine Reise auch ohne gutes Ende
wunderbar sein kann, wenn man von geliebten Menschen
umgeben ist.
Die unglaubliche Stärke gezeigt hat und niemals aufhörte alle
Menschen in ihrem Umfeld zu unterstützen, obwohl sie
manchmal müde und erschöpft war.*

Chapter 1

Introduction

Indispensable for today's society, but still not commonly known, physical plasma drives a lot of industrial sectors and is going to or already is influencing medical treatments and energy production. How does it happen that the term plasma is rather connected to the medical blood plasma and its importance is not commonly known? The term plasma was first used by Irving Langmuir in 1928 [1] inspired by the blood plasma as plasma contains ions and electrons embedded in neutral gas [2]. Before plasma was named plasma, luminous effects have been studied for decades [3] and were also already identified as "fourth state of matter" [4]. On earth, plasma can be observed in nature during thunderstorms in the form of lighting or at night in the sky as Aurora Borealis [5–7]. Besides these phenomena plasma on earth is mainly limited to specialized industrial sectors and scientific laboratories. Its non-equilibrium character enables chemical reactions and surface modifications of temperature-sensitive substrates, as the energy is mainly stored in electrons and ions which in most cases only represent about 1 % of the plasma's gas mixture [8–12]. These electrons and ions can drive chemical reactions and surface modifications while only slightly heating the neutral gas temperature and, thus, enabling modifications of temperature sensitive substrates or even human skin [13–17].

Since the 1970s plasma methods such as plasma etching, plasma deposition and plasma bonding have been developed on an industrial scale for the production of semiconductor devices [18, 19]. Semiconductors and respective integrated circuits rely on these plasma processes for their production, as today features of a few nanometers can be etched over 1 μm in depths and controlled film deposition is possible down to Angstroms [20–22]. Without these techniques it would not have been possible to keep up with Moore's law [23], as shrinking of the single transistor dimensions was necessary to double the number of transistors per integrated circuit chip in each technology generation [24]. The average price of a single transistor on such an integrated circuit decreased by a factor of 100 000 000 since the 1970s [18], enabling the affordability of computers, smartphones and microelectronic devices. Worldwide 336 billion¹ USD have been produced in semiconductor sales in 2014 and an ongoing growth of 10 % annually was predicted [25]. Further, close to a quarter million jobs in the semiconductor industry were estimated for the US in 2015, each of them directly supporting 4.9 times more jobs in the US [26]. Despite the already more than successful industrial application, R&D expenditures in respect to sales are with 18.4 % higher than in any other key industrial sector in the EU [27], showing the necessity to constantly improve the processes and the general understanding of the plasma surface interaction.

In the beginning, motivated by the success of the plasma processes in the semiconductor industry, the optics and glass industry adapted the low-pressure plasma processes

¹ 1 billion equals 1×10^9 according to conventions of American English

for their products [28]. Capable of producing precise micro- and nanostructures to improve functional and mechanical properties, such as scratch-resistance or hardness, plasma-enhanced chemical vapor deposition (PECVD) became the technique of choice to refine glass and even plastic surfaces [19, 29]. Not only glasses are coated with antireflection coatings, also architectural glass and windshields can be equipped with infrared blocking layers to ensure pleasant temperatures inside. In the near future, smart and energy-harvesting windows will help to save energy [30, 31].

While most glass modifications are performed under low-pressure conditions, which allow a more precise process control, different atmospheric pressure plasma sources have emerged over the past decades [32, 33]. As they can be operated without vacuum chambers at ambient pressure it is easy to integrate them into industrial assembly line production for surface activation processes of polymers and textiles [34–37]. The surface activation enables better adhesion between the treated polymer and ink or glue as hydrophilic groups are formed at the surface of the polymer [38]. Thus, chemical primers can be replaced by plasma treatment or even new processes can be established. Several big industrial companies such as Volkswagen, Miele & Cie. KG, Ford Motor Company, and BSH Bosch und Siemens Hausgeräte GmbH, have successfully integrated plasma processes into their productions [39].

Another promising application of atmospheric pressure plasmas is the use of their antimicrobial efficacy in the field of plasma medicine [40, 41]. The cold gas temperatures of non-equilibrium atmospheric pressure plasmas enable direct skin treatment and can reduce the bacterial load in wounds [42]. Furthermore, a complex redox chemistry is produced by the plasma as well as ultraviolet (UV) radiation and electric fields which all interact with the human body [40]. The complete mechanisms of action are not yet fully understood, but first results are promising also for cancer therapy [43–46].

In the near future plasma will also help to solve the global energy crisis by providing a new, rather clean, and weather-independent energy source [47–49]. While the basic concept of fusion is well known since the Cold War era, the technical realization is quite difficult. Different concepts have been developed to confine the plasma either by electric and magnetic fields or by inertia of the particles [11, 50–52]. Prominent examples for fusion experiments are the Wendelstein 7-X [53, 54] located in Greifswald, Germany, based on the stellarator concept [55] and the International Thermonuclear Experimental Reactor (ITER) [56–59] which is being built in Cadarache, France. ITER, will be the largest experimental tokamak nuclear fusion reactor and aims to demonstrate that magnetic confinement fusion is capable of producing energy.

Even apart from fusion, plasma is present already in today's power distribution systems as arc discharges appear during switching of currents at high voltages. Specialized circuit breakers had to be developed to suppress these arc discharges, as they would damage the plasma facing components, thus, limiting the life times of these switches [60]. With increasing demand for renewable energy sources like off-shore wind parks or solar thermal generation in the desert, electricity must be bridged over greater distances. High-voltage direct current (HVDC) networks would help to reduce line losses but rely on the availability of HVDC circuit breakers [61]. To improve these HVDC circuit breakers a better understanding and control of the during switching generated plasma, especially the plasma surface interaction, is necessary.

The given applications and examples only scratch the surface and can just provide an impression of the importance of physical plasmas. The plasma surface interaction was stressed in particular, as this thesis aims at providing new insights into this field with

the ultimate goal of developing a microplasma cell for integration into a transmission electron microscope (TEM). State of the art techniques are mostly limited to separation of plasma treatment and surface diagnostic by transferring the treated sample from the plasma chamber into the respective diagnostic device. Thus, surface changes only appearing during the plasma treatment or vanishing during the transport due to, e.g. reactions with ambient species, are not recognized. Overcoming this transportation barrier and developing *in situ* diagnostics to better understand the plasma surface interaction is one of the main challenges in the plasma physics community [14]. The idea of introducing a microplasma into a TEM was first published in 2013 [62] and showed plasma-induced gold thin film growths. In 2018 I had the opportunity to visit the group of Prof. Dr. Gary Eden and discuss their *in situ* TEM experiments, learning about their problems and getting input for a good start for the project beginning in 2019. Since their first and only publication in 2013 no similar achievements were reported by them or other groups, as the technological requirements are quite high. The microplasma cell has to fit into the specimen volume of the TEM which is the actual reason why a microplasma has to be chosen. Microplasmas have typically spatial dimensions in the μm -range and are operated at atmospheric pressure [63–66]. The operation at atmospheric pressure is necessary due to the low electrode distance and usually beneficial, as no vacuum equipment is needed. For TEM integration, however, its problematic, as the TEM itself is evacuated to pressures below 0.001 % of an atmosphere. Thus, the microplasma cell has to be sealed and withstand a pressure gradient of over 8 orders of magnitude.

While a successful sealing is mandatory, the image mechanism of the TEM has to be kept in mind. The electron beam has to be able to transmit through the microplasma cell which limits the thickness of at least two parallel walls of the cell to a thickness of ideally below 100 nm. These surfaces are of course highly sensitive and any kind of plasma instability like arcing onto them could result in destruction. The microplasma cell would be evacuated instantly, making plasma ignition impossible and even worse, the sudden pressure increase inside of the TEM leads to emergency shut down or misalignment of the electron optics. Thus, stability of the microplasma and the whole cell has to be ensured.

This thesis is structured as follows: First, plasma basics are addressed in chapter 2 followed by an introduction to the used plasma and surface diagnostics in chapter 3. The developed microplasma source is introduced in chapter 4 as well as the results obtained using the previously addressed conventional and non-conventional plasma diagnostics. The diagnostics focus on the stability of the microplasma and the energy flux towards the electrodes, as the plasma-induced surface modifications hopefully will be observable *in situ*.

Ex situ studies of the microplasma-induced surface modifications given in chapter 5 connect them to the energy flux measurements and in a way benchmark what to expect from the *in situ* experiments.

In chapter 6 a small digression to low-pressure plasma treatments of highly porous materials is made. These materials are of great interest due to diverse application possibilities and might be well suited to be filled into the microplasma cell to image their plasma modifications *in situ*. As preparation for the ambitious *in situ* experiments a reactive plasma environment for the modification of the porous material has to be found.

The design concerns and resulting development steps of the *in situ* microplasma cell are given in chapter 7. Two similar designs with different boundary conditions will be introduced as one is more versatile but harder to realize due to its smaller dimensions.

Within this thesis the smaller cell was not finalized due to time reasons and unavailability of special components, but still the design could prove useful for future work. Finally, images of the microplasma cell introduced into the TEM are shown in chapter 8. Sadly, no microplasma could be ignited inside of the TEM yet, but the image quality and accessible analytic techniques are discussed. The reasons why the microplasma could not be ignited and how the problems will be solved will be addressed repeatedly throughout the thesis, specifically in chapter 7.

Chapter 9 concludes the thesis and shows future perspectives of the developed microplasma cell. Upcoming scientific challenges will be addressed as well as engineering concerns on building the next generation *in situ* microplasma cell with the available knowledge gained by this thesis.

In addition to the publications used within this thesis, several scientific projects have been perused which are not directly connected to the development of the *in situ* microplasma cell. These are listed together with a few selected talks given at international conferences in the appendix.

Chapter 2

Plasma Basics

2.1 Plasma - the fourth State of Matter

Plasma is a fully or partially ionized gas composed of ions, electrons and neutral gas atoms. As "fourth state of matter" [4] it is created by adding additional energy towards a gas to enforce a phase transition similar to melting ice. By adding heat to the ice, it turns to water. Further heating of the water results in it turning into water vapor. These phase transitions are temperature and pressure dependent. If an energy input to a gas results in the creation of a considerable amount of ionized species and free electrons the plasma state is reached. Based on various parameters such as pressure or temperature plasmas can be characterized. The most important ones are the electron and ion densities (n_e, n_i) and temperatures (T_e, T_i), latter are typically given in units of energy, electron volt, where $1 \text{ eV} \equiv e_0/k_B \approx 11\,600 \text{ K}$. For most plasmas these temperatures as well as the neutral gas temperature T_g differ from each other, $T_e \neq T_i \neq T_g$. This non-equilibrium is important as already addressed in the introduction and origins mainly from the mass difference between electrons and ions. But also isothermal plasma with $T_e = T_i$ exists, e.g. in the solar plasma of the sun.

Here on earths, plasmas are usually generated by utilizing electric fields as the charged ions and electrons can be influenced by them and, thus, electrical energy can be coupled into the plasma. These charges also result in a collective behavior of the plasma, as charged species are coupled by Coulomb forces. A short overview on the plasma basics will be given, followed by the principles of plasma generation for direct current (DC) and high frequency (HF) discharges. Reactive plasmas will be shortly broached before the focus will be changed towards atmospheric pressure and more precise microplasmas. For more detailed insights, the interested reader is referred to different textbooks [5, 8–12, 67–71] or review articles [15, 32, 63–65, 72–74].

2.1.1 Quasineutrality and Collective Behavior

Plasma contains electrons and ions, still it is created from neutral gas, thus, on a macroscopic scale it should stay neutral. The charge of the ions (q_i) is usually positive, but can also be negative if the plasma-forming gas is electronegative. In total, more positive, or highly positive charged, ions are needed to fulfill the quasineutrality condition, as electrons are always negatively charged by one elementary charge e_0 :

$$\sum_k q_{i,k} n_{i,k} - e_0 n_e \approx 0. \quad (2.1)$$

For the simplest case of only single positively charged ions Eq. 2.1 can be rewritten as $n_i \approx n_e$ which basically expresses the plasma creation from neutral gas. Still, on the microscopic scale the quasineutrality can be violated and space charge zones formed.

These zones tend neutralize themselves on short timescales due to the collective behavior of plasmas.

The collective behavior characterizes a plasma and is based on Coulomb forces which describes the electrostatic interaction. In a neutral gas, particles only interact on short distances (r) during collisions due to the r^{-6} dependency of the van der Waals force. The Coulomb force, on the other hand, decays comparably slow with a r^{-2} dependency, thus, a large number charged particles interact with each other in a plasma [11].

The introduced principles of quasineutrality and collective behavior are necessary to define a plasma as follows:

“A plasma is a quasineutral gas of charged and neutral particles which exhibits collective behavior.”[8]

2.1.2 Debye-Shielding

The effect of the collective behavior becomes visible if an external, point-like extra charge Q is placed into a plasma. The Coulomb forces will lead to an attraction of electrons towards the extra charge Q while ions will be repelled from Q . Depending on the kinetic energy of the electrons and ions, their trajectories will be bent by the electric potential of Q . Higher kinetic energies result in stiffer trajectories, therefore the zone disturbed by Q should be increased with higher T_e and T_i . Within this disturbed zone the quasineutrality will be violated, but due to the collective behavior of the plasma the disturbing charge Q will be shielded by electrons and ions with the result that the quasineutrality is fulfilled on a macroscopic scale.

The size of the disturbed zone can be determined starting with a statistical description of the electrons and ions thermal motion. The so-called Boltzmann factor

$$\exp(e_0\Phi(r)/k_B T), \quad (2.2)$$

where $\Phi(r)$ denotes the electric potential, is used to calculate the number of charged species in the thermal distribution that have overcome the electric potential barrier. Poisson's equation is used to obtain a self-consistent solution for the electric potential, as it is modified by the charged particles. This approach results in a second order differential equation which solution is given by the Debye-Hückel potential [75] or sometimes called Yukawa potential [11]:

$$\Phi(r) = \frac{Q}{4\pi\epsilon_0 r^2} e^{-r/\lambda_D}, \quad (2.3)$$

ϵ_0 is the vacuum permittivity and λ_D is called the Debye shielding length (or linearized Debye length), the distance where only $1/e$ of Q 's potential is present. The Debye length λ_D is composed of the electron Debye length λ_{De} and the ion Debye length λ_{Di} in a way similar to a parallel circuit of two resistors in electricity, as in the shielding process electrons and ions work in parallel [11]:

$$\frac{1}{\lambda_D^2} = \frac{1}{\lambda_{De}^2} + \frac{1}{\lambda_{Di}^2}, \quad (2.4)$$

with

$$\lambda_{De} = \sqrt{\frac{\epsilon_0 k_B T_e}{n_e e_0^2}} \quad \lambda_{Di} = \sqrt{\frac{\epsilon_0 k_B T_i}{n_i e_0^2}} \quad (2.5)$$

as solutions of the differential equations. As expected, with increasing $T_{e,i}$ the shielding length increases as the trajectories are stiffer. Further, the shielding length decreases with increasing $n_{e,i}$ as more charged particles increase the shielding efficiency. To fulfill the quasineutrality condition it should be clear that the spatial dimensions of a plasma have to surpass its Debye length.

After the spatial dimensions have been addressed a closer look at the necessary time scale to achieve quasineutrality is taken. The electron and ion velocities ($u_{e,i}$) can be assumed to be thermal ($u_{e,i} \approx (k_B T_{e,i} / m_{e,i})^{1/2}$), if the disturbing charge Q and its potential is small. The response time τ of the electrons and ions is the time needed to travel the respective Debye length $\tau_{e,i} = \lambda_{De,Di} / u_{e,i}$. More commonly used is the so called electron or ion plasma frequency $\omega_{pe,pi}$ which is the inverse of the response time τ :

$$\omega_{pe,pi} = \frac{u_{e,i}}{\lambda_{e,i}} = \sqrt{\frac{n_{e,i} e_0^2}{\epsilon_0 m_{e,i}}}. \quad (2.6)$$

The mass dependency results in electrons reacting faster towards disturbing potentials. The collective behavior and quasineutrality can thus only be achieved if the plasma exists for a longer time period than the electron response time $\tau_e = \omega_{pe}^{-1}$.

2.2 Plasma Generation

For most technical applications the gas is converted into plasma by the introduction of electrical energy. An electrical breakdown is generated in the gas and a subsequent current flow results in the electrical discharge. Depending on the power source, electrode arrangement, and working pressure, different kinds of plasmas can be realized. Still, the gas breakdown mechanism is similar in all of them and is going to be introduced first, followed by a more detailed look at plasmas generated by direct current (DC) and high frequency (HF) sources.

2.2.1 Gas Breakdown

For an electric current flow through a plasma a sufficient number of charge carriers (electrons and ions) is necessary. These are mainly generated within the gas volume itself. Free electrons created by, e.g., cosmic radiation, are accelerated in the externally applied electric field and after a typical mean free path of ionization λ_I the electrons have gained sufficient energy to ionize a gas atom upon collision. The ionization process results in an electron-ion pair additionally to the colliding electron, thus, two electrons are now accelerated in the electric field, creating additional ion-electron pairs after λ_I and doubling again. An electron avalanche is created as illustrated in Fig. 2.1. The ions are also accelerated in the electric field towards the cathode. Upon impact they have a certain chance to emit a free electron out of the surface. This electron can start the next electron avalanche. For a self-sustained discharge, sufficient ions have to be created and reach the cathode within one avalanche process to result in the release of a free electron to start the next avalanche.

The process is described by the number of additional electrons dn_e per traveled distance dz created of the existing electrons n_e with a given probability $\alpha = \lambda_I^{-1}$:

$$\frac{dn_e}{dz} = \alpha n_e. \quad (2.7)$$

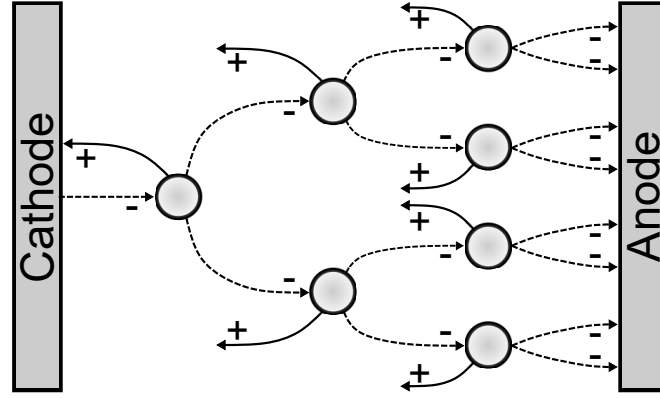


FIGURE 2.1: Schematic of the electrical breakdown process of a gas by an electron avalanche. Neutral gas atoms are drawn as circles, becoming ions (pathway marked with + and solid lines) after an ionizing electron collision. Pathways of electrons are marked with - and dashed lines. An electron emitted from the cathode can start the process or already present free electrons in the gas created by e.g. cosmic radiation.

α is called the first Townsend coefficient and it describes the already addressed electron impact ionization which is for this reason also called α -process [76]. The differential equation is solved by an exponential electron growth process

$$n_e(d) = n_e(0) \exp(\alpha d), \quad (2.8)$$

where the position 0 denotes the cathode and d the anode, as the electrode distance is defined as d . Based on the idea of an equal amount of electrons and ions produced within the avalanche process, the ion flux to the cathode $\Gamma_i(0)$ should be equal to the electron flux reaching the anode $\Gamma_e(d)$ reduced by the electron flux leaving the cathode $\Gamma_e(0)$:

$$\Gamma_i(0) = \Gamma_e(d) - \Gamma_e(0). \quad (2.9)$$

Note that the directions of the fluxes is neglected here as only the amount of particles is necessary within the present context. The electron fluxes are given by the electron density n_e , electron mobility μ_e and the applied electric field E :

$$\Gamma_e(x) = n_e(x) \mu_e E, \quad (2.10)$$

and, thus, only differ in the spatially dependent electron density. The difference in the electron density is given by the exponential factor which emphasizes if Eq. 2.9 is rewritten to

$$\Gamma_i(0) = -\Gamma_e(0) (e^{\alpha d} - 1). \quad (2.11)$$

With the introduction of $\gamma = \Gamma_e(0) / \Gamma_i(0)$, which describes the probability of releasing an electron from the cathode upon ion impact, Eq. 2.11 becomes

$$\gamma (e^{\alpha d} - 1) = 1. \quad (2.12)$$

The γ coefficient is called secondary electron emission (SEE) coefficient or second Townsend coefficient and plays a crucial role for the plasma surface interaction. Despite being normalized to incident ions, also other processes such as impacting metastable atoms or photoemission by UV radiation can result in the release of electrons.

Gas	$A / \text{Pa}^{-1} \text{m}^{-1}$	$B / \text{V Pa}^{-1} \text{m}^{-1}$
Air	10.95	273.8
Ar	10.2	176.3
He	2.25	25.5

TABLE 2.1: Gas characteristic constants for Townsends empirical law and the Paschen law [83].

Thus, one has to distinguish between purely ion induced SEE emission and effective SEE emission as these parameters can differ significantly from each other [77–80]. Here, the effective SEE coefficient is meant to formulate the balance equation Eq. 2.12 which has to be fulfilled for the gas breakdown and a self-sustained operation of the plasma.

2.2.2 Paschen Law

The dependency of gas breakdown on the electrode distance d and the pressure p (hidden in the mean free path of ionization λ_i) was first observed in 1880 [81]. In 1889 Paschen formulated the famous Paschen law [82], which empirically describes the dependence of the necessary breakdown voltage U_{bd} on the product of pressure and electrode distance pd . Townsend connected his balance equation with an empirical law for the dependence of α on the electric field, which resulted also in the Paschen law, showing that the Paschen law was a special case of a more general similarity theorem [65, 76].

Townsend's empirical law

$$\frac{\alpha}{p} = A \exp\left(-\frac{B}{E/p}\right) \quad (2.13)$$

depends on two gas characteristic constants A and B . Metaphorically speaking, the left-hand side of the equation represents the electron multiplication per mean free path and the E/p term in the exponential function represents the energy gain of an electron per mean free path. Combining Eq. 2.13 with the balance equation for self-sustained operation (Eq. 2.12) and substituting the electrical field E necessary for breakdown with the breakdown voltage $U_{\text{bd}} = Ed$ results in the Paschen law:

$$U_{\text{bd}} = \frac{Bpd}{C + \ln(pd)} \quad \text{with} \quad C = \ln\left(\frac{A}{\ln(1 + 1/\gamma)}\right). \quad (2.14)$$

The importance of the Paschen law becomes visible if the so-called Paschen curve is plotted as it is done in Fig. 2.2 for three different gases. The gas dependent constants A and B are listed in table 2.1. The value 0.1 was chosen as γ for all gases.

The necessary breakdown voltage U_{bd} is plotted on the y-axis vs. the pressure distance product pd on the x-axis. All curves show a pronounced minimum for the breakdown voltage U_{bd} , which can be explained by the following: On the left side of the minimum too few atoms are available for ionization between the electrodes. On the right side, too many atoms are present, resulting in not enough energy gain per mean free path of the electrons. Thus, the mean electron energy is insufficient to create an electron avalanche. Higher electric fields and, thus, higher breakdown voltages, can compensate for these effects.

For most cases the Paschen law can be used to gain reliable breakdown voltages. For the design of a whole plasma reactor or just an electrode arrangement it is necessary to

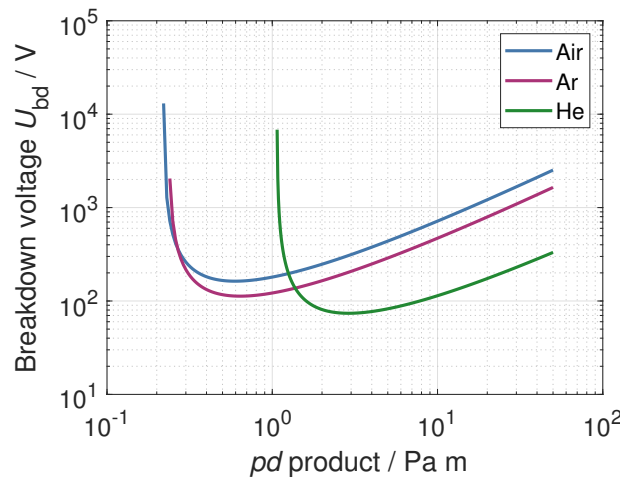


FIGURE 2.2: The Paschen curves exemplarily given for air, argon and helium to highlight the sole dependence of the breakdown voltage U_{bd} on the product of pressure and electrode distance pd .

optimize the pd product to achieve an efficient plasma generation. While low-pressure plasmas usually have larger spatial dimensions, their atmospheric pressure counterparts are restricted to small spatial dimensions as the pressure is high and, thus, the electrode distance has to be small.

At very small electrode distances below roughly $10\text{ }\mu\text{m}$ at atmospheric pressure, deviations from the Paschen law have been found in a way, that the breakdown voltage decreases while moving towards smaller pd products and no characteristic minimum is found [84–86]. Electron field emission from the cathode was found as origin of these deviations [86, 87]. The small electrode distances result in high electric fields, enabling field emission and, thus, creating a new electrode source term which can be amplified by the α -process. These deviations have to be kept in mind for the design of microplasmas which will be introduced in section 2.3.

2.2.3 Direct Current (DC) Plasma

A direct current (DC) can be used to maintain the plasma state. After plasma ignition the plasma itself acts as resistor in the electric circuit. The current flowing through the plasma influences its resistivity and, thus, the voltage drop across the discharge gap also changes, resulting in different discharge regimes. These discharge regimes and their typical current voltage characteristics are shown in 2.3.

The rather untypical procedure of current variation and measurement of the resulting voltage drop across the plasma is realized by a variable series resistor. Starting with a high series resistance and no plasma ignition, the total resistance of the circuit is infinity, as the plasma electrodes act as capacitor. Thus, the applied voltage drops across the electrodes and a plasma can be ignited if the necessary breakdown voltage is reached. Even before breakdown currents in the nA-range can be measured as a result of free electrons created by background ionization which are accelerated in the electric field. A sufficiently strong electric field leads to the α -process and, thus, a current increase through the electrode gap. The voltage approaches the breakdown voltage and for discharge currents up to $1\text{ }\mu\text{A}$, the discharge regime is called Townsend dark discharge as no luminosity is visible in the discharge gap. The discharge voltage stays close to the breakdown voltage and is nearly independent of the current.

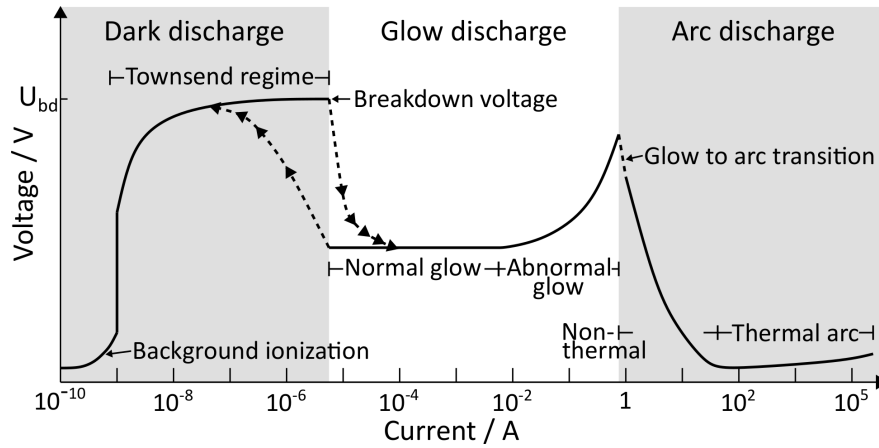


FIGURE 2.3: The current dependent discharge regimes of a direct current plasma. Adapted from [68], Fig. 4.12.

In succession to gas breakdown, a current increase results in a decreased voltage drop across the plasma as the resistivity of the plasma drops. Luminosity is only visible in the cathode region and the regime of decreasing discharge voltage is called subnormal glow. A typical feature of the subnormal glow region is a hysteresis phenomenon. Decreasing the current again does not result in a discharge voltage increase at the same threshold current. The already ignited plasma results in the creation of secondary electrons at the cathode, enabling plasma operation at lower currents.

In the current range from roughly 0.1 mA to 10 mA, the normal glow regime is found. The discharge voltage is independent of the current and the electrode gap is filled with typical luminous regions discussed in context of Fig. 2.4. Current increase in this regime results in a growth of the discharge channel dimensions until the full cathode is covered. The current density is almost constant during this growth process. As soon as the full cathode is covered, further current increase results in a rise of the discharge voltage. The current density and plasma resistivity are increasing in the so-called abnormal glow regime.

The increase in the discharge voltage rapidly changes to a fast decrease at about 1 A. The beginning of the negative differential resistance marks the glow to arc transition point. The arc discharge regime is divided in a non-thermal and a thermal arc region which differ whether the electron and ion/neutral gas temperatures are in equilibrium or not. The glow to arc transition marks the beginning of thermionic emission of electrons from the cathode. These additional electrons result in the negative differential resistance and the subsequent drop of the discharge voltage.

For most technical applications glow discharges are intended as they are operated in the non-equilibrium regime and are stable due to their ohmic behavior. If a large plasma area is striven for, such as plasma surface treatment, the transition region between normal and abnormal glow discharge is chosen, as the full cathode area is used and the increasing resistivity with increasing currents stabilizes the discharge against fluctuations.

In the glow regime several distinct luminous and dark zones can be found in the inter-electrode gap. These zones are another characteristic typical for a glow discharge and could help to verify the successful built up of a DC glow discharge. In addition to the visible, luminous zones, characteristic trajectories of plasma potential, electric field and net charge density can be found and are shown in Fig. 2.4. Close to the cathode

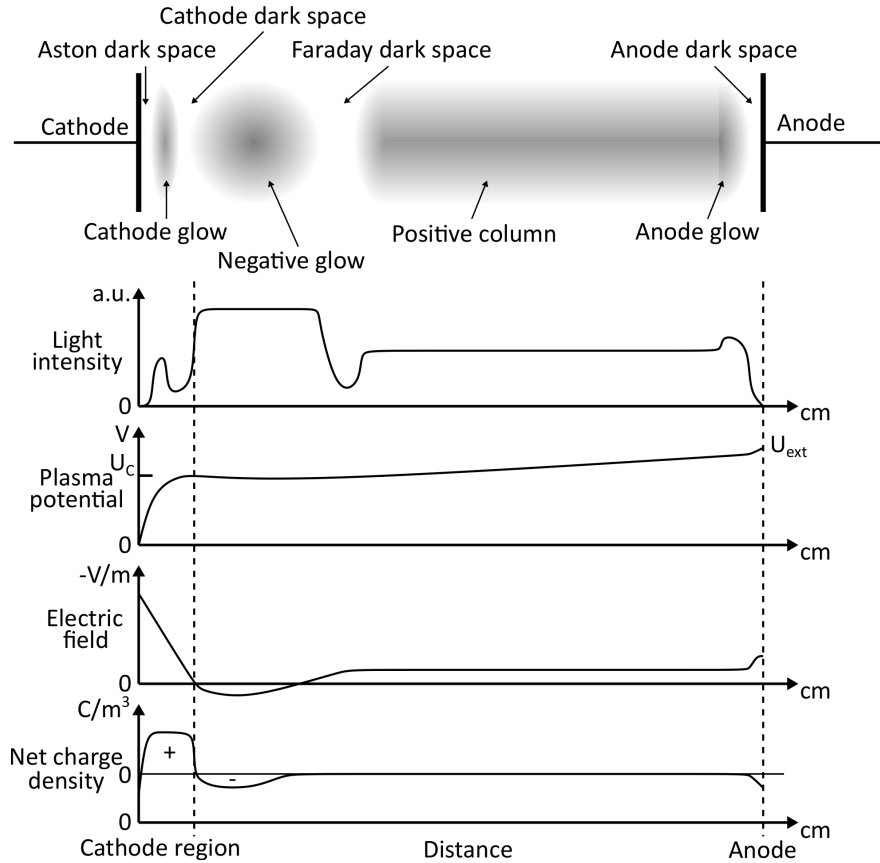


FIGURE 2.4: Typical luminous regions of a DC glow discharge and other characteristic values. Adapted from [68], Fig. 9.4.

the Aston dark space is located. It contains slow electrons accelerating from the cathode. The energy of the electrons is too low to excite or ionize atoms, thus, the region is dark. Further, the electrons lead to a negative space charge and the electric field in this region is maximized.

The Aston dark space is sometimes overlaid by the cathode glow, a luminous region, which emission is caused by excited sputtered¹ atoms from the cathode or positive ions moving to the cathode. The ion density in this region and the adjacent cathode (sometimes called Hittorf or Crookes) dark space is quite high and a positive net charge carrier density is found.

The cathode dark space concludes the cathode region, which edge is found at the boundary between the cathode dark space and the negative glow. Most of the applied voltage drops across the cathode region, which is reflected in the electric field. The voltage drop, called cathode fall, results in most power being dissipated in the cathode region, accelerating electrons to energies sufficient for ionization. The size of the cathode fall will adjust in a way that the corresponding pd product establishes the minimum in the respective Paschen curve.

The negative glow is the brightest region of the discharge. Electrons accelerated by the cathode fall ionize and excite gas atoms. The electric field in this region is the lowest of the whole discharge, still ions drift towards the cathode into the negative glow. Electrons slowed down due to the energy loss on ionization keep on moving towards the anode into the Faraday dark space.

¹Sputtering is a phenomenon where atoms are ejected from a solid surface due to bombardment of the surface with energetic particles and will be addressed in section 2.4.4.

In the Faraday dark space again mainly low energy electrons are present resulting in a negative charge density and no emission. Some electrons even drift back in the direction of the negative glow and recombine there with ions as the local electric field is reversed due to the local charge carrier densities.

Most electrons accelerate again in the Faraday dark space and enter the positive column. Here a quasi-neutral plasma is present and the electric field strength is just about high enough to maintain the required amount of ionization for secondary electron production at the cathode. The positive column usually shows a continuous, uniform glow which can be disturbed by spontaneous moving ionization waves triggered by instabilities. The length of the positive column can vary depending on the available electrode distance. While the length of the cathode region is fixed by the Paschen law, the length of the positive column will grow or shrink to fill the available space. In extreme cases the positive column can even shrink down to non-existence. A microplasma is one of these extreme cases, therefore no positive column should be existent. Furthermore, the short mean free path at atmospheric pressure should result in a heavy shrinking of all regions and most probably only the negative glow and two dark regions at the sides will be visible.

On the anode side of the positive column, the anode glow can be found, a region with slightly stronger emission. It marks the boundary of the anode sheath² and is not always visible.

The anode dark space concludes the different regions in the simplest low-pressure DC discharge and again has a negative space charge, as electrons get extracted from the positive column. The electric field rises again as the plasma shielding influence is missing. The electrons are lost for the discharge as soon as they reach the anode. The α -process leads to more electrons leaving the discharge towards the anode than entering it via the cathode which is compensated by ions as positive charge carriers move towards the cathode. In different discharge regions, especially close to the electrodes, different charge carriers are dominant for the current flowing through the discharge. These are important for any kind of plasma surface interaction and, thus, will be discussed in detail.

2.2.4 Plasma Sheath

If the plasma comes in contact with a surface, the quasineutrality is locally broken. The collective behavior leads to a shielding of the surface potential independent of the actual potential of the surface. The boundary layer needed to restore the quasineutrality is called plasma sheath. The sheath appears darker compared to the bulk plasma which is a first hint of electron depletion as these are needed to excite neutral atoms. Further insight into the sheath is necessary to understand, which species are present and, thus, can interact with the surface.

First, the contact of plasma with a plane surface is illustrated in Fig. 2.5. The surface is electrically floating. Electrons will reach the surface first due to their higher thermal velocity and mobility and will charge the initially uncharged wall negative. The negative potential repels electrons and attracts ions which results in an equal electron and ion flux to the surface. The self-stabilizing fluxes lead to a floating potential of the surface. The negative floating potential breaks the quasineutrality in the sheath with a thickness d_s as electrons are pushed out. The quasineutrality is restored again in the presheath with dimensions of roughly the ion mean free path $\lambda_{mf,i}$ as a collisionless

²The plasma sheath will be discussed in the next section 2.2.4 as it is the key region for any kind of plasma surface interaction.

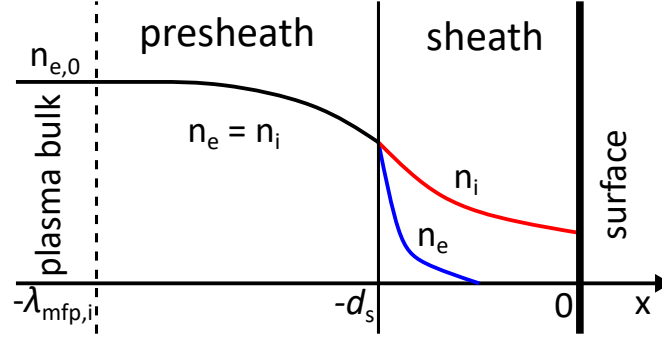


FIGURE 2.5: Schematic of a plasma surface boundary layer. The quasineutrality is broken in a region with the thickness d_s ; the so-called sheath. An again quasineutral presheath with a comparable size to the ion mean free path $\lambda_{\text{mfp},i}$ connects the plasma bulk with the sheath. Adapted from [11], Fig. 7.1.

sheath ($p \leq 0.5$ Pa [88, 89]) is assumed here for simplicity.

Child-Langmuir Law

In the next step, an external potential is given to the surface in a way that the potential difference between the surface and the sheath edge is large compared to the thermal electrons $|\Phi(0) - \Phi(-d_s)| \gg k_B T_e / e_0$. The Boltzmann factor ensures only a few electrons can overcome the potential barrier, thus, the electron density becomes

$$n_e(x) = n_e(-d_s) \exp\left(\frac{e_0(\Phi(x) - \Phi(-d_s))}{k_B T_e}\right). \quad (2.15)$$

With the assumption of a collisionless sheath, the ion velocity $u_i(x)$ in the sheath is given by energy conservation:

$$\frac{1}{2} m_i u_i^2(x) + e_0 \Phi(x) = \frac{1}{2} m_i u_i^2(-d_s) + e_0 \Phi(-d_s), \quad (2.16)$$

with an initial velocity $u_0 = u_i(d_s)$ and setting $\Phi(-d_s) = 0$ to be

$$u_i(x) = \sqrt{u_0^2 - \frac{2e_0 \Phi(x)}{m_i}}. \quad (2.17)$$

For a steady-state solution for the ion flux towards the surface without ionization or recombination in the sheath, the velocity can be combined with the continuity equation $n_i(x) u_i(x) = n_i(-d_s) u_0$ to obtain the reduced ion density:

$$n_i(x) = n_i(-d_s) \left[1 - \frac{2e_0 \Phi(x)}{m_i u_0^2}\right]^{-1/2}. \quad (2.18)$$

Poissons' equation is used to self-consistently determine the electric potential distribution and ion density. Assuming $2e_0 |\Phi(x)| \gg m_i u_0^2$, which states that the ions gain

much more energy due to the acceleration in the sheath compared to their initial energy, Poissons' equation becomes

$$\Phi''(x) \approx -\frac{e_0 n_i(-d_s)}{\epsilon_0} \left(-\frac{2e_0 \Phi(x)}{m_i u_0^2} \right)^{-1/2}. \quad (2.19)$$

Solving the differential equation and introducing the (constant) ion current density $j_i = e_0 n_i(-d_s) u_0$ the potential distribution in a space charge sheath reads [11]:

$$\Phi(x) = \left(\frac{3}{2}\right)^{4/3} \left(\frac{m_i}{2e_0}\right)^{1/3} \left(\frac{j_i}{\epsilon_0}\right)^{2/3} (x + d_s)^{4/3}, \quad (2.20)$$

which can be rephrased using the total voltage drop across the sheath U to connect ion current density j_i , sheath thickness d_s and the voltage drop $U = \Phi(-d_s) - \Phi(0)$:

$$j_i = \frac{4}{9} \epsilon_0 \sqrt{\frac{2e_0}{m_i}} \frac{U^{3/2}}{d_s^2}. \quad (2.21)$$

Equation 2.21 is the famous Child-Langmuir law for the collisionless sheath [90, 91]. Further, the initial ion velocity u_0 of ions entering the sheath can be clearly defined following the Bohm-criterion [11, 92]

$$u_0 = v_B = \sqrt{\frac{k_B T_e}{m_i}} \quad (2.22)$$

and v_B is the so called Bohm velocity.

Another quantity which can be determined for the collisionless sheath is the potential and the electron and ion density at the sheath edge. The ions are accelerated to the Bohm velocity v_B in the presheath and, thus, the potential at the sheath edge can be estimated to be

$$\Phi(-d_s) \approx -\frac{1}{2} \frac{k_B T_e}{e_0} \quad (2.23)$$

based on the energy conservation $1/2 m_i v_B^2 = 1/2 k_B T_e$. Accordingly, the electron and ion density can be estimated with the Boltzmann factor similar as done in Eq. 2.15:

$$n_i(-d_s) = n_e(-d_s) = n_{e,0} \exp\left(\frac{e_0 \Phi(-d_s)}{k_B T_e}\right) = n_{e,0} \exp\left(-\frac{1}{2}\right) \approx 0.61 n_{e,0}, \quad (2.24)$$

where $n_{e,0}$ represents the electron density in the plasma bulk.

Collisional Sheath

For the collisional sheath the situation is way more complex as, e.g., the energy conservation has to account for collisions. Further, already for weakly collisional plasmas, a unique sheath edge position is not exactly defined and is a matter of definition [93]. Numerical calculations including kinetic treatment of collisions have to be performed to calculate the sheath thickness, transitions regions, ion velocities and electric potentials [94, 95]. For a detailed description the reader is referred to the given literature as only a few relations will be given here for comparison with the collisionless sheath to give an impression of how collisions affect these.

For a highly collisional plasma where the ion mean free path $\lambda_{\text{mfp},i}$ is in the order of or

even below the Debye length $\lambda_{D,s}$ near the sheath edge, $\lambda_{mfp,i} \leq \lambda_D$, the ion mobility is limited due to the large number of collisions. The sheath width d_s becomes

$$d_s \approx K (\lambda_{De}^2 d)^{1/3} \approx (\pi K^3)^{1/2} \lambda_{D,s}, \quad (2.25)$$

where K is a coefficient of order unity, λ_{De} the electron Debye length in the plasma bulk, $\lambda_{D,s}$ the Debye length near the sheath edge and d the electrode distance [96]. K was later identified to be dependent on the ionization frequency ν_{iz} and the ion-neutral momentum transfer frequency ν_{mi} , $K \approx 2.2 + \log_{10}(\nu_{iz}/\nu_{mi})$ [97].

The initial ion velocity while entering the sheath is reduced due to the collisions and lies below the Bohm velocity v_B :

$$u_0 \approx v_B \sqrt{C \lambda_{mfp,i} / \lambda_{D,s}}, \quad (2.26)$$

where C is again a coefficient in the order of unity [98].

In addition, the Child-Langmuir law has to be modified to take collisions into account as the assumption of energy conservation fails. If the ionization within the sheath region is negligible the continuity equation still holds, but the ion velocity now depends on the ion mobility μ_i which itself is a function of the ion mean free path $\lambda_{mfp,i}$ and the ion velocity u_i . For an intermediate pressure regime (0.5 Pa to 20 Pa [88, 89]) $\lambda_{mfp,i}$ is found to be relatively independent of u_i and can thus be assumed constant [9]. Utilizing Gauss' law and performing two integration results in the collisional form of the Child-Langmuir law for the intermediate pressure regime where $\lambda_{mfp,i}$ is independent of u_i [9]:

$$j_i = \frac{2}{3} \left(\frac{5}{3}\right)^{3/2} \epsilon_0 \sqrt{\frac{2e_0 \lambda_{mfp,i}}{\pi m_i}} \frac{U^{3/2}}{d_s^{5/2}}. \quad (2.27)$$

For the high pressure case (above 20 Pa [88, 89]) the ion mobility μ_i itself is found independent of the ion velocity u_i . Following the same steps as before results in

$$j_i = \frac{9}{8} \epsilon_0 \mu_i \frac{U^2}{d_s^3} \quad (2.28)$$

the Child-Langmuir law for a highly collisional sheath. Depending on the pressure regime the scaling of the ion current density j_i , or total current density if the current in the sheath is not mainly driven by ions [9], with the voltage drop U and the sheath thickness d_s change. Thus, knowledge about the collisional regime is necessary to make predictions about the relation between j_i , U and d_s . For the development and validation of microplasmas within this thesis, the highly collisional Child-Langmuir law will be utilized, as these microplasmas are operated at atmospheric pressure. If it is possible to experimentally determine j_i , U and d_s , and these values fulfill Eq. 2.28, an additional proof for the successful built up of a glow discharge could be given.

2.2.5 High Frequency (HF) Plasma

An alternative way for plasma generation is the usage of an electrical high frequency (HF) signal with alternating applied voltages instead of the time invariant direct current (DC). Despite the fact, that no HF signal was used for the generation of the microplasma, several experiments of the present thesis have been performed in a low-pressure HF plasma and, therefore, its foundations are addressed here. HF plasmas, sometimes also called rf (radio frequency) plasmas, are realized utilizing radio waves with frequencies between 1 MHz and 100 MHz. Usually, and also in this thesis,

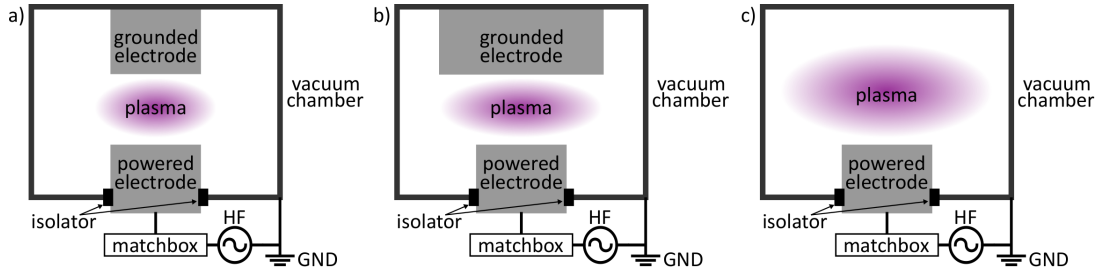


FIGURE 2.6: Schematic sketches of different possibilities to generate a capacitively coupled HF plasma (CCP) in a grounded vacuum chamber. A matchbox uses variable capacitors and inductors to match the plasmas impedance to the typically $50\ \Omega$ output impedance of the HF generator. a) A symmetric CCP setup as both electrodes have the same area. b) An asymmetric CCP setup with a larger grounded electrode. c) Again an asymmetric CCP utilizing the vacuum chamber walls as electrodes.

13.56 MHz and its harmonics are used for plasma generation, as these frequencies are approved for technical applications. According to Eq. 2.6 with typical electron densities in the range of 10^{15} m^{-3} to 10^{16} m^{-3} , the electron plasma frequency is in the range of GHz while the ion plasma frequency is comparably slow in the low MHz range. Electrons exposed to an alternating electric field with a frequency of 13.56 MHz can follow the field smoothly while ions are too inert and rest in the plasma bulk only reacting to mean electric fields.

Electrons typically reach energies in the range of 1 eV to 5 eV and collide with neutral gas atoms creating new electron ion pairs due to impact ionization. Kinetic energy, however, is barely transferred due to the large mass difference between electrons and ions or neutral gas atoms. The ion and neutral gas temperature consequently stays near room temperature at roughly $25\text{ meV} \cong 290\text{ K}$, which enables the plasma treatment of temperature sensitive materials [69]. An advantage of HF plasmas is the possibility to use dielectric electrodes or place insulating samples on the electrodes. In DC plasmas the dielectric between the electrodes prevents a current flow, thus, no plasma can be ignited. The HF alternating electric field results in a displacement current which creates an indirect contact between electrode and plasma.

The forming plasma sheath is time-dependent for alternating electrical fields, as the formed positive space charge region in the sheath is either enlarged as electrons are pushed away from the electrode during the negative half cycle of the alternating current or narrowed during the positive half cycle [99]. The relations discussed in section 2.2.4 for the DC case are also applicable in HF plasmas. The time averaged electron and ion current density as well as an averaged, DC-like, voltage drop across the sheath is again connected with the sheath dimensions via the Child-Langmuir law with a small change. The sheath thickness enlarges by a factor of $\sqrt{50/27} \approx 1.36$ in the collisionless case due to the time averaging of the electron and ion densities [9].

Capacitively coupled HF discharges can either be symmetric or asymmetric depending on the electrode setup. Fig. 2.6 shows schematic sketches of capacitively coupled plasma (CCP) reactors for both cases. In the symmetric case (Fig. 2.6a) the plasma facing area of both electrodes is equal. Changing the area ratio to values except for 1 results in an asymmetric CCP (Fig. 2.6 b & 2.6 c).

A plasma sheath is formed at both electrodes and in the symmetric case the voltage drop across both sheaths is identical. Based on the continuum equation the current I or the amount of charge \dot{Q} flowing through both electrodes indexed with a and b has

to be equal,

$$I_a = I_b \quad \dot{Q}_a = \dot{Q}_b. \quad (2.29)$$

Thus, the amount of charge transferred during one period of the HF signal \bar{Q} is also equal $\bar{Q}_a = \bar{Q}_b$. Assuming the the plasma electrode transitions as series circuit with two parallel plate capacitors C_a and C_b [100], the voltage drop across both sheath regions can be expressed as follows:

$$\bar{Q}_{a,b} = \bar{U}_{a,b} C_{a,b} = \epsilon_0 \bar{U}_{a,b} \frac{A_{a,b}}{d_{s,a,b}}, \quad (2.30)$$

where $A_{a,b}$ denotes the electrode areas. A direct connection between the electrode areas, the mean voltage drop and the mean sheath thickness is found utilizing $\bar{Q}_a = \bar{Q}_b$:

$$A_a \frac{\bar{U}_a}{d_{s,a}} = A_b \frac{\bar{U}_b}{d_{s,b}}. \quad (2.31)$$

Further connections between the voltage drop across the sheath and the sheath's dimensions are found based on the Child-Langmuir law for the collisionless sheath (Eq. 2.21), the intermediate pressure regime (Eq. 2.27), or the high pressure case (Eq. 2.28). Provided that an equal current density is present at the electrodes the following relations can be derived:

$$\text{collisionless:} \quad \frac{\bar{U}_a^{3/2}}{d_{s,a}^2} = \frac{\bar{U}_b^{3/2}}{d_{s,b}^2} \quad (2.32)$$

$$\text{intermediate pressure:} \quad \frac{\bar{U}_a^{3/2}}{d_{s,a}^{5/2}} = \frac{\bar{U}_b^{3/2}}{d_{s,b}^{5/2}} \quad (2.33)$$

$$\text{high pressure:} \quad \frac{\bar{U}_a^2}{d_{s,a}^3} = \frac{\bar{U}_b^2}{d_{s,b}^3} \quad (2.34)$$

Combining these equations with Eq. 2.31 results in three expressions which connect the voltage drops with the electrode areas:

$$\frac{\bar{U}_a}{\bar{U}_b} = \left(\frac{A_a}{A_b} \right)^{5/2 \dots 3 \dots 4}. \quad (2.35)$$

The theoretical exponent depends on the pressure regime. Experiments showed the exponent being slightly below 5/2 [9].

Equation 2.35 closes the loop to Fig. 2.6 and the reasoning to differentiate between symmetric and asymmetric CCPs. In asymmetric CCPs an additional voltage at the smaller electrode is necessary to fulfill the equal charge transport requested by the continuum equation and assumed in the preceded derivation. A DC self-bias forms as a result of the geometrical asymmetry if the smaller electrode is galvanically isolated as its usually the case due to capacitors in the matchbox. The forming self-bias is usually negative and, thus, accelerates positive ions towards the smaller electrode. The additional kinetic energy of the ions can be used to enhance plasma surface processes discussed in section 2.4 and can be therefore beneficial.

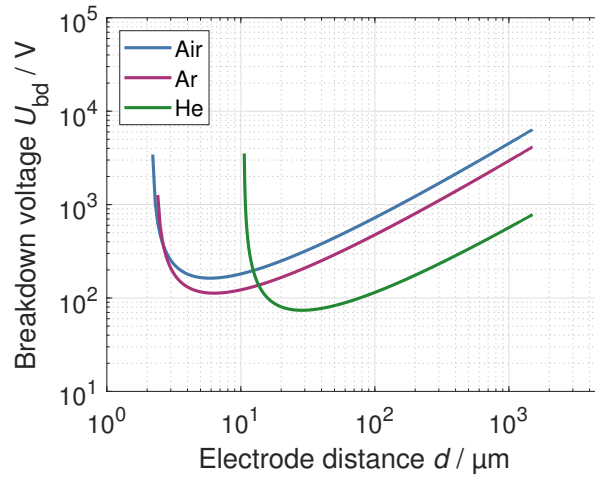


FIGURE 2.7: Paschen curves for air, Ar and He at a fixed pressure of 101 325 Pa (1 atm) and γ value of 0.1. The fixed pressure results in a solely dependence of the breakdown voltage U_{bd} on the electrode distance d .

2.3 Microplasma

A microplasma, sometimes also called microcavity plasma or microdischarge, is "*a weakly-ionized, nonequilibrium plasma spatially confined to a cavity having a characteristic dimension d between nominally 1 μm and 1 mm [...]*" [63]. According to the Paschen law (cf. section 2.2.2), the gas pressure p has to be in the range of or even above atmospheric pressure to obtain favorable pd products for plasma ignition. Fig. 2.7 shows the Paschen curves for atmospheric pressure (101 325 Pa) and a γ -value of 0.1. The fixed pressure results in a solely dependence on the electrode distance. The minima are found at 30 μm for He or 6 μm for air and Ar, respectively, which indicate optimal electrode distances for the discharge design.

Aside from their ability to be operated at and above atmospheric pressure, microplasmas combine several unique properties. Their characteristic specific power loadings are in the range from $10 \times 10^4 \text{ W cm}^{-3}$ to $10 \times 10^6 \text{ W cm}^{-3}$ which is of particular importance for the efficient production of radiation from short-lived atomic or molecular species [63]. Their small volume enables these high-power densities but also aggravates the plasma diagnostics. Thus, diagnostics are mostly limited to optical diagnostics and electrical measurements. Also, plasma modeling was performed on different microplasma geometries confirming measurement results and delivering new insights [101–105]. The electron energy distribution function (EEDF) was found to be non-Maxwellian independent of the discharge geometry. The short mean free paths, among other things, is the origin of the non-Maxwellian behavior. The electron temperatures T_e can locally reach up to 5 eV or even higher values if the discharge is operated in a pulsed operation mode. Mean values for T_e are typically in the range of 1 eV to 2 eV. Electron densities n_e were found six orders of magnitude larger compared to typical low-pressure plasmas reaching from $1 \times 10^{21} \text{ m}^{-3}$ to $5 \times 10^{22} \text{ m}^{-3}$ in noble gases depending on the operation mode and from $1 \times 10^{19} \text{ m}^{-3}$ to $1 \times 10^{22} \text{ m}^{-3}$ in atmospheric air. While operated in noble gases and below atmospheric pressure, the non-equilibrium state is achieved and gas temperatures are found close to room temperature. For atmospheric air, on the other hand, the neutral gas was heated up to

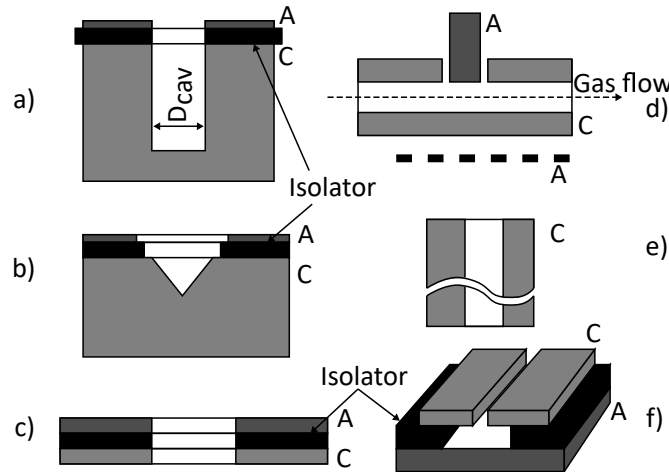


FIGURE 2.8: Schematic sketch of different MHCD setups where A denotes the anode and C the cathode. Adapted from [64], Fig. 2.

2000 K. A list of these typical parameters as well as the applied diagnostic for determination and the literature sources for more information is given in table 2.2.

Microplasmas have been realized in various setups. These setup designs were in the beginning motivated by the pure possibility of realizing stable discharges at high pressure but rapidly the setups were designed directly for different applications. The first and most of the diffuse microplasmas have been realized with hollow cathode setups. The basic idea of a hollow cathode is to increase an electrons path to the anode, enabling more ionizing collisions with neutral gas atoms prior to the electron impinging on the anode. Therefore, typically a cylindrical cathode is chosen, as e.g. sketched in Fig. 2.8 a), resulting in pendulum electrons oscillating in between the opposing cathode fall regions while slowly drifting towards the anode.

A few realized microhollow cathode discharge (MHCD) setups are sketched in Fig. 2.8. The cathodes were mechanically or laser drilled but also produced by Si etching profiting from the experience from the microelectromechanical systems (MEMS) industry. Individual discharges, but also large arrays of these individual MHCDs were realized. For the design of MHCD not only the Paschen law plays an important role, but also the White-Allis similarity law [106, 107], which connects the necessary discharge sustaining voltage U_{sus} to the pd product and the ratio of discharge current over cathode cavity size (I/D_{cav}). According to the White-Allis similarity law, high-pressure operation of hollow cathodes can be possible by reducing the cathode cavity D_{cav} . A lower limit for D_{cav} is fundamentally given by the fact, that the cathode cavity and, thus, the distance between two opposing cathodes, can not be smaller as two cathode fall regions and a negative glow region. For Ar as working gas the upper limit of the pD_{cav} product is 1.33 Pa m [108] which results in values of D_{cav} 10 μm for atmospheric pressure operation. Stable operation in the range of this minimal dimensions could be experimentally demonstrated in mechanically drilled cavities [109]. Still, despite working in the theoretical accessible regime, modeling [102, 103], emission studies [110] and current-voltage characteristics [108, 111] showed, that many MHCD devices lack characteristic features of conventional hollow cathodes and rather operate as a glow discharge. Thus, one has to be careful to not characterize a microplasma purely by the setup.

Parameter	Value/Range	Operation	Gas	Pressure	Diagnostic	Source
EEDF	Non-Maxwellian	DC	air	67 Pa	Langmuir probe	[112]
	Non-Maxwellian	DC & pulsed	Xe, Ar, He	5333 Pa to 101 325 Pa	Excimer excitation	[113]
Electron temperature T_e	1 eV	DC	Ar	101 325 Pa	OES ¹	[64, 114]
	1 eV	DC	Ar	101 325 Pa	OES ¹	[115]
	2.25 eV	pulsed	Ar	101 325 Pa	OES ¹	[115]
Electron density n_e	$1 \times 10^{21} \text{ m}^{-3}$	DC	Ar	101 325 Pa	Stark ²	[115]
	$9 \times 10^{20} \text{ m}^{-3}$ to $5 \times 10^{21} \text{ m}^{-3}$	DC	Ar	5000 Pa to 40 000 Pa	Stark ²	[116]
	$5 \times 10^{22} \text{ m}^{-3}$	pulsed	Ar	101 325 Pa	Stark ²	[115]
	$1 \times 10^{19} \text{ m}^{-3}$ to $1 \times 10^{22} \text{ m}^{-3}$	pulsed	air	101 325 Pa	HIRI ³	[64, 117–119]
Neutral gas temperature	400 K	DC	Ne	53 329 Pa	OES ¹	[120]
	380 K to 1700 K	DC	Ar	5000 Pa to 40 000 Pa	Abs. spectroscopy ⁴	[116]
	1000 K to 2000 K	pulsed	air	101 325 Pa	HIRI ³	[64, 117–119]
	360 K	DC	He	101 325 Pa	OES ¹	[121]
	460 K to 860 K	DC	Ar	101 325 Pa	OES ¹	[121]

¹ Optical emission spectroscopy, evaluation of line intensity (T_e) or rotational N_2 bands (gas temperature)

² Stark broadening and shift, caused by localized electric fields and is sensitive to n_e and T_e

³ Heterodyne infrared (IR) interferometry, free electrons induce a phase shift in an IR laser

⁴ Absorption spectroscopy, Doppler broadening of (in this case) Ar lines

TABLE 2.2: Characteristic values of microplasmas and how they were determined. For details regarding the microplasma setups or more information on the different diagnostics the interested reader is referred to the respective literature.

Contrary to the diffuse microplasmas also filamentary microplasmas have been realized, which excel by a different excitation mechanism and setup [15, 73]. The so-called streamer mechanism can take over and replace the previously described Townsend breakdown (cf. 2.2.1). A high gas density results in a high number of ionizing collisions per unit volume. A space charge zone can form, which locally enhances the applied electric field and leads to additional electron avalanches forming in the gas phase [70, 71, 122]. The ionization region rapidly grows until a distinct plasma channel is formed. This channel is called streamer and forms within nanoseconds [15].

Similar to the Townsend-criterion being the foundation for the breakdown voltage in a Townsend discharge, the Meek criterion, $\exp(\alpha d) = 10^8$, relates to the charge number density in the primary avalanche necessary for significant space charge field perturbations [122]. Thus, the Meek criterion describes conditions for streamer initiation. Obviously, the α -coefficient plays a major role for the tendency of a specific gas to form a streamer. Additionally, the reduced electric field (E/n) will influence the streamer formation. The increased ionization rate due to changes in the local electric field is determined by the partial derivative $\partial(\alpha/n)/\partial(E/n)$ [123]. He and Ne suppress rapid formation of field gradients and have a relatively high α -coefficient, thus, these gases tend to form a rather diffuse breakdown. Ar and most molecular gases, on the other hand, tend to form streamers and, thus, rather filamentary discharges are obtained. For a successful discharge development, the choice of the right working gas is of great importance.

Streamers are typically small with channel radii in the range of 100 μm and channel length depending on the discharge geometry and applied voltages ranging from μm to a few mm. The small radii can result in high current densities and, thus, trigger the glow to arc transition (cf. 2.2.3). Dielectric materials covering at least one electrode can be used to limit the current and suppress the arc transition. The non-equilibrium character of the plasma can be preserved by strictly limiting the current. Setups utilizing at least one dielectric to separate the electrodes are called dielectric barrier discharges (DBD) [34, 124, 125].

DBD discharges have to be operated with AC currents or in a pulsed mode, as the dielectric interrupts the current flow and, thus, results in charge carrier accumulation on its on surface. These charges result in an electric field opposing the externally applied one. The electric fields cancel each other and the plasma state can not be maintained. If the direction of the applied field is switched due to AC operation, the accumulated charge carrier will enhance the electric field strength and simplify the next gas breakdown. This memory effect results in effluents forming at the same locations and only barely moving.

For industrial applications and large-scale surface or gas treatments, surface dielectric barrier discharges (SDBDs) have been developed, where the electrodes are embedded in or separated by a ceramic and a plasma layer forms on top of the ceramic [126–132]. Despite of the partly diffuse looking appearance of these discharges, the plasma layer is build up from individual microdischarges [133].

Microplasmas, with or without a dielectric barrier, can also be utilized as plasma source for cold atmospheric pressure plasma jets [134] and are mentioned here for the sake of completeness. A continuous gas flow between the electrodes transports reactive, plasma generated species out of the plasma jet, thus, an effluent is formed, which can be used for, e.g., surface treatments [135]. Famous examples for these kinds of jets are the kINPen [136] and the COST jet [137].

The, geometry-wise, simplest microplasmas can be generated between two parallel electrodes. In contrast to MHCD geometries, the open area, where radiation can

leave the microplasma or ambient species can interact with the plasma, is significantly smaller, thus, for many applications the MHCD setup is superior. Still, the simplicity of the geometry simplifies modeling and some plasma diagnostics. Fundamental research on the applicability of fundamental plasma physics laws formulated and validated under low-pressure conditions can be done, to ensure their transferability to atmospheric pressure conditions. As the MCHD are not only working in the conventional hollow cathode regime, simulation could show, that determined characteristic values for MHCDs (cf. table 2.2) also apply for a parallel electrode setup [101, 138]. Further, experimental studies could proof the validity of the Paschen law [86, 139, 140] and the possibility to reach different stable and diffuse operation regimes via controlling the current [141, 142]. Overall, a simple parallel plate geometry is well suited to be realized, especially when the discharge geometry is subject to external restrictions.

2.4 Plasma Surface Interaction

The plasma surface interaction is a complex topic, due to several processes taking place simultaneously on similar or completely different time scales. Moreover, these processes are not limited to the field of plasma physics, as chemistry and solid state physics are heavily involved. Separating these processes to gain a fundamental understanding is nearly impossible. Still, great efforts have been taken in the past, as a better understanding of the plasma surface interaction is necessary to overcome current limitations in, e.g., material synthesis, etching, thin film deposition and plasma catalysis [14, 143–149].

2.4.1 Secondary Electron Emission

Section 2.2.1 already briefly introduced the secondary electron emission (SEE) coefficient γ and addressed processes influencing the SEE generation. To understand the fundamental process, the confinement of electrons in a solid is shortly addressed. In metals, electrons fill the conduction band, a set of specific energy levels, up to a certain energy, the so-called Fermi energy. The difference between the Fermi energy and the potential energy level of a free electron is the work function of the metal [150]. If an electron gains enough energy to overcome the work function of the specific metal, it is emitted from the surface.

In the gas phase an ion can not be neutralized by an electron impact without a third collision partner, as energy and momentum can not be conserved. However, if an ion is approaching a surface, the surface can act as third collision partner. At a critical minimal distance between the ion and the surface, an electron can tunnel through the work function potential barrier and neutralize the ion. The electron either enters an excited state, which results in radiation until a metastable state or ground state of the previously ion, now atom is reached. The electron could also directly enter the ground state while the excess recombination energy is absorbed by a second electron, which is still in the conduction band. The so-called Auger neutralization thus involves two electrons. Depending on the gained recombination energy of the second electron it may be released from the solid. This second option is called Auger emission or secondary emission.

The SEE coefficient γ depends on the work function W of the material³ and the recombination/ionization energy E_{rec} of the approaching ions. An empirical expression

³Despite being illustrated for metals, the same principle is also valid for semiconductors and insulators.

considering these quantities could be identified [71]:

$$\gamma \approx 0.016 (E_{\text{rec}} - 2W). \quad (2.36)$$

The Auger emission process purely depends on the transferred recombination energy of the ion. But there are more processes, which can transfer energy to a surface and therefore, can result in secondary emission. Thus, one has to differentiate between purely ion induced SEE and effective SEE. The effective SEE coefficient γ_E is still defined by the number of electrons released from the surface per incident ion, but also allows for energetic contributions not transferred by ions such as de-excitation of metastables at the surface, radiation towards the surface or impinging fast neutrals [78, 80, 151]. Especially in highly collisional plasmas, ions will transfer energy towards neutral species via collisions, thus, a comparably high amount of energy will be transferred to the surface via non-ionic species.

The transferred energy usually also heats the surface which can result in thermionic emission. A charge carrier is liberated from the surface as it gained sufficient thermal energy from the surface to overcome the work function of the respective surface material. For electrons the thermal electron emission or also called Edison effect [152] from a hot cathode in vacuum only becomes significant at temperatures above 1000 K. The Richardson equation describes the current density j of the thermal electron emission as follows [153–155]:

$$j = AT^2 e^{-W/(k_B T)}, \quad (2.37)$$

where A denotes the Richardson constant, T the temperature, and W the work function. The Richardson constant is actually not a constant, instead depends on a universal constant A_0 multiplied by a material-specific correction factor λ_R in the order of 0.5. The universal constant is given by $A_0 = 4\pi m_e k_B^2 e_0 / h^3 \approx 1.2 \times 10^6 \text{ A m}^{-2} \text{ K}^{-2}$ with h representing the Planck constant [154, 156, 157]. In case of the surface being the negatively charged cathode, the Schottky effect can enhance the electron thermal emission, as the electric field lowers the effective, energetic surface barrier given by the work function [158, 159]. For, e.g. fusion plasmas, it is quite obvious that thermionic emission influences the plasma [160], but also for low-pressure plasmas [161] or more specific glow discharges [162], the thermionic emission can play a crucial role given specific conditions. For the DC microplasma aimed for in this thesis, the thermionic emission should not be significant. Except when the power transfer from the plasma to the surface leads to highly localized heating of the surface.

But not only the plasma generated species can influence the SEE, also the surface condition, morphology, impurities, and contamination play a crucial role [163, 164]. Therefore, the determination of ion-induced or effective SEE coefficients is challenging but important for modeling and discharge design. A theoretical approach to calculate SEE values, as well as a more detailed description and several previously determined SEE values can be found in literature [9, 77–79, 139, 151, 163–170].

2.4.2 Adsorption and Desorption

Adsorption is the reaction of an atom or molecule with a surface, where as a consequence the atom or molecule is bound to the surface. The reversed reaction is called desorption [171]. Adsorption is separated into two different processes.

Physisorption is based on the rather weak van der Waals force between the atom or molecule and the surface. The binding energy is in the range of 4 meV to 40 meV per bond and the binding is a consequence of fluctuating polarizations of the atoms due

to quantum mechanics [172]. Physisorbed atoms and molecules can rapidly diffuse along the surface which can be beneficial to achieve uniform thin film growths, as they might diffuse to a free spot to get chemisorbed. If the impinging species did not thermalize with the surface upon impact they will diffuse across the surface as "hot precursors" [173] which significantly increases their chance to chemisorb at the surface. A typical example for the adsorption of "hot precursors" is the adsorption of H on an otherwise H-terminated silicon surface [174, 175].

Chemisorption is the result of a chemical bond such as, e.g., ionic or covalent bonding. The foundation of these forces is an electromagnetic force in between the negatively charged electron cloud and the positively charged nuclei. In the bonding participating atoms share and transfer electrons, which results in the strong bonding with binding energies of a few eV. Therefore, surfaces are chemically transformed by chemisorption [176].

All forming bonds at the surface are an exothermic reaction. A bond specific minimum energy of the atom or molecule is necessary to initiate the reaction. In plasma processes, with the possibility to accelerate ions towards the surface or create fast neutrals due to collision, the energy barrier can be overcome and the following bond formation will dissipate energy to the surface. The adsorption rate dn_a/dt at the surface is dominated by the surface coverage Θ dependent sticking coefficient s . The surface coverage is defined by the fraction of total number sites on the surface that are occupied by adsorbing species. In the simplest adsorption model, the Langmuir adsorption model [177], the sticking coefficient has a linear dependence on the surface coverage:

$$\frac{dn_a}{dt} = s(\Theta) \Gamma_p = s_0 (1 - \Theta) \Gamma_p, \quad (2.38)$$

where Γ_p denotes the particle flux to the surface and s_0 is the initial or zero coverage sticking coefficient; a temperature, surface and adsorbate depending constant. A few examples for s_0 on an Si substrate would be roughly 1 for H, a few percent for H_2 and only 10^{-4} to 10^{-3} for O_2 [178].

Adsorption at the surface is the foundation of thin film growth [179, 180]. First, impinging species are physisorbed at the surface. These can diffuse across the surface and may find a reaction partner to form a chemical bond, thus, get chemisorbed. Depending on their interaction with the surface species or other adsorbed species different growth modes of the forming film are present. If the adsorbate-surface and adsorbate-adsorbate interactions are balanced and the lattice of the surface and the forming film are matching, the Frank-van der Merwe growth [181–183], also called "layer-by-layer" growth is obtained. A complete and uniform layer is formed on top of the surface prior to growth of the second layer on top of the first one.

In case of stronger adsorbate-surface interactions compared to adsorbate-adsorbate interactions the Stranski-Krastanov growth [184], also called "layer-plus-island" growth is observed. Again, layers are formed on top of the surface, but these are not completed prior to adsorption of additional species on top of the formed layers. Therefore, so-called islands are formed on top and during the formation of the single layers.

Stronger adsorbate-adsorbate interactions compared to the adsorbate-surface interactions result in Volmer-Weber growth [185], also called "isolated island" growth. No uniform layers are formed, instead only islands with already multiple layers are forming and merge at some point to completely cover the surface.

The complex plasma environment aggravates a complete understanding of all ongoing surface processes during thin film growth and a more detailed overview is given in [186]. A change of surface conditions due to the growing thin film can alter the plasma environment, resulting in different growth, or more generalized, adsorption processes, which results in most cases in the necessity to slowly optimize the deposition processes via multiple iterations. A more applied view onto thin film deposition, especially how its realized using different plasma based techniques is given in section 2.4.5.

A thin film can only be grown if the adsorption surpasses the desorption. Desorption is mainly driven by the thermal movement of the adsorbed species. If the adsorbed species can overcome the potential well of their bond, they can escape from the surface. In thermal equilibrium, surface adsorption and desorption must balance out. The desorption rate K_{desor} has an Arrhenius form and depends on the number of attempted escapes per second K_0 , the substrate temperature T_S and the bond potential E_{bond} [187]

$$K_{\text{desor}} = K_0 e^{E_{\text{bond}}/k_B T_S}. \quad (2.39)$$

K_0 is in the order of 10^{12} s^{-1} to 10^{14} s^{-1} for physisorption and 10^{13} s^{-1} to 10^{15} s^{-1} for chemisorption. If an atom or molecule escapes the surface, the amount of energy necessary to overcome the previously existing bond is taken off the surface by the atom or molecule. Thus, the surface loses energy if atoms or molecules desorb from it.

2.4.3 Surface Reactions

Adsorbates can also react at the surface with other adsorbates or gas phase species, utilizing the surface as third reaction partner to either take excess energy and/or momentum, or to enhance the reaction as a catalyst or by providing thermal energy to start the mostly exothermic reaction. The produced new species usually desorbs after the reaction and the surface is not chemically changed. Two different reaction types are mainly present for this kind of surface reactions [186, 188]

Eley-Rideal process [189], where an incoming gas phase species does not thermalize with the surface upon adsorption ("hot precursor") and instead directly reacts with a surface atom. The newly formed molecule desorbs from the surface. The reaction process is quite rare due to the limited possible reaction time as gas surface collisions are in the order of ps [190]. The reaction rate r_{reaction} is proportional to the flux of the impinging species A j_A , the surface coverage of species B Θ_B , the total number of surface sites N_0 and the reaction cross section σ_{reaction} [69]:

$$r_{\text{reaction}} \sim j_A \Theta_B N_0 \sigma_{\text{reaction}}. \quad (2.40)$$

Typically, the reaction cross section is small and limits the reaction. Further, it is a first order kinetics reaction as it is directly proportional to the impinging species. Usually, only weakly bound surface species are involved in the Eley-Rideal process. Examples are ^2H (deuterium) extraction from surfaces [174] or the generation of H_2 from a-C:H coatings upon H impact [191].

Langmuir-Hinshelwood process, the more common process, describes most heterogeneously catalyzed reactions [192]. Both reacting species are previously adsorbed

to the surface, therefore their lifetimes are in the range of μs and the available reaction time is longer compared to the Eley-Rideal process [193]. This reaction obeys second order kinetics and the reaction rate is proportional to the surface coverage of both species A and B, as well as their reaction cross section and the total number of adsorption sites:

$$r_{\text{reaction}} \sim \Theta_A \Theta_B N_0^2 \sigma_{\text{reaction}}. \quad (2.41)$$

An example for this reaction is the recombination of H atoms to H_2 at the surface. For the recombination of H atoms a third reaction partner is necessary [194]. The surface serves as this third reaction partner and therefore the recombination energy of H_2 is partly transferred to the surface. Surface reactions are an important power transfer mechanism from the plasma to the surface, will heat the surface and can enhance other surface reactions such as desorption or etching (cf. section 2.4.6).

2.4.4 Sputtering

Ions or heavy fast neutrals with a sufficient energy can sputter atoms from the surface. The threshold energy for a heavy particle to sputter a surface is in the range of 20 eV to 50 eV, but a significant sputter yield γ_{sput} is reached at energies from 200 eV to 1000 eV. The sputter yield γ_{sput} is defined by the number of atoms released from the surface due to sputtering per incident ion. The physical sputtering process itself is based on a collision cascade within the solid. The incident particle collides with surface atoms which transfer the gained momentum into the solid. Random collisions within the solid might result in a surface atom being ejected due to a momentum transfer directed outwards of the solid. Detailed illustrations of this process can be found in dedicated textbooks [195–198].

The mass of the incident ion or heavy particle, as well as the mass of the solid atoms, are also of great importance for the sputtering process, as the momentum transfer is mass dependent. For similar atomic numbers (Z) of incident particles (index i) and target atoms (index t) with $0.2 \lesssim Z_t/Z_i \lesssim 5$ and $Z_t, Z_i \gg 1$ a reasonable sputter yield can be given by [199]:

$$\gamma_{\text{sput}} \approx \frac{0.06}{E_t} \sqrt{\bar{Z}_t} \left(\sqrt{E_i} - \sqrt{E_{\text{thr}}} \right), \quad (2.42)$$

where E_t denotes the isotropic mean energy of atoms in the solid after the impact, E_i the energy of the impacting particle, E_{thr} the threshold energy and \bar{Z}_t the mass dependence expressed in terms of atomic numbers:

$$\bar{Z}_t = \frac{2Z_t}{(Z_i/Z_t)^{2/3} + (Z_t/Z_i)^{2/3}}. \quad (2.43)$$

The threshold energy can be estimated for mass ratios $Z_i/Z_t \gtrsim 0.3$ as [200]:

$$E_{\text{thr}} \approx 8E_t (Z_i/Z_t)^{2/5}. \quad (2.44)$$

In addition to the already mentioned mass and energy dependence, also an angular dependence on the impinging particles, as well as the released atoms is known [195, 201–203].

For atmospheric pressure plasmas a sputtering process is usually not expected to be present as the highly collisional environment limits the energy of ions and fast neutrals to typically below 1 eV. The limitation is collision based, thus, it is not impossible for single ions to reach energies above the necessary threshold energy by randomly

avoiding collisions, but highly unlikely. Still, some experimental and modeling results suggest the existence of sputtering under atmospheric pressure conditions [204–209].

2.4.5 Thin Film Growth

Controlled thin film growth on the nanometer scale is one of the most important plasma applications. If the deposition is based on the adsorption of species from the gas phase it is called vapor deposition. Further, a distinction is made between chemical vapor deposition (CVD), where chemically reactive gas phase species adsorb to the surface [210], plasma enhanced chemical vapor deposition (PECVD), where plasma creates the chemically reactive gas phase species by electron impact dissociation of molecules [211], and physical vapor deposition (PVD), where gas phase atoms for adsorption on the surface are generated by heating or sputtering [212, 213].

The chemically reactive molecules in the gas phase are called precursors. Their chemical composition obviously strongly defines the forming thin film. Silane gas (SiH_4) can be fragmented in the plasma and result in amorphous (a-Si) or micro-/nanocrystalline Si (mc/nc-Si) deposition on a substrate surface [214, 215]. Methane (CH_4) or Acetylene (C_2H_2) gas can be used for the production of amorphous (a-C), diamond-like (DLC) or even single crystal diamond carbon [216–219].

The film quality and topography are heavily influenced by the adsorption probabilities, thus, the sticking coefficient. Patterning and design of micro- or nanostructures is enabled by spatially resolved modification of the sticking coefficients [220]. Also the film thickness can be tuned via the sticking coefficient. If all surface reaction sites are occupied, the deposition stops. This self-limiting process enables monolayer deposition. Additional processing steps reactivate the surface and enable the next monolayer. Repeating this process results in atomic layer deposition (ALD) [221] for the synthesis of ultra-thin films with sub-nanometer thicknesses.

Furthermore, plasma does not only create the reactive species in the gas phase, it also modifies the surface before, during and after the deposition. Plasma species can open or activate surface reaction sites by particle impact or energetic radiation and, thus, enable film growth. Plasma species transfer energy towards the surface and (locally) increase its temperature. The increased temperature enhances (surface) diffusion, which allows for solid defects to heal, increases the crystallinity and also leads to desorption of foreign atoms. In addition to the energy transfer, also momentum can be transferred, which condenses the growing thin film.

To visualize the plasma effects during thin film growth structure zone diagrams (SZDs) were developed, which reduce deposition parameters to a minimum while representing universal features of the thin film [222–225]. Figure 2.9 shows such a SZD for energetic deposition. The film thickness t^* and structure depends on a generalized temperature T^* of the substrate and the normalized energy flux E^* towards the substrate. None of these parameters can be tuned individually, as the energy flux strongly affects the heat balance of the substrate [223, 226–229]. The depicted trends of, e.g., a more crystalline structure at higher temperature and/or higher energy flux, or porous structures at low temperatures and energy flux are also applicable for thin film modification by plasma treatment, due to the universal character of such SZDs.

2.4.6 Plasma Etching

The plasma etching process consists of multiple already mentioned processes and is of great importance for the production of nanostructured materials such as the ZnO

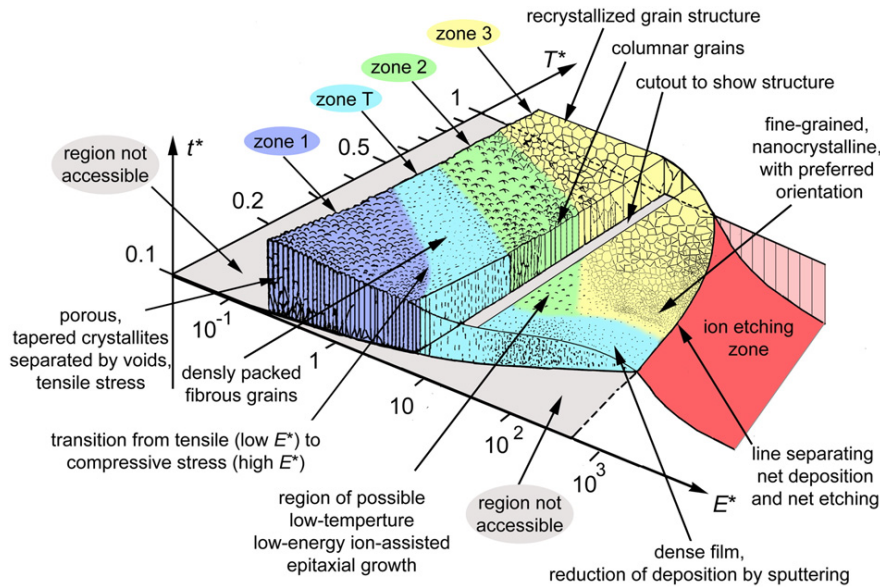


FIGURE 2.9: Structure zone diagram showcasing typical thin film features during energetic deposition. The film thickness t^* and structure depends on the generalized temperature T^* and energy flux E^* . The given numbers on the axes are only for orientation as actual numbers depend on the material and other conditions. Reprinted from Publication [225] with permission from Elsevier.

nanobrushes which will be discussed in chapter 6. Plasma electrons produce ions, atoms, radicals and so forth which can interact with the surface. The key part for plasma etching is the right choice of reactive molecules contained in the plasma. These must be able to form gaseous products as a result of reactions with surface atoms and, furthermore, the newly formed molecules should have a high vapor pressure to easily desorb from the surface. If the vapor pressure of the newly formed molecules at the substrate temperature of usually around 300 K is high enough, plasma etching and, thus, the removal of atoms from the surface can take place without further plasma assistance.

To achieve higher etch rates, or etch surfaces where the resulting surface reaction products have a low vapor pressure, ion bombardment of the surface is used to combine the chemical etching with physical sputtering and local energy transfer to the surface. The synergistic effect of chemical etching and physical sputtering can be large and result in etching rates ten times as high as the rates obtained by only one of the processes [230]. Therefore, plasma etching is sometimes also called chemical sputtering [231].

The ion assistance during plasma etching offers patterning opportunities. Either by utilizing a focused ion beam or photoresist masks which passivate the substrate surface. The photoresist is patterned via (mostly) UV-radiation and shields the surface from etching reaction. The incident direction of ions can be controlled well via electric fields or with the usage of ion beams, thus, etching of deep and steep trenches is possible [144, 147, 232].

Chapter 3

Plasma and Surface Diagnostics

For the successful design of the *in situ* TEM microplasma cell, the microplasma geometry has to be developed and must pass several tests. Available plasma diagnostics are quite limited due to the small dimensions of the microplasma. Typically, optical diagnostics would be the means of choice [64, 65, 73, 109], but with the goal of observing real time surface changes *in situ* and understand them, one has to go beyond conventional diagnostics.

Electrical measurements are utilized to determine current voltage characteristics. Further, these electrical diagnostics have the advantage of also being applicable during the aspired *in situ* measurements, enabling an *in situ* process control.

Confirmation of the gas purity, discharge stability, and additional proofs of setting up a DC normal glow microplasma are obtained by optical diagnostics. Time-resolved optical emission spectroscopy and spatially resolved optical imaging are not accessible inside of the TEM, but *ex situ* setups utilizing the same microplasma geometry are sufficient for a better understanding of the microplasma.

The power transfer from the plasma to the electrodes is investigated by utilization of passive thermal probes (PTPs) [233–235] as electrodes. This non-conventional calorimetric diagnostic tool allows to measure the energy flux [229] towards the electrodes. In section 2.4.5 the concept of structure zone diagrams was introduced, which visualizes the importance of the energy flux for plasma surface modifications quite well.

Electron microscopy techniques have been used for the surface analytics of the plasma treated samples. The utilized devices will be briefly introduced as well as the foundations of the different techniques. For more details regarding the electron imaging, especially concerning the TEM imaging techniques, influence of the gas column within the microplasma cell on the TEM image quality, and limitations of the TEM techniques due to the unconventional sample, the interested reader is referred to the PhD thesis of Niklas Kohlmann [236], who was mainly responsible for the TEM operation in our joint project.

3.1 Plasma Diagnostics

3.1.1 Electrical Measurements

Voltages of at least 100 V are necessary to ignite the plasma according to the Paschen law depicted in Fig. 2.7. Thus, the electrical circuit and measurement equipment has to be chosen carefully. The basic electrical circuit is shown in Fig. 3.1. It is powered by the Heinzinger PNC 20000-10 ump, a DC power source with adjustable polarity, capable of delivering up to 20 kV and 10 mA (a in Fig. 3.1). The voltage output of the source is measured by utilizing the Tektronix P6015A high voltage probe (b). The

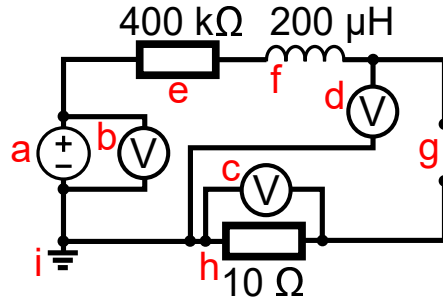


FIGURE 3.1: The basic electrical circuit used for the generation of the microplasma. a) DC power source with adjustable polarity; b,c,d) (high) voltage probes; e,h) resistors, f) inductance; g) connections to electrodes & i) ground.

P6015A has an attenuation ratio of 1000:1 and can safely be used for voltages of up to $20 \text{ kV}_{\text{DC}}$ or $40 \text{ kV}_{\text{Pulse}}$. More important is the high 75 MHz bandwidth and 4 ns rise time, which can detect fast fluctuations in the voltage signal. Voltage measurements in general are today typically performed by analog-to-digital converters. As these are limited by the analog input voltage, precise voltage divider or voltage transforming circuits are used within the high voltage probe to transform high voltages down to typically below 50 V. Further limitations of analog-to-digital converters are given by the necessary conversion of a continuous-time and -amplitude analog signal to a quantized digital signal with discrete-time and -amplitude steps [237].

A $400 \text{ k}\Omega$ resistor (e) is connected in series to the circuit to limit the current as soon as the plasma, whose electrodes are connected to the open contacts (g) illustrated here, is ignited. Without plasma ignition no current is going through the circuit, as the electrodes act as parallel plate capacitor. Higher voltages are necessary for the plasma breakdown compared to the steady-state operation (cf. Fig. 2.3). The voltage necessary for plasma ignition could result in high currents going through the circuit, only depending on the electrical resistance of the plasma itself. If the current surpasses the point of the glow to arc transition, the characteristic negative slope of the resistance will lead to an even higher current flow and an arc discharge is formed until the current is limited by the maximum current output of the power supply. To avoid this glow to arc transition, the current is limited by the total resistance of the electric circuit, which adds up from the series resistor and the plasma resistance. As the plasma resistance is depending on the current going through the discharge (cf. Fig. 2.3), the series resistor is the only reliable possibility to limit the current. It has to be chosen in a way, that the overall resistance of the electrical circuit results in currents in the mA range to obtain a stable glow discharge. For the microplasma geometry developed in this thesis, $400 \text{ k}\Omega$ were determined to work well for gold, copper, indium tin oxide (ITO) and platinum electrodes, if the power supply is set to voltages in the range of 500 V to 1000 V. Breakdown was achieved for most parameters at about 700 V. However, for magnesium electrodes the series resistor had to be reduced to $200 \text{ k}\Omega$ to operate the microplasma, which is a good example that the series resistor has to be chosen carefully and always has to match the microplasma geometry.

The $200 \mu\text{H}$ inductor (f) was added to the electrical circuit to stabilize the discharge. Fast current changes, which would occur during arc formation, should be suppressed by, metaphorically speaking, slowing down the current through the inductance. The combination of resistor, inductor and capacitor results in a damped electric resonant circuit, which can suppress fast current changes. Ideally, an overdamped RLC-circuit

is aspired with a damping factor $\zeta > 1$ given by [238]:

$$\zeta = \frac{R}{2} \sqrt{\frac{C}{L}}, \quad (3.1)$$

where R denotes the resistance, L the inductivity and C the capacity. Assuming the electrodes as parallel plate electrodes with a diameter (A) of 1 mm and a distance (D) of 100 μm the capacity can be calculated by [238]:

$$C = \epsilon_0 \epsilon_r \frac{A}{D} \approx 7 \times 10^{-14} \text{ F} \quad (3.2)$$

for the given values using a relative permittivity $\epsilon_r = 1$. The assumed values here for the electrode distance and diameter have proven to work well (see chapter 4) and are also suited for the construction of the *in situ* cell addressed in chapter 7. The damping factor ζ of the given electrical circuit becomes roughly 3.7, which fulfills the aspired overdamping. Of course, in this consideration, no plasma was assumed. Taking the plasma into account is not trivial but will mainly change the resistance and the capacitance of the electrical circuit. The resistance will increase, as it turns out that the plasma itself has a resistance in the order of hundreds of $\text{k}\Omega$ for the found operation parameters. The capacitance on the other hand will decrease, as the relative permittivity ϵ_r will drop to values of < 1 . Overall, the increasing resistance is expected to influence the damping factor stronger due to the square root dependence of the capacitance. Thus, the damping factor of the electrical circuit should stay > 1 .

An additional high voltage probe (d), the Tektronix P5100A with an attenuation ratio of 100:1 and a maximum operating voltage of 1 kV ($2.5\text{kV}_{\text{peak}}$) is connected close to the high voltage electrode connection (g). Its 500 MHz bandwidth surpasses the P6015A, thus, fast voltage fluctuations should be resolvable. The voltage probe is utilized to measure the voltage at the electrodes, as it will differ from the one applied at the power supply as soon as the plasma is ignited, due to the series resistor (e) and the plasma resistance forming a voltage divider.

On the ground side (i) of the circuit a 10 Ω shunt resistor (h) is used to measure the current going through the microplasma. A Tektronix P2200 (c) is used to measure the voltage drop across the resistor. As the resistor and the currents are small, the 1:1 attenuation had to be chosen, which limits the bandwidth to 6 MHz. Still, current fluctuations should be visible. Following Ohm's law $U = R * I$ the measured voltage has to be divided by 10 to obtain the current.

A digital oscilloscope, the PicoScope 5442B, was used to measure the voltages. Its compactness and ease of data storage outweigh the disadvantage of a limited bandwidth to maximum 60 MHz, at least for the measurements in context of this thesis, which are mainly limited to DC currents.

A typical electrical measurement is shown in Fig. 3.2. The graph in the middle of the figure shows the full measurement, while the left and right graphs zoom into the switch on and off regions. The microplasma was operated in a He atmosphere with an Au electrode distance of 100 μm for roughly 10 s. The measured voltages directly at the power supply and at the electrodes are shown in blue and in cyan and correspond to the left y-axis. The current measured via the shunt resistor is shown in red and corresponds to the right y-axis. During the microplasma operation the power supply voltage was set to 900 V, which resulted in a current of approx. 1.9 mA and a voltage of 170 V at the electrodes. The noise level of the current measurement in the middle graph is exaggerated due to the large temporal range. The enlarged graphs on

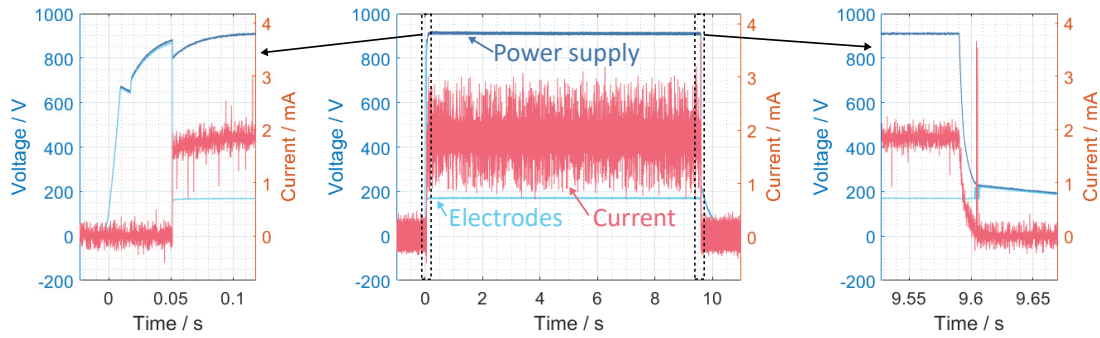


FIGURE 3.2: Typical electric measurement of a microplasma ignition. Voltages, shown in blue and corresponding to the left y-axis, were measured directly at the power supply and at the microplasma electrodes. Discharge current, shown in red and corresponding to the right y-axis, was measured utilizing the $10\ \Omega$ shunt resistor. The discharge was ignited for roughly 10 s as visible in the center image. Voltage set at the power supply was 900 V and resulted in an electrode voltage of roughly 170 V and a current of 1.9 mA. The microplasma was operated in He with an Au electrode distance of $100\ \mu\text{m}$. The left figure is a zoom into the breakdown region. The voltage ramp up of the power supply is visible. The right figure shows the switch off region, where the voltage and current ramps down.

the left and the right side give a better impression of the actual noise level, which is also present while the discharge is switched off. The multiplication of the current and electrode voltage values results in the electrical power coupled into the microplasma. During one plasma ignition the measured voltages, the current and, thus, the power, stayed constant, if set constant at the power supply. This is of course the first indicator of a stable atmospheric pressure DC microplasma.

The ramp up and down of the power supply, shown enlarged in the graphs on the left and right, introduces short phases of lower, inconsistent power coupled into the microplasma. But these ramping phases are actually useful from the diagnostics perspective. In the ramp up phase on the left, the breakdown voltage is, for this example, visible at roughly 875 V. Prior to the breakdown a discontinuity in the ramp up is visible, which is an artifact given by the utilized power supply. With the breakdown the current starts to go through the circuit and the voltages at the electrodes and the power supply start to differ from each other. Breakdown voltages determined during the ramp up turned out to significantly differ even for identical parameters, as the ramp up happens within 0.05 s and the breakdown depends on available free electrons (cf. section 2.2.1). The amount of available electrons fluctuates over time, thus, the breakdown voltage can fluctuate, if only applied for a short amount of time.

After breakdown the power supply still ramps up resulting in an increasing current. These current and electrode voltage value pairs can be used to create an I-V characteristic, which can serve as process control during plasma processes where a constant current is required.

During the ramp down, shown on the right, the switch off current and voltage are visible, here 0.2 mA and 170 V, which confirm the expected hysteresis-like behavior shown and discussed in context of Fig. 2.3. Again, the decreasing current values in combination with the measured electrode voltage can be used for an I-V characteristic. The current range is enlarged compared to the ramp up region.

In addition to the I-V characteristics created by targeted measurements with variable

discharge current, the data base can be further expanded by taking advantage of the power supply's ramping up and down to control processes with constant power as, e.g., calorimetric measurements (see section 3.1.4) or surface treatment (see chapter 5).

3.1.2 Optical Emission Spectroscopy

Optical emission spectroscopy (OES) is a powerful non-invasive tool to investigate plasmas [73, 239–246]. It offers access to crucial parameters such as the electron density and temperature [247–251], electric fields [252, 253], neutral gas temperatures [254], and gas composition [255]. Commercial and free software [256–259] is already available to determine rotational temperatures, still data acquisition and analysis is challenging for non-equilibrium plasmas and has to be done carefully [254].

Recently, absorption spectroscopy was applied to microplasmas, mostly plasma jets, and proved to provide several advantages over the different emission spectroscopy techniques [260]. It is mentioned here for the sake of completeness, as the experimental setups for absorption spectroscopy are more challenging and costly compared to emission spectroscopy and not necessary for the goals in context of this thesis. The interested reader is referred to several textbooks and publications regarding absorption spectroscopy as it is not further addressed here [241, 260–266].

Within the scope of this work, OES was used to verify the gas purity and stability of the discharge. The OES data acquisition and analysis was therefore limited to the usage of a compact, low resolution OceanOptics HR2000+ spectrometer and evaluation of the visible atomic lines and their temporal development.

The characteristic atomic lines result of electron transitions from a higher energy to a lower energy state [240]. Within a plasma, electrons of atoms or molecules can be excited by, e.g., collisions or radiation. During the de-excitation process, an electron transitions from the excited, high-energy state to a lower energy state. Multiple transitions are possible, until the ground state of the electron is reached. Each of these transitions radiates a photon with the wavelengths corresponding to the energy difference of the different energy states. The transition probability differs as well as the probability of the electron to be excited into the different high energy states. The different probabilities result in different amounts of emitted photons, and, thus, relative intensity differences between the emitted wavelengths. The available energy states and transitions are species dependent and, therefore, the detected radiation can be used to gain information about the excited species.

The OceanOptics HR2000+ consists of a grating, which is responsible for the diffraction. Multiple mirrors focus the incoming light, coming through a slit, onto the grating and the diffracted light originating from the grating towards a CCD detector. Each pixel of the CCD detector corresponds to a specific wavelength, enabling to determine the different wavelengths contributions of the incoming light [267].

For the measurements, the OceanOptics HR2000+ was equipped with a fiber optic and a focusing lens aligned and focused to the microplasma. Exposure times of 0.3 s for Ar, or 1 s for He, respectively, have been chosen for most measurements. During early experiments the exposure time was reduced to 0.1 s to obtain a better temporal resolution, but a worse signal to noise ratio. These measurements with short exposure time were used to check for overall intensity fluctuations over time during the microplasma operation. With no fluctuations being visible in the overall intensity under common operation conditions, the exposure times have been prolonged for a better signal to noise ratio.

Figure 3.3 shows expected atomic lines given by the NIST database [255] and microplasma emission spectra for the wavelength regime where emission was detected.

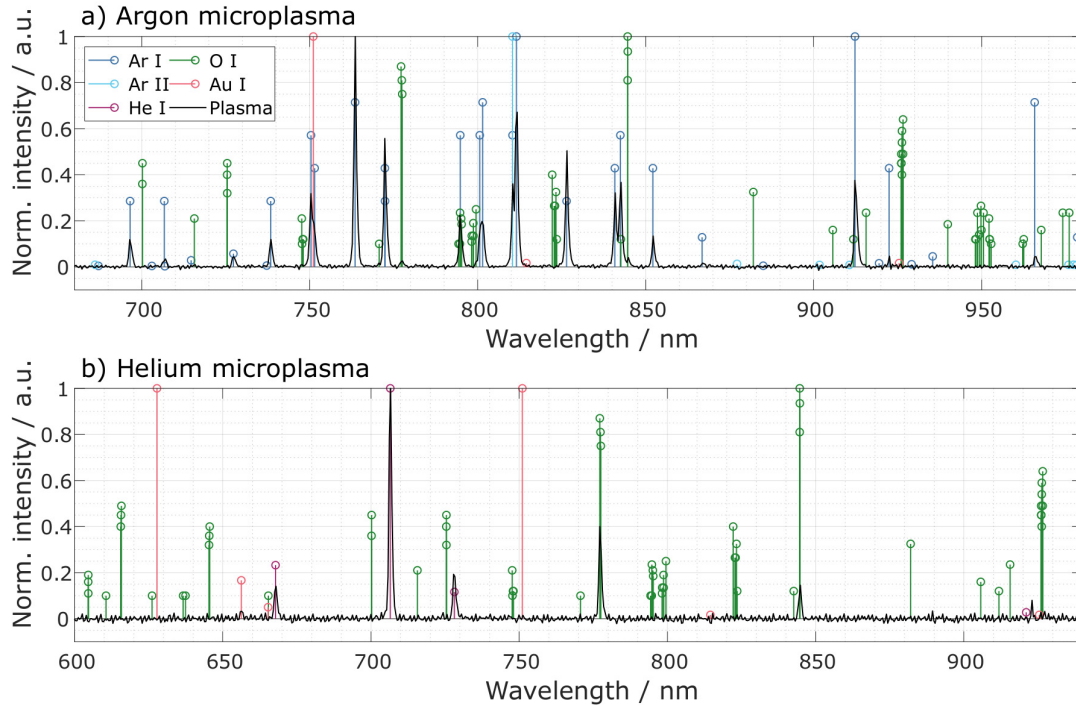


FIGURE 3.3: Two exemplary optical emission spectra of the microplasma operated in Ar (a) or He (b) with Au electrodes and an electrode distance of 100 μm . The normalized intensities turned out to be current and voltage independent, thus, the spectra are averaged over multiple currents. Additionally, potentially relevant atomic lines from the NIST database [255] normalized to their given maximum intensity in the region of interest are shown for the identification of the found spectral lines originating from the microplasma.

Intensity normalization for the atomic lines given by the NIST database was done by normalizing to the maximum intensity within the given wavelength region individually for each species. Normalization of the measured plasma intensity was done to the maximal measured intensity within each spectrum. For the microplasma operated in Ar shown in Fig. 3.3 a) the spectra were normalized to the Ar I line at approx. 763.6 nm and for operation in He shown in Fig. 3.3 b) spectra were normalized to the He I line at approx. 706.6 nm. Both spectra show the expected pressure and temperature broadened Ar I or He I lines. Further, some O I lines (approx. 777 nm and 845 nm for Ar and He) and an Au I line (656 nm for He) are visible in the spectra. Furthermore, O I or Au I lines, which were predicted by the NIST database, could not be measured, either because they are overshadowed by other lines, or their intensity is too low, due to no or just minor excitation of the necessary electronic energy states.

The normalized intensity values of all measured lines (Ar I or He I, resp., O I, and Au I) were evaluated in dependence of operating parameters (current, applied polarity, electrode distance and electrode material) and plasma on time. No significant differences in the normalized intensity values could be identified except for changing electrode materials (see chapter 4).

3.1.3 Optical Imaging

Investigations of the spatial and temporal resolved plasma emission patterns have been used for a long time to understand self-organized structures, (chemically) active regions and fundamental aspects as the streamer mechanism [73, 141, 268–273]. The combination of optical imaging with, e.g. optical wavelength filters or dust particles, was used for analytical photometry to obtain plasma parameters or flow patterns [274–278]. For a parallel plate electrode, DC plasma characteristic emission is expected as introduced in section 2.2.3. In a low-pressure discharge, these luminous regions can expand over tens of cm and more, depending on the pressure and chamber size. However, under atmospheric pressure conditions, the spatial expansions of the luminous regions are in the μm range and, thus, not trivial to resolve.

A high zoom objective, the Navitar 12x Zoom Lens System [279], in combination with the 12X Xtender [280], was used to obtain sufficient spatial resolution. The 12X Xtender decreases maximum zoom to 6x as a 0.5x lens is necessary to keep the internal focus with the equipped Xtender. On the other hand, the lens working distance is increased up to infinity from 120 mm and, thus, enables to setup the imaging equipment outside of the necessary gas box. The images were captured with a Ximea MQ042CG-CM [281] equipped with a CMOS RGB Bayer Matrix chip enabling colored pictures. A potential problem with the utilized imaging equipment is an insufficient illumination. The LED construction spotlight Bauhaus 50254-3 providing 1850 lm turned out to be sufficient for focused images at high magnifications. An advantage of using a DC LED source is a constant illumination without potential flickering effects.

For plasma observations the ambient light was mostly turned off to maximize the contrast. Exposure times of 0.3 s to 1 s were chosen to collect enough photons for an image with a good signal to noise ratio. The long exposure times prevent evaluation of any dynamic effects that may be present. An intensified charge-coupled device (ICCD) camera could overcome this limitation given by the exposure time. Still, for a stable DC microplasma no dynamic effects are expected.

Spatial calibration of the images was always done by two methods. First, the microplasma electrodes were exchanged with a 1 mm stage micrometer with 10 μm divisions (Thorlabs, R1L3S2P). Pixel to mm factors in vertical and horizontal directions were calculated based on the imaged, well-defined distances as illustrated in Fig. 3.4. Vertical or horizontal cuts were done across nearly the full image. From the overall nearly 2000 cuts, pixel to distance median and mean values including their respective standard deviations have been calculated. The median was calculated as an outlier control, as its less affected by those. Mean and median values never differed significantly from each other. The mean values were used to calculate the conversion factors. After the calibration no changes on the optical system are allowed and the microplasma has to be aligned in focus of the camera to avoid systematic errors in the calibration.

The second calibration was done with actual images from the measurements. Characteristic dimensions, such as the electrode distance for the side-view imaging or the inner diameter of the Kapton spacer for the top-view imaging, with defined distances were also analyzed and pixel to distance factors were calculated. If these factors differed from the first calibration, the plasma to camera distance probably changed during the alignment. The first calibration was redone as a consequence to ensure correct conversion factors.

The experimental setups, as well as further details regarding the evaluation are given in context of the measurements in chapter 4.

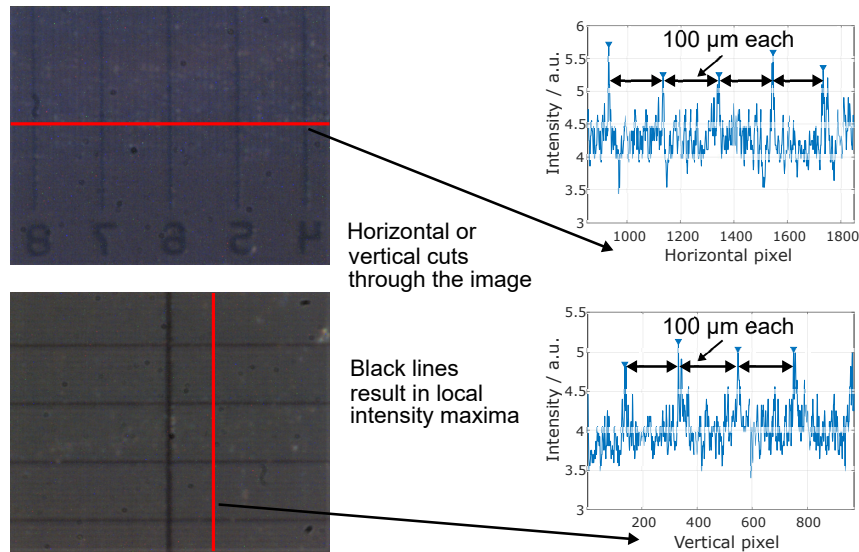


FIGURE 3.4: Illustrating one of the spatial calibration methods. A ruler with defined distances is imaged instead of the plasma. The intensity profiles along horizontal and vertical cuts through the images are analyzed. Distances between maxima correspond to the 100 μm distances between thick lines on the ruler.

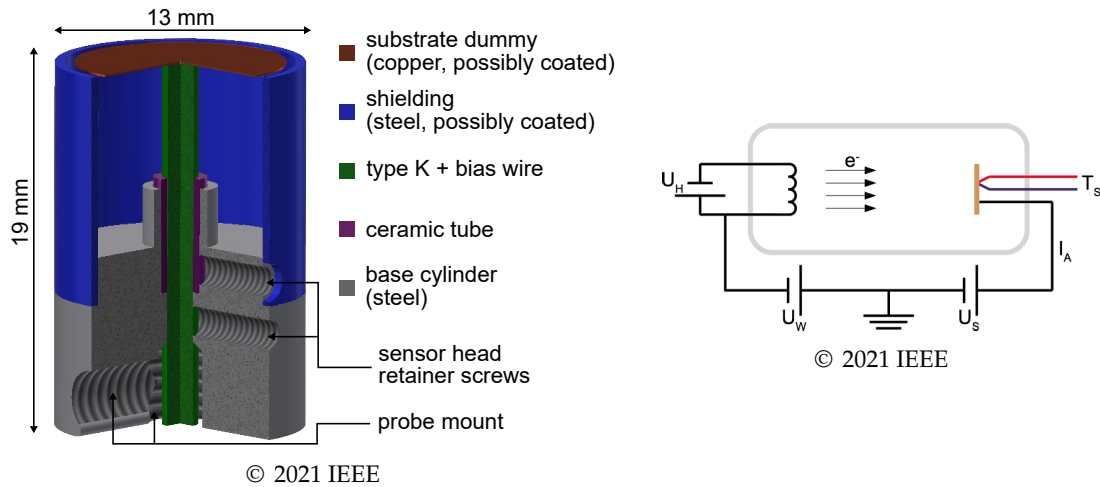
3.1.4 Calorimetric Measurements

Publication I

The Use of Passive Thermal Probes for the Determination of Energy Fluxes in Atmospheric Pressure Plasmas

Authors	L. Rosenfeldt, L. Hansen, and H. Kersten
Journal	IEEE Transactions on Plasma Science [282]
Technique	Calorimetry on various atmospheric pressure plasma sources
Utilized diagnostics	Passive thermal probes (PTPs), electrical diagnostics, and water contact angle (WCA) measurements
Own contribution	Approx. 40 %

Experimental Setup:



Motivation:

Energy flux measurements based on calorimetry already have a long history and the passive thermal probe (PTP), developed in recent years, was already subject of reviews [229] and book chapters [234]. Still, most experiments addressed in these publications were restricted to low-pressure plasma environments. Adaption of the PTP and its evaluation procedures to atmospheric pressure plasmas was necessary as atmospheric pressure plasmas became more important for scientific and industrial applications.

Main Results:

An introduction into the field of calorimetry for plasma diagnostics is given and its importance is emphasized. The integral energy flux and its components are addressed and a historical overview on the development of calorimetric probes is given. The setup is described in detail to offer the reader the possibility to perform energy flux measurements easily by themselves. Theoretical basics and their application for the different evaluation procedures are given and exemplary shown in reference to real experimental data obtained on different atmospheric pressure plasma sources. A brief selection of recent results obtained at different atmospheric pressure plasma sources concludes the overview of energy flux measurements under atmospheric pressure conditions.

The Use of Passive Thermal Probes for the Determination of Energy Fluxes in Atmospheric Pressure Plasmas

Lukas Rosenfeldt¹, Luka Hansen¹, and Holger Kersten

Abstract—Atmospheric pressure plasmas receive great interest due to their industrial relevance based on lower cost compared with vacuum systems. To optimize these applications and possibly improve them, one has to understand plasma–surface interaction. This study will emphasize the energy flux as a key parameter in plasma–surface interaction. The technique of passive thermal probes (PTPs) as a suitable diagnostic to measure the energy flux is described and discussed. With such probes, the heating and cooling of a “substrate dummy” with a well-defined surface is measured. From the obtained temperature as a function of time, the integral energy flux can be deduced. This integral energy flux consists of various contributions, e.g., chemical contributions such as recombination or oxidation and kinetic energy of plasma species such as impinging ions, electrons, and neutrals. Beginning with a historical overview, this work aims to present the technique of the PTP in its entirety. This includes an explanation of the design along with different calibration and evaluation methods. Exemplary experimental results will be provided to emphasize its versatility and significance as diagnostic for modern atmospheric pressure plasma research.

Index Terms—Atmospheric pressure plasmas, calorimetric probe, plasma diagnostics.

I. INTRODUCTION

FOR industrial applications, low-temperature nonequilibrium plasmas—especially at atmospheric pressure [1], [2]—have received growing interest in many technological fields as in gas conversion for ozone chemistry [3], in illumination with special light sources [4], and, in particular, in surface modification and coating for plasma–surface engineering [5]. Concerning the latter, there has been increasing use of atmospheric pressure plasmas for materials treatment, with extension from inorganic to organic surfaces (such as polymers) and biological tissues (skin, wound treatment) [6]. Recently, atmospheric pressure plasmas entered also the field for synthesis of new materials and structures and major advancements have been made in plasma synthesis of nanoparticles and nanostructured materials [7], [8].

In general, plasma–surface interaction is at present one of the fastest growing branches in plasma technology and has

got a leading position in the new field of applied surface science. However, its basic question includes the mastering of an old problem: the contact of different states of matter. The interaction between plasma and solid is of both high practical and principal interest and will result in a new insight of many questions in the broad area of plasma–surface engineering [8], [9]. Sometimes, the control of plasma parameters and their interplay with the surrounding surfaces is still more an art than a science. This is founded on the fact that the description of plasmas in contact with solid walls is incomparably much more complicated than that of free plasmas; plasma–surface interaction requires the consideration of marked anisotropies and inhomogeneities, deviations from quasi-neutrality, exchange of energy, momentum, and matter resulting in strongly nonlinear equations containing many unknown quantities [10]. Since a further development has seen the shift of research in plasma processing from metals and semiconductor to “soft” materials such as liquids, biomaterials, and even agricultural products, the fragile operating conditions have the development of new and nonconventional diagnostics that require unprecedented temporal and spatial resolution to monitor exceptionally large gradients and changes in plasma properties [8]. Hence, diagnostic is the key to gain insight and understanding of the physical and chemical processes going on in the gas phase and at the plasma-facing surfaces. By suitable probe diagnostics, the fluxes of charge, heat, or momentum of the species in or from plasma can be experimentally determined to obtain quantitative information about plasma–surface interaction [10], [11]. Among the various quantities, the energy flux (or deposited power) is a key parameter for controlling and optimizing the interaction processes [12]. In general, the energy transfer between plasma and solid is a very complex mechanism. In the case of thermal plasmas, the transfer can be described by means of classical terms as thermal conductivity and heat transfer coefficients. However, for nonequilibrium plasmas, such an approach is not possible because the term “heat” has no precise meaning. In those plasmas, the thermal conditions at the surface must be described by a detailed energy balance, which considers the different heat sources and losses [12]–[15].

Various elementary plasma–surface processes affect the thermal balance and energetic conditions of a substrate surface during plasma processing. The energy and momentum of particles originating from the plasma or from electrodes, respectively, influence due to energy flux density and substrate temperature of the surface properties of the treated substrates. The total energy influx (deposited power) includes

Manuscript received May 3, 2021; accepted June 19, 2021. Date of publication July 12, 2021; date of current version November 18, 2021. The review of this article was arranged by Senior Editor S. J. Gitomer. (Corresponding author: Lukas Rosenfeldt.)

The authors are with the Institute of Experimental and Applied Physics, 24098 Kiel, Germany (e-mail: rosenfeldt@physik.uni-kiel.de; lhansen@physik.uni-kiel.de; kersten@physik.uni-kiel.de).

Color versions of one or more figures in this article are available at <https://doi.org/10.1109/TPS.2021.3092752>.

Digital Object Identifier 10.1109/TPS.2021.3092752

0093-3813 © 2021 IEEE. Personal use is permitted, but republication/redistribution requires IEEE permission.

See <https://www.ieee.org/publications/rights/index.html> for more information.

heat radiation, kinetic, and potential energy of charged particles and neutrals, thin-film condensation energy, as well as enthalpy of involved surface reactions and recombination [12], [16]–[19]. For suitable experimental conditions, most of these contributions except the neutral component and radiation can be separately determined and, hence, one can even obtain information about the flux and energy of the neutral species [12], [20].

This publication structures as follows. First of all, the history of passive thermal probes (PTPs) is summarized in Section II. Next, the structure of PTPs and different versions is presented in Section III followed by an overview of existing calibration methods in Section IV as well as evaluation methods in Section V. Finally, exemplary results are discussed in Section VI before a conclusion is drawn in Section VII.

II. HISTORY

Before this work shortly dives into the history of calorimetric probes, it should be noticed that the energy flux between plasma and substrate is also an important similarity parameter for comparing or upscaling, respectively, of different plasma processes or from laboratory to industrial scale [21], [22].

A common method for the determination of the energy influx from a process plasma to a solid surface is the use of rather simple calorimetric probes (either as PTPs [12], [23]–[26] or as active thermal probes (ATPs) [27]). In an ATP, first, with plasma off, the probe is set to a given temperature by means of controlled electrical heating. Then, with plasma on, the energy influx by the plasma is compensated by decreasing the heating power until the original temperature is reached again. The ATP does not need a determination of the heat capacity of the probe. In contrast, the PTP is based on the determination of the temporal change of surface temperature of the probe during a heating phase with plasma operation and a cooling phase with plasma off [24], [26]. With the known heat capacity of the sensor [25], the difference of the time derivatives yields the integral energy influx to the surface. It should be noted that the PTP measures a time and energy integrated value of the energy flux that is generated by the various energy sources and processes mentioned above. Simultaneously, the electric current to the substrate can be obtained, and by variation of the probe voltage (bias), the energetic contributions of charge carriers can be separated and determined. By comparison with model assumptions on the involved plasma–surface mechanisms, the different energetic contributions to the total energy influx can be separated. Furthermore, the flat PTP can also be used as a planar Langmuir probe to get information on plasma density and electron temperature [19], [28].

The use of PTP-type probes for the determination of the integral energy influx and its importance for thin-film growth and surface modification has been demonstrated for many different technological applications. Examples for such applications in low-pressure plasmas are the deposition of metallic and ceramic films in magnetron sputtering [16], [18], [20], [23], [28]–[40], etching of semiconductors [17], [41], [42] or the modification of metallic samples by plasma ion immersion implantation [43]. However, not only for low-pressure gas discharges but also for atmospheric-pressure plasmas, this method for determination of energy influx has been

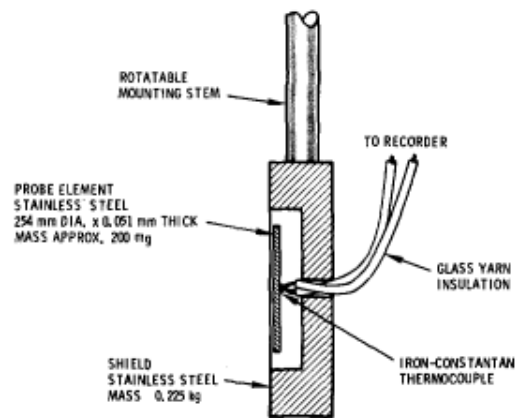


Fig. 1. Design of a simple thermal probe for energy flux measurements in plasma–surface engineering (sputtering) by Thornton. Taken from [24].

employed—as, for example, in coplanar diffuse surface barrier discharges [26], [44] or plasma jets [45]–[49].

The origin of experimental calorimetry can be traced back to Lavoisier and Laplace, who presented an ice calorimeter in the 18th century [50]. In their setup, a solid body was placed in a hollow sphere filled with ice. The quantity of melted ice is then directly proportional to the heat absorbed from the body. Using this setup, the heat dissipation of animals was investigated [50], [51].

Of course, in many scientific and technological areas as physical chemistry, thermodynamics, and so on, calorimetric methods are quite common tools in research. However, in plasma–surface engineering, it took until 1969 to adapt the idea of calorimetry for suitable utilization by Jackson [52]. By measuring the temperature of a copper block with an embedded thermocouple, he could deduce the dissipated heat in a radio frequency sputtering system. Quite similar setups are used for energy flux measurements to the various surfaces in fusion devices [53]. Probably, Jackson [52] phrased the first theoretical foundation for modern energy flux measurements in plasma technology.

While, in the pioneering investigations in calorimetry, only the heat is measured, it is credited to Thornton to develop a probe for energy flux density measurements in 1978 [24]. In the context of plasma physics, this quantity is often referenced as energy flux. Thornton's rather simple probe is shown in Fig. 1. As a substrate dummy for his probe, he used a shielded stainless steel disk to have a defined surface and suppress energy flux to the backside of the probe.

In 2000, a modern version of this probe based on work of Thornton [24] and Wendt *et al.* [16] was presented [54], [55]. By welding a bias wire to the substrate, we could measure the energy flux depending on the probe's potential and use it also as a planar Langmuir probe [19]. This method allows to deduce the contribution of the ions, electrons, and neutrals to the energy flux which are consistent with theoretical expectations, at least in low-pressure plasmas [54], [56]–[58]. A vital part in the advancement of calorimetric probes was the development of calibration techniques where the probe is exposed to a defined power source. Modern methods either utilizes an ion beam [26], [44] or an electron beam [16], [25] as power source, whereas before, starting in 2000, lasers were used for

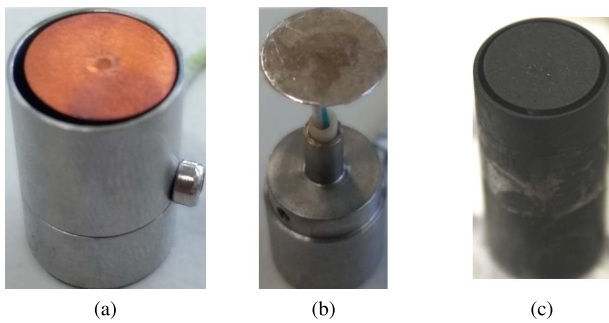


Fig. 2. PTPs with different probe materials. (a) Copper probe. (b) Ceramic Mica probe without shielding. (c) Copper probe insulated by silicon resin spray.

calibration [46], [59]. The calibration methods are discussed in detail in Section IV.

In 2010, Cormier *et al.* [60] presented a heat flux microsensor based on a thermopile. It allows to directly measure the energy flux in contrast to the previously mentioned probe designs. Because of the fragility of the sensor, it is unsuitable for higher energy fluxes [60], which are encountered at atmospheric pressure. Another atypical approach to energy flux measurements was presented in 2018 by Primc and Mozetic [61]. They used a catalytic sensor to measure the density of O-atoms in a low-pressure plasma. This sensor uses the energy flux by recombination as a measure for atom density. While this is no calorimetric probe, nonetheless, it is based on the same principles.

Beginning in 2011, PTPs, or slightly modified versions, were also applied to atmospheric pressure plasmas. For these plasmas, other factors such as fluid dynamics [26], [46], [49] have a significant influence on the results. Still biasing of the probe allowed to show the influence of charged species on the energy flux [49]. Two additional factors convolute the measurements with PTPs at atmospheric pressure. First, the reduced dimensions complicate the normalization of power to the probe area as the effluent of an atmospheric pressure plasma can be as large or even smaller than typical probe areas. Second, the largely increased voltages can lead to the formation of parasitic discharges onto the metallic head of a PTP. To tackle the latter problem, Mance *et al.* [46] introduced a dielectric probe in 2018. This probe was insulated by placing a Mica plate over the copper substrate dummy. Hansen *et al.* [26] refined this principle in 2019. Their PTP was insulated by a nonconductive layer of silicon resin spray. Recently, a PTP with a fully ceramic substrate dummy made from mica was used to investigate a dielectric barrier discharge (DBD) [44]. The different probe types can be seen in Fig. 2. These are very promising developments, as the type of a surface can influence the chemistry and discharge dynamics of an atmospheric pressure plasma [62]–[65].

III. MEASUREMENT SETUP

The PTP setup can be divided into two parts: the sensor head, which can be adapted to represent the usual plasma-treated substrate best, and the data acquisition electronics, which can be used with any adaption of the sensor head.

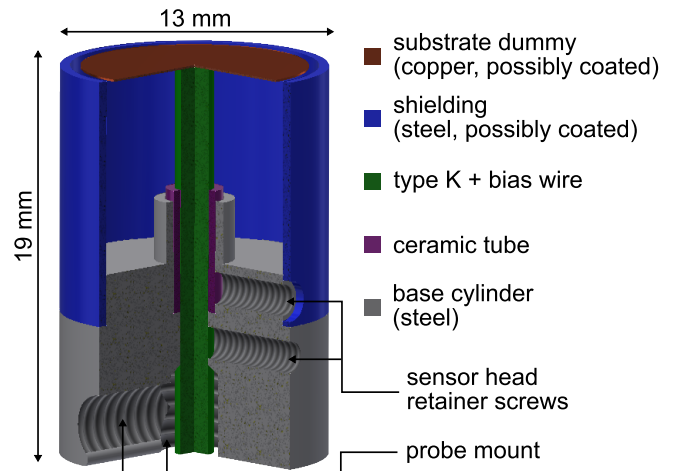


Fig. 3. Schematic drawing of the common PTP sensor head. Typical materials are given for the different parts but can be adapted to fit the experimental needs.

A. Sensor Head

The key part of the sensor head is a “substrate dummy” connected with a type K thermocouple. The connection between the substrate dummy and the thermocouple is usually realized by spotwelding of the thermocouple directly on the backside of the thin substrate [24], [25], [43], [45]. A schematic drawing of a typical PTP sensor head is shown in Fig. 3. The substrate dummy, mostly a copper platelet with a diameter between 5 and 11 mm and a thickness of 100–500 μm , is free standing on the spotwelded thermocouple to be thermally isolated [28], [38], [47], [49], [66], [67]. Size and thickness depend on the plasma source and the expected energy flux. Larger substrate dummies result in higher heat capacities and, thus, slower temperature increase of the probe during the plasma treatment. An additional bias wire is connected to the probe to enable grounding or biasing. The platelet is surrounded by a stainless steel shield to ensure energy flux only from the half-space in front of the probe. A ceramic tube enhances the thermal isolation of the cable passage through the base cylinder made from stainless steel. The base cylinder connects all parts and also enables easy mounting of the probe by an ISO metric screw thread. The outer diameter of the PTP is 13 mm and the height amounts to 19 mm. Both dimensions can be adapted to fit experimental needs.

With the increased importance of atmospheric pressure plasma operation and the necessity of plasma diagnostics to ensure reproducibility, the PTP was adapted to match the challenges of atmospheric pressure plasmas. The high voltages and small dimensions of atmospheric pressure discharges can lead to electrical breakdown to the probe itself and, thus, disturb the plasma and results in systematically wrong values. Therefore, dielectric probe materials have been used in the past to avoid electrical breakdowns. For example, heat resistant silicon resin spray [26] was used to coat the copper platelet to create a dielectric surface. For better breakdown protection, a ceramic mica plate can be mounted on top of the copper plate [46]. Even, for nearly complete avoidance of metallic parts, a mica plate was used as substrate dummy and connected to the type K thermocouple using TorSeal [49]. Again, based

on the experimental needs, the calorimetric probe will be adapted and further developed in the future.

B. Data Acquisition Electronics

The circuit board is optimized in size to fit into KF40 flanges with outer dimensions of $116 \text{ mm} \times 20 \text{ mm} \times 36 \text{ mm}$. It is split into two parts, data acquisition on one side and communication on the other, divided by galvanic isolation up to 5 kV to protect the circuit board itself and also the connected computer.

The data acquisition side contains multiple low-pass filters to enable measuring of the small dc voltage created by the thermoelectric effect without disturbance of the plasma generating voltage. A MAX1402 analog-to-digital converter measures the thermoelectric voltage as well as the signal of a PT100 as a reference temperature. The PT100 reference temperature enables calibration of the circuit board to determine absolute temperatures. In the near future, even more channels of the MAX1402 will be used to measure the temperature of multiple sensor heads to enable PTP arrays and single-shot spatially resolved energy flux measurements with one circuit board.

The AD converter signal passes the galvanic isolation and is interpreted by an atmega644-20au microcontroller. For the transmission to computer, RS232 serial communication is used. The probe temperature is recorded over time with a sample rate of 90 Hz. The high sample rate is necessary because the time derivative of the temperature is needed for the evaluation (see Section V).

IV. CALIBRATION PROCEDURE

When the probe receives any energy flux, the temperature changes and the heat capacity C_S is the proportional factor. Thus, the proper determination of this quantity is needed. The elementary approach is to calculate the heat capacity C_S from the specific heat capacity c_S and the mass m_S of the probe via $C_S = c_S \cdot m_S$ [14]. Because of the welded thermocouple and contact to the holder, this calculation is incorrect [25] and an experimental calibration is needed. A general approach to determine the heat capacity is to expose the PTP to a defined power source, while the temperature $T_S(t)$ is measured as a function of time.

As power source, a laser can be used [46], [59], but one has to know the absorbance of the probe, which is not easily estimated as it depends on the material type and the surface structure [25].

A. Electron Beam

A more reliable calibration is achieved by the use of an electron beam [25]. The electrons can either be extracted from a plasma [16] or generated from a hot filament [25]. The latter method is superior, particularly, because of its simplicity and will be summarized here.

A schematic of a typical experimental setup for calibration by electrons is shown in Fig. 4. The electrons are generated by thermionic emission from a filament by applying a voltage U_H . The electrons are pushed away by U_W and accelerated by U_S . The calibration is carried out in a high vacuum chamber at about 10^{-4} Pa to ensure collisionless propagation.

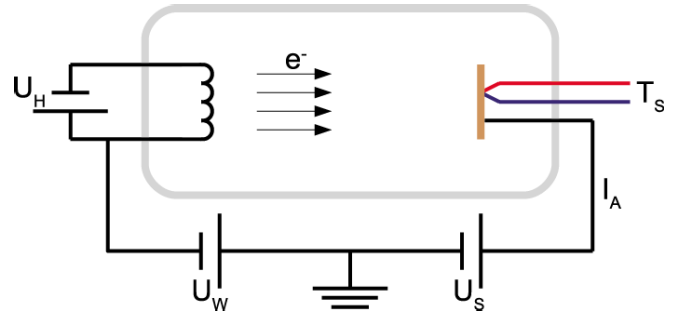


Fig. 4. Schematic setup of the calibration experiment for PTPs using an electron beam as presented in [25].

Therefore, the incoming power at the probe can be calculated from the current I_A through the probe and the applied voltages [25]. The requirement to measure the current I_A limits this calibration method to probes with a conducting substrate dummy [26], [44].

B. Ion Beam

Alternatively, an ion beam can be used as defined power source. For the calibration, an additional arbitrarily calibrated probe is needed. By placing both probes in a homogeneous section of the ion beam, they will be affected with the same energy flux. The measurements of both probes are then evaluated as described in Section V. By comparison with the already calibrated probe, the heat capacity for the tested probe can be calculated. This method allows to calibrate PTPs that are not electrically conducting [26], [44]. It also allows to calibrate multiple probes at once which is especially useful. A possible ion beam source for such calibration was presented in [68] and [69].

V. EVALUATION PROCEDURE

The determination of the energy flux can be achieved by different methods [19], [24], [48], [55], [56], [70]. For atmospheric pressure plasmas, the *dT-method* as well as the so-called *kink-method* have been proofed to be successful for the evaluation of the temperature over time. Hence, these methods will be introduced here and their utilization is demonstrated in Section VI.

A. Measurement Principle

The enthalpy (H) describes the energy of a thermodynamic system and is a measure for the total amount of stored energy. Temporal change of the substrates enthalpy (\dot{H}_S) equals its temperature change ($\dot{T}_S = dT_S/dt$) times its heat capacity (C_S). Assuming no processes taking place inside the substrate, the change of enthalpy results due to exchange processes with the environment. Thus, the substrates change of enthalpy equals the difference of power coming to the substrate (P_{in}) and power leaving the substrate (P_{out})

$$\dot{H}_S = C_S \dot{T}_S = P_{in} - P_{out}. \quad (1)$$

Normalizing the power to the substrate area (A_S) results in the energy fluxes

$$J_{in} = P_{in}/A_S \quad \text{and} \quad J_{out} = -P_{out}/A_S \quad (2)$$

with power being defined as absolute value. The minus sign in P_{out} is necessary as the energy flux J_{out} is leaving the substrate and, thus, negative.

To consider the term P_{out} , it is possible to switch off the power P_{in} transferred from the plasma to the substrate by switching off the plasma or stopping the substrates exposure to the plasma. Finally, two equations are obtained to describe the change of enthalpy, one during heating of the substrate and one during cooling

$$\text{Heating: } \dot{H}_{S,h} = C_S \dot{T}_{S,h} = P_{\text{in}} - P_{\text{out}} \quad (3)$$

$$\text{Cooling: } \dot{H}_{S,c} = C_S \dot{T}_{S,c} = -P_{\text{out}}. \quad (4)$$

With the assumptions of a constant energy influx during heating and power losses (mainly caused by conduction), it is possible to solve the first-order linear differential equations for the substrate temperature during heating and cooling. The power losses are dependent on a geometrical and material-specific cooling coefficient α , the equilibrium temperature of the substrate $T_{S,\text{eq}}$, and the substrates starting temperature $T_{S,\text{st}}$ when the cooling begins

$$P_{\text{out}} = \alpha(T_{S,\text{st}} - T_{S,\text{eq}}). \quad (5)$$

The solution of (3) for $T_{S,h}$ is [56], [71]

$$T_{S,h}(t) = \left(T_{S,\text{eq}} + \frac{P_{\text{in}}}{\alpha}\right) - \left(\frac{P_{\text{in}}}{\alpha}\right) \exp\left(-\frac{\alpha}{C_S}t\right) \quad (6)$$

where t denotes the time. The first time derivative of (6) is

$$\dot{T}_{S,h} = -\frac{\alpha}{C_S}T_{S,h} + \frac{P_{\text{in}} + \alpha T_{S,\text{eq}}}{C_S} \quad (7)$$

which becomes again dependent on the substrate temperature by equating the exponential terms of the derivative and (6).

The solution for $T_{S,c}$ of (4) is

$$T_{S,c}(t) = T_{S,\text{eq}} + (T_{S,\text{st}} - T_{S,\text{eq}}) \exp\left(-\frac{\alpha}{C_S}t\right) \quad (8)$$

and its temporal derivative becomes

$$\dot{T}_{S,c} = -\frac{\alpha}{C_S}T_{S,c} + \frac{\alpha T_{S,\text{eq}}}{C_S}. \quad (9)$$

Both (7) and (9) show a linear dependence with equal slopes of \dot{T}_S on T_S , which is important for the *dT-method*.

Furthermore, assuming equal power losses during heating and cooling of the substrate, (3) and (4) can be combined and rearranged to calculate the energy flux

$$J_{\text{in}} = \frac{P_{\text{in}}}{A_S} = \frac{C_S}{A_S}(\dot{T}_{S,h} - \dot{T}_{S,c}). \quad (10)$$

B. *dT-Method*

The *dT-method* enables a graphical visualization of the energy flux. The time derivative of the probe temperature of one heating and subsequent cooling phase is numerically determined and plotted against the substrate temperature T_S (see Fig. 5). This depiction shows the temperature change \dot{T}_S as a function of its temperature T_S as described in (7) and (9). Two parallel lines, one resulting from the heating phase and one of the cooling phase, separated by a constant offset are expected. The offset between the lines is used in (10)

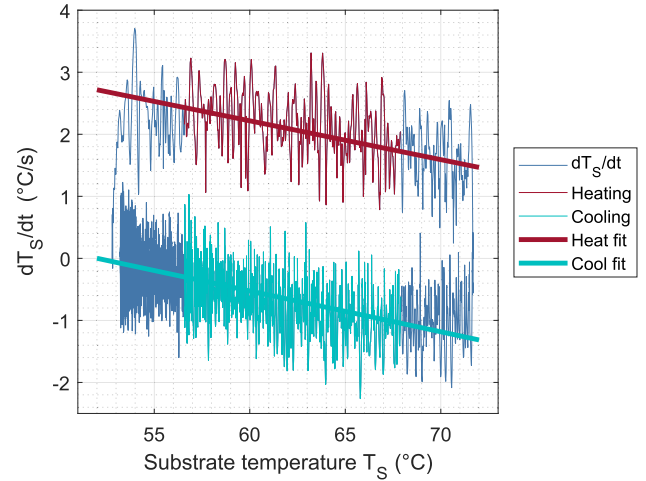


Fig. 5. *dT-depiction* of measurement data obtained for a surface barrier discharge as example for the *dT-method* evaluation. The offset between the parallel fit lines represent the energy flux to the substrate. More details are given in the text and in [49].

to calculate the energy influx and should be constant for all substrate temperatures. Deviations of this expected behavior can have multiple reasons and have to be addressed to either systematical errors or temperature- and/or time-dependent changing energy fluxes.

As an example for the *dT-method*, data from energy flux measurements on a diffuse coplanar surface barrier discharge (DCSBD, [72]–[74]) are shown in Fig. 5. A detailed description of the measurements can be found in [49].

The derivation of the temperature data shown in dark blue indicates a nonoptimal behavior, as the heating and cooling phase data points are not parallel over all substrate temperatures. Such deviations from the expected behavior are visible, in particular, at the beginning of the heating (upper line, low temperature) and cooling (lower line, high temperature) phases. They are an artifact of the deployed substrate dummy since a fully ceramic substrate was used. Its thermal inertia and high heat capacity results in blurred transitions due to energy stored inside the probe itself and the time frame needed to heat the full probe volume to equal temperature. To exclude this systematic error, linear fitting was performed only between 20 % and 80 % of the substrates maximum temperature. Hence, the resulting linear lines are parallel to each other, and from their distance, the energy flux can be easily determined by 10.

This example illustrates how the *dT-method* can be applied and how it can be used to detect systematic errors, exclude them, and successfully obtain energy flux values even for nonideal conditions. Other evaluation methods are also based on the *dT-method* but do not consider the full temperature range. For example, the *kink-method*, which will be introduced next, is one of these methods, which has been proved useful under atmospheric pressure conditions, too. Still, it should be mentioned that the *dT-depiction* should be used at least once to verify the applicability of the made assumptions.

C. *Kink-Method*

The *kink-method* first introduced in low-pressure environments only uses short time periods of the temperature curve around the beginning and ending of the heating phase

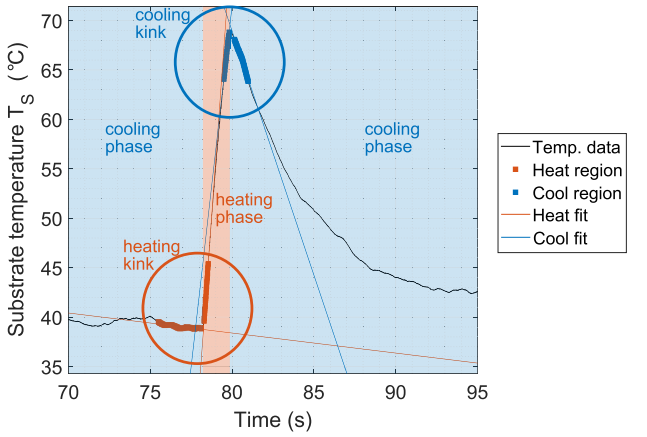


Fig. 6. Illustration of the *kink-method*. Measured data are obtained for a surface barrier discharge. The substrate dummy is in contact with the plasma during the heating phase. Linear fitting is used around the heating and cooling kink to determine the energy flux. More details are given in the text and in [26].

[75], [76]. The advantage of using only short time periods is to ensure the assumption of equal power loss terms, as the substrate temperature is nearly constant during this time. For short time periods, (6) and (8) can be approximated as linear functions using the Taylor series

$$T_{S,h}(t) = \frac{P_{in}}{C_S}t + T_{S,eq} \quad (11)$$

$$T_{S,c}(t) = (T_{S,eq} - T_{S,st})\frac{\alpha}{C_S}t + T_{S,st}. \quad (12)$$

These equations can be used to determine $(\dot{T}_{S,h} - \dot{T}_{S,c})$ in (10) and calculate the energy flux.

To illustrate the *kink-method* a temperature curve obtained on the DCSBD is shown in Fig. 6. The heating (contact between probe and plasma) and cooling (no contact between probe and plasma) phase is marked in the figure, as well as the so-called heating and cooling kink. The kinks denote the points, where the heating or cooling of the substrate starts. Around the kinks, linear fitting is applied to determine the slopes of (11) and (12). The difference of these slopes represents the energy flux following (10).

Using this method, the energy flux is punctually evaluated at the beginning and the end of the heating phase. Thus, two energy flux values are obtained for one heating phase, which should match. To visualize this, one has to go back to the *dT-depiction* in Fig. 5. While the *dT-method* evaluates the full (or parts of) substrate temperature range, the *kink-method* only evaluates the energy flux at the minimal and maximal substrate temperature. One can recognize that the *kink-method* applied to the measurement data shown in Fig. 5 would result in systematically wrong values due to the thermal inertia of the substrate dummy addressed in Section V-B. Therefore, before using the *kink-method*, one has to validate whether it can be applied to the measured data. As an example, for the $T_S(t)$ -measurement shown in Fig. 6, a thin copper probe with dielectric coating was used, which is less inert and, thus, the *kink-method* could be applied [26].

Overall, the *kink-method* has several advantages, such as short measurement time, no necessity for complex fitting or

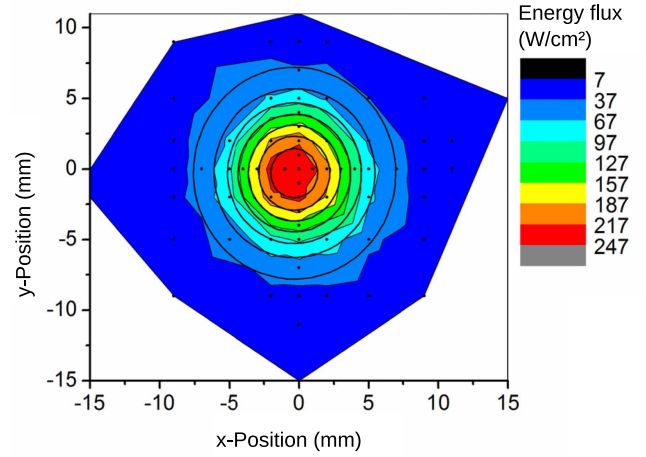


Fig. 7. Radial profile of the energy flux in the effluent of a plasma jet described in [48]. The black dots depict a 2-D-Gaussian fit of the measured energy flux. For the measurements, a PTP was placed at a distance of 6 mm to the nozzle and the jet was operated at a primary power of 2.4 kW with a gas flow of 30-slm air. Reprinted in modified form from [47].

numerical derivatives, and negligible influence of substrate and/or ambient temperature changes.

VI. EXPERIMENTAL RESULTS

A. Spatial Characterization of an Atmospheric Pressure Plasma Jet

Atmospheric pressure plasma jets receive great interest due to their broad range for different surface treatments [45], [77]–[80]. Therefore, an understanding of the plasma–surface interaction is crucial to optimize the respective processes. For this purpose, the energy flux of a commercially available plasma jet was investigated with a PTP [48].

The jet consists of an inner electrode and an outer metal cylinder that is insulated on the inside by a ceramic layer. The discharge emerges from the inner electrode toward the metallic nozzle. To suppress any contact of the discharge with treated surfaces in the effluent and to enhance the plasma turbulence, a grid is placed inside the nozzle head [48].

Results of the experiments are shown in Fig. 7. The jet was driven by a rectangular signal with a frequency of 19 kHz and a duty cycle of 50 %. The gas flow through the jet was 30-slm air. A PTP with a copper substrate dummy described in [48] was placed in 6-mm distance to the nozzle, while the radial position relative to the effluent was varied.

The resulting energy flux ranges from 7 W/cm² at the edges of the effluent up to 247 W/cm² in the center. It reveals a high radial symmetry that was compared with a 2-D-Gaussian fit shown as black dots in Fig. 7. The fit result reinforced the observation of high radial symmetry. One has to consider that the probe diameter of 5 mm is in the order of the size of the effluent. Hence, the shown profile is a convolution of the probe area and the energy flux, and thus, the real profile is assumed to be steeper and narrower.

As the energy flux is a key parameter for applications [21], [22], the results help to choose an optimized parameter set where the thermal load is acceptable, while the desired effect can be maximized. To untangle the effect of different parameters such as discharge voltage and gas flow, the energy

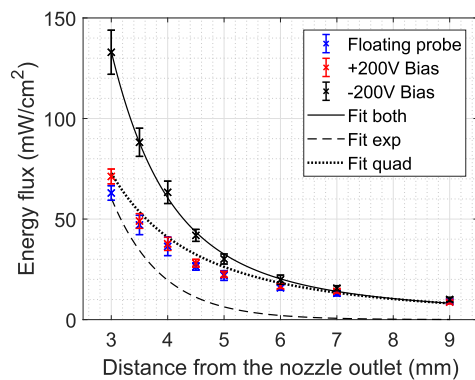


Fig. 8. Energy flux of a plasma jet as a function of the distance to the nozzle at different bias voltages. The discharge was generated by a nanosecond pulse generator with voltages of around 5.5 kV. The jet was operated with a gas flow of 500-sccm He and 500-sccm air coflow through a gas shielding device. Reprinted from [49].

flux measurements in [48] were performed for varying conditions.

B. Contribution of Ions and Electrons to the Energy Flux of a Cold Atmospheric Pressure (CAP) Plasma Jet

Measurement by PTP allows to determine the integral energy flux with little effort required for the experimental setup. To gain more insight into the fundamental processes involved in plasma–surface interactions, it is desired to unravel the contribution of the plasma species, e.g., electrons, ions, and fast neutrals to the integral energy flux. By biasing the PTP, one can repel either positive or negative charged particles and, thus, distinguish between their contributions. For plasma jets, this method is complicated mainly by three things. First, all the lifetimes of the plasma species are short and, therefore, the mean free path of particles in, e.g., air is limited to a few tenth of nm [81]. Second, a jet can operate at a turbulent regime, and thus, the actual path of a particle is not necessarily equal to the distance between the discharge and the probe. Third, because of the dimensions, a PTP has to be placed near the electrodes. Hence, the bias or even the floating potential of the probe can affect the discharge [44], [49], [63]–[65].

In [49], a cold plasma jet was successfully characterized with a biased PTP. The PTP featured a copper substrate dummy. A custom-made jet was used consisting of a polyoxymethylene (POM) housing, a ceramic cylinder as dielectric barrier, three symmetrically arranged gas inlets to achieve an even gas flow distribution, and steel needle electrode. A copper ring embedded into the polymer around the ceramic acts as counter electrode. The jet was powered by high-voltage nanosecond pulse generator that produces pulses of 40-ns length with voltages of around 5.5 kV at a repetition frequency of 1 kHz. In addition, a shielding gas curtain was used to create a coflow around the effluent. A detailed description can be found in [49].

In Fig. 8, the energy flux in dependence on the distance to the nozzle of the jet is shown for different bias voltages. The jet was operated with a flow of 500-sccm He and a coflow of 500-sccm artificial air (80/20 N₂/O₂). These parameters ensure a laminar flow, which was confirmed by the Rayleigh scattering [49], [82]. An exponential decay of the energy flux

can be observed with a maximum value of (63 ± 4) mW/cm² at a distance of 3 mm for the floating PTP. This exponential decay is caused by a change of the different contributions to the integral energy flux. The more pronounced decay at shorter distances is due to fewer reactive particles reaching the surface of the probe. An estimation based on the flow rate and the jet geometry results in particles propagating up to 5 mm in 2.4 ms, while the lifetimes of ionic species are only in order of tens of μ s [49]. At distances above 5 mm, the energy flux is, therefore, dominated by radiation. Thus, the decay gets slower. Only slight difference can be seen between the floating and the positively biased probe. At a distance of 3 mm, the energy flux of the positively biased probe is slightly higher (71 mW/cm²).

With a negatively biased PTP, the energy flux increases to 133 mW/cm² for a distance of 3 mm. This significant increase can be seen up to a distance of 6 mm. A large contribution from positive ions to the energy flux is, therefore, implied. These ions are attracted toward the PTP by a potential difference of -365 V because the floating potential was 165 V at 3 mm distance. Yet, the higher kinetic energy of the plasma ions is unlikely to dominate the energy flux increase due to the small mean free paths in air and He. This leads to the conclusion that the Penning ionization is crucial. The Penning ionization allows the formation of positive ions outside the discharge if He metastables are available. These metastables follow the gas flow and, hence, enable the generation of positive ions at even greater distances.

The fits applied to the energy flux values of the negatively biased PTP show the postulated change of contributions to the integral energy flux once more. As fit function (both), the sum of an exponential (exp) and a quadratic (quad) decay was chosen, as the exponential part reflects less particles reaching the surface of the probe, whereas the quadratic part represents the radiation. For distances above 6 mm, only radiation seems to contribute to the integral energy flux. A detailed analysis along with the fitting equations and results can be found in [49].

While measurements with a biased PTP at atmospheric pressure remain challenging still, one can gain insight into the discharge on a fundamental level.

C. Diffuse Coplanar Surface Barrier Discharge

The characteristic feature of DBDs is an electrode configuration that contains an insulating material in the discharge. Because of the dielectric barrier, the discharge turns into a self-pulsing and consequently a nonthermal plasma at atmospheric pressure [5]. DBDs have many applications, such as gas, liquid, and surface treatment along with appliance in medicine [1], [5]. A detailed introduction can be found in [1] and [5].

DCSBDs are a special type of DBDs that produces a visually diffuse discharge by structuring the electrodes such as two interlocking combs. The electrodes are embedded into an insulating ceramic [1], [26], [72]–[74].

In [44], a commercial DCSBD by Roplass was investigated. From the measured oil temperature along with the electrical input power and the energy flux, the energy balance could be deduced. The DCSBD is powered by a sinusoidal signal with a frequency from 14 up to 18 kHz and an input power of up to 380 W. A full description of the DCSBD is found in [72]–[74].

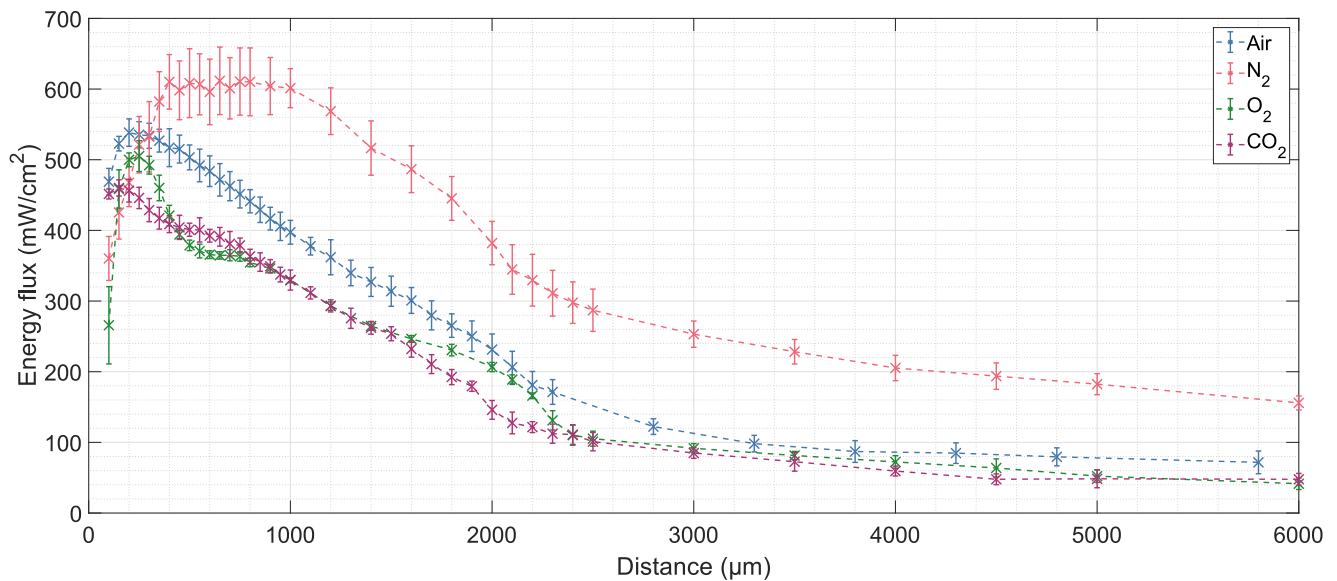


Fig. 9. Energy flux as a function of the distance between the ceramic surface of a DCSBD and a PTP for different working gases. The error bars show the statistical error from multiple measurements. Reprinted from [44].

For energy flux measurements, a PTP with a ceramic substrate dummy was placed above the ceramic surface of the DCSBD. To adjust the height of the probe relative to the ceramic surface, a micrometer screw was utilized. The DCSBD was placed in a polymethyl methacrylate (PMMA) gas box with a volume of 1 l. While operating the DCSBD, a gas flow of 3 slm of air, N₂, O₂, or CO₂ was generated. The setup is presented in detail in [44].

In Fig. 9, the measured energy flux depending on the height of the PTP above the electrode is shown for the different gases. For each gas, a maximum is reached but at different distances. CO₂ reaches a maximum energy flux of (460 ± 11) mW/cm² at a distance of 150 μm followed by air with its maximum of (538 ± 19) mW/cm² at 200 μm. At 250 μm, the energy flux is maximal for O₂ with (505 ± 22) mW/cm², while N₂ shows a maximum energy flux of (612 ± 48) mW/cm² at 650 μm. It is suspected that the shift of the maximum toward greater distances is an effect of the electronegativity of oxygen-containing gases. In such gases, the inert negative ions would stay close to surface. Thus, a negative potential barrier would be created, which hinders electrons from moving considerably far away from the surface. Hence, the discharge would be forced to form in the vicinity of the surface.

Another striking feature of the height-dependent energy flux in Fig. 9 can be found for the falling flank with increasing distances. In addition to the overall drop of the energy flux at greater distances, a second turning point with a slower reduction of the energy flux can be recognized. This relates to the various components of the integral energy flux. The probe surface participates either directly in chemical reactions (such as oxidation) or indirectly as third collision partner that soaks up the excess energy. Furthermore, the probe interacts with the plasma species, e.g., ions, electrons, and fast neutrals or radicals, which can impinge with high kinetic energy or recombine at the probe surface. As described above, the lifetimes and the mean free path of these species are very small at atmospheric pressure. The fast drop of the energy flux is induced by the decreasing amount of plasma species reaching

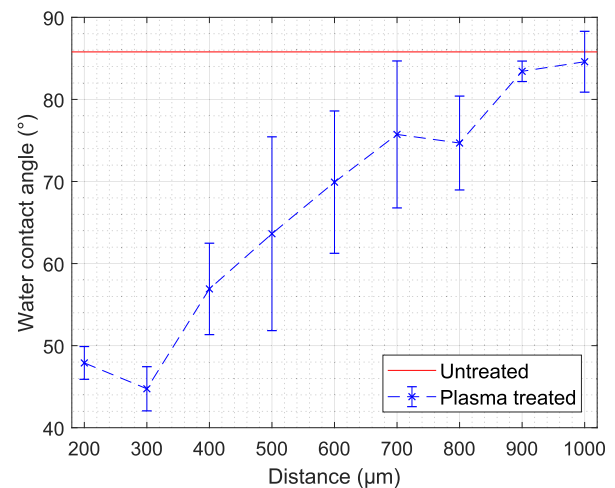


Fig. 10. WCA measurements on PP foils plasma-treated at different distances to the DCSBD electrode surface. The DCSBD was operated in air at 380-W input power and the plasma treatment time was 1 s. The untreated WCA of the PP foil is shown as a red line. The error bars result from multiple measurements.

the probe, whereas at greater distances, radiation dominates the energy flux leading to slower reduction of the energy flux.

These results can help to understand the spatial extension of the discharge, which are of immense interest when plasma treatment with the DCSBD shall be optimized. A full discussion of the results, including the energy balance of a DCSBD, can be found in [44].

An important field of application for surface barrier discharges is surface activation [5], [73], [83]. During the plasma treatment, functional groups are generated on the substrate surface and influence the surface free energy of the substrate [84]. A high surface free energy enables the substrate to form chemical bonds easier, which enhances the wettability of the surface. Thus, print or glue will stick better or at all on the plasma-treated surface [85]–[88].

A measure for the surface free energy is the water contact angle (WCA). Small WCAs indicate a high surface free energy

and, thus, a successful plasma treatment [89]. Polypropylene (PP) foils were plasma-treated using the DCSBD with air as working gas at 380-W electrical power for 1 s at different distances to the ceramic surface of the DCSBD. The WCAs were measured using the sessile drop method [89] and are shown in Fig. 10. The WCA of an untreated PP foil is shown as a red line. The best treatment success is visible at a distance of $300\ \mu$, which matches the maximal energy flux determined with the same working gas in Fig. 9. Furthermore, the course of the energy flux values reflects the inverted course of the WCA measurements. This behavior was expected since a high energy transfer (up to a material-dependent threshold) should result in an effective surface activation process. The faster decrease in surface activation to higher distances compared to the decrease in the energy flux is probably due to the different contributions of the energy flux. The energy flux decreases slower as a major contributor is radiation, which decreases slower for larger distances compared to, e.g., energy being transferred by energetic particles or radicals [44], [49]. For the surface activation of PP, it seems that the energetic particles and, especially, O radicals are more important.

VII. CONCLUSION

PTPs have had an extensive advancement since its start with Thornton, and the energy flux was proved to be a key parameter for applications, e.g., thin-film deposition and surface activation. Effective calibration and evaluation allow to make full use of the potential of calorimetric methods. By electric insulated substrate dummies of different sizes, the PTP can be adapted for various setups. Hence, PTPs are nowadays a versatile tool that can be easily integrated into different atmospheric pressure plasma environments.

As shown in the exemplary results, a PTP can be utilized to characterize the structure of the plasma–surface interaction for atmospheric pressure plasmas. By careful analysis, one can even gain insight into fundamental processes. While the influence of a PTP on the discharge can impose a problem, it likewise creates also new opportunities. The influence of different substrate materials on the discharge is crucial for applications. Varying the material of the probe allows to simulate these effects. This will be one main goal for future developments. Another objective in this regard is the adaptation of the PTP method for more extreme conditions, e.g., further decrease the diameter of the probe to achieve fine spatial resolution.

The development of calorimetric probes started more than 50 years ago and there is still no end to this development in sight. With the increased importance of atmospheric pressure plasmas, the first steps were made roughly ten years ago to make energy flux measurements available for atmospheric pressure conditions. Recent studies showed the successful adoption of calorimetric probes for atmospheric pressure plasmas. Not only do they provide a simple, robust and comparably cheap plasma diagnostic to compare and optimize plasma sources but they also enable insight into elementary processes and help to understand plasma–surface interaction under atmospheric pressure conditions.

ACKNOWLEDGMENT

The authors would like to thank Michael Poser, Frank Brach, and Volker Rohwer for their technical assistance. They would also like to thank the company Plasmatrete for

supplying their plasma jet system as well as the company Roplass for providing the DCSBD.

REFERENCES

- [1] R. Brandenburg, “Dielectric barrier discharges: Progress on plasma sources and on the understanding of regimes and single filaments,” *Plasma Sour. Sci. Technol.*, vol. 26, no. 5, Mar. 2017, Art. no. 053001, doi: [10.1088/1361-6595/aa6426](https://doi.org/10.1088/1361-6595/aa6426).
- [2] K. H. Becker, H. Kersten, J. Hopwood, and J. L. Lopez, “Microplasmas: Scientific challenges & technological opportunities,” *Eur. Phys. J. D*, vol. 60, no. 3, pp. 437–439, Dec. 2010, doi: [10.1140/epjd/e2010-00231-4](https://doi.org/10.1140/epjd/e2010-00231-4).
- [3] U. Kogelschatz, *Advanced Ozone Generation. In: Process Technologies for Water Treatment*. Boston, MA, USA: Springer, 1988, doi: [10.1007/978-1-4684-8556-1_9](https://doi.org/10.1007/978-1-4684-8556-1_9).
- [4] U. Kogelschatz, H. Esrom, J.-Y. Zhang, and I. W. Boyd, “High-intensity sources of incoherent UV and VUV excimer radiation for low-temperature materials processing,” *Appl. Surf. Sci.*, vol. 168, nos. 1–4, pp. 29–36, Dec. 2000. [Online]. Available: <https://www.sciencedirect.com/science/article/pii/S0169433200005717>
- [5] U. Kogelschatz, “Dielectric-barrier discharges: Their history, discharge physics, and industrial applications,” *Plasma Chem. Plasma Process.*, vol. 23, no. 1, pp. 1–46, 2003.
- [6] R. Matthes *et al.*, “Antimicrobial efficacy of two surface barrier discharges with air plasma against *in vitro* biofilms,” *PLoS ONE*, vol. 8, no. 7, pp. 1–11, Jul. 2013, doi: [10.1371/journal.pone.0070462](https://doi.org/10.1371/journal.pone.0070462).
- [7] O. Sakai and K. Tachibana, “Plasmas as metamaterials: A review,” *Plasma Sour. Sci. Technol.*, vol. 21, no. 1, Jan. 2012, Art. no. 013001, doi: [10.1088/0963-0252/21/1/013001](https://doi.org/10.1088/0963-0252/21/1/013001).
- [8] National Academies of Sciences, Engineering, and Medicine, *Plasma Science: Enabling Technology, Sustainability, Security, and Exploration*. Washington, DC, USA: The National Academies Press, 2021, doi: [10.17226/25802](https://doi.org/10.17226/25802).
- [9] H. Deutsch, H. Kersten, and A. Rutscher, “Basic mechanisms in plasma etching,” *Contrib. Plasma Phys.*, vol. 29, no. 3, pp. 263–284, 1989, doi: [10.1002/ctpp.2150290304](https://doi.org/10.1002/ctpp.2150290304).
- [10] J. Benedikt, H. Kersten, and A. Piel, “Foundations of measurement of electrons, ions and species fluxes toward surfaces in low-temperature plasmas,” *Plasma Sour. Sci. Technol.*, vol. 30, no. 3, Mar. 2021, Art. no. 033001, doi: [10.1088/1361-6595/abe4bf](https://doi.org/10.1088/1361-6595/abe4bf).
- [11] M. A. Lieberman and A. J. Lichtenberg, *Principles of Plasma Discharges and Materials Processing*. New York, NY, USA: Wiley, 1994.
- [12] H. Kersten, H. Deutsch, H. Steffen, G. M. W. Kroesen, and R. Hippler, “The energy balance at substrate surfaces during plasma processing,” *Vacuum*, vol. 63, no. 3, pp. 385–431, Aug. 2001. [Online]. Available: <https://www.sciencedirect.com/science/article/pii/S0042207X01003505>
- [13] D. E. Rapakoulis and D. E. Gerassimou, “Simulation of energy transfer from a glow discharge to a solid surface,” *J. Appl. Phys.*, vol. 62, no. 2, pp. 402–408, Jul. 1987, doi: [10.1063/1.339811](https://doi.org/10.1063/1.339811).
- [14] H. Steffen, H. Kersten, and H. Wulff, “Investigation of the energy transfer to the substrate during titanium deposition in a hollow cathode arc,” *J. Vac. Sci. Technol. A, Vac. Surf. Films*, vol. 12, no. 5, pp. 2780–2783, Sep. 1994, doi: [10.1116/1.579104](https://doi.org/10.1116/1.579104).
- [15] H. Kersten, H. Steffen, D. Vender, and H. Wagner, “On the ion energy transfer to the substrate during titanium deposition in a hollow cathode arc discharge,” *Vacuum*, vol. 46, no. 3, pp. 305–308, Mar. 1995. [Online]. Available: <https://www.sciencedirect.com/science/article/pii/S0042207X94000689>
- [16] R. Wendt, K. Ellmer, and K. Wiesemann, “Thermal power at a substrate during ZnO:Al thin film deposition in a planar magnetron sputtering system,” *J. Appl. Phys.*, vol. 82, no. 5, pp. 2115–2122, Sep. 1997, doi: [10.1063/1.366092](https://doi.org/10.1063/1.366092).
- [17] R. Dussart *et al.*, “Direct measurements of the energy flux due to chemical reactions at the surface of a silicon sample interacting with a SF₆ plasma,” *Appl. Phys. Lett.*, vol. 93, no. 13, Sep. 2008, Art. no. 131502, doi: [10.1063/1.2995988](https://doi.org/10.1063/1.2995988).
- [18] W. P. Leroy, S. Konstantinidis, S. Mahieu, R. Snyders, and D. Depla, “Angular-resolved energy flux measurements of a DC- and HIPIMS-powered rotating cylindrical magnetron in reactive and non-reactive atmosphere,” *J. Phys. D, Appl. Phys.*, vol. 44, no. 11, Mar. 2011, Art. no. 115201, doi: [10.1088/0022-3727/44/11/115201](https://doi.org/10.1088/0022-3727/44/11/115201).
- [19] S. Bornholdt and H. Kersten, “Transient calorimetric diagnostics for plasma processing,” *Eur. Phys. J. D*, vol. 67, no. 8, pp. 1–11, Aug. 2013.
- [20] P.-A. Cormier *et al.*, “Titanium oxide thin film growth by magnetron sputtering: Total energy flux and its relationship with the phase constitution,” *Surf. Coatings Technol.*, vol. 254, pp. 291–297, Sep. 2014. [Online]. Available: <https://www.sciencedirect.com/science/article/pii/S0257897214005489>

- [21] J. Ding *et al.*, "Etching rate characterization of SiO₂ and Si using ion energy flux and atomic fluorine density in a CF₄/O₂/Ar electron cyclotron resonance plasma," *J. Vac. Sci. Technol. A, Vac. Surf. Films*, vol. 11, no. 4, pp. 1283–1288, Jul. 1993, doi: [10.1116/1.578540](https://doi.org/10.1116/1.578540).
- [22] J. G. Han, "Recent progress in thin film processing by magnetron sputtering with plasma diagnostics," *J. Phys. D, Appl. Phys.*, vol. 42, no. 4, Jan. 2009, Art. no. 043001, doi: [10.1088/0022-3727/42/4/043001](https://doi.org/10.1088/0022-3727/42/4/043001).
- [23] J. A. Thornton, "Influence of apparatus geometry and deposition conditions on the structure and topography of thick sputtered coatings," *J. Vac. Sci. Technol.*, vol. 11, no. 4, pp. 666–670, Jul. 1974, doi: [10.1116/1.1312732](https://doi.org/10.1116/1.1312732).
- [24] J. A. Thornton, "Substrate heating in cylindrical magnetron sputtering sources," *Thin Solid Films*, vol. 54, no. 1, pp. 23–31, Oct. 1978. [Online]. Available: <https://www.sciencedirect.com/science/article/pii/0040609078902730>
- [25] M. Stahl, T. Trottenberg, and H. Kersten, "A calorimetric probe for plasma diagnostics," *Rev. Sci. Instrum.*, vol. 81, no. 2, Feb. 2010, Art. no. 023504, doi: [10.1063/1.3276707](https://doi.org/10.1063/1.3276707).
- [26] L. Hansen, K. Reck, and H. Kersten, "Energy flux measurements on an atmospheric pressure surface barrier discharge," *J. Phys. D, Appl. Phys.*, vol. 52, no. 32, Aug. 2019, Art. no. 325201.
- [27] R. Wiese, H. Kersten, G. Wiese, and R. Bartsch, "Energy influx measurements with an active thermal probe in plasma-technological processes," *EPJ Techn. Instrum.*, vol. 2, no. 2, pp. 2195–7045, 2015, doi: [10.1140/epjti/s40485-015-0013-y](https://doi.org/10.1140/epjti/s40485-015-0013-y).
- [28] F. Zahari *et al.*, "Correlation between sputter deposition parameters and $I - V$ characteristics in double-barrier memristive devices," *J. Vac. Sci. Technol. B, Microelectron.*, vol. 37, no. 6, Nov. 2019, Art. no. 061203.
- [29] K. Ellmer and T. Welzel, "Reactive magnetron sputtering of transparent conductive oxide thin films: Role of energetic particle (ion) bombardment," *J. Mater. Res.*, vol. 27, no. 5, pp. 765–779, 2012, doi: [10.1557/jmr.2011.428](https://doi.org/10.1557/jmr.2011.428).
- [30] T. Welzel and K. Ellmer, "Comparison of ion energies and fluxes at the substrate during magnetron sputtering of ZnO: Al for DC and RF discharges," *J. Phys. D, Appl. Phys.*, vol. 46, no. 31, Jul. 2013, Art. no. 315202, doi: [10.1088/0022-3727/46/31/315202](https://doi.org/10.1088/0022-3727/46/31/315202).
- [31] R. Mientus, M. Weise, S. Seeger, R. Heller, and K. Ellmer, "Electrical and optical properties of amorphous SnO₂:Ta films, prepared by DC and RF magnetron sputtering: A systematic study of the influence of the type of the reactive gas," *Coatings*, vol. 10, no. 3, p. 204, Feb. 2020. [Online]. Available: <https://www.mdpi.com/2079-6412/10/3/204>
- [32] S. D. Ekpe and S. K. Dew, "Theoretical and experimental determination of the energy flux during magnetron sputter deposition onto an unbiased substrate," *J. Vac. Sci. Technol. A, Vac., Surf., Films*, vol. 21, no. 2, pp. 476–483, Mar. 2003, doi: [10.1116/1.1554971](https://doi.org/10.1116/1.1554971).
- [33] G. Abadias, W. P. Leroy, S. Mahieu, and D. Depla, "Influence of particle and energy flux on stress and texture development in magnetron sputtered tin films," *J. Phys. D, Appl. Phys.*, vol. 46, no. 5, Dec. 2012, Art. no. 055301, doi: [10.1088/0022-3727/46/5/055301](https://doi.org/10.1088/0022-3727/46/5/055301).
- [34] P.-A. Cormier *et al.*, "Measuring the energy flux at the substrate position during magnetron sputter deposition processes," *J. Appl. Phys.*, vol. 113, no. 1, Jan. 2013, Art. no. 013305, doi: [10.1063/1.4773103](https://doi.org/10.1063/1.4773103).
- [35] Y. Matsuda, T. Hashimoto, S. Akiba, Y. Sakaguchi, S. Wakiyama, and M. Shinohara, "Energy flux to a substrate in ICP assisted magnetron sputtering," in *Proc. 12th Asia Pacific Phys. Conf.* 2014, Art. no. 015063, doi: [10.7566/JPSCP.1.015063](https://doi.org/10.7566/JPSCP.1.015063).
- [36] Y. Matsuda, K. Mine, S. Wakiyama, and M. Shinohara, "Measurement of energy flux to a substrate by thermal and Langmuir probes during inductively coupled plasma assisted DC magnetron sputtering," *Jpn. J. Appl. Phys.*, vol. 54, no. 1S, Nov. 2014, Art. no. 01AB02, doi: [10.7566/jjap.54.01ab02](https://doi.org/10.7566/jjap.54.01ab02).
- [37] A.-L. Thomann, A. Caillard, M. Raza, M. E. Mokh, P. A. Cormier, and S. Konstantinidis, "Energy flux measurements during magnetron sputter deposition processes," *Surf. Coatings Technol.*, vol. 377, Nov. 2019, Art. no. 124887. [Online]. Available: <https://www.sciencedirect.com/science/article/pii/S025789721930859X>
- [38] S. Gauter, F. Haase, and H. Kersten, "Experimentally unraveling the energy flux originating from a DC magnetron sputtering source," *Thin Solid Films*, vol. 669, pp. 8–18, Jan. 2019.
- [39] N. P. Poluektov, Y. P. Tsar'gorodsev, I. I. Usatov, and A. G. Evstigneev, "Energy flux to the substrate in a magnetron discharge with hollow cathode," *Thin Solid Films*, vol. 640, pp. 60–66, Oct. 2017. [Online]. Available: <https://www.sciencedirect.com/science/article/pii/S0040609017306478>
- [40] A. Anders, "A structure zone diagram including plasma-based deposition and ion etching," *Thin Solid Films*, vol. 518, no. 15, pp. 4087–4090, May 2010. [Online]. Available: <https://www.sciencedirect.com/science/article/pii/S0040609009018288>
- [41] B. B. Sahu and J. G. Han, "Comparison of plasma excitation, ionization, and energy influx in single and dual frequency capacitive discharges," *Phys. Plasmas*, vol. 23, no. 12, Dec. 2016, Art. no. 123504, doi: [10.1063/1.4969088](https://doi.org/10.1063/1.4969088).
- [42] C.-F. Han, C.-C. Lin, and J.-F. Lin, "Applications of energy flux and numerical analyses to the plasma etching of silicon deep trench isolation (DTI) structures," *Precis. Eng.*, vol. 71, pp. 141–152, Sep. 2021. [Online]. Available: <https://www.sciencedirect.com/science/article/pii/S0141635921000945>
- [43] F. Haase, D. Manova, D. Hirsch, S. Mändl, and H. Kersten, "Dynamic determination of secondary electron emission using a calorimetric probe in a plasma immersion ion implantation experiment," *Plasma Sour. Sci. Technol.*, vol. 27, no. 4, Apr. 2018, Art. no. 044003.
- [44] L. Hansen, L. Rosenfeldt, K. A. Reck, and H. Kersten, "Understanding the energy balance of a surface barrier discharge for various molecular gases by a multi-diagnostic approach," *J. Appl. Phys.*, vol. 129, no. 5, Feb. 2021, Art. no. 053308, doi: [10.1063/5.0035671](https://doi.org/10.1063/5.0035671).
- [45] S. Bornholdt, M. Wolter, and H. Kersten, "Characterization of an atmospheric pressure plasma jet for surface modification and thin film deposition," *Eur. Phys. J. D*, vol. 60, no. 3, pp. 653–660, Dec. 2010, doi: [10.1140/epjd/e2010-00245-x](https://doi.org/10.1140/epjd/e2010-00245-x).
- [46] D. Mance, R. Wiese, T. Kewitz, and H. Kersten, "Atmospheric pressure plasma jet for biomedical applications characterised by passive thermal probe," *Eur. Phys. J. D*, vol. 72, no. 6, Jun. 2018, doi: [10.1140/epjd/e2018-80768-8](https://doi.org/10.1140/epjd/e2018-80768-8).
- [47] T. Kewitz, M. Fröhlich, J. von Frieling, and H. Kersten, "Investigation of a commercial atmospheric pressure plasma jet by a newly designed calorimetric probe," *IEEE Trans. Plasma Sci.*, vol. 43, no. 5, pp. 1769–1773, May 2015.
- [48] T. Kewitz, M. Fröhlich, and H. Kersten, "Analysis of passive calorimetric probe measurements at high energy influxes," *EPJ Techn. Instrum.*, vol. 4, no. 1, pp. 1–9, Dec. 2017.
- [49] L. Hansen, B. M. Goldberg, D. Feng, R. B. Miles, H. Kersten, and S. Reuter, "Energy transfer in interaction of a cold atmospheric pressure plasma jet with substrates," *Plasma Sour. Sci. Technol.*, vol. 30, no. 4, Apr. 2021, Art. no. 045004, doi: [10.1088/1361-6595/abe955](https://doi.org/10.1088/1361-6595/abe955).
- [50] T. H. Lodwig and W. A. Smeaton, "The ice calorimeter of Lavoisier and Laplace and some of its critics," *Ann. Sci.*, vol. 31, no. 1, pp. 1–18, Jan. 1974, doi: [10.1080/00033797400200101](https://doi.org/10.1080/00033797400200101).
- [51] S. V. Meschel, "A brief history of heat measurements by calorimetry with emphasis on the thermochemistry of metallic and metal-nonmetal compounds," *Calphad*, vol. 68, Mar. 2020, Art. no. 101714. [Online]. Available: <https://www.sciencedirect.com/science/article/pii/S0364591619302755>
- [52] G. N. Jackson, "Substrate bombardment in RF sputtering systems," *Vacuum*, vol. 19, no. 11, pp. 493–496, 1969. [Online]. Available: <https://www.sciencedirect.com/science/article/pii/S0042207X69917837>
- [53] B. Koch, W. Bohmeyer, G. Fussmann, P. Kornejew, and H.-D. Reiner, "Energy flux measurements in a steady-state discharge at PSI-2," *J. Nucl. Mater.*, vols. 290–293, pp. 653–657, Mar. 2001. [Online]. Available: <https://www.sciencedirect.com/science/article/pii/S0022311500005973>
- [54] H. Kersten *et al.*, "Energy influx from an RF plasma to a substrate during plasma processing," *J. Appl. Phys.*, vol. 87, no. 8, pp. 3637–3645, Apr. 2000, doi: [10.1063/1.372393](https://doi.org/10.1063/1.372393).
- [55] S. Bornholdt, M. Fröhlich, and H. Kersten, *Calorimetric Probes for Energy Flux Measurements in Process Plasmas*. Cham, Switzerland: Springer, 2014, pp. 197–234, doi: [10.1007/978-3-319-05437-7_6](https://doi.org/10.1007/978-3-319-05437-7_6)
- [56] H. Kersten *et al.*, "On the determination of energy fluxes at plasma-surface processes," *Appl. Phys. A, Solids Surf.*, vol. 72, no. 5, pp. 531–540, May 2001, doi: [10.1007/s003390100811](https://doi.org/10.1007/s003390100811).
- [57] M. Wolter, M. Stahl, and H. Kersten, "Spatially resolved thermal probe measurement for the investigation of the energy influx in an RF-plasma," *Vacuum*, vol. 83, no. 4, pp. 768–772, Nov. 2008. [Online]. Available: <https://www.sciencedirect.com/science/article/pii/S0042207X08003308>
- [58] H. Kersten *et al.*, "Examples for application and diagnostics in plasma-powder interaction," *New J. Phys.*, vol. 5, p. 93, Jul. 2003.
- [59] H. Kersten, D. Rohde, J. Berndt, H. Deutsch, and R. Hippler, "Investigations on the energy influx at plasma processes by Means of a simple thermal probe," *Thin Solid Films*, vols. 377–378, pp. 585–591, Dec. 2000. [Online]. Available: <https://www.sciencedirect.com/science/article/pii/S0040609000014425>

- [60] P.-A. Cormier *et al.*, "On the measurement of energy fluxes in plasmas using a calorimetric probe and a thermopile sensor," *J. Phys. D, Appl. Phys.*, vol. 43, no. 46, Nov. 2010, Art. no. 465201, doi: [10.1088/0022-3727/43/46/465201](https://doi.org/10.1088/0022-3727/43/46/465201).
- [61] G. Primc and M. Mozetič, "Neutral reactive gaseous species in reactors suitable for plasma surface engineering," *Surf. Coatings Technol.*, vol. 376, pp. 15–20, Oct. 2019. [Online]. Available: <https://www.sciencedirect.com/science/article/pii/S0257897218314026>
- [62] L. Hansen, A. Schmidt-Bleker, R. Bansemer, H. Kersten, K.-D. Weltmann, and S. Reuter, "Influence of a liquid surface on the NO_x production of a cold atmospheric pressure plasma jet," *J. Phys. D, Appl. Phys.*, vol. 51, no. 47, 2018, Art. no. 474002.
- [63] T. Darny, J.-M. Pouvesle, V. Puech, C. Douat, S. Dozias, and E. Robert, "Analysis of conductive target influence in plasma jet experiments through Helium metastable and electric field measurements," *Plasma Sour. Sci. Technol.*, vol. 26, no. 4, Mar. 2017, Art. no. 045008, doi: [10.1088/1361-6595/aa5b15](https://doi.org/10.1088/1361-6595/aa5b15).
- [64] A. Sobota *et al.*, "Plasma-surface interaction: Dielectric and metallic targets and their influence on the electric field profile in a KHz AC-driven He plasma jet," *Plasma Sour. Sci. Technol.*, vol. 28, no. 4, Apr. 2019, Art. no. 045003, doi: [10.1088/1361-6595/ab0c6a](https://doi.org/10.1088/1361-6595/ab0c6a).
- [65] K. Urabe, T. Morita, K. Tachibana, and B. N. Ganguly, "Investigation of discharge mechanisms in Helium plasma jet at atmospheric pressure by laser spectroscopic measurements," *J. Phys. D, Appl. Phys.*, vol. 43, no. 9, Feb. 2010, Art. no. 095201, doi: [10.1088/0022-3727/43/9/095201](https://doi.org/10.1088/0022-3727/43/9/095201).
- [66] J. Cipo, F. Schlichting, F. Zahari, S. Gauter, H. Kohlstedt, and H. Kersten, "Diagnostics of process plasma used for the production of memristive devices," *J. Phys., Conf. Ser.*, vol. 1492, Apr. 2020, Art. no. 012002.
- [67] T. Kewitz, C. Regula, M. Fröhlich, J. Ihde, and H. Kersten, "Influence of the nozzle head geometry on the energy flux of an atmospheric pressure plasma jet," *EPJ Techn. Instrum.*, vol. 8, no. 1, Dec. 2021.
- [68] M. Klette, M. Maas, T. Trottenberg, and H. Kersten, "Directionally resolved measurements of momentum transport in sputter plumes as a critical test for simulations," *J. Vac. Sci. Technol. A, Vac. Surf. Films*, vol. 38, no. 3, May 2020, Art. no. 033013, doi: [10.1116/6.0000109](https://doi.org/10.1116/6.0000109).
- [69] M. Zeuner *et al.*, "A unique ECR broad beam source for thin film processing," *Surf. Coatings Technol.*, vols. 142–144, pp. 11–20, Jul. 2001. [Online]. Available: <https://www.sciencedirect.com/science/article/pii/S0257897201011446>
- [70] H. Kersten and G. M. W. Kroesen, "The thermal balance of substrates during plasma processing," *Contrib. Plasma Phys.*, vol. 30, no. 6, pp. 725–731, 1990.
- [71] S. Bornholdt, T. Peter, T. Strunskus, V. Zaporozhchenko, F. Faupel, and H. Kersten, "The method of conventional calorimetric probes—A short review and application for the characterization of nanocluster sources," *Surf. Coatings Technol.*, vol. 205, pp. S388–S392, Jul. 2011.
- [72] M. Šimor, J. Ráhel, P. Vojtek, M. Černák, and A. Brablec, "Atmospheric-pressure diffuse coplanar surface discharge for surface treatments," *Appl. Phys. Lett.*, vol. 81, no. 15, pp. 2716–2718, Oct. 2002.
- [73] M. Černák, L. Černáková, I. Hudec, D. Kováčik, and A. Zahoranová, "Diffuse coplanar surface barrier discharge and its applications for in-line processing of low-added-value materials," *Eur. Phys. J. Appl. Phys.*, vol. 47, no. 2, p. 22806, Aug. 2009.
- [74] M. Černák *et al.*, "Generation of a high-density highly non-equilibrium air plasma for high-speed large-area flat surface processing," *Plasma Phys. Controlled Fusion*, vol. 53, no. 12, Dec. 2011, Art. no. 124031.
- [75] S. Gauter, M. Fröhlich, W. Garkas, M. Polak, and H. Kersten, "Calorimetric probe measurements for a high voltage pulsed substrate (PBII) in a HiPIMS process," *Plasma Sour. Sci. Technol.*, vol. 26, no. 6, May 2017, Art. no. 065013.
- [76] S. Gauter *et al.*, "Calorimetric investigations in a gas aggregation source," *J. Appl. Phys.*, vol. 124, no. 7, Aug. 2018, Art. no. 073301.
- [77] M. Noeske, J. Degenhardt, S. Strudthoff, and U. Lommatzsch, "Plasma jet treatment of five polymers at atmospheric pressure: Surface modifications and the relevance for adhesion," *Int. J. Adhes. Adhesives*, vol. 24, no. 2, pp. 171–177, Apr. 2004. [Online]. Available: <https://www.sciencedirect.com/science/article/pii/S0143749603001246>
- [78] J. Benedikt, V. Raballand, A. Yanguas-Gil, K. Focke, and A. von Keudell, "Thin film deposition by Means of atmospheric pressure microplasma jet," *Plasma Phys. Controlled Fusion*, vol. 49, no. 12B, pp. B419–B427, Nov. 2007, doi: [10.1088/0741-3335/49/12B/s39](https://doi.org/10.1088/0741-3335/49/12B/s39).
- [79] F. Fanelli and F. Fracassi, "Atmospheric pressure non-equilibrium plasma jet technology: General features, specificities and applications in surface processing of materials," *Surf. Coatings Technol.*, vol. 322, pp. 174–201, Aug. 2017. [Online]. Available: <https://www.sciencedirect.com/science/article/pii/S0257897217300124>
- [80] S. Daria *et al.*, "Surface modification of highly porous 3D networks Via atmospheric plasma treatment," *Contrib. Plasma Phys.*, vol. 58, no. 5, pp. 384–393, Jun. 2018, doi: [10.1002/ctpp.201700120](https://doi.org/10.1002/ctpp.201700120).
- [81] S. G. Jennings, "The mean free path in air," *J. Aerosol Sci.*, vol. 19, no. 2, pp. 159–166, Apr. 1988. [Online]. Available: <https://www.sciencedirect.com/science/article/pii/0021850288902194>
- [82] R. B. Miles, W. R. Lempert, and J. N. Forkey, "Laser Rayleigh scattering," *Meas. Sci. Technol.*, vol. 12, no. 5, pp. R33–R51, Apr. 2001, doi: [10.1088/0957-0233/12/5/201](https://doi.org/10.1088/0957-0233/12/5/201).
- [83] J. R. Roth, *Industrial Plasma Engineering*. Boca Raton, FL, USA: CRC Press, 2001.
- [84] J. Friedrich, *The Plasma Chemistry of Polymer Surfaces*. Hoboken, NJ, USA: Wiley, 2012.
- [85] D. Dixon and B. J. Meenan, "Atmospheric dielectric barrier discharge treatments of polyethylene, polypropylene, polystyrene and poly (ethylene terephthalate) for enhanced adhesion," *J. Adhes. Sci. Technol.*, vol. 26, nos. 20–21, pp. 2325–2337, Nov. 2012.
- [86] J. Žigon *et al.*, "Treatment of wood with atmospheric plasma discharge: Study of the treatment process, dynamic wettability and interactions with a waterborne coating," *Holzforschung*, 2020, Art. no. 000010151520200182, doi: [10.1515/hf-2020-0182](https://doi.org/10.1515/hf-2020-0182).
- [87] J. Žigon, M. Pavlič, M. Petrič, and S. Dahle, "Surface properties of coated MDF pre-treated with atmospheric plasma and the influence of artificial weathering," *Mater. Chem. Phys.*, vol. 263, Apr. 2021, Art. no. 124358.
- [88] M. Thomas and K. Mittal, *Atmospheric Pressure Plasma Treatment of Polymers: Relevance to Adhesion*. Hoboken, NJ, USA: Wiley, 2013.
- [89] M. Stamm, "Polymer surface and interface characterization techniques," in *Polymer Surfaces and Interfaces*, M. Stamm, Ed. Berlin, Germany: Springer, 2008, doi: [10.1007/978-3-540-73865-7_1](https://doi.org/10.1007/978-3-540-73865-7_1).



Lukas Rosenfeldt received the bachelor's degree in physics from the Faculty of Mathematics and Natural Sciences, Kiel University, Kiel, Germany, in 2019, where he is currently pursuing the master's degree. His thesis focused on the energy balance of a surface barrier discharge using a multidiagnostics approach.

He is a Research Assistant with the Institute of Experimental and Applied Physics, Kiel University. He is involved with diagnostics for atmospheric pressure plasmas and in particular the development of a passive thermal probe (PTP) array.



Luka Hansen received the master's degree in physics from the Faculty of Mathematics and Natural Sciences, Kiel University, Kiel, Germany, in 2018. His master thesis was focused on energy and particle transport in atmospheric pressure plasmas performed at Princeton University, Princeton, NJ, USA, funded by a Deutscher Akademischer Austauschdienst (DAAD) Promos grant. He is currently pursuing the Ph.D. degree with the Plasma Technology group of Prof. Dr. Holger Kersten, Institute of Experimental and Applied Physics, Kiel University.

His current work focuses on plasma-surface interaction with the goal of observing plasma-surface effects in real time inside a TEM using a self-developed microplasma cell.



Holger Kersten received the Ph.D. degree from the University of Greifswald, Greifswald, Germany, in 1990.

He was a Post-Doctoral Researcher with the University of Eindhoven, Eindhoven, The Netherlands, from 1996 to 1997, and the Head of the Department for Plasma Process Technology with the Leibniz Institute for Plasma Science and Technology, Greifswald, from 2003 to 2006. He has been a Full Professor with Kiel University, Kiel, Germany, since 2006. His current research interests include plasma-surface interaction for technological applications, plasma diagnostics, and complex (dusty) plasmas as well as the fundamentals of gas discharge physics.

3.2 Electron Microscopy

Optical imaging systems like microscopes, telescopes, or cameras are diffraction limited and, thus, can only resolve features up to a minimum size d_f [283]. The Abbe diffraction limit [284, 285] for a microscope limits its resolution to [286]:

$$d_f = \frac{\lambda}{2n_{\text{ref}} \sin \Theta_h} = \frac{\lambda}{2\text{NA}}, \quad (3.3)$$

where λ denotes the wavelength of the light, n_{ref} the refractive index of the medium, Θ_h the half-angle of the converging spot, and NA ($= n_{\text{ref}} \sin \Theta_h$) the numerical aperture. Typical values for the numerical aperture in modern optics are in the range of 1.4 to 1.6. Considering green light ($\approx 500 \text{ nm}$) in the center of the visible spectrum, the minimum resolvable feature size results in $d_f = 500 \text{ nm}/3 \approx 167 \text{ nm}$, which is useful to observe most biological cells with diameters in the range of $1 \mu\text{m}$ to $100 \mu\text{m}$, but not able to resolve nanoparticles or nanostructured surfaces.

The wavelength of the electromagnetic radiation has to be lowered to resolve these kind of structures. Based on the De Broglie hypothesis [287] electrons have wave-like properties and their wavelength is given by:

$$\lambda = \frac{h}{p} = \frac{h}{\sqrt{2m_e E_{\text{kin},e}}}, \quad (3.4)$$

where h represents the Planck constant [156], p the impulse of electrons, m_e the electron mass, and $E_{\text{kin},e}$ the kinetic energy of an electron. Eq. 3.4 shows that accelerating electrons to high kinetic energies results in decreased wavelengths. Typical acceleration voltages in transmission electron microscopes (TEMs) are in the range of 300 kV, resulting in kinetic energies of 300 keV and, thus, relativistic effects have to be taken into account [288]. Eq. 3.4 becomes

$$\lambda = \frac{h}{\sqrt{2m_e E_{\text{kin},e} \left(1 + \frac{E_{\text{kin},e}}{2m_e c_0^2}\right)}}, \quad (3.5)$$

with c_0 representing the speed of light. The relativistic wavelengths of an electron accelerated with 300 kV is 0.00197 nm , which is capable of resolving nanostructures, and, thus is the foundation of using electron microscopy.

Today, two different types of electron microscopes are mainly used for surface investigations. The TEM relies on the transmission of electrons through a very thin sample, while the scanning electron microscope (SEM) scans an electron beam across a sample surface to create secondary electrons. Thus, the setups of these microscopes differ drastically from each other and are schematically shown in Fig. 3.6. As both microscopes rely on the interaction of electrons with the sample, these electrons should not interact with other media. Pressure inside of these devices is therefore in the range of $1 \times 10^{-5} \text{ Pa}$ to avoid interaction with the ambient media. Further details are given in the respective following sections.

3.2.1 Transmissions Electron Microscopy (TEM)

The development of the first TEM in 1931 by Max Knoll and Ernst Ruska was honored with the Nobel Prize in physics for Ernst Ruska in 1986 showing the importance of

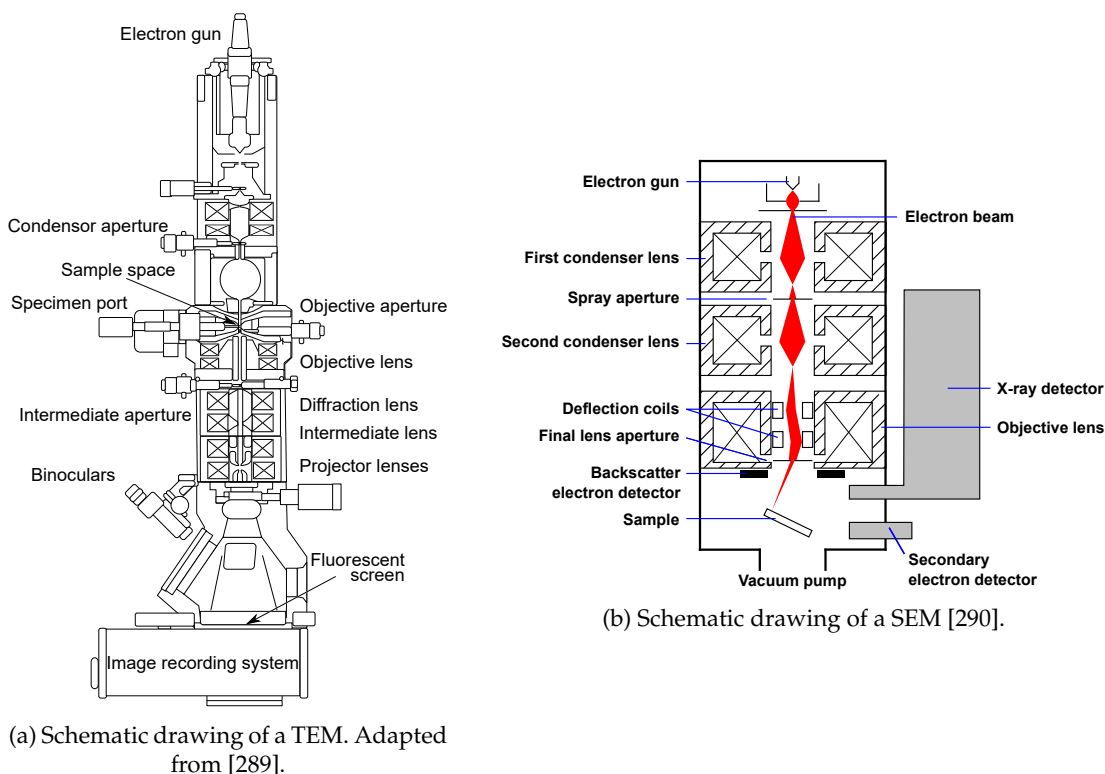


FIGURE 3.6: Schematic drawings of a transmission electron microscope (TEM) and a scanning electron microscope (SEM) to showcase the different imaging mechanisms (transmission or surface signal generation) and complexity of the electrostatic lens systems, especially for the TEM.

this instrument for and beyond the scientific community [291]. The image is generated by the interaction of a high-energy electron beam during the transmission of an ultra-thin sample (usually below 100 nm). Preparation of these samples is challenging until today, as already little contamination or too thick samples can result in useless images. On the other hand, under optimal conditions and with a specialized microscope, resolutions below 50 pm could be obtained [292]. Realistically, resolutions in the nm range are achieved, again, depending on the microscope.

The schematic setup of a TEM is shown in Fig. 3.6a. Similar pictures with detailed descriptions can be found in several text books [288, 293, 294]. Here, the schematic is used to obtain a basic understanding of the imaging mechanism, the electrons pathway, and the available sample space. The electrons are generated in the electron gun, usually using a thermionic source (W or LaB₆) or a field-emission source (W) arranged in a Wehnelt cylinder [295], and are accelerated using hundreds of kV. The electron beam passes multiple apertures and lenses prior to reaching the sample. The sample, or sometimes called specimen, is surrounded by the most important lens in the TEM, the objective lens. The objective lens forms the images and diffraction patterns which are magnified by the other lenses [288]. In most cases, it is a magnetic lens and its pole pieces have to be close to the sample. For this reason, the available volume for the sample is strictly limited and different depending on the available TEM.

After transmitting and interaction with the sample, the electrons can either hit a fluorescent screen, whose fluorescence reflects the beam intensity, directly showing the image, or a CCD detector to record the image. Depending on the imaging mode the TEM is operated in, different contrast mechanism dominate. For conventional or

bright field TEM mass-thickness (arises from incoherent elastic (Rutherford) scattering) and diffraction (arises from coherent elastic (Bragg) scattering) contrast dominate the image created by all elastically and inelastically forward scattered electrons. For the planned *in situ* microplasma cell, bright field TEM imaging will be used in the first place, as it requires no assumptions in the interpretation of the images and is also not too sensitive to imperfect sample conditions.

Other imaging modes relevant within the context of this thesis are:

- **High-resolution TEM (HRTEM):** HRTEM combines the information from the transmitted and the diffracted electron beams by reconstructing the phase information from the electron wave in the image plane [288, 296]. If the incident electron wave transmits through a crystallographic structure, the electrons are attracted by the positive atomic potentials of the cores and channel along the atom columns [297]. Further, electron waves in different channels interact with each other, which leads to Bragg diffraction. The spatially resolved electron exit wave below the sample is a superposition of the transmitted plane wave and multiple diffracted beams, which now has to pass through the TEM optics to the detector. Changes of the electron exit wave due to limiting apertures and aberrations in the imaging lenses of the microscope are accounted by the so-called contrast transfer function, which is microscope specific. Once the electron exit wave is measured, the sample and its effect on the incident electron wave can be modeled and the modeled exit wave compared to the measured one.
- **Scanning TEM (STEM):** The incident electron beam is focused into a 0.05 nm to 0.2 nm small spot and scanned across the sample. The electrons transmit through the sample as for the bright field TEM. The intensity is recorded and combined with the spatial information of the focused spot for the reconstruction of the image. The rastering of the spot enables several analytical techniques such as energy dispersive X-ray (EDX, see section 3.2.3) [298, 299] or electron energy loss spectroscopy (EELS, as a result of inelastic scattering events) [300, 301].
- **Selected-area electron diffraction (SAED):** SAED is a crystallographic technique to image a two-dimensional projection of the reciprocal crystal lattice. The crystal lattice of the sample acts as a diffraction grating for the incident electron beam. The forming interference pattern shows constructive interference if the Bragg condition is fulfilled [293]. A selected area aperture is located below the sample. This aperture usually contains different sized small holes and allows to select the area of the sample, from which the interference pattern is imaged. Depending on the sample either a regular pattern of bright spots is formed for a single crystal or concentric rings are formed in a polycrystalline sample, due to the superposition of diffraction spots from all possible crystallographic planes in different orientations.
- **Dark-field TEM (DF):** A small aperture is placed below the sample only allowing electrons to pass, which fulfill a certain condition. The image is created only from electrons, which were, e.g., scattered by a specific lattice plane. Thus, only diffraction contrast is present in the image, which can be used to map specific grains within a thin film.

More information on the shortly introduced imaging modes as well as the mathematical descriptions and more imaging techniques can be found in the already addressed literature [288, 293, 294, 302–304].

In situ TEM

With the TEM being such a powerful tool, it is no surprise, that a lot of efforts have been made to realize *in situ* possibilities for various processes. Specialized materials change their properties based on ambient influences like temperature, illumination, electrical biasing, or even ambient gases or liquids. Even the energy transfer from the incident electron beam can alter the samples. An analysis of these materials under these conditions is necessary to understand the origin of the changing properties. Thus, specialized sample holders or even microscopes have been developed over the years and are commercially available today. An overview of available techniques is given in the thesis of Niklas Kohlmann, who was responsible for the TEM imaging within this project [236], or in more detail in available textbooks [305, 306].

The sample thickness was already mentioned as key parameter, as the electrons have to transmit the sample and interact with it ideally only once, as multiple scattering events deteriorate the image quality. Commercial TEM grids for sample preparation are available in various styles and commonly consisted of a real fine grid structure on which samples could be prepared on. The electron beam could transmit the sample and a clear image was created in areas of the holes in the grid. More recently, driven by the progress in the MEMS manufacturing, free standing, ultra-thin membranes in the center of a Si wafer could be manufactured. These low-stress SiN_x membranes used as windows for the electron beam enhanced the possibilities to build closed atmosphere cells as they combined mechanical stability, chemical inertness, and electron transparency. Even though these SiN_x membranes are not grids any more, they will be referred as TEM grids within this thesis.

For closed cell designs, as the intended *in situ* microplasma cell is going to be, the electron beam has to transmit at least two SiN_x membranes and the encapsulated gas atmosphere. In case of the microplasma cell, electrode material (Au) is going to be coated on top of the SiN_x membranes. Thus, the electron beam has to transmit through two SiN_x membranes, two Au thin films and an atmospheric pressure He atmosphere, as He turned out to provide the most stable conditions (see chapter 4). The electron mean free path of these materials has to be kept in mind for the design of the *in situ* microplasma cell, as it is going to be a tradeoff between stability and image quality. The total scattering mean free path (electron beam energy of 200 keV) for He at atmospheric pressure and room temperature is 1279 μm , for solid Si₃N₄ 102 nm, and for Au 19 nm [236]. These are mainly given here for the sake of completeness and to show that the He atmosphere will not deteriorate the image quality too much. The most crucial factor is going to be a thin Au layer, as most electron collisions are going to take place here. A more complete list, as well as the literature sources and details regarding the calculation of these scattering mean free paths are again given in [236].

3.2.2 Scanning Electron Microscopy (SEM)

The invention of the scanning electron microscope in 1937 is attributed to Manfred von Ardenne [307, 308] who used a fine focused electron beam to raster a surface with the intention of surpassing the resolution obtained by already rarely available TEMs. Fig. 3.6b shows the schematic setup of a modern SEM. Similar to the TEM, an electron gun is used to generate an electron beam. The beam is accelerated towards energies of up to 40 keV and is focused by condenser lenses to a 0.4 nm to 5 nm spot, which is scanned across a sample surface by scanning coils or deflector plates [309]. The electron beam penetrates into the sample and loses its energy due to scattering and absorption in the so-called interaction volume. The interaction volume can extend up

to 5 μm into the sample, depending on the sample itself and the electron beam energy. The transferred energy from the incoming electron beam results in elastically scattered reflected electrons with high energies, emitted secondary electrons as a result of inelastic scattering, and electromagnetic radiation which can be used for energy dispersive X-ray spectroscopy (see section 3.2.3).

Imaging is done by detection of the emitted secondary electrons. Collecting electrons with low energies below 50 eV ensures that they originate from a few nm below the surface, thus, SEM imaging is considered a surface-sensitive technique [309]. The signal intensity depends on the secondary electron emission, which is strongly dependent on the surface topography and the secondary electron emission coefficient of the present material. As the focused electron beam is scanned across the sample, the image is reconstructed by the spatial information from the scanning beam and the detected intensity at the specific locations. Resolutions between 1 nm and 20 nm can be obtained, which is worse compared to a TEM, but one is not restricted to thin samples. Thus, TEM and SEM imaging should not be seen as competing, but complementing each other.

3.2.3 Energy dispersive X-ray spectroscopy (EDX)

The inelastic scattering of an incident electron beam transfers energy towards the atoms of a sample as mentioned before. If the interaction results in the release of an electron from an inner electron shell, an electron hole is created. An electron from an outer, higher energy shell will fill the created electron hole and the energy difference between the shells may be released as X-ray. These X-rays are characteristic for each atom, as the transitions and, thus, the energy levels of the shells, depend on the atomic number of the atoms as described by Moseley's law [310, 311].

Spatially resolved atom excitation via a focused electron beam can be used to map the chemical composition of a sample. In SEM or STEM microscopes the focused electron beam is already available, thus, only an energy resolved detector is necessary. Combining energy resolved measurements with total intensity measurements enables coincident contrast and chemical mapping. The spatial resolution of both techniques depends on the electron beam spot size and is connected to the microscope used. Thus, by combining EDX with a STEM, resolutions of up to 0.05 nm to 0.2 nm can be obtained, and up to 1 nm to 20 nm in a SEM.

3.3 Additional Surface Diagnostics

Electron microscopy is a powerful but also costly and time-consuming surface diagnostic. EDX enables insight into the chemical composition of the surface, but lacks information regarding the chemical bonds. X-ray photoelectron spectroscopy (XPS) allows to determine the chemical state of surface species and therefore delivers information about the chemical bonds. Still, XPS is also a costly and time-consuming diagnostic and usually cannot be used to analyze a large number of samples. Water contact angle (WCA) measurements are easy to perform and allow to measure the wettability of a solid surface. The wettability represents hydrophilic groups at the surface, which may be created as a result of plasma surface activation. Both diagnostics will be introduced as they were used to measure the surface activation of a polymer in context of the plasma permeability studies in chapter 6.

3.3.1 X-ray Photoelectron Spectroscopy (XPS)

X-ray photoelectron spectroscopy (XPS) is based on the photoelectric effect. A monochromatic X-ray interacts with the surface of a sample which leads to absorption of the X-ray photons by the surface electrons. These electrons gain enough energy to leave the surface and are detected by an energy-resolved detector. According to the conservation of energy and the photoelectric effect, the kinetic energy of the electrons $E_{\text{kin,e}}$ is given by [312]:

$$E_{\text{kin,e}} = E_{\text{photon}} - E_{\text{bond}} - W, \quad (3.6)$$

where E_{photon} denotes the photon energy of the incoming X-ray, E_{bond} the binding energy of the electrons and W the work function of the material, sometimes adjusted based on instrumental correction factors. The measured kinetic energy allows to calculate the binding energy if the other parameters are known. The determined binding energies are characteristic for different elements and their electronic states, which are different based on the chemical bound of the element [313–315]. XPS is surface sensitive and probes surfaces up to 10 nm in depth, as it is based on the absorption of X-rays. Therefore, it is well-suited to characterize a surface and identify plasma-induced surface modifications.

3.3.2 Water Contact Angle (WCA)

Multiple methods for the determination of the contact angle as well as their theoretical foundations are available in literature [312, 316–321]. Within this thesis the so-called sessile drop method is utilized to measure the contact angle. According to the Young equation, the contact angle Θ_C depends on the interfacial energy γ between the different phases (solid-vapor γ_{SV} , solid-liquid γ_{SL} and liquid-vapor γ_{LV}), which are in equilibrium at the edge of a sessile drop [322]:

$$\cos \Theta_C = \frac{\gamma_{\text{SV}} - \gamma_{\text{SL}}}{\gamma_{\text{LV}}}. \quad (3.7)$$

Functional groups, such as OH-groups, increase the surface free energy γ_{SL} and, thus, result in a lower contact angle. Plasma treatment of polymer surfaces usually leads to surface activation of the polymer by production of functional groups [38]. The contact angle reduction of a polymer surface can be used as measure for the plasma-induced surface activation of the polymer.

Chapter 4

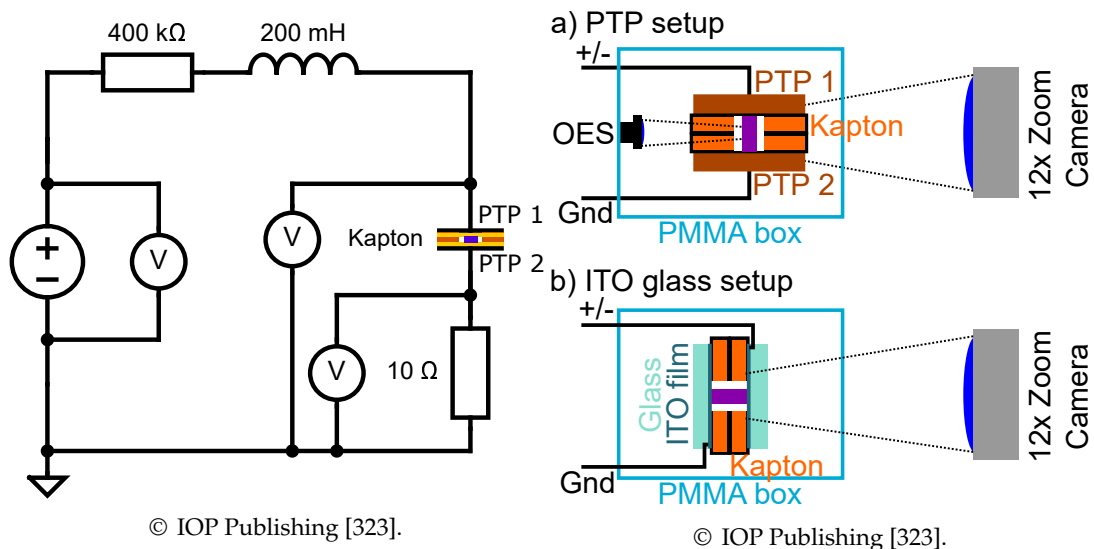
Atmospheric Pressure DC Microplasma

Publication II

Conventional and non-conventional diagnostics of a stable atmospheric pressure DC normal glow microplasma discharge intended for *in situ* TEM studies

Authors	L. Hansen, N. Kohlmann, U. Schürmann, L. Kienle, and H. Kersten
Journal	Plasma Sources Science and Technology [323]
Technique	Dummy setups utilizing PTP's and ITO coated glass as electrodes
Utilized diagnostics	I-V characteristics, optical emission spectroscopy (OES), optical imaging and energy flux measurements
Own contribution	Approx. 85 %

Experimental Setup:



Motivation:

This work is the foundation of the intended *in situ* microplasma cell. A stable atmospheric pressure microplasma discharge is necessary to be introduced into the TEM.

Based on Paschens law, previous microplasma studies and restrictions given by the TEM, which will be discussed in section 7.1, the proposed discharge geometry realized via clamping and the usage of Kapton spacers was developed. Different diagnostics were applied to verify the design goal was achieved and to gain information on the operation regime of the discharge. Further, particular attention was given to plasma surface processes and their diagnostics as knowledge about them is necessary to understand the expected plasma-induced surface modifications.

Main Results:

The developed discharge geometry proved to satisfy the previously identified needs of stability within the identified operating parameters. The discharge turned out to operate in the normal glow regime which was confirmed by the I-V characteristics and optical diagnostics. These showed nearly constant current densities and the applicability of the collision-dominated Child-Langmuir law. Energy flux measurements revealed an asymmetric power transfer towards the cathode caused by ions despite their short mean free path due to the atmospheric pressure conditions. The high energy flux, as well as visible Au I lines in the OES spectra, indicate a strong plasma surface interaction, which should result in *in situ* observable surface modifications. Effective secondary electron coefficients could be determined based on the comparison of electric and thermal power.

Conventional and non-conventional diagnostics of a stable atmospheric pressure DC normal glow microplasma discharge intended for *in situ* TEM studies

Luka Hansen^{1,*} , Niklas Kohlmann² , Ulrich Schürmann²,
Lorenz Kienle² and Holger Kersten¹ 

¹ Institute of Experimental and Applied Physics, Kiel University, 24098 Kiel, Germany

² Institute for Material Science, Kiel University, 24098 Kiel, Germany

E-mail: lhansen@physik.uni-kiel.de, niko@tf.uni-kiel.de, usc@tf.uni-kiel.de, lk@tf.uni-kiel.de and kersten@physik.uni-kiel.de

Received 29 November 2021, revised 21 January 2022

Accepted for publication 1 February 2022

Published 14 March 2022



Abstract

A simple setup utilizing parallel flat electrodes with a 50–150 μm interelectrode distance divided by a Kapton spacer with a 1 mm diameter hole as discharge region intended for *in situ* transmission electron microscope studies is presented. The rather small setup operated in Ar or He results in an atmospheric pressure DC normal glow discharge and is investigated using various diagnostics. I – V characteristics show a glow-like behavior of the microplasma. Significant differences due to the working gas, electrode material and electrode distance have been observed. Currents in the range of 0.5–3 mA resulted in electrode potentials of 140–190 V for most experimental conditions. Optical emission spectroscopy and imaging revealed stable plasma operation and enabled the determination of current densities (approx. 16 mA mm^{−2} for He, or 28 mA mm^{−2} for Ar) independent of the input current as the discharge channel grows in diameter. Sheath thicknesses in the range of a few μm have been calculated by the collision-dominated Child–Langmuir law and trends are confirmed by the optical imaging. Energy flux measurements revealed a pronounced effect of ions on the measurement process and resulted in high energy fluxes locally up to 275 W cm^{−2}. Effective secondary electron emission coefficients ranging from 1 to 1.6 depending on the discharge conditions have been determined based on the energy balance at the cathode.

Keywords: microplasma, energy flux, plasma surface interaction, glow discharge, I – V characteristics, optical imaging, secondary electron emission

(Some figures may appear in colour only in the online journal)

1. Introduction

Plasma surface interaction is one of the most emerging topics in plasma technology due to its relevance for the production and modification of micro- or even nano-scaled structures [1–8]. Still, state of the art diagnostics are mostly limited

to the separation of plasma processing and surface analytics since real time observations on a nanoscale during the plasma treatment are challenging. To overcome this separation successful attempts have been made to introduce a microplasma discharge into a transmission electron microscope (TEM) for *in operando* (*in situ*) observation [9]. Based on this idea a suitable microplasma discharge cell is being developed to provide an *in situ* tool to directly analyze plasma surface interactions.

* Author to whom any correspondence should be addressed.

Microplasmas in general are of great interest for many different applications from light sources, analytical atomic spectrometry, nanotechnology to lab-on-chip biomedical devices [10–18]. Downscaling the electrode distance to sub-mm range results in high pressure discharges as breakdown voltages are represented by the Paschen law [19–21]. The combination of small dimension and high pressure aggravates common plasma diagnostics. Still, knowledge about the plasma itself is key to understand the plasma surface interaction on elementary scale.

The current work is focused on a microplasma and its diagnostic. Even though our microplasma geometry is mainly motivated by its planned application for *in situ* TEM measurements, the simple setup enables easy adaptability to other desired applications and the gained results also apply to similar microplasmas. First, electrical diagnostics will be used to obtain I – V characteristics of the microplasma to validate its glow discharge character and operational stability under several conditions. Optical emission spectroscopy (OES) is used to control the gas purity and temporal stability. Optical imaging should reveal discharge structures and enable the determination of current densities to gain further validation of the normal glow-like character of the discharge [11, 20, 22].

Focusing on the plasma surface interaction, energy flux measurements utilizing passive thermal probes (PTPs) have been used to measure the power transferred from the plasma to the electrode surfaces [23–26]. This calorimetric diagnostic determines the integral energy flux which adds up from different contributions. These contributions can either transfer energy to the surface by e.g. ion impact or recombination on the surface and radiation or transport energy off the surface by e.g. secondary electrons leaving the surface or thin film desorption [24, 27, 28]. Knowledge about the energy flux enables the understanding of several surface processes making it a key parameter of the plasma surface interaction [24, 29–32]. Based on the energy balance at the cathode effective secondary electron emission (SEE) coefficients are calculated for Au, Cu and Mg surfaces. Effective SEE coefficients depict electrons leaving the cathode per impinging ion but not only taking the transferred ion energy resulting in the electron extraction into account, but also including energy transferred from non-ionic species and radiation [33–35].

The combination of different applied conventional and non-conventional diagnostics enables the verification of the microplasma being an atmospheric pressure DC normal glow discharge and provides more insight to understand the plasma surface interaction of microplasmas.

2. Experimental setup

2.1. Electrical setup

The electric circuit for the microdischarge cell used for all experiments is shown in figure 1. A 400 k Ω resistor, or 200 k Ω in case of Mg electrodes, limits the current generated by a DC high voltage supply (Heinzinger PNC

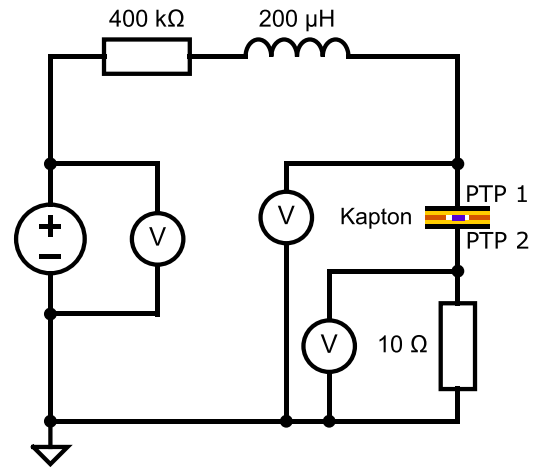


Figure 1. Schematic of the electrical circuit of the microplasma. Two PTPs with variable coatings divided by a Kapton spacer with variable thickness and a 1 mm diameter hole have been used as electrodes. High voltage probes measured the voltages present at the power supply, the microplasma and the shunt resistor.

20000—10 ump) with adjustable polarity. The 200 μ H inductor stabilizes the discharge by suppression of fast current changes. In the setup shown two 100 μ m thick passive thermal probes (PTPs, see section 2.3) are used as electrodes. The electrodes are two parallel conductive plates pressed towards each other and separated by a Kapton spacer as dielectric barrier with a 1 mm diameter hole for the discharge volume (see figure 2(a)). The thickness of the Kapton spacer was varied by stacking multiple layers of 50 μ m thick foil on top of each other. During most experiments a 100 μ m thick spacer was used, otherwise it will be noted. A 10 Ω shunt resistor enables the determination of the current through the plasma discharge. The applied voltages were measured simultaneously using different high voltage probes (Tektronix P6015A 1000:1 at the power supply, Tektronix P5100A 100:1 at the electrodes and Tektronix P2200 1:1 at the shunt resistor) connected to an oscilloscope (PicoScope 5442B).

2.2. Optical setup

The electrodes as well as the lens and optical fiber for the optical emission spectroscopy (OES, OceanOptics HR2000+) setup, are encapsulated in a 30 \times 30 \times 30 cm³ PMMA gas box. The box is flushed with 3 slm of Ar or He, respectively, for 1 h followed by a continuous inflow of 1 slm for another 2 h. The inflow was always kept at 1 slm during the experiments. The long flushing times are necessary to ensure gas purity inside the box and, especially, between the electrodes. In addition to the electric, spectroscopic, and calorimetric diagnostics optical imaging was used to observe the plasma glow through the Kapton spacer by using a zoom objective (Navitar 12x Zoom incl. 12x Xtender) mounted on a camera (Ximea MQ042CG-CM) placed outside the gas box oriented in line to the parallel electrodes (see figure 2(a)).

Exchanging the PTPs as electrodes to indium tin oxide (ITO) coated glass (Adafruit, film thickness: 185 nm, total

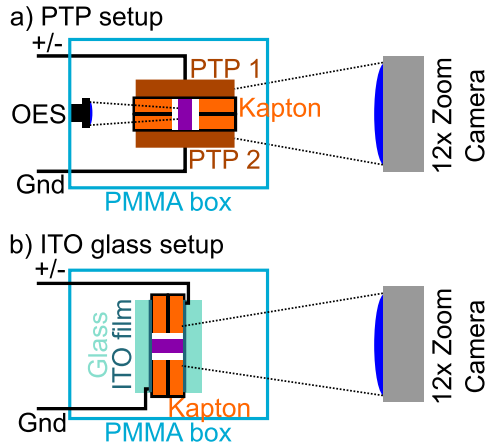


Figure 2. Schematic of the electrode setup utilizing either PTPs (a) or ITO coated glass plates (b)). The electrical connections (+/- or Gnd) are connected to the electrical circuit as shown in figure 1. The PMMA box was flushed constantly with Ar or He during the experiments. The electrodes were pressed together only divided by the Kapton spacer possibly setup from multiple 50 μm thick layers either by mounting the PTP's housing on movable tables or clamping the ITO glass in a reverse action tweezer. The PTP setup was used for all experiments except the top-view imaging (section 3.3.1).

Table 1. Heat capacities of the different PTPs used for the experiments. Differences despite same construction are due to the manual spot-welding.

PTP name	Surface material	Heat capacity/J/K
Cu P/N	Cu (uncoated)	0.0117 ± 0.0007
Cu Gnd	Cu (uncoated)	0.0109 ± 0.0004
Au P/N	Au	0.0122 ± 0.0005
Au Gnd	Au	0.0127 ± 0.0008
Mg P/N	Mg	0.0116 ± 0.0007
Mg Gnd	Mg	0.0125 ± 0.0007

thickness: 1.2 mm) enables imaging of the discharge perpendicular to the Kapton spacer as sketched in figure 2(b)). Thus, the full 1 mm diameter hole in the spacer and the discharge channel are visible (see figure 6).

2.3. Passive thermal probe (PTP)

The PTP is a diagnostic device to measure the power transferred from the plasma to its surface based on calorimetry [24–26]. It consists of a 5.2 mm diameter and 100 μm thick copper platelet, which is spot-welded to a type K thermocouple and a copper wire for separate electrical connection. The sampling frequency of the temperature measurements is 90 Hz. A 2–3 μm thick Au or Mg layer, resp., was sputtered on top of the copper platelet as desired surface. As the probes were transferred through ambient air, oxidation of the Mg film is probable, thus, a MgO surface cannot be excluded. The heat capacity of the probes were determined using an electron beam based calibration experiment described in [23]. The determined heat capacities of the various PTP's are given in table 1.

The heat capacity C of the Cu substrate connects the temporal change of the substrates enthalpy \dot{H} with its temperature change \dot{T} . Under the assumption of no processes taking place inside the substrate, the changing enthalpy results just from power coming to the substrate P_{in} and power leaving the substrate P_{out}

$$\dot{H} = C\dot{T} = P_{\text{in}} - P_{\text{out}}. \quad (1)$$

Switching on the plasma enables to heat the substrate due to the additional power transfer from the plasma to the substrate. After switch-off of the plasma the substrate will cool down again, as the additional power influx is no longer present. Thus, two equations are obtained during the heating (h) and cooling (c) of the substrate

$$\text{Heating : } \dot{H}_h = C\dot{T}_h = P_{\text{in}} - P_{\text{out}} \quad (2)$$

$$\text{Cooling : } \dot{H}_c = C\dot{T}_c = -P_{\text{out}}. \quad (3)$$

With the assumption of equal power losses P_{out} during heating and cooling equations (2) and (3) can be combined and rearranged. Normalization by the contact area A between the plasma and the substrate results in the energy flux J_{in}

$$J_{\text{in}} = \frac{P_{\text{in}}}{A} = \frac{C}{A} (\dot{T}_h - \dot{T}_c). \quad (4)$$

3. Results and discussion

3.1. Electrical measurements

The different voltage probes enable an electrical characterization of the microplasma. The aim of design was to set up a stable normal glow discharge, thus, currents in the range of 0.1–10 mA have to be realized [22]. The 400 k Ω resistor limits the current which otherwise would surpass the expected values at the moment when the necessary breakdown voltage is applied to the electrodes.

Figure 3 shows the current voltage characteristics of the microplasma for the case of Au electrodes and for different electrode distances operated in Ar (figure 3(a)) or He (figure 3(b)), resp., atmosphere. For both polarities, gases and all electrode distances two similar features are visible. First, a minimum current of about 0.5 mA is necessary to obtain a stable microplasma. The plasma becomes unstable and shows a kind of self-pulsing behavior, if the minimum current is not reached [36–38]. The electrical potential across the electrodes drops too low during the plasma ignition and cannot sustain the discharge. If the plasma vanishes the potential builds up again and leads to another ignition [39]. The ignition frequency increases with higher currents, as the recharge time of the capacitor given by the electrodes is decreased. The large errorbars depict this behavior, as the measured voltage is rapidly changing and, thus, results in a large standard deviation while building the mean over time. Second, the voltage is nearly constant even if the current is increased as soon as the minimum current is surpassed. This behavior is typical for DC normal glow discharges and is a good indicator that the design of the requirement for the microdischarge was achieved.

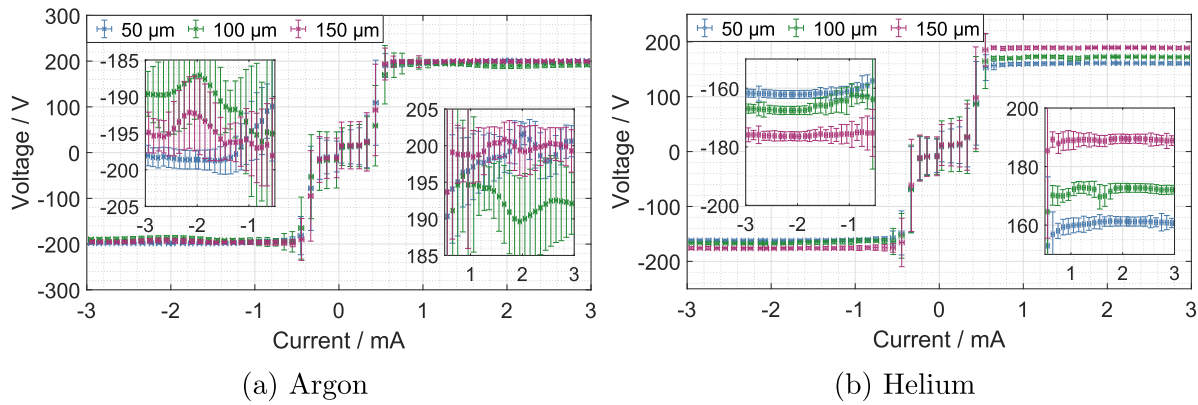


Figure 3. I – V characteristics of the microdischarge using Au electrodes and Kapton spacers with different thicknesses. A minimum current is necessary for a stable discharge operation. The nearly constant voltage with increasing current indicates a normal glow discharge. The insets highlight the voltage differences in the current regime of stable operation.

A closer look at figure 3(a) shows a stable discharge operation starting at a minimum current of 0.65 ± 0.02 mA independent on the electrode distance, at least within the accuracy of the applied diagnostics. For the negative polarity a minimum current of -0.55 ± 0.02 mA for a stable operation has been determined, again, independent on the electrode distance. When changing the polarity of the applied voltage the measured current-dependent voltages behave asymmetric despite of a symmetric setup and equal amounts of applied voltage. This asymmetry probably originates due to differences in the reduced electric field. In particular, differences in the sheaths regions can have significant impact on the discharge, as the surface to volume ratio is large and, thus, surface processes like SEE will play a crucial role [40, 41].

The I – V characteristics of the stable regime of the Ar microplasma are shown enlarged in the insets of figure 3(a). For the positive and negative polarity differences depending on the electrode distance are visible. For the positive case, the voltage varies between 190 ± 6 V at 1.95 ± 0.03 mA using an electrode distance of $100 \mu\text{m}$ and 202 ± 2 V at 2.04 ± 0.02 mA for an electrode distance of $50 \mu\text{m}$. The current-dependent voltages for each electrode distance stay within the statistical errors constant with increasing currents. A difference in the voltages depending on the distance is visible.

For the negative polarity a similar behavior is observed. The voltages vary between -187 ± 6 V at -1.95 ± 0.03 mA for a distance of $100 \mu\text{m}$ and -199 ± 2 V at -1.66 ± 0.03 mA using a distance of $50 \mu\text{m}$. Again, the voltages for a single electrode distance are nearly constant and differences between the electrode distances are visible. Furthermore, similar to the minimum current, the voltages are slightly lower compared to the positive polarity.

For He as working gas the obtained results are shown in figure 3(b). Several similarities to Ar are visible. The effects are even more pronounced in this case, as the noise level is lower. The minimum currents necessary for a stable operation are with 0.65 ± 0.02 mA or -0.55 ± 0.02 mA, respectively, almost equal to Ar. The current-dependent voltages for the positive polarity vary from 158 ± 3 V at 0.75 ± 0.03 mA using a

distance of $50 \mu\text{m}$ to 189 ± 1 V at 0.65 ± 0.03 mA for an electrode distance of $150 \mu\text{m}$. For each distance the voltage stays constant during the current increase and an increase of the voltage with increasing electrode distance is visible. The voltage differences for He are larger compared to Ar and all measured voltages are smaller, which results in a smaller plasma resistance.

A variation from -159 ± 4 V at -0.65 ± 0.03 mA to -176 ± 2 V at -1.97 ± 0.03 mA is visible with identical behavior as for the positive polarity. Comparing both polarities, the asymmetry of lower absolute voltages and currents can be seen. Overall, these distance and gas-dependent differences in the I – V characteristics enable to gain information on possible problems of assembly, wear marks, or bending of electrodes due to the pressure gradient.

Changing the electrode material (figure 4) can have significant impact on the microplasma and prevent a stable operation, as it was seen using Mg as electrode material in combination with Ar as working gas. This combination resulted in the already mentioned self-pulsing behavior of the discharge. Hence, no I – V characteristics for Ar/Mg are shown in figure 4.

First, Cu and ITO electrodes with an electrode distance of $100 \mu\text{m}$ will be compared to Au as electrode material. Again, in figure 4 the I – V characteristics for Ar (figure 4(a)) and He (figure 4(b)), resp., for the different electrode materials are compared. Normal glow discharge properties are visible as soon as the already discussed minimum current is surpassed. For Ar as working gas and ITO as electrode material even the dark discharge regime and the Townsend transition to the normal glow region is visible at low currents [11, 22]. This transition, not being present for other material and gas combinations, can have several reasons. Surface roughness could be the main difference, as it influences the local electric fields, spark transitions and SEE [40, 42]. The Cu surface of the PTP, which was coated with Au or Mg, is rougher when compared to the ITO coated glass electrodes as revealed by scanning electron microscope (SEM) imaging. This effect could be investigated in more detail in further studies and is beyond the scope of the current work.

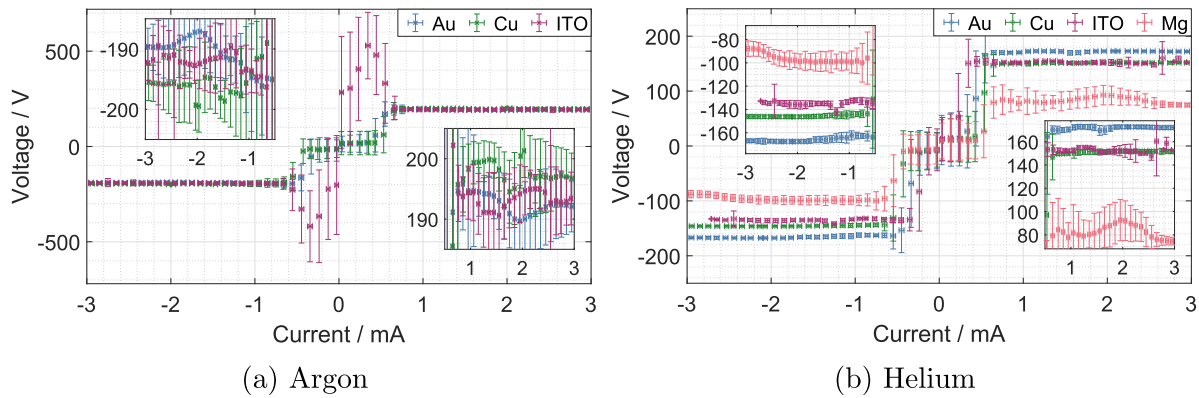


Figure 4. I - V characteristics of the microdischarge using different electrode materials and Kapton spacer of 100 μm thickness. A minimum current is necessary for a stable discharge operation. The nearly constant voltage with increasing current indicates a normal glow discharge. The insets highlight the voltage differences in the current regime of stable operation.

Nevertheless, the changes at small currents for ITO electrodes in figure 4(a) for different electrode materials behave similar to the already discussed Au electrodes. For He as working gas (figure 4(b)) material-depending differences are observable. First, during the use of ITO electrodes a lower minimum current of $\pm 0.45 \pm 0.03$ mA is necessary. Second, in the stable region a difference, even more pronounced for the negative polarity, between the materials is visible. ITO electrodes result in the smallest voltages of about 150 V, or -135 V, Cu shows voltages around 150 V, or -145 V, and Au electrodes are operated at around 170 V, or -168 V. Again, these voltages are related to the different resistivity of the microplasma, which can result of different factors.

Mg as electrode material results in the lowest measured voltages between 75 ± 3 V at 2.95 ± 0.03 mA and 93 ± 18 V at 1.95 ± 0.03 mA, or -88 ± 7 V at -2.95 ± 0.03 mA and -99 ± 8 V at -1.65 ± 0.03 mA, respectively. The low resistivity of the plasma itself aggravates the current limitation while keeping up with the necessary voltage. The origin of the low resistivity could be a larger effective SEE coefficient, which will be discussed in more detail in section 3.4.3.

3.2. Optical emission spectroscopy

The aim of OES was to verify the gas purity and confirm the stability of the microplasma by taking time-resolved spectra. Exposure times in the range of 0.3–1 s have been used to take repetitive spectra of the discharge. The absolute intensity values changed with time as the discharge itself is moving within the accessible diameter of 1 mm, which was confirmed by optical imaging in section 3.3.1. Still, the ratio between the different measured spectral lines was constant over time indicating a stable discharge glow.

Typical spectra with the identified lines are shown in figure 5 for common operating conditions. Mainly, Ar I or He I lines, resp., are visible in the spectra which show some broadening effects due to pressure and temperature. Furthermore, O I lines are visible in all spectra, while no N I lines were detected, which indicates that oxygen originates from the probe surfaces and not due to leakage of the gas box. For He as working gas (figure 5(b)) even Au I lines were detected

stressing the importance of the plasma surface interaction. The lines are most pronounced for the smallest interelectrode distance of 50 μm . The reason for this artifact could be that the same 100 μm Kapton spacer was used for all electrode materials to keep the discharge conditions identical. Probably, the spacer got contaminated during the first measurements using Au electrodes. Au lines missing in the Ar spectrum (figure 5(a)) can have several reasons: either the excitation mechanisms by metastables are more favorable using He as working gas or the lines are simply overshadowed by Ar I lines, as it could be the case for the 750 nm line. The limited spectral resolution of the spectrometer used unfortunately prevents a more detailed evaluation. Nevertheless, the intended observations within the scope of this work could be achieved.

3.3. Optical imaging

3.3.1. Top-view imaging. Replacing the PTPs by ITO coated glass plates enables a view through the electrodes and the discharge. In figure 6(a) a glow discharge in the observed area with the diameter of the Kapton spacer is clearly visible. Figure 6(b) shows the same area with ambient lights switched off and a plasma ignited. For all studied conditions only one glow discharge channel could be observed which was constant in size for one set of parameters. However, the channel could move within the accessible region. The motion could happen slowly or rapidly jumping from one spot to another. Noticeable was the motion becoming more rapidly in time most likely as a result of increased electrode surface roughness, which was observed using SEM examination of used electrodes.

By measuring the diameter of the nearly circular footprints of the tubular plasma the areas of the discharge channels were determined in dependence of the discharge current (figure 7(a)). Conversion from pixels to mm was done by using the 1 mm diameter whole in the Kapton spacer (marked in red) as scale. If a pixel's intensity surpassed 50% of the pictures maximum intensity the plasma was assumed to be present at this pixel. For Ar the area grew from 0.03 ± 0.02 mm² at 1.1 ± 0.2 mA to 0.08 ± 0.02 mm² at 2 ± 0.1 mA. The increasing area was expected, as it is a typical feature of a normal DC

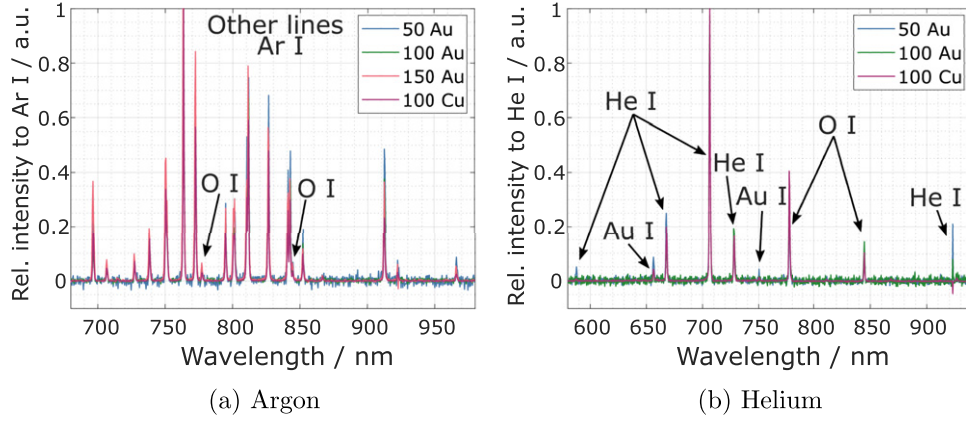


Figure 5. Normalized optical emission spectra in the interested wavelength range where emission was detected for different electrode distances and materials. The visible lines have been assigned using the NIST database [43].

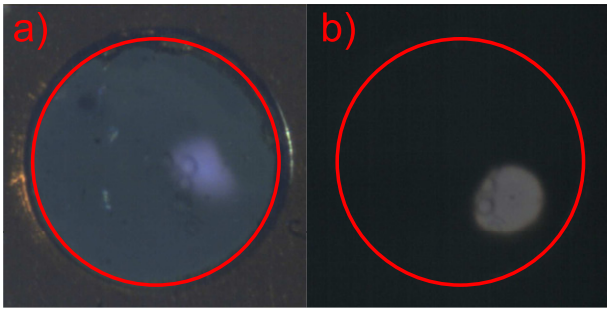


Figure 6. Top-view of the discharge with ambient lights switched on (a) or off (b). The 1 mm diameter accessible discharge region is marked in red. The plasma was operated in Ar at approx. 2 mA/200 V using ITO electrodes.

glow discharge. Furthermore, the discharge area being smaller compared to He, which grew from $0.038 \pm 0.007 \text{ mm}^2$ at $0.9 \pm 0.06 \text{ mA}$ to $0.155 \pm 0.004 \text{ mm}^2$ at $2.17 \pm 0.07 \text{ mA}$, is a result of Ar having a lower ionization coefficient and higher reduced electric field gradients compared to He and, thus, tends to form filaments [44–46]. The higher variance in the He measurements using a negative polarity is again caused by a higher surface roughness, as the measurements were performed using the same setup starting with the positive polarity.

The calculated current densities are shown in figure 7(b), which are in the range of $28 \pm 2 \text{ mA mm}^{-2}$ for Ar or $16 \pm 2 \text{ mA mm}^{-2}$ for He. They are nearly constant and independent on the current which again is a typical feature of the normal glow regime. Measurements of the current density j and the applied voltage V enable to apply the collision-dominated Child–Langmuir-law [20],

$$j = \frac{9}{8} \epsilon_0 \mu_i \frac{V^2}{d^3}, \quad (5)$$

where ϵ_0 depicts the vacuum permittivity, μ_i the ion mobility and d the sheath thickness. The ion mobility is calculated based on the ion mean free paths λ_i and velocity u_i

$$\mu_i = \frac{2e\lambda_i}{\pi M_i |u_i|}, \quad (6)$$

e represents the elementary charge and M_i the ion mass. The ion–atom collision crosssection σ_i is estimated to be $\sigma_{\text{Ar}} = 10^{-14} \text{ cm}^2$ [20] and $\sigma_{\text{He}} = 5 \times 10^{-14} \text{ cm}^2$ [20]. Together with the neutral gas density n_g ($2.1 \times 10^{25} \text{ m}^{-3}$, ideal gas law using atmospheric pressure and a gas temperature of 80°C , which corresponds to the measured electrode temperature during the PTP measurements) the respective λ_i values are estimated:

$$\lambda_i = \frac{1}{n_g \sigma_i}. \quad (7)$$

The ion velocity u_i is calculated numerically by a collision based model. The ions are accelerated in the electric field E of the as capacitor assumed discharge $E = V/D$, where D represents the electrode distance. Even though the voltage mainly drops in the sheath which results in higher electric fields, the saturated ion velocity is independent on the electric field as the collisions limit the velocity. The acceleration a is constant over time $a = (E^* e)/M_i$. The acceleration, velocity and traveled distance of the ion is updated in femtosecond time steps and each time step the traveled distance surpasses the mean free paths λ_i of the respective ion a collision takes place by reducing the kinetic energy of the ion by 50% and, thus, reducing its velocity. After a few hundreds of femtoseconds and a few cycles of colliding and accelerating the ion velocity reaches saturation. Finally, the saturated velocity is used to calculate the ion mobility μ_i .

The calculated sheath thicknesses d from equation (5) are shown in table 2. Significant differences depending on gas and polarity are visible. Ar results in remarkably smaller sheaths dimensions compared to He which is in accordance with the larger electric field gradients of Ar [45, 46]. Furthermore, the polarity-depending difference indicates changes in the reduced electric field. The assumption that the applied voltage mainly drops over the sheaths and, thus, being used to calculate the sheath thickness in equation (5) causes a systematic error of the sheaths thickness calculation. Nevertheless, the obtained values seem to be realistic and showcase the

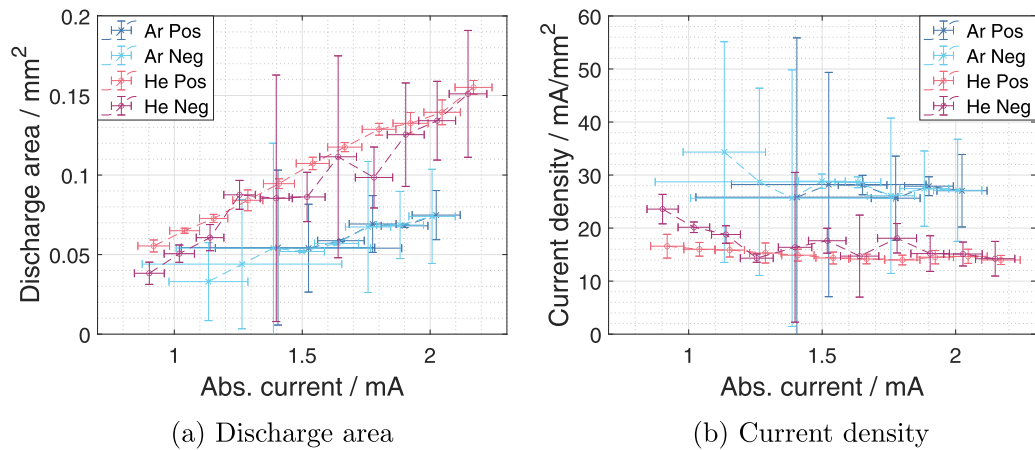


Figure 7. (a) Observed area of discharge channels determined by optical imaging and the resulting current densities for Ar and He operated at positive or negative polarity, respectively. Linear dependencies of the discharge area on the current are visible, which result in the nearly constant current densities (b). The statistical errorbars are a result of over 100 analyzed photographs (exposure time: 100 ms) and simultaneously measured currents with a 50 kHz sample rate, resulting in 5×10^5 current measurements for each data point. Neg/Pos label in the legends refers to the applied polarity.

Table 2. Calculated sheath thickness of the microplasma using the collision-dominated Child–Langmuir law. Two ITO electrodes of a distance D of 100 μm were used with different currents applied to the plasma. The statistical error of measurements using multiple currents is given.

Working gas	Polarity	Sheath thickness/ μm
Ar	Pos	4.99 ± 0.07
Ar	Neg	1.06 ± 0.03
He	Pos	19.0 ± 0.3
He	Neg	6.6 ± 0.4

applicability of the collision-dominated Child–Langmuir-law at atmospheric pressure and the validity of the normal glow discharge characteristics of the microplasma.

3.3.2. Side-view imaging. In the setup utilizing two PTPs as electrodes the camera was also mounted on the side of the discharge perpendicular to the discharge channel. The necessity to observe and image the discharge through the Kapton spacer massively decreases the image quality. However, the photographs still reveal typical glow discharge features and help to verify the results regarding the sheaths thickness.

Figure 8(a) shows the copper electrodes separated by two 50 μm Kapton foils, indicated by the transparent orange box, which add up to the 100 μm spacer. The erratic textured and frayed surface of the in-shape cut Kapton foils is visible as well as a dark slit where the foils are connected to each other. These features in addition to the reduced light transmission through the Kapton foil result in remarkable systematic errors, as seen in figure 8(b). The results from section 3.3.1 as well as expectations from literature [39, 47–51] suggest a homogeneous glow in horizontal direction while gradients or separated emission zones along the vertical direction should be visible. Unfortunately, fractured emission features reflecting the sub-optimal structures of the Kapton spacer can be recognized. Still the concept of the Kapton spacer was used to keep the setup as

close as possible intended for the *in situ* TEM measurements in future.

Many videos of all addressed operating conditions utilizing PTP's as electrodes have been analyzed to distinguish between emission features originating from the Kapton spacer (artifacts) and real features of the discharge showing dependencies on plasma parameters. The red dashed line in figure 8 marks an image column which, together with its surrounding, was identified to mainly showcase emission caused by the microplasma. This dashed image column was chosen for a closer evaluation. A 10 μm spaced ruler (Thorlabs R1L3S2P) has been used for spatial calibration of the images. The calibration results were crosschecked with the thickness of the Kapton foils. The electrode positions marked in figure 8 were identified by eye using the pictures at ambient lights on. The exposure time was kept constant at 1 s for all parameters and copper electrodes (PTP) have been chosen for the investigations presented here, since copper showed the best agreement to the I – V characteristics (see figure 4) obtained using ITO electrodes. Similar photographs have been obtained for the other addressed conditions, too.

The emission intensity between the electrodes along the red dashed line is shown in figure 9. A dip in the intensity is visible at 50 μm in the center of the electrodes which is caused by the connecting slit of the Kapton foils. The light intensity for Ar as working gas is higher compared to He operation, which was already observed during emission spectroscopy and top-view imaging and which is expected due to the higher current densities. Furthermore, a shift of the intensity maximum towards the negative electrode is visible and higher light intensities have been observed for the negative polarity of the microplasma. The asymmetry in emission is larger using Ar, or the negative polarity in general, as well.

Comparison of the emission profiles with the calculated sheaths thicknesses (table 2) shows at least agreement in the trends of Ar having smaller sheaths compared to He

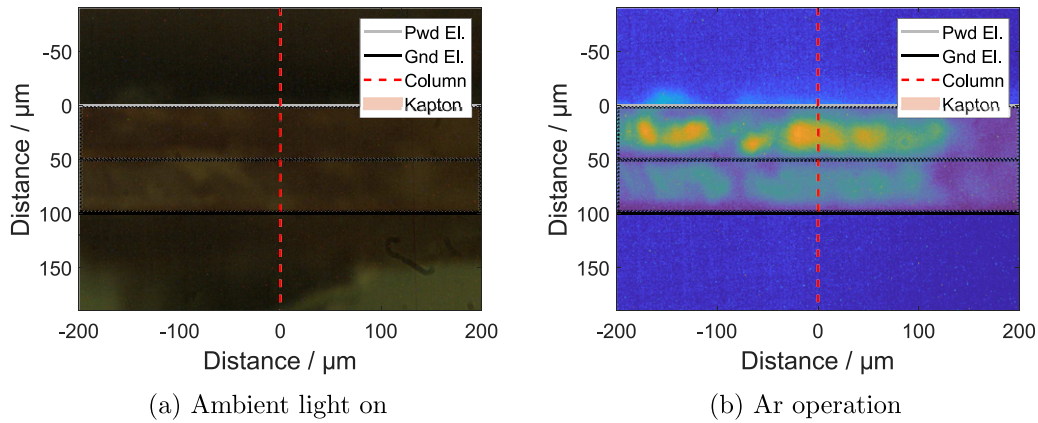


Figure 8. Side-view photographs of the electrodes and the Kapton spacer (setup from two 50 μm Kapton foils) at ambient light without plasma (a) and while operating using Ar as working gas at approx. $-2\text{ mA}/-200\text{ V}$ (b).

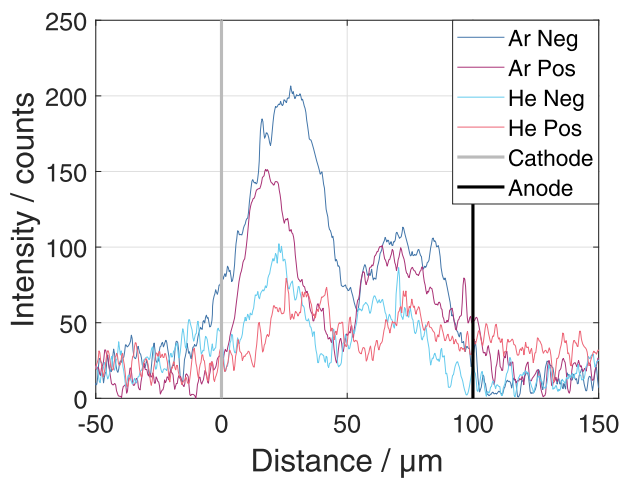


Figure 9. Intensity profile of the light emission along the red dashed line in figure 8 for different operating conditions. The light emission profiles have been smoothed by a moving average (window width of 5 pixel/ $1.67\text{ }\mu\text{m}$) and the neg/pos label in the legend refers to the applied polarity.

and the negative polarity resulting in smaller sheaths compared to the positive one. The image quality especially close to the electrodes as well as discord in literature about the possibility to pin down the sheath edges based on the emission [52, 53] prevent a validation of the calculated values. Still, the proposed trends for Ar and applied negative polarity resulting in smaller sheath thicknesses based on the collision-dominated Child–Langmuir law are in accordance with the observed emission. Hence, the normal glow character of the microplasma as well as the applicability of the collision-dominated Child–Langmuir law at atmospheric pressure have been demonstrated once more.

3.4. Energy flux measurements

3.4.1. *dT-depiction and evaluation procedure.* The use of PTP's as electrodes of the microplasma allows the measurement of the energy flux to the electrodes in addition to other applied diagnostics. For the experiments the plasma was ignited for 10 s ten times for each process parameter. Between

the duration of plasma operation (10 s) the electrodes cooled down for 60 s. The measured temperature data was smoothed (moving average, window width 50 data points/ 0.56 s) and subsequently derived in time numerically. Thus, heating and cooling phases of the electrodes result in positive or negative temperature changes (dT/dt). For the evaluation the *dT-method* [24–26, 54, 55] was used. The *dT-depiction* of three measurements performed with two gold-coated PTP's at a distance of $100\text{ }\mu\text{m}$ using a current of approx. $\pm 2\text{ mA}$ in Ar are exemplary shown in figure 10. The *dT-depiction* method offers direct conversion to the energy flux, as the temperature change \dot{T} necessary for solving equation (4) is directly visualized and the difference of the temperature changes is represented by the gap between the data points. Two parallel lines would be expected for a constant power influx P_{in} and power loss P_{out} during the plasma operation [24, 26, 55, 56].

The positive electrode shown in figure 10(a), as well as for the grounded electrode during operation using the negative polarity shown in figure 10(d), the expected behavior with a deviation at the beginning of the heating or cooling phase is obtained. This deviation is caused by thermal inertia of the probe and was seen before [55]. Larger and unexpected deviations are found for the grounded electrode during operation using a positive polarity in figure 10(b) and for the negative electrode in figure 10(c). These overshoots at the beginning of the heating or cooling phases are unexpected, as they indicate a significantly higher power influx or power loss, respectively, directly after switching the plasma on or off. Effects caused by the placement of the spacer and, thus, the location of the discharge relative to the thermocouple connection of the PTP could be excluded by various experiments with different spacer positions and a simplified COMSOL Multiphysics® [57] simulation showing that the thermal conductivity of copper is high enough to heat the thermocouple connection nearly independent on the discharge position.

The observed overshoots are attributed to ions or fast neutrals due to charge exchange as they only appear on the more negative electrode of the discharge independent of all other conditions. The overshoots are highly reproducible and their maxima are influenced by the electrical input power. High

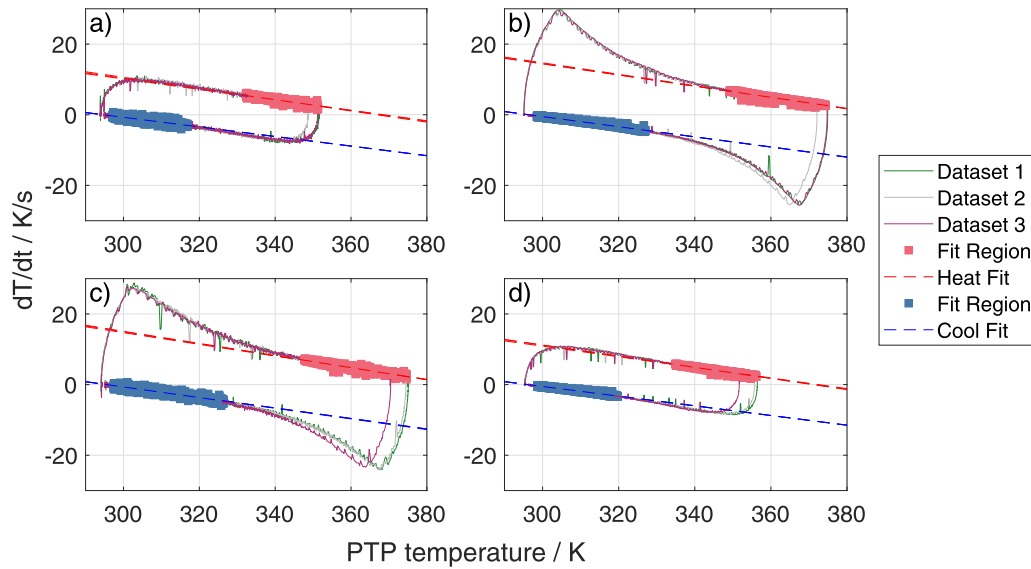


Figure 10. dT -depiction of three measurements performed using two gold electrodes with $100\ \mu\text{m}$ spacing and Ar as working gas. (a) represents the measurement at the positive electrode and (b) at the grounded electrode while a current of approx. 2 mA was used. (c) denotes the measurement at the negative electrode and (d) at the grounded electrode using approx. -2 mA. Different maximum temperatures are a result of unequal plasma operation times, as the power supply was switched on for 10 s while the plasma was not always igniting instantly. The linear fits used for the evaluation as well as the fitting regions are marked in red for the heating phase and in blue for the cooling phase. More details on the evaluation methods are given in the text.

power results in larger overshoots with their maxima at higher temperatures, but appearing constant in time roughly 0.8 s after switch on or off the plasma, while the electrical power is constant during plasma operation. The following mechanism is proposed to explain the observed overshoots: the discharge is ignited and the plasma sheaths are formed, accelerating ions to the electrode. The ions collide due to the high gas pressure and may transfer their energy to non-ionic species, but still the energy will be dumped into the electrode [24, 58–60]. The energy is absorbed by the electrode surface, resulting in the temperature increase of the PTP. After a short time, additional energy absorbed by the surface may result in desorption or even sputtering of surface atoms, which will carry energy off the electrode, resulting in a higher power loss term and, thus, decreasing the temperature rise of the electrode. Au lines being visible in the spectra in figure 5 are a good indicator of surface species getting released into the gas volume. An equilibrium between power influx and power losses is reached, which finally results in the expected linear behavior in the dT -depiction.

For the cooling phase the mechanism is quite similar. But this time the power influx is reduced over time, as the discharge does not switch off instantly. Capacitors inside the power supply as well as the discharge circuit itself become unloaded by the resistance of the plasma and the pre-resistor. The over a short time decreasing current and, thus, the electrical power, are visible in the electrical diagnostics. The high power loss including the surface desorption/sputtering also decreases over time, but slower compared to the power influx, resulting in a net larger cooling which reaches the equilibrium as soon as the increased cooling induced by the plasma vanishes.

For the evaluation linear fitting is performed in the equilibrium region of the dT -depiction. For the heating fit, data points

above 70% of the maximum temperature have been taken into account and for the cooling fit, data points below 40% of the maximum temperature have been included. In figure 10 these regions are marked in red or blue, respectively. The energy flux is then calculated following equation (4) based on the linear fits and their values at the probes minimal and maximal temperature. Hence, two energy flux values per measurement are obtained. Mean values and standard deviations are calculated for each parameter set including all repetitions.

3.4.2. Results for energy flux and power balance. The results of the energy flux measurements using Ar as working gas in combination with different spacer thicknesses, electrode surfaces and currents are shown in figure 11. The values are normalized to an area of $0.79\ \text{mm}^2$ which reflects the spacer diameter of 1 mm. Normalizing the energy flux values to the discharge areas determined in section 3.3.1 results in nearly constant energy fluxes independent on the discharge current. The rescaled values are listed in table 3 where the given errors represent the standard deviation of building the mean values over four different currents measured for each parameter. This observation indicates, that the main energy transfer happens within the formed discharge channel. Still, radiation and other plasma-generated species could leave the discharge channel and contribute to the energy flux outwards of the discharge channel. Therefore, and because only the absolute values change but not the observed trends, the energy flux values normalized to the full electrode area ($0.79\ \text{mm}^2$) are shown in figure 11. The diagram will be discussed now in more detail:

The measured energy flux increases, as expected, with increasing currents and, thus, increasing input power. Furthermore, an asymmetric energy flux is found even with more energy being transferred to the more negative electrode. This

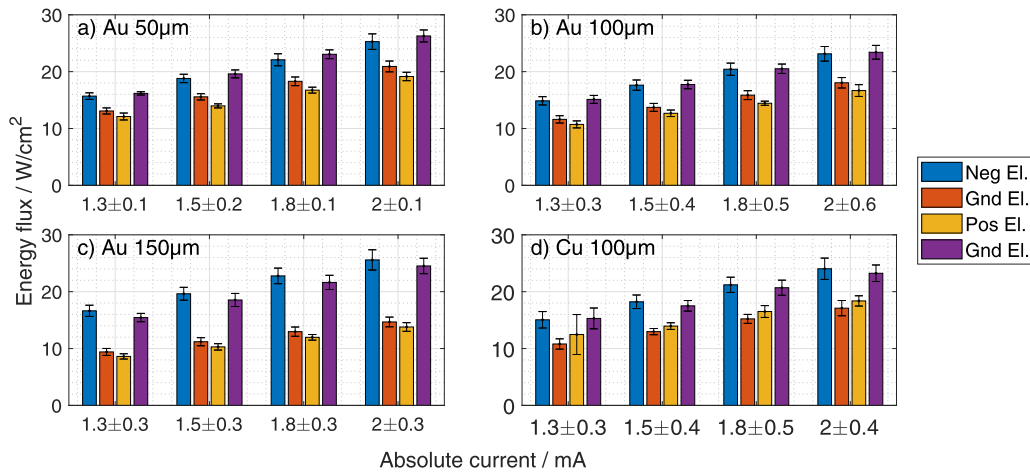


Figure 11. Energy flux measurements performed using Ar as working gas for several combination of electrode material, electrode distance and polarity.

Table 3. Energy flux values normalized to the discharge area determined in section 3.3.1 (rescaled energy flux, REF) in dependence on the electrode material (Mat), electrode distance (D), electrode polarity (El) and working gas (A_r or H_e). Additionally, the in section 3.4.3 calculated and in figure 16 shown effective SEE coefficients are listed for the sake of completeness. Emphasis should be given rather to trends than to exact values as the method has some limitations addressed in the main text.

Mat	$D/\mu\text{m}$	El	$\text{REF}_{A_r}/\text{W cm}^{-2}$	$\text{REF}_{H_e}/\text{W cm}^{-2}$	γ_{E,A_r}	γ_{E,H_e}
Au	50	Neg	275 ± 5	123 ± 1	1.02 ± 0.04	1.18 ± 0.03
		Gnd	215 ± 3	119 ± 1	—	—
		Pos	193 ± 2	98 ± 1	—	—
		Gnd	275 ± 3	117 ± 1	0.99 ± 0.03	1.07 ± 0.02
		Neg	256 ± 1	117 ± 2	1.11 ± 0.05	1.33 ± 0.03
		Gnd	195 ± 1	108 ± 1	—	—
	100	Pos	173 ± 1	88 ± 1	—	—
		Gnd	160 ± 1	111 ± 1	1.15 ± 0.05	1.21 ± 0.03
		Neg	253 ± 2	108 ± 1	0.92 ± 0.06	1.51 ± 0.02
		Gnd	174 ± 4	95 ± 1	—	—
		Pos	149 ± 2	80 ± 4	—	—
		Gnd	250 ± 2	104 ± 5	1.10 ± 0.06	1.40 ± 0.02
Cu	100	Neg	260 ± 1	111 ± 1	1.09 ± 0.08	1.16 ± 0.03
		Gnd	186 ± 1	91 ± 1	—	—
		Pos	199 ± 7	90 ± 1	—	—
		Gnd	249 ± 6	94 ± 1	1.16 ± 0.08	1.38 ± 0.03
		Neg	—	54 ± 5	—	1.57 ± 0.13
		Gnd	—	62 ± 5	—	—
Mg	100	Pos	—	44 ± 2	—	—
		Gnd	—	47 ± 3	—	1.35 ± 0.16

asymmetry increases with increasing electrode distances and is more distinct for the positive polarity if Au is used as electrode material or for the negative polarity if Cu is used. The asymmetric energy flux is assumed to be caused by the ions which are accelerated by the electric field of the sheath in front of the more negative electrode. The ions collide and transfer some of their kinetic energy multiple times on their way to the electrode and, still, the transferred energy will be dumped into the electrode at some point by e.g. metastables, fast neutrals or radiation [24, 33, 58–60]. The area of ion acceleration is shifted further away from the center between the electrodes with increasing electrode distance, as the applied voltage

mainly drops within the sheath region [24, 33, 61]. Thus, the probability of the energy being dumped into the more negative electrode increases with increasing electrode distance.

Estimations of the sheath thicknesses (given in table 2) suggest larger sheaths for the positive polarity, which could be the reason for the larger asymmetry, as the ion acceleration zone is larger. The turnaround of the asymmetry for Cu electrodes is not covered by this explanation attempt. Instead, the surface conditions might explain the change. The Cu electrodes (PTP) were stored in ambient air and, thus, should have an oxidized surface. O lines were observed in the emission spectra (see figure 5) and negative ions could be formed

by the O atoms which also get accelerated in the electric field. The contribution of negative ions to the measured energy flux could be larger for the Cu electrodes, just by the expected larger number density of available O from the oxidized Cu surface.

Similar arguments can be made for the energy flux measurements performed using He as working gas (figure 12). Here the asymmetry is less pronounced compared to Ar and nearly vanishes for the negative polarity using Au electrodes and small distances. The smaller asymmetry can be a result of the larger sheath thicknesses for He and, thus, a less asymmetric ion acceleration region. Furthermore, the contribution of He metastables could have a significant impact because they can store a significant amount of energy and are not influenced by electric fields. Simulations of a comparable He microplasma showed high densities of He^* and He_2^* metastables in the range of $2\text{--}3 \times 10^{14} \text{ cm}^{-3}$ symmetrically present around the discharge center [62]. The same simulations also calculated He^+ and He_2^+ ion densities, which are two orders of magnitude smaller ($0.8\text{--}1 \times 10^{12} \text{ cm}^{-3}$) compared to the metastable densities, stressing the importance of metastables for the energy transfer in He microplasmas once more.

The energy flux results obtained using Mg-coated PTP's separated by a $100 \mu\text{m}$ spacer and He as working gas are separately shown in figure 13. They are not following the trends observed for the other measurements. Higher currents compared to the measurements shown in figure 12 had to be used to provide approximately the same electrical input power to the plasma as in the other experiments. Surprisingly, the asymmetrical behavior of the energy flux changes and a higher energy flux is not measured at the more negative electrode. Instead, the grounded electrode shows a higher energy flux despite the polarity of the discharge. Furthermore, also a noticeable difference were observed in the optical emission of the discharge. Figure 14 shows sideview images of the discharge for both polarities of the discharge between the Mg electrodes (PTP). In contrast to the results obtained for Au and Cu electrodes shown exemplary in figure 9, the highest observed emission is not shifting towards the more negative electrode. This might be a hint for the origin of the changed asymmetry as a lot of power could be converted in radiation in front of the powered electrode and, thus, not reach the powered electrode. The positive polarity showing a more intense emission while resulting in a lower energy flux supports this this speculation.

The reason for this different discharge behavior is not yet resolved. The Mg-coated PTP's showed an expected oxide layer in energy dispersive x-ray spectroscopy examination performed within the SEM after the energy flux measurements. Thus, a quite high SEE coefficient is assumed, which results in a lower resistivity of the plasma itself, already visible in the $I\text{--}V$ characteristics in figure 4(b). The SEE coefficients of Au (approx. 0.02 [63, 64]) and MgO (approx. 0.5 [65]) given in literature for low energy ions are only partly useable for the present discharge and will be discussed in more detail in section 3.4.3. The lower resistivity results in higher currents being necessary to generate a sufficiently large voltage drop across the discharge. This voltage drop is about half as large as for the other electrode materials and should still

Table 4. Determined conversion efficiencies c_{eff} from electrical input power P_{el} to measured calorimetric power P_{cal} by the linear fitting applying $P_{\text{cal}} = c_{\text{eff}} \times P_{\text{el}}$. Given error represent the uncertainty of the linear fit.

Electrode setup	Argon	Helium
50 μm Au	0.918 ± 0.004	0.901 ± 0.004
100 μm Au	0.827 ± 0.005	0.814 ± 0.007
100 μm Cu	0.822 ± 0.006	0.845 ± 0.004
100 μm Mg	—	0.837 ± 0.030
150 μm Au	0.789 ± 0.012	0.729 ± 0.002

influence the asymmetry of the energy flux. In the scope of the current work it is not possible to answer the questions on the different discharge dynamics in detail, but still the effective SEE coefficient for the Mg electrodes will be determined and compared to the coefficients of the other electrodes in section 3.4.3.

The power conversion from electrical to thermal power is addressed in more detail as the thermal power can be reported as the power which is available for surface modifications. Thus, the conversion factor from electrical to thermal power can be understood as efficiency of the discharge for surface treatments. The measured energy fluxes at both electrodes are added and the area normalization revoked to obtain units of power. The obtained power values are plotted versus the measured electrical power in figure 15. Linear fitting is applied to the data points to determine the conversion efficiency c_{eff} following the equation $P_{\text{therm}} = c_{\text{eff}} \times P_{\text{el}}$, where P_{therm} denotes the measured thermal power and P_{el} the electrical input power. The determined conversion efficiencies c_{eff} are given in table 4 and can be divided into three groups based on the electrode distance. The main undetected power loss term is assumed to be radiation [66], which can leave the discharge volume to the sides through the spacer. With increasing electrode distance the potential loss area for radiation increases in absolute numbers as well as relative to the energy flux detection area. Thus, a decreasing conversion efficiency with increasing electrode distance was expected. The determined efficiencies in the range of approx. 80% are quite high compared to other atmospheric pressure plasmas as these offer more power loss pathways [32, 55, 67].

3.4.3. Determination of effective secondary electron emission (SEE) coefficients. Based on the power balance at the cathode, effective SEE coefficients γ_{E} can be determined as reported in literature for low pressure abnormal glow discharges [33, 34]. The effective SEE coefficient describes electrons ejected from the cathode not only by impinging ions, but also by taking into account non-ionic species directed to the cathode, e.g. photons, fast neutrals, and excited species, which may release secondary electrons, too. Therefore, effective SEE coefficients are larger compared to their originally collision-based ion-induced secondary electron coefficients of low pressure plasmas [40]. Especially, for atmospheric pressure plasmas, as the ion kinetic energy is comparably low as the energy is transferred from ions to non-ionic species due to the large number of collisions.

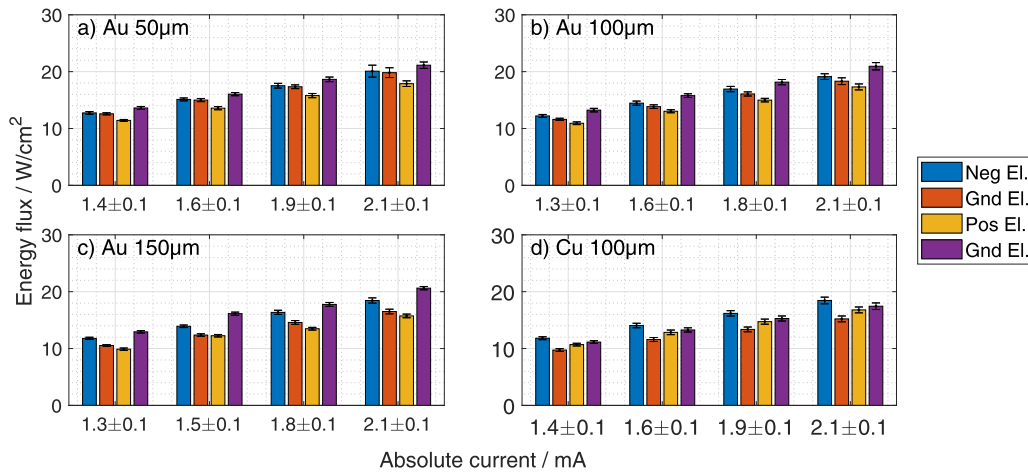


Figure 12. Energy flux measurements performed using He as working gas for several combinations of electrode material, electrode distance and polarity.

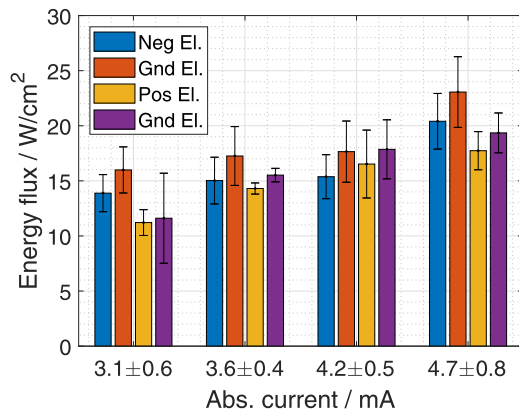


Figure 13. Energy flux measurements performed using 100 μm separated Mg-coated PTP's and He as working gas for different polarities.

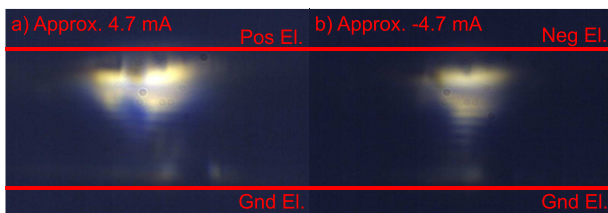


Figure 14. Sideview photographs of the microplasma discharge during energy flux measurements utilizing two Mg-coated PTP's separated by the 100 μm thick Kapton spacer. Exposure time (50 ms) was equal for both polarities.

The measured discharge current I consists of two components, the ion current I_i and the electron current I_e [20, 68]. In the cathode sheath the current is dominated by the ion current $I_{i,C}$ and the secondary electron current $I_{se,C}$ [20, 40, 69]:

$$I = I_{se,C} + I_{i,C}. \quad (8)$$

Similar to ion-induced SEE the effective SEE coefficient γ_E connects both currents at the cathode $I_{se,C} = \gamma_E I_{i,C}$ [33].

Equation (8) can be written as

$$I = I_{i,C} (\gamma_E + 1). \quad (9)$$

Using the assumption, that the measured voltage V mainly drops across the cathode sheath and, thus, the cathode sheath voltage V_C equals almost the measured voltage $V \approx V_C$ [20, 21, 61] equation (9) can be multiplied by V to obtain the expression $I_{i,C} \times V$, which can be understood as the power carried to the cathode by ions $P_{i,C}$ [24, 33, 59].

$$I \times V = I_{i,C} \times V (\gamma_E + 1) \quad (10)$$

$$P_{el} = P_{i,C} (\gamma_E + 1). \quad (11)$$

Even for the highly collisional sheath the ions gain energy in the sheath and may transfer this energy to non-ionic species or radiation during the collisions. Still, the gained energy will be dissipated into the cathode either directly by ion impact or indirectly via radiation or the non-ionic species [24, 33, 58, 59]. The power transferred to the cathode ($P_{therm,C}$) was directly measured by the energy flux measurements in section 3.4.2. Thus, $P_{therm,C}$ can be identified as $P_{i,C}$ and equation (11) rewritten as

$$\gamma_E = \frac{P_{el}}{P_{therm,C}} - 1. \quad (12)$$

The calculated effective SEE coefficients for the different experimental conditions are shown in figure 16. These values have to be taken with care as the here described method depends on oversimplified assumptions and does not take kinetics into account which are an important factor in the production of secondary electrons [40, 69]. Thus, the focus should be set to the obtained trends and not exact values.

As expected, they are way larger compared to their purely ion-induced counterparts which are typically below 0.3 in the expected ion energy range [20, 27, 70–75]. They are also larger compared to other effective SEE coefficients determined by similar measurements [33, 34] or based on breakdown voltages [35]. The main reason for the comparably rather high values is due to the gas pressure. Less energetic ions are actually reaching the cathode, since the short mean free path results in an

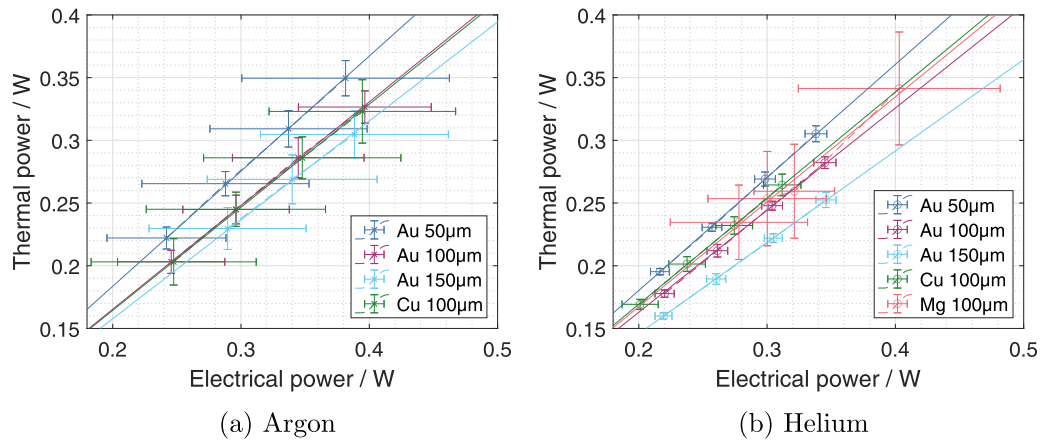


Figure 15. Measured thermal power (P_{therm}) in dependence on the electrical input power (P_{el}) for different parameters using negative polarities for plasma generation. Linear fits using $P_{\text{therm}} = c_{\text{eff}} \times P_{\text{el}}$, where c_{eff} denotes the conversion efficiency, are applied to determine the efficiency of power conversion from electrical power to power reaching the electrodes.

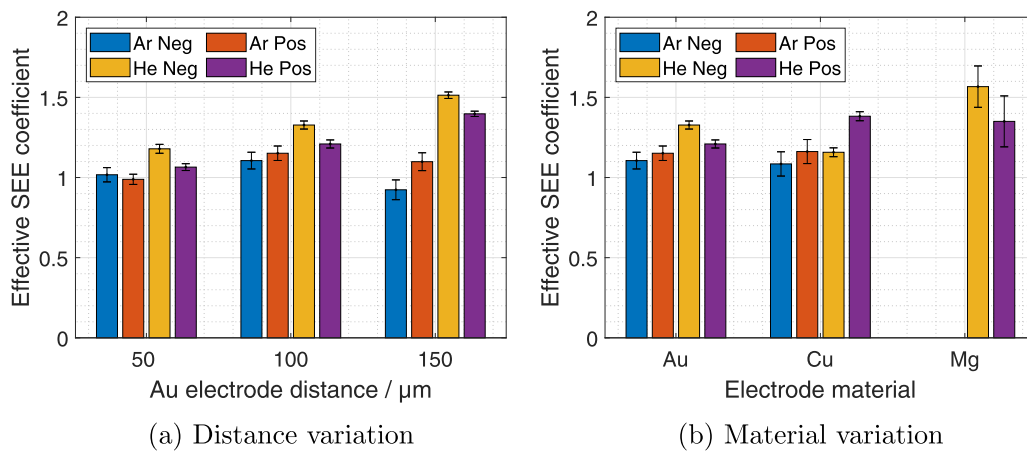


Figure 16. Effective SEE coefficients calculated by equation (12) for (a) different electrode distances using Au electrodes and (b) different electrode material using an electrode distance of 100 μm . Emphasis should be given rather to trends than to exact values as the method has some limitations addressed in the main text. Given error bars are statistical and based on building mean values and standard deviations for P_{el} and $P_{\text{therm,C}}$ followed by building the mean value paired with Gaussian error propagation for the SEE coefficient independent on the input power. Neg/Pos label in the legends refers to the applied polarity.

energy transfer from the ions to non-ionic species as discussed before. Furthermore, ions can recombine within the sheath with secondary electrons produced by ionic and non-ionic species from the electrodes.

Overall, the effective SEE values obtained using He as working gas are slightly larger compared to their Ar counterparts. In low pressure plasmas this is usually the other way around, as Ar with its higher mass acquires higher kinetic energies. Here, due to the short mean free paths the kinetic energy of the ions is negligibly low (below 0.1 eV based on the collision based model from section 3.3.1) compared to the recombination energies of He (24.6 eV) or Ar (15.76 eV, resp.) [20]. Further, the He metastables or more energetic radiation could also favor the higher effective SEE coefficient for He at atmospheric pressure.

The trend of higher effective SEE coefficients with increasing electrode distances (except for Ar 150 μm) might indicate more collisions based on the longer discharge path and, thus, more energetic non-ionic species and radiation contribute to

the effective SEE coefficient. The decreased SEE value for Ar at an electrode distance of 150 μm could indicate a change in the discharge operation mode, even though nothing conspicuous was visible in the electrical and optical diagnostics. Top view imaging could be applied to check on the discharge channel width and behavior, but is beyond the scope of the current study.

The effective SEE coefficients for the different electrode materials again show the dependence not only on the surface material, but also on the discharge conditions, as the effective SEE coefficient is sensitive to e.g. radiation and produced metastables. The determined coefficients for Au and Cu are comparable and in the range of 1.1 to 1.3. The coefficient for Mg is with approx. 1.3 to 1.6 larger and could only be determined for He as working gas. The larger effective SEE coefficient for Mg was already speculated as origin for some significant differences in the behavior of the microplasma presented in the current work.

4. Summary and outlook

Electrical, optical and calorimetric diagnostics have been applied to an atmospheric pressure DC normal glow microplasma discharge to ensure its stability and to gain insight into the discharge properties, especially, focused on the plasma surface interaction. The atmospheric pressure DC glow discharge combines a simple setup with small dimensions, excellent reproducibility and high efficiencies.

Electrical diagnostics were used to determine I – V characteristics which showcased typical normal glow discharge features. Significant differences depending on the working gas, electrode distance and electrode material were shown. These differences enable *in situ* diagnostics of e.g. changing electrodes solely by electrical measurements. Further, the stable operation in the range of investigated conditions enables adaptations of the basic electrical setup depending on the desired application.

The optical diagnostics confirmed the glow-like behavior indicated by the I – V characteristics. OES revealed the expected broadened Ar I or He I lines, but also O I and Au I lines. The excited O and Au atoms origin from the electrode surface and indicate a strong plasma surface interaction. Imaging through ITO coated glass electrodes revealed the discharge channel and enabled the determination of current densities. The current density is almost constant with increasing currents as the discharge channel width increased typically for a normal glow discharge. Sheath thicknesses could be calculated by the collision dominated Child–Langmuir law and the observed trends confirmed by side-view imaging of the discharge.

The energy flux measurements revealed an asymmetric energy flux with an increased power transfer to the cathode probably caused by ions. Furthermore, a non-constant energy flux only to the cathode could be observed using the dT -depiction, which was explained by the different contributions to the measured integral energy flux. The determined energy fluxes were in the range of 10–30 W cm^{−2} or up to 275 W cm^{−2} for Ar as working gas and an electrode distance of 50 μm, if normalized to the observed discharge diameters, which are quite large compared to other atmospheric pressure discharges and should result in several surface changes. In combination with electrical diagnostics the power balance of the different discharge configurations could be measured, which revealed high efficiencies in the range of 70%–90% only depending on the electrode distance. The power losses are mainly due to radiation which can leave the discharge undetected sideways through the spacer.

Effective SEE coefficients have been discussed and calculated based on the power balance at the cathode. As expected, these coefficients are not solely depending on the electrode material. Instead, the discharge conditions play an important role, as the production of non-ionic species and radiation are crucial in the production of secondary electrons. Different effective SEE coefficients in the range of 1.1 to 1.6 depending on electrode material, discharge polarity and working gas have been determined.

The rather simple setup for the generation of a stable atmospheric pressure DC normal glow microplasma discharge presented in the current work enables easy adaptation. The low necessary electrical power and high efficiency enables lab-on-chip applications as compact and cheap HV DC/DC-converters are available. The gained knowledge about the plasma surface interaction is important to understand any surface changes caused by the microplasma. With the planned integration of the presented microplasma cell into TEM these surface changes will become visible in real time and should be interpreted based on the results of the plasma diagnostics.

Acknowledgments

The authors would like to thank K Sgonina for providing the simplified COMSOL simulation, F Brach, V Rohwer and M Poser for technical assistance while setting up the experiments. Funding of the German Research Foundation (DFG, Project No. 413664940, Grant Nos. KE 574/8-1 and KI 1263/17-1) and Kiel Nano, Surface and Interface Science (KINSIS) is gratefully acknowledged.

Data availability statement

The data that support the findings of this study are available upon reasonable request from the authors.

ORCID iDs

Luka Hansen  <https://orcid.org/0000-0003-2656-4069>
 Niklas Kohlmann  <https://orcid.org/0000-0001-8494-118X>
 Holger Kersten  <https://orcid.org/0000-0003-1798-7588>

References

- [1] Samukawa S et al 2012 *J. Phys. D: Appl. Phys.* **45** 253001
- [2] Adamovich I et al 2017 *J. Phys. D: Appl. Phys.* **50** 323001
- [3] Profijt H B, Potts S E, van de Sanden M C M and Kessels W M M 2011 *J. Vac. Sci. Technol. A* **29** 050801
- [4] Oehrlein G S, Metzler D and Li C 2015 *ECS J. Solid State Sci. Technol.* **4** N5041–53
- [5] Lee C G N, Kanarik K J and Gottscho R A 2014 *J. Phys. D: Appl. Phys.* **47** 273001
- [6] Vandenabeele C R and Lucas S 2020 *Mater. Sci. Eng. R* **139** 100521
- [7] Massines F, Sarra-Bournet C, Fanelli F, Naudé N and Gherardi N 2012 *Plasma Processes Polym.* **9** 1041–73
- [8] Slikboer E, Acharya K, Sobota A, Garcia-Caurel E and Guaitella O 2020 *Sci. Rep.* **10** 2712
- [9] Tai K, Houlahan T J, Eden J G and Dillon S J 2013 *Sci. Rep.* **3** 1325
- [10] Becker K H, Schoenbach K H and Eden J G 2006 *J. Phys. D: Appl. Phys.* **39** R55–70
- [11] Franzke J, Meyer C, Müller S, Krähling T and Michels A 2011 Microdischarges for analytical atomic spectrometry: design

- considerations and applications *Encyclopedia of Analytical Chemistry: Applications, Theory and Instrumentation* (New York: Wiley)
- [12] Broekaert J 2002 *Anal. Bioanal. Chem.* **374** 182–7
- [13] Iza F, Kim G J, Lee S M, Lee J K, Walsh J L, Zhang Y T and Kong M G 2008 *Plasma Process. Polym.* **5** 322–44
- [14] Gianchandani Y B, Wright S A, Eun C K, Wilson C G and Mitra B 2009 *Anal. Bioanal. Chem.* **395** 559–75
- [15] Sankaran R M and Giapis K P 2003 *J. Phys. D: Appl. Phys.* **36** 2914–21
- [16] Stark R H and Schoenbach K H 1999 *Appl. Phys. Lett.* **74** 3770–2
- [17] Stark R H and Schoenbach K H 1999 *J. Appl. Phys.* **85** 2075–80
- [18] Sankaran R M and Giapis K P 2001 *Appl. Phys. Lett.* **79** 593–5
- [19] Paschen F 1889 *Ann. Phys., Lpz.* **273** 69–96
- [20] Lieberman M A and Lichtenberg A J 2005 *Principles of Plasma Discharges and Materials Processing* (New York: Wiley)
- [21] Raizer Y P 2011 *Gas Discharge Physics* (Berlin: Springer)
- [22] Roth J 1995 *Industrial Plasma Engineering* (Bristol: Institute of Physics Publishing)
- [23] Stahl M, Trottenberg T and Kersten H 2010 *Rev. Sci. Instrum.* **81** 023504
- [24] Kersten H, Deutsch H, Steffen H, Kroesen G M W and Hippler R 2001 *Vacuum* **63** 385–431
- [25] Bornholdt S, Fröhlich M and Kersten H 2014 *Calorimetric probes for energy flux measurements in process plasmas Complex Plasmas* (Berlin: Springer) pp 197–234
- [26] Rosenfeldt L, Hansen L and Kersten H 2021 *IEEE Trans. Plasma Sci.* **49** 3325–35
- [27] Haase F, Manova D, Hirsch D, Mändl S and Kersten H 2018 *Plasma Sources Sci. Technol.* **27** 044003
- [28] Gauter S, Haase F and Kersten H 2019 *Thin Solid Films* **669** 8–18
- [29] Haase F, Lundin D, Bornholdt S and Kersten H 2015 *Contrib. Plasma Phys.* **55** 701–13
- [30] Gauter S, Fröhlich M, Garkas W, Polak M and Kersten H 2017 *Plasma Sources Sci. Technol.* **26** 065013
- [31] Zahari F et al 2019 *J. Vac. Sci. Technol. B* **37** 061203
- [32] Hansen L, Goldberg B M, Feng D, Miles R B, Kersten H and Reuter S 2021 *Plasma Sources Sci. Technol.* **30** 045004
- [33] Arumugam S, Alex P and Sinha S K 2017 *Phys. Plasmas* **24** 112106
- [34] Arumugam S, Alex P and Sinha S K 2017 *Current Smart Materials* **2** 44–8
- [35] Mariotti D, McLaughlin J A and Maguire P 2004 *Plasma Sources Sci. Technol.* **13** 207–12
- [36] Petrović Z L and Phelps A V 1993 *Phys. Rev. E* **47** 2806–15
- [37] Rousseau A and Aubert X 2006 *J. Phys. D: Appl. Phys.* **39** 1619–22
- [38] Michaud R, Felix V, Stolz A, Aubry O, Lefaucheux P, Dzikowski S, Schulz-von der Gathen V, Overzet L J and Dussart R 2018 *Plasma Sources Sci. Technol.* **27** 025005
- [39] Arkhipenko V I, Kirillov A A, Safronau Y A and Simonchik L V 2010 *Eur. Phys. J. D* **60** 455–63
- [40] Phelps A V and Petrović Z L 1999 *Plasma Sources Sci. Technol.* **8** R21–44
- [41] Hobbs G D and Wesson J A 1967 *Plasma Phys.* **9** 85–7
- [42] Bruggeman P and Brandenburg R 2013 *J. Phys. D: Appl. Phys.* **46** 464001
- [43] Kramida A, Ralchenko Y and Reader J (NIST ASD Team) 1999 *NIST Atomic Spectra Database (version 5.9)* <https://doi.org/10.18434/T4W30F>
- [44] Loeb L B and Meek J M 1941 *The Mechanism of the Electric Spark* (Redwood City, CA: Stanford University Press)
- [45] Brenning N, Axnas I, Nilsson J O and Eninger J E 1997 *IEEE Trans. Plasma Sci.* **25** 83–8
- [46] Fridman A 2008 *Plasma Chemistry* (Cambridge: Cambridge University Press)
- [47] Roth J 2001 *Applications to Nonthermal Plasma Processing* (Bristol: Institute of Physics Publishing)
- [48] Staack D, Farouk B, Gutsol A and Fridman A 2005 *Plasma Sources Sci. Technol.* **14** 700–11
- [49] Staack D, Farouk B, Gutsol A and Fridman A 2008 *Plasma Sources Sci. Technol.* **17** 025013
- [50] Škoro N 2012 *J. Phys.: Conf. Ser.* **399** 012017
- [51] Marić D, Škoro N, Maguire P D, Mahony C M O, Malović G and Petrović Z L 2012 *Plasma Sources Sci. Technol.* **21** 035016
- [52] Marić D, Kutasi K, Malović G, Donkó Z and Petrović Z L 2002 *Eur. Phys. J. D* **21** 73–81
- [53] Schleitzer J, Schneider V and Kersten H 2021 *Phys. Plasmas* **28** 083506
- [54] Hansen L, Reck K and Kersten H 2019 *J. Phys. D: Appl. Phys.* **52** 325201
- [55] Hansen L, Rosenfeldt L, Reck K A and Kersten H 2021 *J. Appl. Phys.* **129** 053308
- [56] Bornholdt S, Peter T, Strunskus T, Zaporozhtchenko V, Faupel F and Kersten H 2011 *Surf. Coat. Technol.* **205** S388–92
- [57] *Comsol Multiphysics®* v. 5.6 (Stockholm, Sweden: COMSOL AB) (<https://www.comsol.com/>)
- [58] Sheridan T E and Goree J 1991 *Phys. Fluids B* **3** 2796–804
- [59] Suraj K S and Mukherjee S 2005 *Surf. Coat. Technol.* **196** 267–70
- [60] Trottenberg T, Richter T and Kersten H 2015 *Eur. Phys. J. D* **69** 91
- [61] Suraj K S and Mukherjee S 2005 *Phys. Plasmas* **12** 113502
- [62] Kothnur P S, Yuan X and Raja L L 2003 *Appl. Phys. Lett.* **82** 529–31
- [63] Lakits G, Aumayr F, Heim M and Winter H 1990 *Phys. Rev. A* **42** 5780–3
- [64] Hippler R 2008 *Low Temperature Plasmas: Fundamentals, Technologies and Techniques* (New York: Wiley)
- [65] Ushio Y, Banno T, Matuda N, Saito Y, Baba S and Kinbara A 1988 *Thin Solid Films* **167** 299–308
- [66] Despax B, Pascal O, Gherardi N, Naude N, Belinger A and Pitchford L C 2012 *Appl. Phys. Lett.* **101** 144104
- [67] Schmidt-Bleker A, Reuter S and Weltmann K-D 2015 *J. Phys. D: Appl. Phys.* **48** 175202
- [68] Chapman C 1980 *Glow Discharge Processes* (New York: Wiley)
- [69] Phelps A V, Pitchford L C, Pédoussat C and Donkó Z 1999 *Plasma Sources Sci. Technol.* **8** B1–2
- [70] Böhm C and Perrin J 1993 *Rev. Sci. Instrum.* **64** 31–44
- [71] Tolias P 2014 *Plasma Phys. Control. Fusion* **56** 123002
- [72] Marcak A, Corbella C, de los Arcos T and von Keudell A 2015 *Rev. Sci. Instrum.* **86** 106102
- [73] Daksha M, Berger B, Schuengel E, Korolov I, Derzsi A, Koepke M, Donkó Z and Schulze J 2016 *J. Phys. D: Appl. Phys.* **49** 234001
- [74] Pamperin M, Bronold F X and Fehske H 2018 *Plasma Sources Sci. Technol.* **27** 084003
- [75] Daksha M, Derzsi A, Mujahid Z, Schulenberg D, Berger B, Donkó Z and Schulze J 2019 *Plasma Sources Sci. Technol.* **28** 034002

Chapter 5

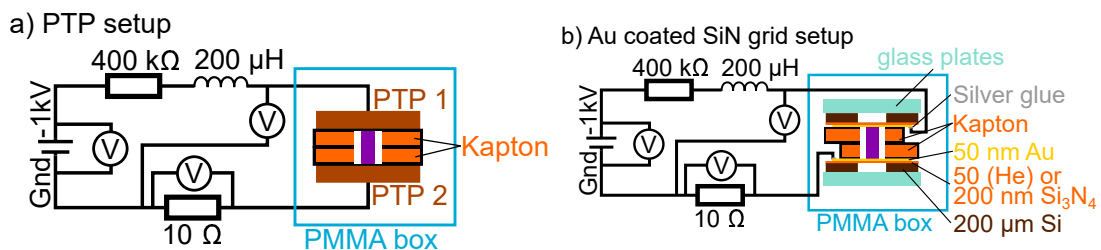
Ex situ Polycrystalline Au Thin Film Modifications

Publication III

Correlations between energy flux and thin film modifications in an atmospheric pressure direct current microplasma

Authors	L. Hansen, N. Kohlmann, L. Kienle, and H. Kersten
Journal	Thin Solid Films [324]
Technique	<i>Ex situ</i> setup of the microplasma utilizing Au coated TEM grids as electrodes
Utilized diagnostics	Electrical and energy flux measurements, light microscopy, SEM and TEM (dark field and SAED) imaging
Own contribution	Approx. 70 %

Experimental Setup:



Reprinted (adapted) from [324].

Reprinted (adapted) from [324].

Motivation:

The electrodes of the developed and in chapter 4 diagnosed microplasma were exchanged to Au coated TEM grids. This change made the setup identical with the intended microplasma geometry for the *in situ* microplasma cell. Both electrodes are TEM electron beam transparent. Therefore, the microplasma induced surface modifications can be directly imaged by comparison of the electrodes before and after the microplasma treatment. The *ex situ* observed surface modifications should serve as benchmarks for the *in situ* experiments. Furthermore, a correlation between the surface modifications and the measured energy fluxes was expected and hopefully can be confirmed.

Main Results:

The microplasma could successfully be operated utilizing two Au coated TEM grids as electrodes. Clear correlations between the energy flux and the modification of the polycrystalline Au thin film could be shown. Higher energy fluxes resulted in more textured films with larger grains as postulated by structure zone diagrams mainly used for low-pressure deposition processes. The ion contribution of the measured integral energy flux seemed to be the most important energetic contribution in regards to the surface modifications despite the atmospheric pressure conditions. Further, utilizing Ar or He as working gas resulted in significant differences in the power transfer by ions from the plasma to the surface. For Ar the major power transfer mechanism is given by the kinetic energy of ions or fast neutrals. For He the ion recombination on the surface seems to be most important. The difference in these power transfer mechanisms (many small doses for Ar, fewer high doses for He) resulted in more or less uniform surface modifications and desorption hot spots in the case of He.



Correlations between energy flux and thin film modifications in an atmospheric pressure direct current microplasma

Luka Hansen^{a,*}, Niklas Kohlmann^b, Lorenz Kienle^b, Holger Kersten^a

^a Institute of Experimental and Applied Physics, Kiel University, 24098 Kiel, Germany

^b Institute for Material Science, Kiel University, 24098 Kiel, Germany

ARTICLE INFO

Keywords:

Plasma surface interaction
Thin film modification
Microplasma
Energy flux
Glow discharge
Transmission electron microscopy
Scanning electron microscopy

ABSTRACT

A custom-built atmospheric pressure direct current microplasma discharge was designed utilizing Au coated Si_3N_4 transmission electron microscopy (TEM) grids as electrodes to enable a direct imaging of the plasma treated anode and cathode surfaces. Significant differences between the anode and the cathode, as well as between Ar or He operation of the microplasma, respectively, were observed already by examination of the electrode surfaces by light microscopy. Scanning electron microscopy as well as TEM imaging revealed details such as grain growth and changes in surface morphology. The energy fluxes from plasma towards the anode and cathode were determined and correlated with the surface modifications. As expected from structure zone diagrams higher energy fluxes result in higher degree of crystallinity even at atmospheric pressure. Furthermore, ions and their respective energy contributions were identified to play a major role for the surface modification, despite their low kinetic energy due to the large number of collisions. Depending on the working gas, Ar or He, the identified energetic contributions of the total ion energy flux change and, subsequently, result in visible differences in the plasma treated Au films.

1. Introduction

A suitable and convenient method of illustrating deposition features of polycrystalline thin films are structure zone diagrams (SZDs). They have been used and modified in the past to reduce deposition parameters to a minimum while representing universal features of the thin films [1–4]. Due to its universal character the shown features can also be recognized during modifications of thin films, as atoms and grains rearrange during plasma treatment. Surface temperature and energy flux to the substrate have been identified as key parameter in SZDs which cannot be tuned individually as any energy flux affects the heat balance of the substrate [2,5–7].

In the present study, for polycrystalline thin film modification an atmospheric pressure direct current (DC) microplasma is used. Microplasmas combine high energy densities, high efficiency and low ignition voltages at atmospheric pressure [8–15]. Energy flux measurements utilizing passive thermal probes (PTPs) [16–21] have been performed to measure the integral energy flux from the custom atmospheric pressure DC microplasma to its electrodes [15]. The integral energy flux consists of various components, e.g., impinging ions and fast neutrals, ion recombination at the surface, metastable de-excitation at the surface, and radiation [19,21,22]. Depending on the plasma

conditions the contribution of each of the different components may change [22–25]. Hereby, measuring the contribution of single components of the energy flux and, thus, a separate consideration of the different processes is difficult.

Using gold coated transmission electrode microscopy (TEM) grids as electrodes instead of the PTPs enables to study simultaneously the surface modifications caused by the microplasma directly. Changes of the properties of the Au thin film electrodes are caused by the different contributions of the measured energy flux [22,23]. Analyzing the energy flux itself as well as its impact on the thin film electrodes allow for statements about the significance of the several contributions in regard to thin film modification. Furthermore, visible correlations between the integral energy flux and the surface modifications are visible and can be interpreted in context of the established SZDs showcasing their applicability even for atmospheric pressure plasma conditions.

In the near future, based on the idea of introducing a microplasma into a TEM [26], the surface modifications caused by the microplasma will also be observable *in situ* during the plasma treatment since the microplasma geometry was developed for TEM integration [15]. The present work aims to investigate the power transfer mechanisms from

* Corresponding author.

E-mail addresses: lhansen@physik.uni-kiel.de (L. Hansen), niko@tf.uni-kiel.de (N. Kohlmann), lk@tf.uni-kiel.de (L. Kienle), kersten@physik.uni-kiel.de (H. Kersten).

<https://doi.org/10.1016/j.tsf.2022.139633>

Received 11 May 2022; Received in revised form 6 December 2022; Accepted 6 December 2022

Available online 12 December 2022

0040-6090/© 2022 Elsevier B.V. All rights reserved.

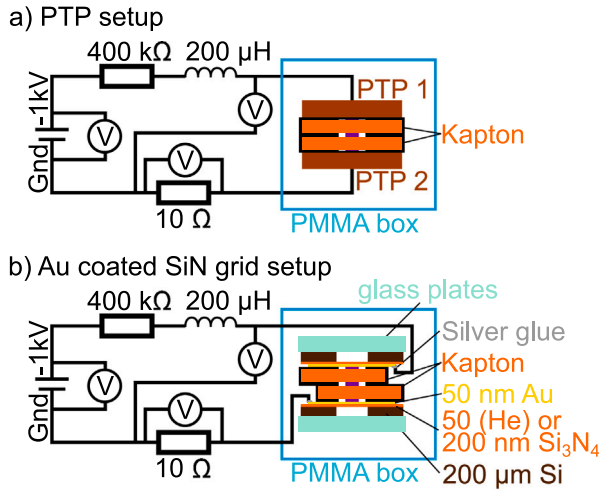


Fig. 1. Schematic sketch of the experimental setup for the energy flux measurements (a) and the gold thin film plasma treatment (b). The surrounding PMMA box was flushed with 3 slm Ar or He for 1 h followed by a constant 1 slm gas inflow during the experiments.

the microplasma to the surface, identifying the main components and their impact on the observable surface modifications.

2. Experimental setup

2.1. Microplasma discharge cell

The schematic setup is shown in Fig. 1 and can be found elsewhere [15]. The electrical circuit is identical for the energy flux measurements and for the thin film plasma treatment. It consists of a 400 kΩ resistor to limit the current generated by a DC high voltage supply (Heinzinger PNC 20,000 - 10 ump) set to -1 kV for all experiments, resulting in approx. -2 ± 0.5 mA current through and -185 ± 10 V voltage at the microplasma [15]. A 200 μH inductor stabilizes the discharge by suppression of fast current changes and a 10 Ω shunt resistor in the ground line enables current measurements. Three different voltage probes connected to an oscilloscope (PicoScope 5442B) were used to measure the voltages at the power supply (Tektronix P6015 A 1000:1), at the electrodes (Tektronix P5100 A 100:1) and at the shunt resistor (Tektronix P2200 1:1). The discharge is housed in a 30×30×30 cm³ Poly(methyl methacrylate) (PMMA) gas box. After flushing the box with 3 slm of Ar or He, respectively, for 1 h a continuous flow of 1 slm for another 2 h was chosen to ensure gas purity inside the box, especially between the electrodes. During the experiments the gas flow was kept at 1 slm.

The electrodes of the plasma discharge differ depending on the experiment. For the determination of the energy flux towards the electrodes two passive thermal probes (PTPs, see Section 2.2) have been utilized as electrodes. They are pressed to each other and separated only by two 50 μm thick Kapton foils with a hole of 1 mm diameter specifying the discharge volume. The dielectric barrier of 100 μm Kapton is set up from two foils to be identical with the setup utilized for the thin film plasma treatment. A sketch of the setup using PTPs as electrodes is given in Fig. 1 (a).

The Si₃N₄ TEM substrates (PELCO® Silicon Nitride Support Films for TEM, Ted Pella inc.), also called “grids”, consist of a 200 μm Si wafer covered by a 50 nm (for He treatment) respectively 200 nm (for Ar treatment) thick low-stress, amorphous Si₃N₄ membrane. A free standing 500 × 500 μm² membrane is formed in the central area as TEM window by etching of the Si wafer. The TEM grid based electrodes used for the study of thin film modification were prepared by DC magnetron sputtering of a 50 nm gold film directly onto the Si₃N₄ TEM substrates.

Table 1

Heat capacities of the PTPs used as anode or cathode. The small differences in the heat capacities originate from the manual spot-welding process despite otherwise identical construction of the PTPs. The given error values represent the standard deviation from multiple calibrations.

PTP	Heat capacity/J/K
Anode	0.0127 ± 0.0008
Cathode	0.0122 ± 0.0005

A shadow mask is used to restrict the gold deposition to the central area of the grid as well as contact pad. Electrical contact of the gold film was realized by gluing a thin isolated copper wire (conductor diameter: 25 μm, insulation material: Polyimide, thickness: 2 μm) on top of the gold film with conductive silver glue (SCP, Silver Conductive Paint, Electrolube). The gold coated Si₃N₄ TEM grids were mounted on top of small glass plates to improve their handling. Afterwards they were pressed together, again, only divided by two slightly displaced 50 μm Kapton foils with a 1 mm diameter hole in their center. The slight displacement of the foils at the edges is necessary to make room for the cable contact placed on opposing sides as sketched in Fig. 1 (b). The plasma on time for the gold coated Si₃N₄ TEM grid treatment was 20 s. However, it can certainly be assumed that not the full electrode areas are completely and homogeneously covered by the microplasma during the treatment time [15].

2.2. Passive Thermal Probe (PTP)

The passive thermal probe (PTP) is a non-conventional diagnostic to measure the power transferred from the plasma to a surface based on calorimetry [19,21,22,27]. A 5.2 mm diameter and 100 μm thick copper platelet is spot-welded to a type K thermocouple and a copper wire for a separate electrical connection. The temperature of the platelet is measured with a sample rate of 90 Hz. Similar to the Au thin film on the TEM grids a 2–3 μm thick Au film was sputtered on top of the copper PTP platelet. The heat capacity of the probe was determined using a calibration described in [28]. The determined heat capacities are given in Table 1.

The temporal temperature change \dot{T} of the substrate is related to its enthalpy \dot{H} via its heat capacity C . A change of the enthalpy results in a power term towards the substrate P_{in} and power term away from the substrate P_{out} if the assumption of no processes inside the substrate is valid.

$$\dot{H} = C\dot{T} = P_{in} - P_{out} \quad (1)$$

An additional power transfer to the substrate is gained while the plasma is switched on. After switching off the plasma the additional power influx is no longer present. Thus, two equations can be obtained during the plasma induced heating or cooling of the substrate

$$\text{Heating : } \dot{H}_h = C\dot{T}_h = P_{in} - P_{out} \quad (2)$$

$$\text{Cooling : } \dot{H}_c = C\dot{T}_c = -P_{out} \quad (3)$$

Assuming equal power losses P_{out} during heating and cooling of the substrate Eqs. (2) and (3) can be combined and rearranged. The transferred power is normalized by the contact area A between the plasma and the substrate to get the energy flux J_{in}

$$J_{in} = \frac{P_{in}}{A} = \frac{C}{A} (\dot{T}_h - \dot{T}_c) \quad (4)$$

For the shown results heating times (plasma on) of 10 s followed by 60 s of cooling (plasma off) have been used. Ten repetitions were done for each parameter.

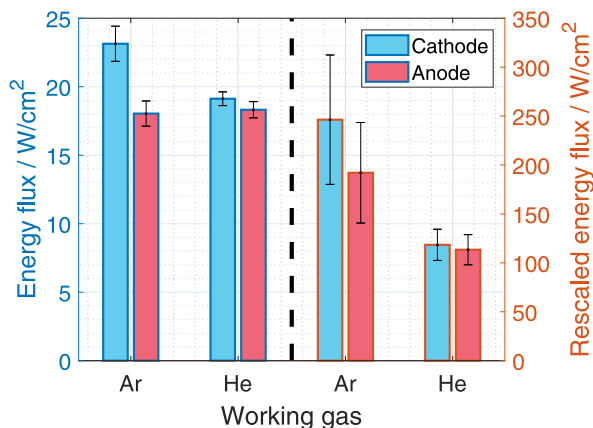


Fig. 2. Energy flux measurements utilizing PTPs as electrodes under identical conditions as the surface treatment of the Au coated Si_3N_4 TEM grids. The given energy flux values for each gas differ as they were scaled to different areas. The values on the left are scaled to the full available discharge area given by the Kapton spacer with a diameter of 1 mm. The values on the right are scaled to the discharge area observed in [15]. The shown error bars represent Gaussian error propagation of standard deviations from multiple measurements.

2.3. Surface diagnostics

The structure of the thin film electrodes was investigated by electron microscopy as well as by optical microscopy. Bright field transmission electron microscopy was performed using a FEI Tecnai F30 G² STwin with an acceleration voltage of 300 kV. Dark field TEM for grain size analysis was performed using a JEOL JEM 2100 with an acceleration voltage of 200 kV. Scanning electron microscopy (SEM) was carried out using a Zeiss Supra 55 V. Visible light microscopy was done using a Polylite SC (Type: 301901) equipped with a Leica DFC280 camera. The combined thickness of the Si_3N_4 membranes and the gold thin film electrodes is still low enough to be electron transparent, thus, TEM investigation of the electrodes can be performed without further modification of the electrodes. Due to the conductive nature of the gold thin films imaging in the SEM is possible without modification as well.

3. Results and discussion

3.1. Energy flux measurements

The energy flux towards the electrodes of the presented microplasma discharge is shown in Fig. 2. More details on the evaluation and a parametric study for this specific microplasma setup is given in [15]. Here, we focus on the correlation between the energy flux consisting of different contributions and the observed surface modifications which is discussed in detail.

Fig. 2 shows two energy flux values per experimental parameter set. The difference is due to the area normalization given in Eq. (4). On the left scale the energy flux is normalized to $A = 0.79 \text{ mm}^2$, which is the whole area corresponding to the 1 mm diameter circle inside of the Kapton spacer, as power gains and losses, e.g. by radiation, could happen on the full accessible area. For Ar as working gas an energy flux of $23.1 \pm 0.9 \text{ W/cm}^2$ towards the cathode and $18 \pm 1.1 \text{ W/cm}^2$ towards the anode was measured. The errors result from the standard deviation while calculating the mean values over ten measurements. A significant asymmetry in the energy flux to the electrodes is most probably caused by the ions being accelerated towards the cathode. Despite the high pressure and, thus, for short mean free path of the ions, their energy gain in the electric field between two collisions will be transferred to non-ionic species and at some point dumped into the cathode [15,22,29–32]. He as the working gas results in energy fluxes of $19.1 \pm 1.9 \text{ W/cm}^2$ to the cathode and $18.3 \pm 2.1 \text{ W/cm}^2$ to the anode.

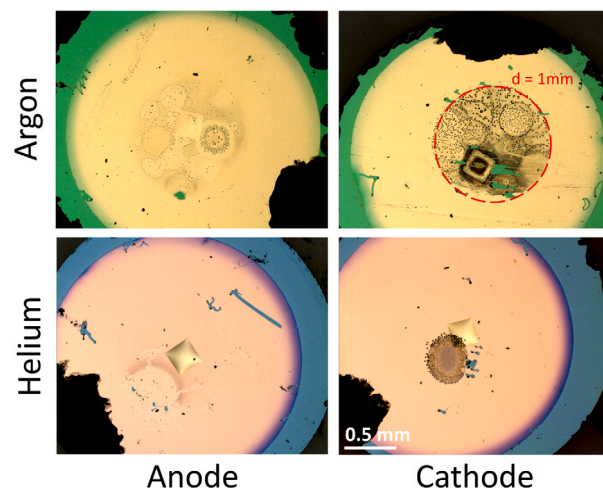


Fig. 3. Optical images taken with a light microscope show visible surface changes caused by the exposure to the microplasma. The rectangular feature in the center of the electrodes is the area of free standing membrane where TEM investigation can be performed. The partly removed gold films are due to handling errors but have no influence on the evaluation in the SEM and TEM. The difference in color are caused by deviating Si_3N_4 membrane thickness.

Again an asymmetry is visible, but not as significant as for Ar. The reason for this smaller difference is probably the power conversion from electrical to thermal power. He tends to form metastables which can store significant amount of energy and are not influenced by the electric field. Simulations of a similar discharge geometry showed He metastable densities surpassing ion densities by two orders of magnitude [33]. Further, also the different thermal conductivities could influence the asymmetry, as the thermal conductivity of He is nearly a magnitude larger compared to Ar [34].

On the right axis in Fig. 2 the energy flux is scaled to the actual (real) discharge area calculated from the current densities determined in [15] multiplied with the measured currents during the energy flux measurements. The error bars enlarge due to additional error sources entering the Gaussian error propagation. As expected, due to the smaller interaction area, the energy flux values increase to $246 \pm 66 \text{ W/cm}^2$ at the cathode and to $192 \pm 51 \text{ W/cm}^2$ at the anode for Ar, and to $118 \pm 16 \text{ W/cm}^2$ and $113 \pm 15 \text{ W/cm}^2$ for He, respectively. These values should be seen as an upper limit for the energy flux as radiation and other species could leave the visible discharge channel and transfer power to the electrodes via not accounted area. The surface diagnostics provide some hints that this is happening, which will be discussed in Section 3.2.2. The contributions of the energy flux and their effect on the gold film will be discussed in Section 3.3 after the surface modifications have been shown.

3.2. Surface modifications

3.2.1. Optical microscopy

Preliminary observations of the plasma treated gold films were taken by an optical microscope. Fig. 3 shows that the effect of the microplasma is clearly visible. The cathodes are more affected by the plasma treatment for the Ar microplasma showing more pronounced changes. The stronger affected cathodes as well as the higher effect when Ar is used as working gas correlate well with the energy flux measurements. The area of the actual discharge channel of the microplasma is clearly visible in the gold films after plasma treatment. The observed circular footprints fit to the observations made on this type of discharge previously [15]. Fig. 3 indicates a more pronounced surface roughness of the electrodes when Ar is used compared to the He microplasma, which will be confirmed by the SEM imaging. Further,

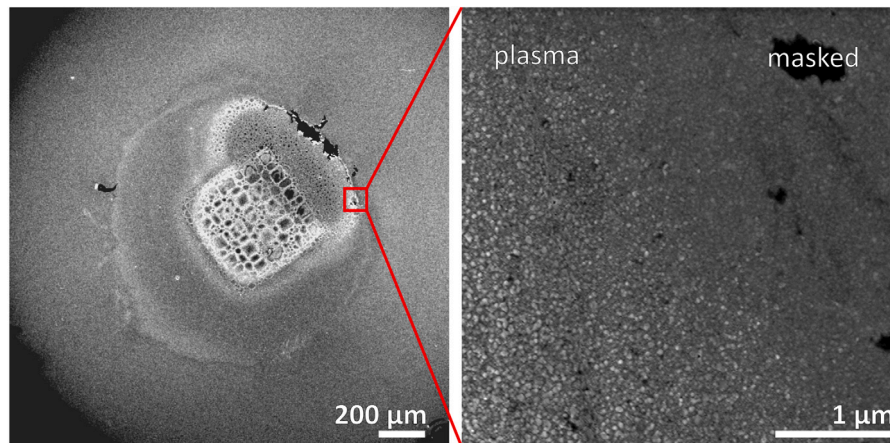


Fig. 4. SEM micrograph of a thin film cathode operated in He for 20 s. The effect of the discharge can clearly be seen tracing the border of the center within the Kapton spacer. At higher magnification the surface modification caused by the plasma can readily be observed. The edge of the discharge volume is visible showing the confinement of the plasma.

with more visible footprints after 20 s of plasma exposure for the Ar operation, the discharge channel is obviously moving more rapidly. The increased movement of the discharge channel on the electrodes with more pronounced surface roughness strengthens the assumption of a faster moving or even jumping discharge channel as a result of the increasing surface roughness first formulated in [15].

The moving discharge channel is a problem for the intended goal of producing one-to-one comparable plasma treated surfaces, as the treatment time of the discharge channel centered above the considered area given by the TEM window can vary for different experiments depending on the spatial stability of the discharge channel. Further, hitting the TEM window either with the edge or the center of the discharge channel can also influence the treatment effect, as an energy flux gradient within the discharge channel is assumed. Still, the shown results and interpretations were reproducible while running multiple iterations of the experiment. An improved setup for these kinds of experiments with an even more restricted discharge region given by a Kapton spacer with a central hole of smaller diameter could be performed in the future but also requires extensive plasma diagnostics as described in [15] to ensure stable operation and is beyond the scope of the current work.

3.2.2. Scanning electron microscopy

The electrodes exposed to the plasma of the micro discharges were transferred into the SEM to take a closer look at the resulting surface structure. Fig. 4 shows a typical SEM micrograph of a He microplasma treated cathode where the discharge area is distinguishable by brighter contrast even after the Kapton spacers have been removed. An image taken at the edge of the Kapton spacer clearly shows the border between the electrode surface affected by the plasma and the unaltered thin film. The plasma treated surface on the left shows an increased surface roughness, visible through the increased contrast variation. On the right the smooth surface still looks similar to the freshly sputtered one. The visible edge of the Kapton spacer indicates that the surface modification is not only just a result of the increased temperature during the plasma treatment. The temperature can be assumed nearly equal over the full electrode surface due to the high thermal conductivity of gold [34].

Furthermore, the edge of the Kapton spacer is visible at all locations, even if no clear footprints of the discharge are visible by optical observations. This indicates a plasma surface interaction or more precise a power transfer over the full accessible area given by the Kapton spacer. Without doubt spatial gradients in the power transfer to the electrode are present, which cannot be resolved with the presented PTP. This observation showcases once more the difficulty of choosing the correct

area for the normalization to obtain energy flux values at atmospheric pressure plasmas [15,25].

Increasing the magnification shows the modified surface in more detail. In Fig. 5 the surfaces of both the cathodes and anodes for He and Ar plasma operation, respectively, are shown. For comparison an untreated (pristine) electrode (a) as well as an electrode subjected to heat treatment (d) are displayed. Heat treatment was used as a benchmark for the surface modification caused by annealing alone. A gold coated TEM grid was heated to 150 °C for 10 min in air within a tube furnace. The temperature of 150 °C was chosen based on the measured maximum PTP temperature during plasma exposure. The maximum PTP temperature was obtained on the cathode during Ar operation and amounted to about 100 °C after 10 s, already showing the first signs of saturation. With the TEM grids being plasma treated for 20 s, a higher temperature and longer heating time was therefore chosen for annealing to exclude surface modifications achieved by plasma treatment only resulting from the temperature increase during plasma operation. All SEM images were taken at identical imaging conditions and at identical magnifications. From the light microscope image (see Fig. 3) it can already be seen that the effect of the plasma on the electrode is not spatially homogeneous. In order to compare parts of the electrodes subjected to similar plasma exposure areas near the outer edge the footprints have been chosen for both anode and cathode and He and Ar alike. The same procedure of selecting the investigated area of the electrodes was again used during TEM analysis.

For the pristine as well as the heated electrodes (Fig. 5(a)(d)) the SEM contrast corresponds to the crystal grains of the thin film, which becomes evident by comparison to the bright field TEM micrographs (see Fig. 6(a)(d)). The heated electrode shows an increased grain size as a result of the annealing. The same is true for the anode of the electrode operated in He (Fig. 5(f)). Plasma treatment on the cathodes (Fig. 5(b),(e)) as well as to a lesser degree for the Ar anode (Fig. 5(c)) on the other hand results in a change on surface morphology in addition to grain growth resulting in an increased surface roughness. Particle-like structures with diameters of approx. 200 nm are visible on the Ar cathode (Fig. 5(b)). On the He cathode (Fig. 5(e)) the plasma treatment created localized dark spots from which considerably less intensity is detected.

Gold atoms seem to partly desorb from the originally flat surface and rearrange in the observed particle-like structures. This process is especially pronounced for the cathode run in Ar, cf. Fig. 5(b). The desorption process fits to the observation of gold lines present in the optical emission spectrum and anomalies in the PTP measurements obtained in previous studies [15]. As no complete, fully spherical particles are visible on top of the surface (except for the Ar cathode

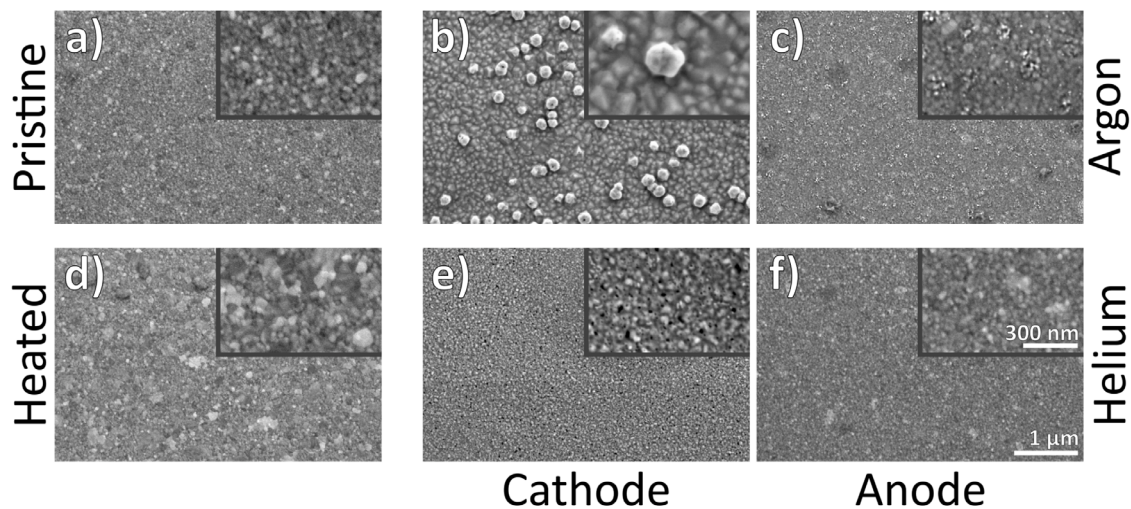


Fig. 5. SEM micrographs with insets at higher magnification of the gold thin film electrodes in pristine condition as well as after the electrodes have been subject to microplasma for 20 s both for Ar and He as working gases. The scale of all micrographs respectively insets is identical. For comparison an electrode heated in air at 150 °C for 10 min (a) is investigated as well. Plasma exposure clearly results in a strongly increased surface roughness for the Ar and He cathodes (b),(c) as well as the Ar anode (c).

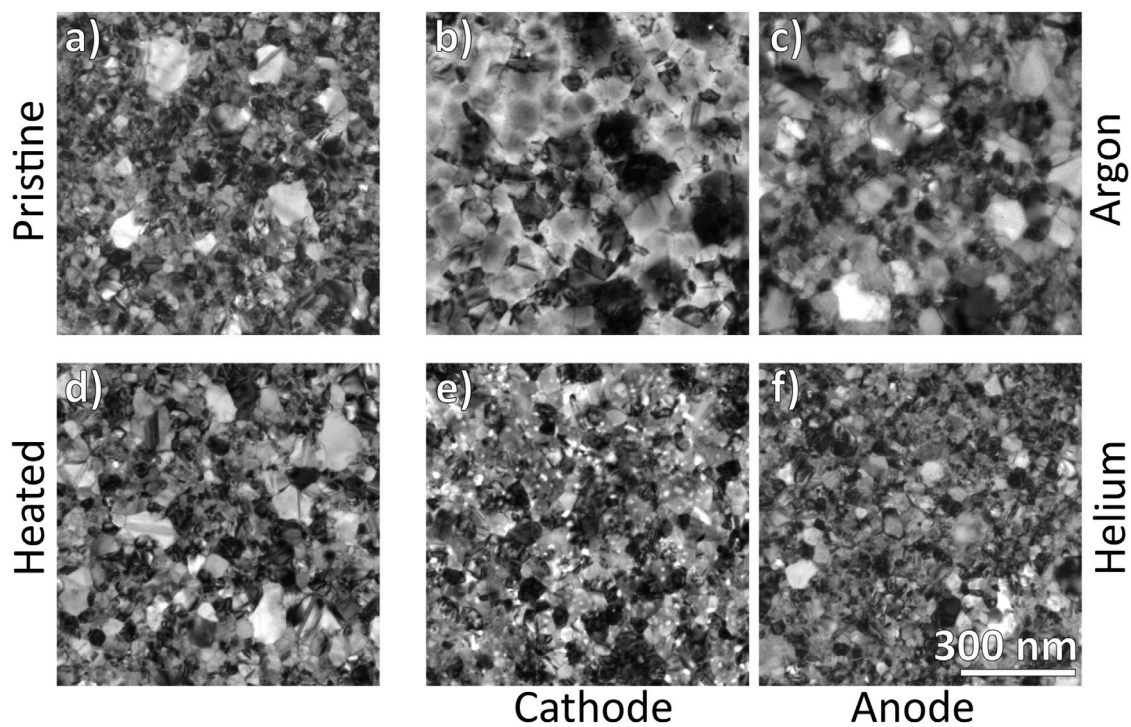


Fig. 6. Bright field TEM micrographs of the gold thin film electrodes. (a) Pristine condition. (b) Cathode after 20 s plasma treatment utilizing Ar as working gas. (c) Anode of the same discharge in Ar. (d) Heated to 150 °C for 10 min. (e) Cathode after 20 s plasma treatment utilizing He as working gas. (f) Anode of the same discharge in He.

which will be discussed in more detail in Section 3.2.3), the rearrangement of the gold atoms seems to take mostly place directly at the surface. This restructuring of the surface being most prominent for the Ar cathode hints to a combination of thermal and ion induced desorption of the gold thin film. While the kinetic energy of the ions is assumed to be comparably low due to the large number of collisions (below 0.1 eV [15]), recombination on the surface can locally release a significant amount of energy (24.6 eV for He or 15.76 eV for Ar, resp.) [13]. Thus, effects of the ions are expected even at atmospheric pressure conditions and are visible here on the micro and nanoscale alike.

3.2.3. Transmission electron microscopy

Insights into the grain structure of the thin films are gained by using bright field TEM and selected area electron diffraction (SAED) to compare to the structure zone diagram as mentioned in the introduction. Fig. 6 shows TEM micrographs of the gold thin film electrodes at the same magnifications after plasma treatment at different conditions. An objective aperture was placed on the non-diffracted beam to increase contrast and reveal the grain boundaries more clearly. In order to obtain the grain size for each sample a small objective aperture was placed on a section of the ring in the diffraction pattern corresponding to the (022) reflection of fcc gold. In the resulting dark field images single

Table 2

Mean grain sizes and their standard deviations determined by TEM dark field imaging of the (022) reflection. The two different regions on the Ar cathode (edge and center) are addressed in the main text in context of Fig. 7. The given error values represent the standard deviation from multiple evaluated grains.

Sample	Grain size/nm
Pristine	14.2 ± 0.4
Heated	16.6 ± 0.7
Ar anode	17.3 ± 0.6
Ar cathode edge	23.3 ± 1.0
Ar cathode center	29.3 ± 2.4
He anode	14.5 ± 0.4
He cathode	17.6 ± 0.6

crystal grains are clearly separated allowing automatic size analysis using the Digital Micrograph 3 suite (Version 3.42.3213, Gatan Inc.). The mean grain diameters as well as the standard deviations are listed in Table 2 for each sample.

In Fig. 6(a) an image of the untreated (pristine) film is presented. One can recognize comparably small, uniformly distributed crystal grains with a mean size G of 14.2 ± 0.4 nm which are formed during the preparation (sputtering) of the Au films. Heating of the thin film alone resulted in a mean grain size of 16.6 ± 0.7 nm and is shown in Fig. 6(d). Fig. 6(b) shows the cathode after Ar operation and Fig. 6(c) the respective anode. Both electrodes for Ar as working gas show increased grain size (anode: $G = 17.3 \pm 0.6$ nm, cathode: $G = 23.3 \pm 1.0$ nm) compared to the as sputtered thin film ($G = 14.2 \pm 0.4$ nm) in Fig. 6(a). Further, the grains on the cathode are significantly larger compared to those on the anode, which corresponds to the energy flux observations of a larger energy flux reaching the cathode. The grain size on the anode is roughly comparable to the heated sample. The cathode shows areas of lowered contrast indicating a smaller amount of material in the direction of the TEM electron beam. The area of increased contrast corresponds to larger local thickness accordingly. For this imaging mode and magnification mass-thickness and diffraction contrast are dominant [35]. Energy-dispersive X-ray spectroscopy (EDXS) shows that after plasma treatment the thin film still consists of pure gold. Combining these considerations it becomes evident, that the low contrast areas correspond to local holes in the gold thin film so that only the Si_3N_4 membrane is left. The area of strongly increased contrast most likely depicts a particle formed during plasma exposition as observed with SEM, see Fig. 5(b).

The He microplasma treated electrodes are shown in Fig. 6(e) (cathode) and 6(f) (anode). Again, differences between the anode and the cathode are visible with increased grain size (anode: $G = 14.5 \pm 0.4$ nm, cathode: $G = 17.6 \pm 0.6$ nm) on the cathode. On the cathode regions of reduced contrast are visible which indicate thinning or even holes within the electrode like for the cathode of the Ar plasma. These areas are much smaller and more evenly distributed in the He case. They are also visible in the surface morphology as observed by SEM (see Fig. 5(e)) here indicated by dark contrast. For the electrodes of the Ar microplasma the holes might be caused by material transfer towards the particles by evaporation or desorption caused by the high energy flux towards the electrode, especially to the cathode. For He the holes might be the result of much more localized desorption hot spots. These hot spots could be caused by ion recombination at the surface, as the recombination energy of He (24.6 eV [13]) surpasses the cohesive energy of gold (approx. 3.2 eV/atom [36]) several times. Both the small size as well as the even distribution of these film defects are in support of recombination as the main reason. The positively charged ions only impacting on the cathode for the case of the DC discharge result in the hot spots only appearing at the cathode. Overall, the anodes show similarity to the heated thin film and the grains of the electrodes operated in He are smaller compared to the Ar treated electrodes. This might indicate again the locally higher energy flux towards the Ar

anode compared to the He electrodes and showcases the challenges given by area normalization as the energy flux to the electrodes during He microplasma operation was determined to be higher as the energy flux to the Ar anode (see Fig. 2).

The TEM micrographs of the Ar and He cathode (Fig. 6(b),(e)) mainly represent the grain structure of the thin film and differ from their SEM counterparts (Fig. 5(b),(e)). This difference is important, as it shows that the SEM indeed reveals changes due to surface morphology and not only related to the grain structure. Of course, the surface morphology is linked to the grain structure, but the SEM contrast is dominated by topological and edge contrast. Therefore, the increase in surface roughness is confirmed again.

As already mentioned an energy flux and, thus, surface modification gradient is assumed to be present within the discharge channel. Results of this gradient were only found on the Ar cathode despite careful analysis of several samples. Fig. 7(a) shows two SEM micrographs stitched together to show the film morphology change from the center of the discharge footprint on the right towards the edge of the visible footprint on the left. In the center of the footprint on the right, holes in the thin film surrounded by a smooth film with large crystal grains are visible. Fig. 7(b) shows a SEM close-up of the central region showcasing the smooth film with its holes. The mean grain size in this region was again determined using the (022) reflections in the TEM dark field and is with $G = 29.3 \pm 2.4$ nm the largest grain size found in the current study (cf. Table 2). A TEM bright field micrograph of this region is shown in Fig. 7(c). The previously shown TEM bright field micrographs in Fig. 6 was taken at the edge of the discharge channel to be best comparable to the He microplasma treated thin films as a complete, sustained thin film is present. The largest grain growths being found in the central region of the discharge footprint confirm the assumed energy flux gradient. Further, holes only being found here are a strong indication of a link between surface desorption and incoming energy flux.

Focusing on the edge of the discharge footprint on the left in Fig. 7(a) particles with diameters of approx. 150 nm on top of the thin film are visible. They do not appear in the central region and their number increases with increasing distance to the central region. To explain this observation the following mechanism is proposed: In the central region Au atoms are desorbed from the surface due to the incoming energy flux which components will be discussed in Section 3.3. The desorbed atoms start to agglomerate quite fast due to the high pressure and charge up negatively while they are growing [37–39], levitating at the edge of the plasma sheaths [40,41]. The temperature gradient within the discharge channel results in a thermophoretic force which pushes the particles outwards [42–44]. As soon as the particles leave the discharge channel the electric field force vanishes and they drop to the cathode surface due to thermophoresis and neutral drag. These forces are supposed to become important, because the cathode was mounted upside down during the experiments, thus, gravity could not play this important role. Particles found between the edge and the central regions in the middle of Fig. 7(a) could either been interrupted in their transport to the edge due to switching off the plasma or due to instabilities in the discharge. The almost uniform size distribution could indicate a self-limiting growth process by, e.g., the acting forces depending on the particle radius a (gravitational force $\propto a^3$, thermophoresis $\propto a^2$ and electric force $\propto a^1$ [40,41]) and, thus, a limited residence time in the discharge channel. Further investigations on the particle formation are beyond the scope of the current work, as the modifications of the thin films is the main topic. Still, evidence of material transport and surface desorption due to the microplasma treatment could be found.

To gain information on the crystal structure of the thin films selected area electron diffraction (SAED) was performed. Fig. 8 shows the reflections corresponding to the different lattice planes of the pristine thin films as well as after microplasma exposure and the annealed electrode. In order to compare the different SAED patterns rotational

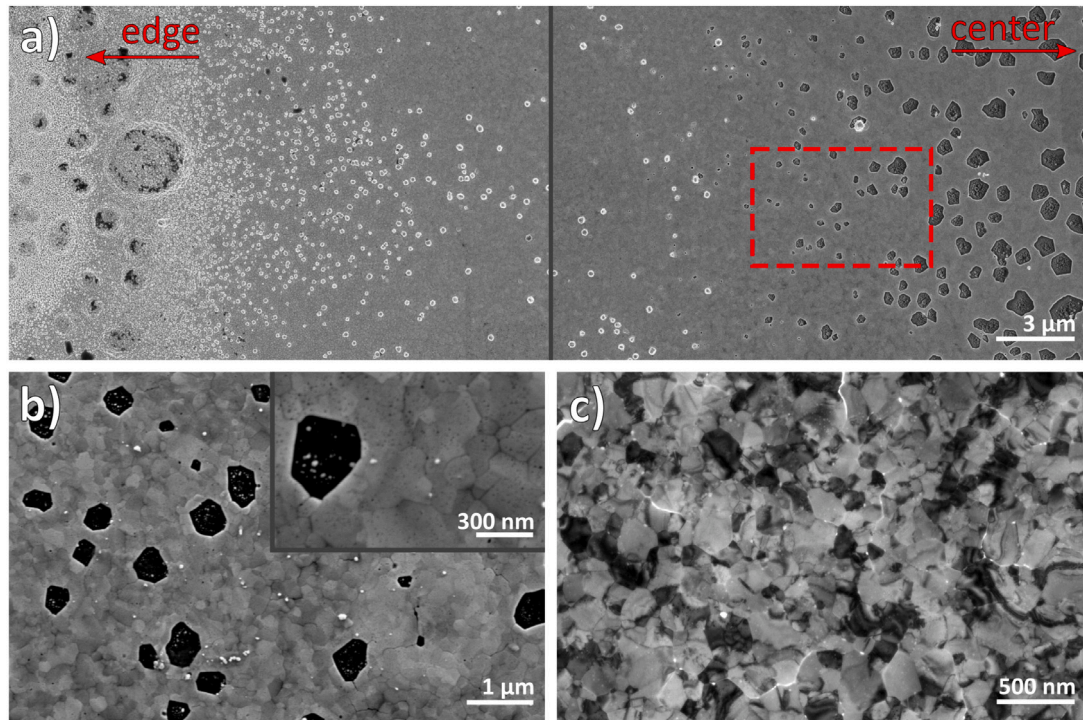


Fig. 7. SEM and TEM investigation of the thin film morphology of the Ar cathode in dependence of the position outwards from the center towards the edge of the discharge footprint. (a) SEM micrograph of the electrode structure with the directions towards the center and edge respectively indicated by arrows. The micrograph consists of two individual images. (b) SEM micrograph of the center region indicated by the dashed rectangle in (a) showing holes in the thin film alongside a smooth film structure with large crystal grains. (c) TEM bright field micrograph (with objective aperture and non-diffracted beam) showing large crystal grains.

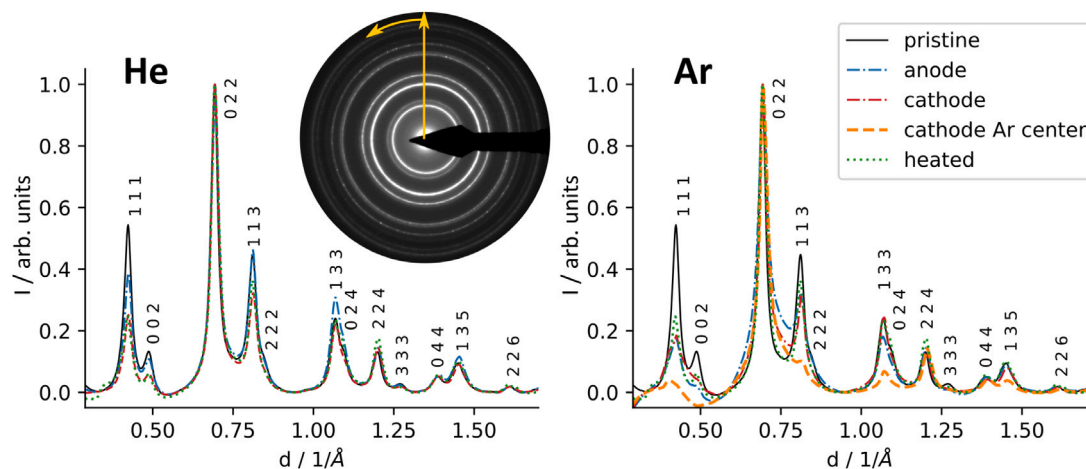


Fig. 8. Electron diffraction investigation of the gold thin film electrodes. The rotational averages of the SAED patterns for both He (left) and Ar (right) plasma exposed electrodes are compared to the pristine as well as annealed electrode. The Ar microplasma treated thin films are shown on the right and show an increase in texturization for both electrodes, but especially in the center of the cathode. On the left the results of the He microplasma treated electrodes are depicted. The increase in texture is not as significant as for Ar yet still clearly present, especially for the cathode.

averages are calculated which describe the angular mean of the intensity profile outwards from the center as indicated by the annotation in the SAED pattern of a pristine thin film electrode. The rotational averages are indexed assuming fcc gold for reference. The SAED investigation confirms the already observed trend of the correlation between the degree of surface modifications and amount of energy flux to the surface. The Ar plasma treated electrodes show a clear intensity shift to the (022) reflection, thus, the gold film becomes more textured. The intensity shift is most pronounced for the central area and varies over the area of the cathode, which was expected from the observed increase in grain size and higher energy flux. For the He microplasma treated electrodes an increase in texture is also visible, albeit less significant.

Here, a clear intensity shift from the (111) and (113) reflections to the (022) plane is only visible for the cathode despite the nearly identical energy flux. Annealing results in a similar degree of texture as the case of the He plasma treated cathode which is in agreement with the mean grain sizes determined by TEM dark field and TEM bright field observations (see Fig. 6). The Ar plasma on the other hand leads to stronger texture for both the anode and cathode alike.

Overall, a direct correlation of high energy flux leading to strong surface modification is not clearly visible. He microplasma treated electrodes show less grain growth and a lower degree of texture compared to the Ar microplasma treated counterparts. With the energy flux towards the He microplasma electrodes being equal or even higher

compared to the Ar microplasma treated anode, larger surface changes were expected. Not fulfilling this expectation can be explained and resolved by the choice of plasma surface contact area for normalization during the PTP evaluation. Most probably higher energy fluxes are present while operating the microplasma in Ar due to a smaller plasma surface contact area. Still, the He microplasma treated anode and cathode receive nearly equally high energy fluxes and should have identical plasma surface contact areas. Thus, the significant differences in the surface morphology observed by the SEM cannot be explained by a faulty area normalization. Ions and their recombination energies are already discussed as explanation attempt. To gain more insight into the power transfer to the electrodes and the role of ions in the surface modification using an atmospheric pressure microplasma a simplified energy balance at the cathode will be postulated.

3.3. Identification of the ion contribution

The described asymmetry (cf. Section 3.1) both in energy flux as well as the degree of surface modification between the anode and cathode can be assigned to ion effects as they are, contrary to, e.g., radiation or metastables, influenced by the polarity of the electric field. Assuming that the difference in the energy flux mainly represents the ion contribution to the cathode, enables the calculation of the so called ion contribution. Identifying the pathways of the power transfer is more complex due to the short mean free paths of ions in the atmospheric pressure regime of the microdischarges operation. Energy gained in the electrical field by the ions will be transferred to non-ionic species via collisions before the ions and the non-ionic species dump the energy into the cathode at some point [22,29,30]. Further, ions can be neutralized due to collisions with secondary electrons in the plasma sheath and subsequently hit the cathode as fast neutrals. In the case of fast neutrals only kinetic energy will be transferred and the recombination energy is not solely gained by the cathode.

An energy balance of the cathode is postulated to check whether ions, and how many, are actually reaching the cathode or get neutralized in the sheaths. First, the power transferred by the ions P_{ion} is defined by the difference of the energy flux to the cathode EF_{Cat} and to the anode EF_{An} multiplied by the thermal probe's substrate area A

$$P_{ion} = (EF_{Cat} - EF_{An}) \times A. \quad (5)$$

The transferred power is divided by the flux of ions per second seemingly reaching the probe (C_{ion}) to be able to set up an energy balance for each ion taking its kinetic E_{kin} and recombination E_{rec} energy into account, as well as energy losses at the cathode due to secondary electron emission $\gamma_{SE}W_{Au}$

$$\frac{P_{ion}}{C_{ion}} = X \times E_{kin} + E_{rec} - \gamma_{SE}W_{Au}, \quad (6)$$

where the scaling factor X , the number of fast neutrals per impinging ion, offers the opportunity for recombination and collisions within the sheaths implying the kinetic energy of ions is transferred to non-ionic species or their recombination energy is not transferred to the cathode. Some of these terms can be directly derived from the experiments, others have to be assumed:

- C_{ion} : The flux of ions per second can be derived from the measured current I under the assumption of singly ionized species, as no higher degrees of ionization were visible in the optical emission spectra [15]. The measured current I has to be separated into the ion current I_{ion} and the electron current I_{el} , $I = I_{ion} + I_{el}$. These currents are connected via the effective secondary electron coefficients $I_{el} = \gamma_{SE}I_{ion}$ and, thus, the ion current can be calculated from the measured current and the previously determined effective secondary electron coefficients $I_{ion} = I / (1 + \gamma_{SE})$ with $\gamma_{SE,Ar} \approx 1.11$ and $\gamma_{SE,He} \approx 1.33$ [15].

$$C_{ion} = \frac{I_{ion}}{e} = \frac{I}{e(1 + \gamma_{SE})}, \quad (7)$$

where e denotes the elementary charge.

- E_{kin} : Is estimated based on a numerically calculated collision-based model similar as in [15]. The electric field E of the capacitor-like discharge is given by the measured voltage V and the electrode distance d , $E = V/d$, which accelerates the ions with an acceleration $a = (Ee)/m_{ion}$, where m_{ion} denotes the respective ion mass. Ion velocity and traveled distance are updated in femtosecond time steps. If the traveled distance overcomes the respective mean free paths the kinetic energy E_{kin} is reduced by 50 % as a collision is assumed. Thus, the velocity drops and the ion is accelerated again. Kinetic energy $E_{ion,kin}$ and ion velocity reaching saturation after a few iterations and a traveled distance below $1 \mu m$. The mean kinetic energy E_{kin} of the saturation regime is used for the energy balance. It should be noted, these estimations for $E_{ion,kin}$ are maximum values.
- E_{rec} : Recombination energies of Ar (15.76 eV) or He (24.6 eV) are available in literature [13].
- W_{Au} : The work function of the gold film is assumed to be $W_{Au} = 5.38$ eV based on the mean value over the three crystallographic planes given in [34]. The kinetic energy of electrons leaving the surface is neglected here.

Rearranging Eq. (6) and substituting the addressed terms results in

$$X = \frac{(EF_{Cat} - EF_{An}) Ae(1 + \gamma_{SE}) - E_{rec}I + \gamma_{SE}W_{Au}I}{E_{kin}I}. \quad (8)$$

Based on the results for X and the measured or assumed quantities additional parameters such as the total flux of particles impacting the surface per second C_{total} , the ion and fast neutral momentum and the resulting total force on the surface can be derived. The momentum p is calculated from the respective kinetic energies of the ions or fast neutrals E_{kin} via $p = \sqrt{2 * E_{kin}/m_{ion}}$. Multiplication of the momentum p with the flux of impacting particles per second C_{total} results in the force F to the surface. These parameters were derived as they might provide insight on the importance of a kinetic component for the plasma surface interaction at atmospheric pressure and will be shortly discussed in Section 3.4.

The derived parameters and assumed inputs are listed in Table 3 and will be discussed together with the measured ion contribution of the energy flux and its calculated contributions shown in Fig. 9. For the calculation of the contributions the different energy terms on the left of Eq. (6) are multiplied by C_{ion} . The given errors result from Gaussian error propagation of the standard deviation from the performed measurements. First off, a significantly larger ion contribution (40 ± 10 mW compared to 6 ± 6 mW) is found for operating the microplasma in Ar. This was already discussed in Section 3.1 and is most probably a result of the He metastable formation [33]. For Ar as working gas the derived parameters seem reasonable. An X value of 1304 ± 703 indicates 1304 fast neutrals with kinetic energy gained by collisions with ions reach the cathode per impinging ion. This value has to be seen as lower limit, as more particles each with less kinetic energy could also reach the cathode. Nevertheless, this does not change the overall transferred kinetic energy and momentum. The power transfer via kinetic energy P_{kin} being the largest contribution despite the low kinetic energy of the ions and fast neutrals due to the collisions results of the large amount of impacting particles. Recombination of ions on the surface also transfers power to the cathode. During the recombination process a nearly three orders of magnitude larger amount of energy is locally transferred to the surface. The more localized power transfer due to recombination could result in uneven surface modification with local hot spots as seen for the He cathode in Fig. 6. The secondary electron emission was introduced as power loss term in Eq. (6) and should not be underestimated despite the atmospheric pressure conditions and low kinetic energies.

For He as working gas the oversimplifications of this approach become visible. The negative X value of -187 ± 123 results from the necessity to emit power from the cathode as the incoming power of

Table 3

Summary of measured or assumed parameters used for solving Eq. (6). The momentum was deduced from the kinetic energy.

	Ar	He
E_{kin}/eV	0.024	0.056
E_{rec}/eV	15.76	24.6
W_{Au}/eV	5.38	5.38
X	1304 ± 703	-187 ± 123
$C_{ion}/1/\text{s}$	$(6.0 \pm 0.5) \times 10^{15}$	$(5.6 \pm 0.2) \times 10^{15}$
$C_{total}/1/\text{s}$	$(8 \pm 4) \times 10^{18}$	$(-1.1 \pm 0.7) \times 10^{18}$
p/Ns	$(2.3 \pm 0.1) \times 10^{-21}$	$(1.1 \pm 0.1) \times 10^{-21}$
$F/\mu\text{N}$	178 ± 98	-11 ± 8

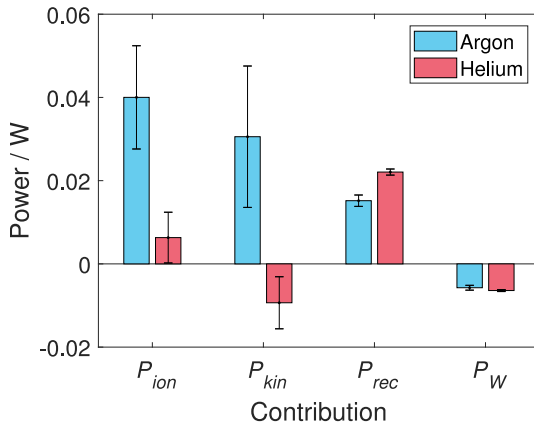


Fig. 9. The difference P_{ion} between power transferred to the cathode and the anode assumed to be mainly caused by ions. As introduced in the main text the ion contribution is separated into its components (P_{kin} = power transferred via kinetic energy, P_{rec} = power transferred due to recombination, and P_W = power lost due to secondary electron emission), which are differently pronounced due to the working gas. The shown error bars represent Gaussian error propagation of standard deviations from multiple measurements.

ion recombination already surpasses the addition of the determined ion power P_{ion} and the power losses due to secondary electron emission P_W . Thus, the flux of incoming particles C_{total} becomes negative as well as the kinetic power contribution P_{kin} . These errors indicate false assumptions or missing contributions in the power balance. A strong assumption was the equal power distribution of all non-ionic species and radiation to both electrodes, except of fast neutrals which got accelerated by ion collisions. For He a more favorable formation and carrying of metastables towards one of the electrodes could falsify this assumption. The presented results hint to an asymmetric power transfer via metastables favoring the anode but simulations on a similar setup showed quite symmetric metastable densities with a slight shift towards the cathode [33]. Asymmetric radiation distribution favoring the anode could also explain the problem of the assumptions used here. Radiation leaving the microplasma through the Kapton spacer was detected in previous work and showed an asymmetry with more radiation being generated on the cathode side [15]. But due to the geometry with large electrodes compared to the interelectrode distance this asymmetry probably only plays a minor role and would also favor the cathode and not the anode. On the other hand, generated radiation, which leaves the discharge through the Kapton spacer, is an unaccounted power loss term. Thus, power of the discharge could be transformed into radiation and not stored in particles which would most probably at some point interact with the surface. Regions of high optical plasma emission intensity would mark areas with larger power losses which would actually result in an asymmetric power transfer favoring the anode. Previous results showed a similar, even stronger, radiation mismatch using Ar as working gas [15]. A stronger mismatch without visible influence within the proposed power balance at the cathode indicates

only a small effect of this possible asymmetric radiation power loss term.

A more probable possibility for the failure of the here suggested power balance of the cathode for He could be a missing power loss term with a significant contribution to the power balance. In Section 3.2.3 the possibility of Au desorption spots as a result of the ion recombination was discussed in context of the TEM micrographs. The ion recombination leads to local heating of the thin film, which could result in local atom evaporation and, therefore, surface desorption. If this desorption occurs gold atoms would leave the surface each causing an energy loss at the cathode of approx. 3.2 eV/atom [36], at least if no significant kinetic energy of the atoms is assumed. Including this desorption term in the simplified power balance (Eq. (6)) is problematic due to the necessity of a proportionality factor similar to X scaling the desorbed atoms per ion. Thus, a modified version of the power balance (Eq. (6)) would not have a distinct solution without even further assumptions.

Despite the impossibility of solving a modified power balance, a short plausibility check for the desorption power loss term is given here by assuming two values for X . The chosen values are $X = 1$ and $X = 1304$, which correspond to no fast neutrals reaching the cathode or the same amount of fast neutrals as for the Ar microplasma are reaching the cathode. These assumed values should result in a lower and an upper limit for the power lost by surface desorption.

Eq. (6) is modified by the cohesive energy of Au E_{coh} and its proportionality factor D , the number of desorbed atoms per incoming ion,

$$\frac{P_{ion}}{C_{ion}} = X \times E_{kin} + E_{rec} - \gamma_{SE} W_{Au} - D \times E_{coh}. \quad (9)$$

First, X is set to 1 to emulate no fast neutrals reaching the cathode. This approach should result in the lowest possible Au atom desorption per incident ion. Solving Eq. (9) for D and applying the values given in Table 3 in addition for $X = 1$ results in $D = 3.3 \pm 2.1$. Thus, three gold atoms per incident ion are released from the surface due to the transferred energy. Of course, these released atoms are not allowed to adsorb again on the surface, as this process would contribute to the energy balance. Au was detected on the edge of the Kapton spacer, which shows the possibility of permanent leaving the cathode. Within the current work it was not possible to determine mass transfer pathways, although a partial thinning and removal of the cathode was observed. Revealing where the Au material from the cathode actually is deposited again has to be done in future work.

For the second case X is assumed to be 1304, the value calculated for the Ar microplasma. Here, D results in 26 ± 13 . In this case each ion would release 26 atoms from the surface, which seems too large, as $26 \times 3.2 \text{ eV}$ equals 83.2 eV and, thus, surpasses the recombination energy of He by over three times. Still, due to the normalization to incident ions and 1304 fast neutrals per ion transferring their kinetic energy to the surface, the overall transferred energy would be sufficient.

The resulting power contributions for both cases are shown in Fig. 10. As expected, the kinetic contribution completely differs based on the assumed X value. Thus, also the necessary power loss due to desorption increases. Depending on the dominance of a single contribution the treated surface could change. If the kinetic component dominates the power should be evenly distributed across the surface, as a lot of particles only transmit a small amount of power. If the recombination component is the main power transfer, less incident particles transmit a large amount of power, thus, local difference on the surface could be visible. These local differences visible in the TEM micrographs (Fig. 6) hint to a power transfer dominated by the recombination energy.

Applying the extended cathode power balance to the Ar data would just increase the dominance of the kinetic contribution, as the power losses due to desorption have to be compensated by the kinetic component. Following the argument made before, the dominating kinetic contribution should result in an evenly distributed effect of the Ar

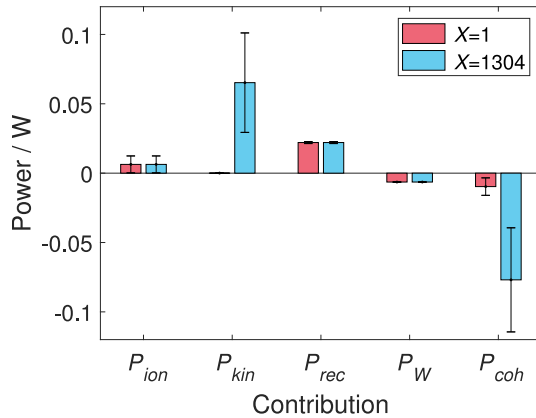


Fig. 10. The positive and negative power contributions to the total ion power P_{ion} for He as working gas using the extended power balance shown in Eq. (9) taking desorption from the surface into account. Two extreme cases of only ions and no fast neutrals reaching the cathode ($X = 1$) and 1304 fast neutrals per ion reaching the surface as determined for Ar as working gas ($X = 1304$). The shown error bars represent Gaussian error propagation of standard deviations from multiple measurements.

microplasma surface treatment. Comparing the TEM pictures of the Ar cathode (Fig. 6(c)) with the He cathode (Fig. 6(f)) a more uniform grain structure is visible. Yet, in the case of the Ar cathode the surface roughness increases the most (Fig. 5(b)). The feature size is, however, still larger than for the He anode with the grains forming almost a continuous film. Thus, this morphology might origin from local melting of the thin film caused by the overall higher energy influx [45]. With the total difference in energy flux towards the cathodes only being less than 25% the composition of the energy flux towards the surface has to play an important role for the resulting, modified surface, despite the atmospheric pressure conditions and low kinetic energies.

3.4. Momentum transfer and temperature

For the assumptions made and based on the collision-dominated numerical model the momentum of the ions can be calculated, as well as the overall transferred momentum acting as a force on the cathode (see Table 3). For He the force was calculated negative, due to the negative X value as discussed before. Again, setting $X = 1$ results in $F = 61 \pm 4$ nN which should represent the minimal force onto the surface. As expected, the momentum of the incident ions or fast neutrals is quite low due to the large number of collisions. Further, due to their mass, Ar ions or fast neutrals gain a larger momentum despite having a lower kinetic energy compared to He species.

In low pressure plasmas the momentum transfer plays a key role for surface modifications as, e.g. sputtering, can alter the surface [46–54]. The resulting force to the cathode of the Ar microplasma is actually in the same order of magnitude as ion beams used for ion beam sputtering, but only due to the large amount of particles impinging on the surface [55–58]. The momentum of a single impacting particle should not be sufficient to create a collision cascade within the Au film, thus, sputtering as a mechanism to change the surface is extremely unlikely at these atmospheric pressure conditions.

In the He microplasma the calculated number of incident particles and momentum per particle is lower compared to the Ar case. Here, the resulting force in the nN-range should not have any significant effects. Still, the number of incident particles and the calculated force are a lower limit and, similar to the Ar conditions, with the current state of work, surface modifications, at least favored by the momentum exchange, cannot be fully excluded. In future work variation of the working gas to change the particle mass and choosing comparable experimental conditions in regards to the current density could help to clarify this issue.

Table 4

Temperature of the passive thermal probes (PTPs) after 10 s of heating (plasma on). The temperatures over time curves already slowly reached saturation, still these temperatures are not exactly comparable to the Au film temperature after 20 s of plasma treatment and should only be seen as indicators for the order of Au film temperatures. The given error values represent the standard deviation from multiple measurements and temperature fluctuations in the data acquisition.

	Ar	He
Anode	$80 \pm 3^\circ\text{C}$	$58 \pm 3^\circ\text{C}$
Cathode	$100 \pm 3^\circ\text{C}$	$61 \pm 3^\circ\text{C}$

Another import aspect for the growth or modification of thin films is the surface temperature of the film, which is usually the second axis in addition to the energy flux in structure zone diagrams (SZDs). During these experiments Au films were not set to a fixed temperature and, thus, only heated due to the plasma treatment, similar as the PTPs during the energy flux measurements. A direct comparison of the temperatures is not suitable due to the different heat capacities of the PTPs and the Au coated TEM grids, the different treatment times, and different thermal connections cooling the samples. Still, the PTP temperatures after 10 s of heating are given in Table 4. The temperatures partly reflect the energy fluxes and their ordering (highest temperature Ar cathode, lowest He anode) can be supposed also for the Au thin film treatment.

A comparison between the plasma treated Au films and a purely heated one was given in the TEM images (Fig. 6). As already mentioned clear differences between the annealed sample (Fig. 6(d)) and the cathodes of both plasma treated samples (Fig. 6(c) and (f)) were visible. Additionally the increase on surface roughness observed by SEM (Fig. 5) is not present in the case of annealing alone. These differences were addressed to plasma generated species and their kinetic (momentum) as well as recombination energy. The microplasma treated anodes (Fig. 6(b) and (e)) show similarities with the heated sample where from SEM investigation modification of the surface morphology can also be seen for the Ar case. With the anode not being exposed to ion or fast neutral bombardment heating seems to be the driving force behind the grain growth and the increased crystallographic texturization. The anode in Ar operation shows a larger effect and reaches a higher temperature, despite receiving a lower energy flux (Fig. 2) if the energy flux is normalized towards the full accessible area. This fact once again shows the difficulty of the area normalization. Normalizing towards the observed area results in the anode for Ar operation receiving a larger energy flux than for the anode in He operation, which would fit the observed surface changes.

The Ar microplasma treated anode showing a larger change in surface topology/morphology than the anode in He plasma indicates that the effect of He metastables on the surface might be small, which is interesting as He metastables have a high excitation energy in the range of 20 eV and can reach the anode. The absence of a kinetic component while metastables reach the surface could be a reason for this rather unexpected observation and would showcase the importance of momentum transfer even at atmospheric pressure. Within the current work, it is not possible to evaluate the isolated effect of metastables as, e.g., the surface temperature can also influence the surface changes. Still, the present results show that there is a possible synergistic effect between transferred energy and momentum. To gain a better understanding of the surface processes additional experiments and simulations would be necessary, which are however beyond the scope of the current work.

4. Summary and outlook

The modification of polycrystalline thin film Au electrodes caused by the plasma surface interaction of an atmospheric pressure DC microplasma operated in Ar and He, respectively, was investigated in

detail and correlated with the energy flux from the plasma to the thin film. Observations on the structure of the thin films confirmed previous plasma diagnostics of the used DC microplasma highlighting the connection between plasma diagnostics and surface modifications [15]. Clear correlations between the integral energy flux to the thin film and the thin film modifications could be shown. As expected, the general idea of higher energy fluxes resulting in more textured films with larger crystal grains postulated by structure zone diagrams (SZDs) mainly used for low pressure deposition processes also holds true for atmospheric pressure thin film modification.

The ion component of the integral energy flux was identified as most important by assuming that the difference in energy flux between anode and cathode is mainly caused by the ions. Ar as working gas resulted in a significantly higher ion contribution compared to He which was explained by the input power being used for the production of He metastables. The composition of the power transferred by ions to the cathode significantly changes based on the working gas. For Ar the main power transfer is given by the kinetic contribution of ions and fast neutrals despite their individual low kinetic energy due to the large number of collisions at atmospheric pressure. Thus, the power is transferred in a lot of small doses, resulting in an more uniform surface modification. For He the main power transfer was identified to be the ion recombination at the surface. The simplified power balance at the cathode had to be extended by a surface desorption term as otherwise a negative kinetic contribution had to be accepted. Surface desorption was already indicated by visible Au I lines in previously taken optical emission spectra [15] and its effect is also visible in the here discussed surface diagnostics and Au coatings on the edge of the Kapton spacer. The observed desorption hot spots on the cathode in He plasma operation fit the determined composition of the ion contribution as the power is mainly transferred by ion recombination at the surface and, thus, is transferred in fewer, high energetic doses resulting in a less evenly distributed surface modification.

The surface modifications of the microplasma treated anodes show similarities to the annealed sample, indicating heating of the surface as the main cause of surface changes. The He microplasma treated anode showing a less significant change compared to the annealed or Ar microplasma treated anode indicates that He metastables only play a minor role for the surface modification. The significant differences between the anodes and cathodes showcase the importance of ions in atmospheric pressure microplasmas for surface modifications. Further, the significant differences despite nearly equal integral energy fluxes and temperatures also hint towards the importance of a momentum transfer, despite the low momentum of individual particles compared to low pressure plasmas. The total force acting on the cathode during Ar operation is actually comparable with forces generated by low pressure ion beams, as the particle density is high enough to compensate the low individual momentum.

Assigning a position in the typical landscape of structure zone diagrams to the treated thin film electrodes is difficult. The characteristics observed here like increase of grain size combined with local formation of pores (holes) cannot be matched to the typical zones presented in the diagrams. Still, the general idea that temperature and energy flux need to be considered separately applies, since the non-thermal character of the process is obvious. Our findings reveal that it is necessary to distinguish further and possibly expand the model of structure zone diagrams by creating separate SZDs in the case of different dominant pathways of energy transfer such as ions, metastables, fast neutrals and recombination events.

The observed surface modifications will be used as benchmarks for the intended *in situ* experiments planned for the near future. The integration of the microplasma into the TEM will enable time-resolved measurements as well as direct spot-wise comparison of the changing thin films. The upcoming *in situ* microplasma cell in combination with additional working gases and film materials will help to gain further insight into the plasma surface interaction.

CRediT authorship contribution statement

Luka Hansen: Conceptualization, Methodology, Investigation, Formal analysis, Visualization, Writing – original draft. **Niklas Kohlmann:** Methodology, Investigation, Resources, Formal analysis, Visualization, Writing – original draft. **Lorenz Kienle:** Writing – review & editing, Supervision, Funding acquisition. **Holger Kersten:** Conceptualization, Writing – review & editing, Supervision, Funding acquisition.

Declaration of competing interest

The authors declare that they have no known competing financial interests or personal relationships that could have appeared to influence the work reported in this paper.

Data availability

Data will be made available on request.

Acknowledgments

Funding of the German Research Foundation (DFG, Project Number 413664940, Grant Number KE 574/8-1 and KI 1263/17-1) and Kiel Nano, Surface and Interface Science (KINSIS) is gratefully acknowledged.

References

- [1] B.A. Movchan, A.V. Demchishin, Structure and properties of thick condensates of nickel, titanium, tungsten, aluminum oxides, and zirconium dioxide in vacuum, *Fiz. Metal. Metalloved.* 653-60 28 (1969) URL <https://www.osti.gov/biblio/4181669>.
- [2] J.A. Thornton, Influence of apparatus geometry and deposition conditions on the structure and topography of thick sputtered coatings, *J. Vac. Sci. Technol.* 11 (4) (1974) 666–670, <http://dx.doi.org/10.1116/1.1312732>.
- [3] P.B. Barna, M. Adamik, Fundamental structure forming phenomena of polycrystalline films and the structure zone models, *Thin Solid Films* 317 (1–2) (1998) 27–33, [http://dx.doi.org/10.1016/S0040-6090\(97\)00503-8](http://dx.doi.org/10.1016/S0040-6090(97)00503-8).
- [4] A. Anders, A structure zone diagram including plasma-based deposition and ion etching, *Thin Solid Films* 518 (15) (2010) 4087–4090, <http://dx.doi.org/10.1016/j.tsf.2009.10.145>.
- [5] R.F. Bunshah, *Handbook of Deposition Technologies for Films and Coatings: Science, Technology, and Applications*, second ed., William Andrew, 1994, <https://www.worldcat.org/isbn/9780815517467>.
- [6] D.M. Mattox, *Handbook of Physical Vapor Deposition (PVD) Processing*, William Andrew, 2010, <http://dx.doi.org/10.1016/C2009-0-18800-1>.
- [7] A. Anders, *Cathodic Arcs: From Fractal Spots to Energetic Condensation*, first ed., in: Springer Series on Atomic, Optical, and Plasma Physics, vol. 50, Springer, New York, NY, 2008, <http://dx.doi.org/10.1007/978-0-387-79108-1>.
- [8] K.H. Becker, K.H. Schoenbach, J.G. Eden, Microplasmas and applications, *J. Phys. D: Appl. Phys.* 39 (3) (2006) R55–R70, <http://dx.doi.org/10.1088/0022-3727/39/3/r01>.
- [9] J. Franzke, C. Meyer, S. Müller, T. Krähling, A. Michels, Microdischarges for analytical atomic spectrometry: Design considerations and applications, in: R. Meyers, R. Meyers (Eds.), *Encyclopedia of Analytical Chemistry*, John Wiley & Sons, Ltd, 2011, <http://dx.doi.org/10.1002/9780470027318.a9187>.
- [10] F. Iza, G.J. Kim, S.M. Lee, J.K. Lee, J.L. Walsh, Y.T. Zhang, M.G. Kong, Microplasmas: Sources, particle kinetics, and biomedical applications, *Plasma Process. Polym.* 5 (4) (2008) 322–344, <http://dx.doi.org/10.1002/ppap.200700162>.
- [11] R.H. Stark, K.H. Schoenbach, Direct current high-pressure glow discharges, *J. Appl. Phys.* 85 (4) (1999) 2075–2080, <http://dx.doi.org/10.1063/1.369505>.
- [12] F. Paschen, Ueber die zum Funkenuebergang in Luft, Wasserstoff und Kohlensäure bei verschiedenen Druecken erforderliche Potentialdifferenz, *Ann. Physics* 273 (5) (1889) 69–96, <http://dx.doi.org/10.1002/andp.18892730505>.
- [13] M.A. Lieberman, A.J. Lichtenberg, *Principles of Plasma Discharges and Materials Processing*, second ed., John Wiley & Sons, Inc. 2005, <http://dx.doi.org/10.1002/0471724254>.
- [14] Y.P. Raizer, *Gas Discharge Physics*, Springer Berlin Heidelberg, 2011, URL <https://www.worldcat.org/isbn/364264760X>.
- [15] L. Hansen, N. Kohlmann, U. Schürmann, L. Kienle, H. Kersten, Conventional and non-conventional diagnostics of a stable atmospheric pressure DC normal glow microplasma discharge intended for *in situ* TEM studies, *Plasma Sources. Sci. Technol.* 31 (2022) 035013, <http://dx.doi.org/10.1088/1361-6595/ac5101>.

- [16] J.A. Thornton, Substrate heating in cylindrical magnetron sputtering sources, *Thin Solid Films* 54 (1) (1978) 23–31, [http://dx.doi.org/10.1016/0040-6090\(78\)90273-0](http://dx.doi.org/10.1016/0040-6090(78)90273-0).
- [17] H. Kersten, D. Rohde, J. Berndt, H. Deutsch, R. Hippler, Investigations on the energy influx at plasma processes by means of a simple thermal probe, *Thin Solid Films* 377–378 (2000) 585–591, [http://dx.doi.org/10.1016/S0040-6090\(00\)01442-5](http://dx.doi.org/10.1016/S0040-6090(00)01442-5).
- [18] S. Bornholdt, T. Peter, T. Strunskus, V. Zaporozhchenko, F. Faupel, H. Kersten, The method of conventional calorimetric probes — A short review and application for the characterization of nanocluster sources, *Surf. Coat. Technol.* 205 (2011) S388–S392, <http://dx.doi.org/10.1016/j.surfcoat.2011.03.079>.
- [19] S. Bornholdt, M. Fröhlich, H. Kersten, Calorimetric probes for energy flux measurements in process plasmas, in: M. Bonitz, J. Lopez, K. Becker, H. Thomsen (Eds.), *Complex Plasmas*, in: Springer Series on Atomic, Optical, and Plasma Physics, Springer International Publishing, 2014, pp. 197–234, http://dx.doi.org/10.1007/978-3-319-05437-7_6.
- [20] T. Kewitz, M. Fröhlich, J. von Frieling, H. Kersten, Investigation of a commercial atmospheric pressure plasma jet by a newly designed calorimetric probe, *IEEE Trans. Plasma Sci.* 43 (5) (2015) 1769–1773, <http://dx.doi.org/10.1109/tps.2015.2420679>.
- [21] L. Rosenfeldt, L. Hansen, H. Kersten, The use of passive thermal probes for the determination of energy fluxes in atmospheric pressure plasmas, *IEEE Trans. Plasma Sci.* 49 (11) (2021) 3325–3335, <http://dx.doi.org/10.1109/tps.2021.3092752>.
- [22] H. Kersten, H. Deutsch, H. Steffen, G.M.W. Kroesen, R. Hippler, The energy balance at substrate surfaces during plasma processing, *Vacuum* 63 (3) (2001) 385–431, [http://dx.doi.org/10.1016/S0042-207X\(01\)00350-5](http://dx.doi.org/10.1016/S0042-207X(01)00350-5).
- [23] S. Gauter, F. Haase, H. Kersten, Experimentally unraveling the energy flux originating from a DC magnetron sputtering source, *Thin Solid Films* 669 (2019) 8–18, <http://dx.doi.org/10.1016/j.tsf.2018.10.021>.
- [24] L. Hansen, L. Rosenfeldt, K.A. Reck, H. Kersten, Understanding the energy balance of a surface barrier discharge for various molecular gases by a multi-diagnostic approach, *J. Appl. Phys.* 129 (5) (2021) 053308, <http://dx.doi.org/10.1063/5.0035671>.
- [25] L. Hansen, B.M. Goldberg, D. Feng, R.B. Miles, H. Kersten, S. Reuter, Energy transfer in interaction of a cold atmospheric pressure plasma jet with substrates, *Plasma Sources. Sci. Technol.* 30 (4) (2021) 045004, <http://dx.doi.org/10.1088/1361-6595/abe955>.
- [26] K. Tai, T.J. Houlahan, J.G. Eden, S.J. Dillon, Integration of microplasma with transmission electron microscopy: Real-time observation of gold sputtering and island formation, *Sci. Rep.* 3 (1) (2013) <http://dx.doi.org/10.1038/srep01325>.
- [27] J. Benedikt, H. Kersten, A. Piel, Foundations of measurement of electrons, ions and species fluxes toward surfaces in low-temperature plasmas, *Plasma Sources. Sci. Technol.* 30 (3) (2021) 033001, <http://dx.doi.org/10.1088/1361-6595/abe4bf>.
- [28] M. Stahl, T. Trottenberg, H. Kersten, A calorimetric probe for plasma diagnostics, *Rev. Sci. Instrum.* 81 (2) (2010) 023504, <http://dx.doi.org/10.1063/1.3276707>.
- [29] K.S. Suraj, S. Mukherjee, Effect of ion neutral collisions on the ion and neutral velocity distribution on negatively biased electrodes, *Surf. Coat. Technol.* 196 (1–3) (2005) 267–270, <http://dx.doi.org/10.1016/j.surfcoat.2004.08.101>.
- [30] T.E. Sheridan, J. Goree, Collisional plasma sheath model, *Phys. Fluids B* 3 (10) (1991) 2796–2804, <http://dx.doi.org/10.1063/1.859987>.
- [31] T. Trottenberg, T. Richter, H. Kersten, Measurement of the force exerted on the surface of an object immersed in a plasma, *Eur. Phys. J. D* 69 (3) (2015) <http://dx.doi.org/10.1140/epjd/e2015-50743-2>.
- [32] S. Arumugam, P. Alex, S.K. Sinha, Effective secondary electron emission coefficient in DC abnormal glow discharge plasmas, *Phys. Plasmas* 24 (11) (2017) 112106, <http://dx.doi.org/10.1063/1.4997622>.
- [33] P.S. Kothnur, X. Yuan, L.L. Raja, Structure of direct-current microdischarge plasmas in helium, *Appl. Phys. Lett.* 82 (4) (2003) 529–531, <http://dx.doi.org/10.1063/1.1540246>.
- [34] W. Haynes, *CRC Handbook of Chemistry and Physics: A Ready-Reference Book of Chemical and Physical Data*, CRC Press, Boca Raton, Florida, 2017, URL <https://www.worldcat.org/isbn/9781498754293>,
- [35] D.B. Williams, C.B. Carter, *Transmission Electron Microscopy*, second ed., Springer-Verlag GmbH, 2009, <http://dx.doi.org/10.1007/978-0-387-76501-3>.
- [36] C. Wang, H. Wang, T. Huang, X. Xue, F. Qiu, Q. Jiang, Generalized-stacking-fault energy and twin-boundary energy of hexagonal close-packed Au: A first-principles calculation, *Sci. Rep.* 5 (1) (2015) <http://dx.doi.org/10.1038/srep10213>.
- [37] D. Mariotti, R.M. Sankaran, Microplasmas for nanomaterials synthesis, *J. Phys. D: Appl. Phys.* 43 (32) (2010) 323001, <http://dx.doi.org/10.1088/0022-3727/43/32/323001>.
- [38] T. Peter, M. Wegner, V. Zaporozhchenko, T. Strunskus, S. Bornholdt, H. Kersten, F. Faupel, Metal/polymer nanocomposite thin films prepared by plasma polymerization and high pressure magnetron sputtering, *Surf. Coat. Technol.* 205 (2011) S38–S41, <http://dx.doi.org/10.1016/j.surfcoat.2010.12.045>.
- [39] U.R. Kortshagen, R.M. Sankaran, R.N. Pereira, S.L. Girshick, J.J. Wu, E.S. Aydil, Nonthermal plasma synthesis of nanocrystals: Fundamental principles, materials, and applications, *Chem. Rev.* 116 (18) (2016) 11061–11127, <http://dx.doi.org/10.1021/acs.chemrev.6b00039>.
- [40] M.S. Barnes, J.H. Keller, J.C. Forster, J.A. O'Neill, D.K. Coultas, Transport of dust particles in glow-discharge plasmas, *Phys. Rev. Lett.* 68 (3) (1992) 313–316, <http://dx.doi.org/10.1103/physrevlett.68.313>.
- [41] A. Piel, *Plasma Physics*, first ed., Springer Berlin Heidelberg, 2010, <http://dx.doi.org/10.1007/978-3-642-10491-6>.
- [42] L. Talbot, R.K. Cheng, R.W. Schefer, D.R. Willis, Thermophoresis of particles in a heated boundary layer, *J. Fluid Mech.* 101 (4) (1980) 737–758, <http://dx.doi.org/10.1017/s0022112080001905>.
- [43] G.M. Jellum, D.B. Graves, Particle-plasma interactions in low-pressure discharges, *Appl. Phys. Lett.* 57 (20) (1990) 2077–2079, <http://dx.doi.org/10.1063/1.103946>.
- [44] O. Havnes, T. Nitter, V. Tsytovich, G.E. Morfill, T. Hartquist, On the thermophoretic force close to walls in dusty plasma experiments, *Plasma Sources. Sci. Technol.* 3 (3) (1994) 448–451, <http://dx.doi.org/10.1088/0963-0252/3/3/031>.
- [45] M. Wolter, I. Levchenko, H. Kersten, K. Ostrikov, Hydrogen in plasma-nanofabrication: Selective control of nanostructure heating and passivation, *Appl. Phys. Lett.* 96 (13) (2010) 133105, <http://dx.doi.org/10.1063/1.3374324>.
- [46] H. Oechsner, Sputtering—a review of some recent experimental and theoretical aspects, *Appl. Phys.* 8 (3) (1975) 185–198, <http://dx.doi.org/10.1007/bf00896610>.
- [47] P. Sioshansi, Ion beam modification of materials for industry, *Thin Solid Films* 118 (1) (1984) 61–72, [http://dx.doi.org/10.1016/0040-6090\(84\)90106-8](http://dx.doi.org/10.1016/0040-6090(84)90106-8).
- [48] J.J. Cuomo, S.M. Rossmagel, H.R. Kaufman, *Handbook of Ion Beam Processing Technology*, 1989, URL <https://www.osti.gov/biblio/6950203>.
- [49] G.K. Wolf, Modification of mechanical and chemical properties of thin films by ion bombardment, *Surf. Coat. Technol.* 43–44 (1990) 920–935, [http://dx.doi.org/10.1016/0257-8972\(90\)90032-8](http://dx.doi.org/10.1016/0257-8972(90)90032-8).
- [50] F.A. Smidt, Use of ion beam assisted deposition to modify the microstructure and properties of thin films, *Int. Mater. Rev.* 35 (1) (1990) 61–128, <http://dx.doi.org/10.1179/095066090790323975>.
- [51] H. Randhawa, Review of plasma-assisted deposition processes, *Thin Solid Films* 196 (2) (1991) 329–349, [http://dx.doi.org/10.1016/0040-6090\(91\)90377-a](http://dx.doi.org/10.1016/0040-6090(91)90377-a).
- [52] I. Safi, Recent aspects concerning DC reactive magnetron sputtering of thin films: a review, *Surf. Coat. Technol.* 127 (2–3) (2000) 203–218, [http://dx.doi.org/10.1016/S0257-8972\(00\)00566-1](http://dx.doi.org/10.1016/S0257-8972(00)00566-1).
- [53] K. Sarakinos, J. Alami, S. Konstantinidis, High power pulsed magnetron sputtering: A review on scientific and engineering state of the art, *Surf. Coat. Technol.* 204 (11) (2010) 1661–1684, <http://dx.doi.org/10.1016/j.surfcoat.2009.11.013>.
- [54] T. Som, D. Kanjilal (Eds.), *Nanofabrication by ion-beam sputtering: Fundamentals and applications*, first ed., Jenny Stanford Publishing, 2012, <http://dx.doi.org/10.1201/b13726>.
- [55] T. Trottenberg, A. Spethmann, V. Schneider, M. Stahl, M. Giesenhausen, H. Kersten, Non-electrostatic diagnostics for ion beams, *Contrib. Plasm. Phys.* 52 (7) (2012) 584–592, <http://dx.doi.org/10.1002/ctpp.201210054>.
- [56] T. Trottenberg, A. Spethmann, J. Rutscher, H. Kersten, Non-electrostatic diagnostics for ion beams and sputter effects, *Plasma Phys. Contr. F* 54 (12) (2012) 124005, <http://dx.doi.org/10.1088/0741-3335/54/12/124005>.
- [57] A. Spethmann, T. Trottenberg, H. Kersten, Measurement and simulation of forces generated when a surface is sputtered, *Phys. Plasmas* 24 (9) (2017) 093501, <http://dx.doi.org/10.1063/1.4997444>.
- [58] M. Klette, M. Maas, T. Trottenberg, H. Kersten, Directionally resolved measurements of momentum transport in sputter plumes as a critical test for simulations, *J. Vac. Sci. Technol. A* 38 (3) (2020) 033013, <http://dx.doi.org/10.1116/6.0000109>.

Chapter 6

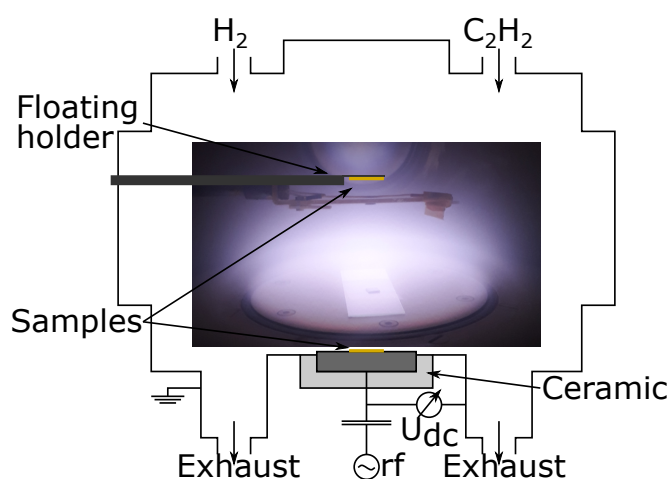
Low-Pressure Plasma Treatment of Highly Porous Framework Materials

Publication IV

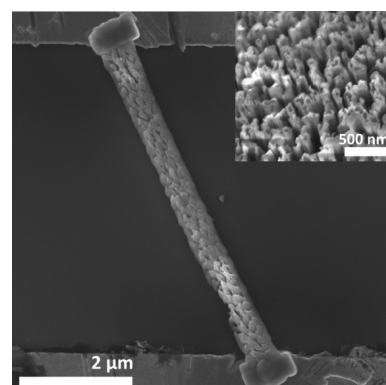
Fabrication of ZnO Nanobrushes by H_2 - C_2H_2 Plasma Etching for H_2 Sensing Applications

Authors	N. Kohlmann, L. Hansen, C. Lupan, U. Schürmann, A. Reimers, F. Schütt, R. Adelung, H. Kersten, and L. Kienle
Journal	ACS Applied Materials & Interfaces Reprinted (adapted) with permission from [325]. © 2021 American Chemical Society.
Technique	Low-pressure plasma etching of microsensors
Utilized diagnostics	Power, pressure and DC bias monitoring, SEM, TEM and EDX imaging, and gas sensing characteristics
Own contribution	Approx. 35 %

Experimental Setup:



Reprinted (adapted) with permission from [325]. © 2021 American Chemical Society.



Reprinted (adapted) with permission from [325]. © 2021 American Chemical Society.

Motivation:

The development of the microplasma cell enables *in situ* observations of plasma induced morphology changes. Thus, a combination of the cell with interesting and over time in morphology changing materials is necessary to use the full potential of the cell. Tetrapod-shaped Zinc Oxide (t-ZnO) combines the advantages and application possibilities of ZnO with a large surface to volume ratio based on the interconnected tetrapods. Increasing this surface to volume ratio even more by plasma etching could benefit a wide range of applications such as gas sensing and reveal an interesting morphology change suited for *in situ* observations.

Main Results:

A successful etching process utilizing a low-pressure capacitively coupled, asymmetric rf discharge operated with an $\text{H}_2\text{-C}_2\text{H}_2$ (mostly 99 %-1 %) gas mixture could be established. The plasma etching resulted in a strong texturing of the ZnO tetrapods which formed a nanobrush structure. The etching process turned out to be self-patterning and preferential in the direction of the incident ions. Sidewall passivation by a-C:H deposition enables nanobrush wire lengths of up to 900 nm which result in an improved surface to volume ratio by a factor of 12.9 compared to the pristine t-ZnO. The increased surface to volume ratio and the small diameters (≈ 50 nm) of the etched nanowires result in a highly sensitive, selective and fast hydrogen sensor. More applications of the etched nanobrushes could include catalysis or production of enhanced highly porous aeromaterials which benefit from the largely increased surface to volume ratio.

Fabrication of ZnO Nanobrushes by H_2 – C_2H_2 Plasma Etching for H_2 Sensing Applications

Niklas Kohlmann, Luka Hansen, Cristian Lupan, Ulrich Schürmann, Armin Reimers, Fabian Schütt, Rainer Adelung, Holger Kersten, and Lorenz Kienle*



Cite This: *ACS Appl. Mater. Interfaces* 2021, 13, 61758–61769



Read Online

ACCESS |



Metrics & More



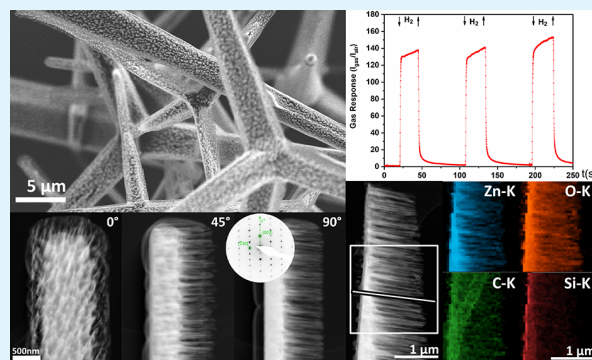
Article Recommendations



Supporting Information

ABSTRACT: Zinc oxide has widespread use in diverse applications due to its distinct properties. Many of these applications benefit from controlling the morphology on the nanoscale, where for example gas sensing is strongly enhanced for high surface-to-volume ratios. In this work the formation of novel ZnO nanobrushes by plasma etching treatment as a new approach is presented. The morphology and structure of the ZnO nanobrushes are studied in detail by transmission and scanning electron microscopy. It is revealed that ZnO nanobrush structures are fabricated by self-patterned preferential etching of ZnO microtetrapods in a hydrogen–acetylene plasma. The etching process was found to be most effective at 1% C_2H_2 admixture. Nanowire arrays are formed enabled by sidewall passivation due to a-C:H deposition. The nanobrush structures are further stabilized by simultaneous deposition of a SiO_x layer from the opposite direction. Highly sensitive (gas response $S = 148$), selective, and fast (response time 15 s, recovery time 6 s) hydrogen sensors are fabricated from single nanobrushes. Single nanobrush sensors show enhanced sensing performance in increased gas response S of at least 10 times and improved response as well as recovery times when compared to nonporous single ZnO nanorod sensors due to the small diameters (≈ 50 nm) of the formed nanowires as well as the strongly enhanced surface-to-volume ratio of the nanobrushes by a factor of more than 10.

KEYWORDS: nanobrush, ZnO, plasma, etching, nano-on-micro, electron microscopy, gas sensing, nanowires



1. INTRODUCTION

Zinc oxide has been a material of enormous research as well as application interest in recent decades.¹ Its intrinsic properties such as a high band gap semiconductor, chemically stable, biocompatible, and piezo-/pyroelectric material give ZnO a wide range of applications. Consequently, ZnO is used to a great extent in gas sensing, catalysis, optoelectronics, transistors, energy generation (e.g., solar cells), and many more applications.^{2–4} To further tailor its properties to these applications, adjustment of the morphology and surface structure is frequently required.

Distinct ZnO morphologies such as wires or rods,⁵ particles,⁶ and other morphologies⁷ can be synthesized. Recently, tetrapod-shaped ZnO crystals have become the focus of research,⁸ where individual tetrapods as well as networks of interconnected tetrapods are being investigated. The control of crystal morphology to achieve large surface areas is especially important in sensing,⁹ energy generation,¹⁰ and catalytic applications.¹¹ Alongside structure and morphology control, doping,¹² thermal annealing,¹³ and chemical surface modification¹⁴ are employed among other techniques to achieve beneficial material properties. Thus, control over both morphology and chemical and structural properties is

needed to tailor the properties of zinc oxide to its diverse applications.

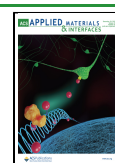
Plasma treatment of zinc oxide crystals shows great promise to allow for modification of morphology as well as structural and surface properties. Plasma surface treatment of ZnO has been reported to improve optical properties,¹⁵ alter electrical behavior,¹⁶ and enhance sensing properties.¹⁷ Additionally, reactive ion or dry etching plasma processes of ZnO have been used in the fabrication of devices^{18–20} as well as modification of surface morphology.^{21,22}

Dry etching of zinc oxide has been performed by using different gases as reactive species: chlorine-,²³ bromine-,²⁴ and fluorine-based plasma chemical agents.²⁵ However, combination of hydrogen and a hydrocarbon compound is most widely used in plasma-based reactive ion etching of zinc oxide.

Received: September 27, 2021

Accepted: December 1, 2021

Published: December 15, 2021



Especially $\text{H}_2\text{-CH}_4$ or $\text{H}_2\text{-CH}_4\text{-Ar}$ plasmas are commonly employed.^{21,26,27}

(Deep) reactive ion etching (DRIE) or dry etching is well established to create micro- or nano-structured zinc oxide. However, conventional patterning of thin films is limited to creating nonhierarchical, effectively two-dimensional structures while also requiring multistep processes and cleanroom conditions. Consequently, additional techniques for creating structures are being explored today. In particular, the formation of hierarchical or nano-on-micro structures, e.g., via etching²⁸ or growth processes,²⁹ is of great interest. Cactus³⁰ or tree-like³¹ morphologies on the nanoscale have been fabricated. Such nano-on-micro structures possess large surface areas and are thus well suited for applications such as gas sensing. ZnO as a material itself is widely used for highly selective and effective sensing of hydrogen.^{32,33}

We report on a novel approach for the fabrication of ZnO nanobrushes and their application as a highly selective, sensitive, and fast H_2 sensor. Nanobrushes are created via surface modification of single-crystalline zinc oxide tetrapods³⁴ by dry etching using a $\text{H}_2\text{-C}_2\text{H}_2$ plasma. The presented plasma etching procedure allows for the single-step creation of highly porous (porosity >50%) ZnO nano-on-micro structures. By fabricating a gas sensor using a single ZnO nanobrush, a strongly enhanced gas response to hydrogen by more than a factor of 10 is achieved when compared to pristine ZnO microrods/nanorods. Consequently, the authors present a technique allowing for efficient morphology modification of ZnO microcrystals.

2. EXPERIMENTAL SECTION

2.1. Sample Preparation. Powders of zinc oxide tetrapods (shown in Figure 2a) synthesized as described elsewhere^{8,34} have been used as source material for the fabrication of porous nanobrush structures. For plasma treatment the tetrapods are prepared onto silicon (100) wafers as the substrate. To break up mechanical interlocking and, thus, isolate single tetrapods along individual arms, ZnO powder is gently ground in a mortar before application via suspension in butanol.

2.2. C_2H_2 Plasma Etching of ZnO Micro-Tetrapods. Most commonly, hydrogen plasmas with a methane (CH_4) admixture of a few up to around 10% are used^{18,26,35} for plasma-induced etching of ZnO. The proposed mechanism allowing for the removal of ZnO material is breaking up of Zn–O bonds via ion bombardment alongside reduction by H^+ ions and subsequent formation of a volatile Zn metal–organic compound of high vapor pressure at room temperature.^{26,36,37} Dissociation of CH_4 in the plasma environment leads to the formation of CH radicals and other hydrocarbon species which can react with the bare zinc atoms. Compounds such as $\text{Zn}(\text{CH}_3)_2$ have a particularly high vapor pressure. Thus, they are believed to have major contribution to higher etch rates observed when comparing CH_4 -based plasmas to fluorine- or chlorine-based plasmas.²⁶

In this work an $\text{H}_2\text{-C}_2\text{H}_2$ (hydrogen–acetylene) plasma is used in contrast to previous studies, where $\text{H}_2\text{-CH}_4$ or $\text{H}_2\text{-CH}_4\text{-Ar}$ plasmas were utilized. C_2H_2 mainly forms various hydrocarbon species with even numbers of C atoms in rf plasmas.³⁸ However, surface interactions lead to the presence of species such as CH_3 allowing formation of the Zn metal–organic compound^{38,39} and, thus, enabling effective etching of zinc oxide using acetylene.

Dry etching has been performed in a capacitively coupled, asymmetric rf discharge that is sketched in Figure 1 and described in more detail elsewhere.⁴⁰ Samples are mounted directly atop the rf electrode as well as placed in the bulk plasma. The working gas pressure in the chamber was measured during processing by a MKS Instruments dual pressure gauge and a MKS Instruments baratron. A

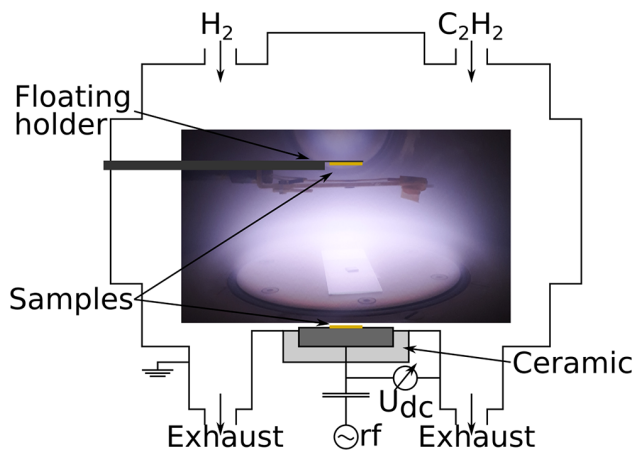


Figure 1. Sketch of the plasma chamber used for etching of ZnO tetrapods showing the electrical wiring as well as the gas inlets and outlets. A photo during treatment showing the plasma glow is given as an inset.

MKS Instruments flow controller regulated the gas influx and the vacuum was created by using an Edwards nXDSi scroll pump and a Varian turbo molecular pump. The plasma is generated by an Advanced Energy Cesar power generator and a matchbox with up to 100 W power at 13.56 MHz. The pressure, gas flow, and forwarded and reflected power as well as the dc bias voltage were logged during the plasma treatment as process control. The power was set to 50 W for all experiments, which resulted in a dc bias voltage of ~ 370 V.

The ratio of H_2 to C_2H_2 was varied by keeping the total flow constant and adjusting C_2H_2 content in the range of 1%–10%. A total flow of 14 sccm results in a working pressure of 30 Pa. During the plasma treatment the total flow was reduced stepwise to 10 sccm to keep the pressure constant at 30 Pa. The pressure rises during the plasma treatment as the H_2 ions are heated by the applied external electrical field, and thus the gas temperature rises, resulting in a pressure increase.

The etching times were varied from 1 to 120 min and best etching results were obtained by using a 1% C_2H_2 content. Thus, all shown samples in the current work were treated with a 1% C_2H_2 admixture to the H_2 plasma. After the plasma etching the samples were treated with an O_2 plasma for 5 min at a pressure of roughly 18 Pa and 50 W power. The dc bias was ~ 500 V during O_2 plasma treatment. The O_2 follow-up treatment was performed to remove excess a-C:H from the ZnO tetrapods.

Samples are both placed directly onto the powered electrode as well as in the bulk plasma via a floating sample holder. If the sample material is placed on the rf electrode, it becomes located within the plasma sheath. Thus, it is subject to bombardment by high-energy ions. This configuration is most alike to the reactive ion etching (RIE) setups most commonly used for ZnO etching in hydrogen–hydrocarbon plasmas.^{26,36,37}

2.3. Analysis. Samples were analyzed via scanning electron microscopy (SEM) and transmission electron microscopy (TEM) with a Zeiss Supra 55 V and a FEI Tecnai F30 G² STwin, respectively. For TEM analysis sample material was transferred from the Si wafer onto lacey carbon Cu TEM grids mechanically by gentle dipping. Elemental analysis is performed by energy-dispersive X-ray spectroscopy (EDX). An EDAX Si/Li EDX detector mounted to the FEI Tecnai F30 is used to acquire elemental distribution maps and line scans in scanning TEM (STEM) mode.

2.4. Preparation of Sensor Devices. Sensor device structures were made from a single ZnO nanobrush following the procedure developed by Lupan et al.⁴¹ Because maskless sputtering of electrical contacts cannot be achieved by the conventional chemical vapor deposition (CVD) approach, focused ion beam (FIB)-SEM metal deposition was used to contact the sensor. Two electrical contacts

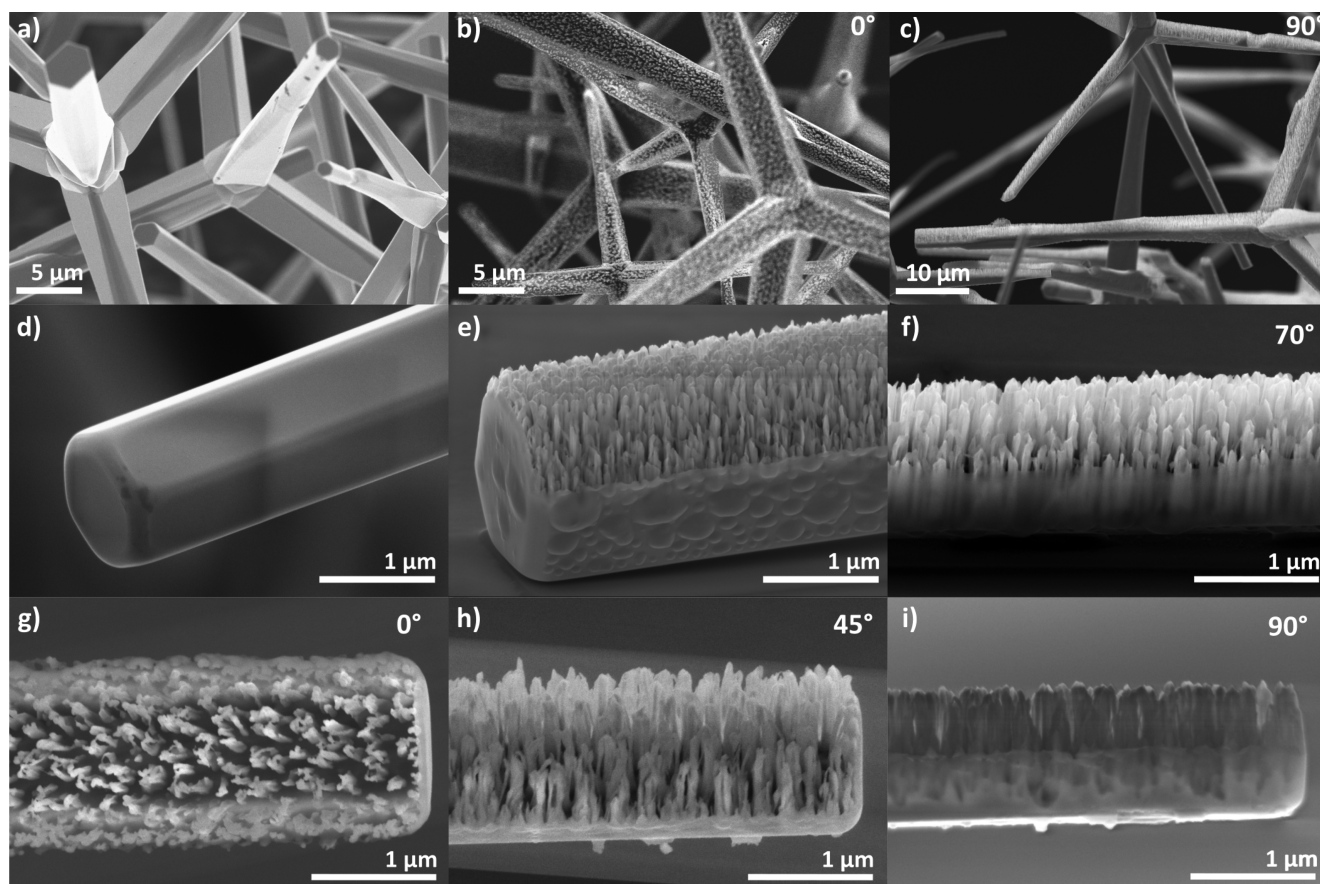


Figure 2. SEM images of plasma-etched as well as pristine ZnO microstructures. (a, b) Micrographs of multiple interconnected ZnO tetrapods in pristine or etched condition, respectively, in top view (0°). Tetrapods shown in (b) have been etched for 60 min. (c) Multiple tetrapods in side view (90°) after etching for 80 min. (d) Close-up of a single tetrapod arm in pristine condition. (e) Tip of a tetrapod arm after plasma etching for 45 min viewed similarly to (d). (f) Tetrapod arm etched for 60 min viewed at 70° . (g–i) Tilt series of a ZnO tetrapod arm etched for 50 min from top to side view imaged at 0° , 45° , and 90° , respectively. Plasma parameters were adjusted to 50 W, 30 Pa, and 1% C_2H_2 for all shown samples.

were deposited on a single ZnO nanobrush on the sensor chip (quartz with Cr/Au contact electrodes).

The gas sensing test characteristics were studied by placing the sensor structure connected to an external electrode in the test setup consisting of a closed quartz chamber connected to a gas flow system as reported earlier.³²

Experimental data acquisition is performed and controlled via a LabView interface.⁴²

3. RESULTS AND DISCUSSION

3.1. Micro- and Nanostructure of Plasma-Etched ZnO Tetrapods. The morphology of the plasma-etched tetrapods is investigated by SEM. For the SEM investigation the samples are imaged on the same substrate as for plasma treatment and, thus, have unchanged positions and orientations. Figure 2 shows untreated as well as plasma-etched ZnO tetrapods and single tetrapod arms. Because of the method of sample preparation, the surface of Si wafer substrates is partially covered by multiple layers of mechanically interlocked tetrapods (see Figure 2a). The resulting packing density is low so that an unobstructed view onto single tetrapod arms, also termed microrods or, depending in size, nanorods, is possible. Treatment in $\text{H}_2\text{--C}_2\text{H}_2$ plasma results in a strong texturing of the ZnO tetrapods (Figure 2b,c,e–i). Single tetrapod arms exhibit a brush-like morphology on the

nanoscale after treatment. Thus, we report on the fabrication of single ZnO nanobrushes as well as nanobrush networks.

Pristine tetrapods have a smooth surface where arms exhibit hexagonal cross sections, as seen in Figure 2d. After prolonged plasma exposure, however, the morphology of the tetrapod arms is strongly changed. The effect of the treatment further revealed by tilting the stage during SEM investigation (see Figure 2g–i). Tilting shows that an array of wires and trenches is formed covering the plasma facing sides of the ZnO tetrapods. Figure 2e shows that the morphology of the envelope with a hexagonal cross section of the tetrapod arms is preserved on the micro scale.

For a closer look, the specimen depicted in Figure 3 was tilted over a wide range of -70° to 70° relative tilt in the TEM to observe the nanowire arrays in side view. Consequently, the brush-like structure becomes apparent: the etched trenches penetrate almost through the whole tetrapod arm, making it highly porous. The varying height of the arm reveals areas where they seem to have a base of untreated ZnO, as indicated by mass thickness contrast shown in Figure 3a. The tip, on the other hand, appears to consist entirely of ZnO nanowires.

Both selected area electron diffraction (SAED) and high-resolution TEM (HRTEM) confirm that pristine ZnO tetrapod microstructures have a wurtzite-type crystal structure with arms growing along the $[001]$ direction³⁴ (Figure 3b,c). The crystallinity and crystallographic orientation of the ZnO

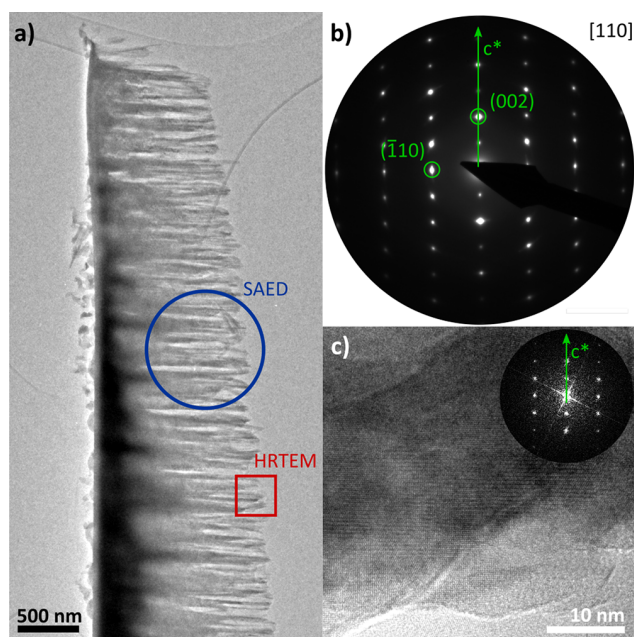


Figure 3. Crystal structure of a ZnO needle etched for 80 min at 50 W, 30 Pa, and 1% C_2H_2 investigated by TEM. (a) TEM bright-field micrograph of a single tetrapod arm. The stage is tilted to a side view of the specimen showing the complete depth of the etched brush structure. (b) SAED pattern with the aperture positioned at the area marked in (a) showing alignment in zone axis $[110]$. (c) HRTEM micrograph of a single ZnO nanowire with FFT (inset).

nanowires are investigated likewise. The SAED pattern shown in Figure 3b indicates that the nanowires retain the original crystallographic phase and orientation of the pristine ZnO tetrapods. In consequence, the etched structure as a whole still appears as a single crystal in SAED. HRTEM of a single nanowire given in Figure 3c confirms the retention of the crystallographic orientation. Fast Fourier transformation (FFT) shows that the crystallographic orientation is along the zone axis (ZA) $[110]$ of wurtzite-type ZnO for both the tetrapod arm and single nanowires. The retained crystallographic orientation of the nanowires together with the physical orientation of the wires observed in Figures 2 and 3 indicates that the nanowires created by the plasma etching process are generally not oriented along the c -axis in contrast to ZnO nanowires created by using growth processes.

Further investigation of the etched crystals is performed via high angle annular dark field scanning TEM (HAADF-STEM). The combination of HAADF-STEM with energy dispersive X-ray spectroscopy (EDX) is used to map the elemental distribution within an etched tetrapod arm. Figure 4a shows a HAADF-STEM micrograph for the same tetrapod arm given in Figure 3a with the positions of EDX line scan and map marked.

The nanobrush structure is replicated in the Zn-K map (Figure 4b) with the nanowires being clearly visible. Additionally, it becomes apparent that there is a base of nonporous, pristine ZnO which is in agreement with the results from TEM bright-field investigation. Both observations confirm that the nanowires are single crystalline ZnO. It is thus shown that nanowire formation is via a top-down etching process of pristine tetrapod arms where the original crystallinity is preserved.

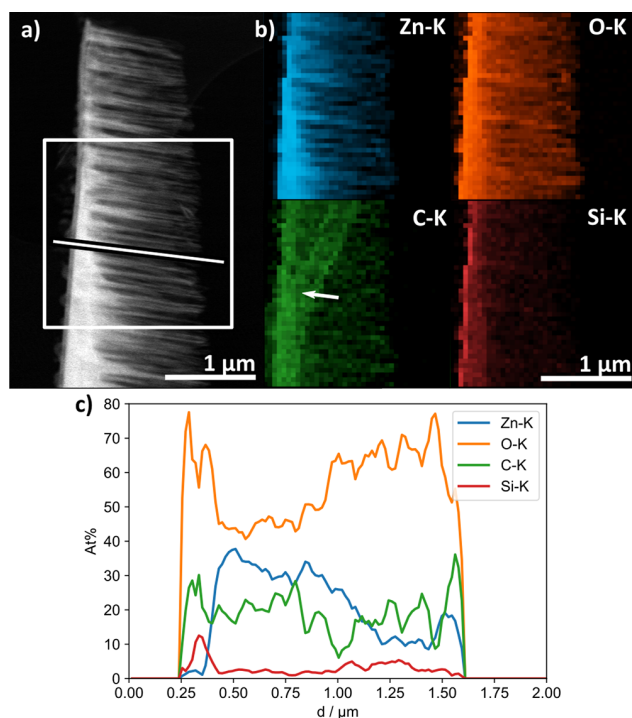


Figure 4. (a) HAADF-STEM micrograph of a single tetrapod arm etched for 80 min at 50 W, 30 Pa, and 1% C_2H_2 . The locations of EDX line scan and map are marked. (b) STEM-EDX elemental distribution maps for selected emission lines. (c) Quantified EDX line scan across the tetrapod arm. The error of EDX quantification is ± 2 atom %.

Despite oxygen plasma follow-up treatment, there still is a homogeneously distributed C-K signal visible in the EDX elemental map given in Figure 4b, indicating the formation of an a-C:H film (section 2.2) simultaneous to etching during plasma treatment. The area of enhanced C-K emission is an artifact from sample preparation: the ZnO tetrapods are placed upon a spiderweb-like carbon mesh for TEM investigation causing the “Y” shape in the C-K map in Figure 4b (see arrow).

Interestingly, not only zinc, oxygen, and carbon are found but also a significant amount of silicon. From Figure 4b, it can be seen that there is an area of increased Si content toward the base of the tetrapod arm. This finding is further showcased when looking at the EDX line scan in Figure 4b, where the horizontal axis indicates the distance from the bottom to the top of the tetrapod arm. There is a clear peak in the Si content before there is a Zn signal when scanning across the tetrapod arm oriented in side view. Obviously, the arm has an additional layer at the bottom, which was facing away from incoming ions during plasma treatment. The coinciding peak of carbon content makes it likely that this layer is based on a mixture of amorphous hydrocarbons and silicon. The distribution of oxygen appears more homogeneously spread compared to the Zn-K signal. Together with the correlated occurrence of oxygen and C/Si content in Figure 4c, these homogeneous distributions indicate that the secondary components are oxidized. Because of the fact that most oxidized carbon species are volatile the majority of the oxygen is assumed to be bound to silicon. Therefore, a Si/SiO_x layer is supposed.

In addition, the hypothesis of a pristine, nonporous ZnO base is also supported by an EDX line scan. There is an area of

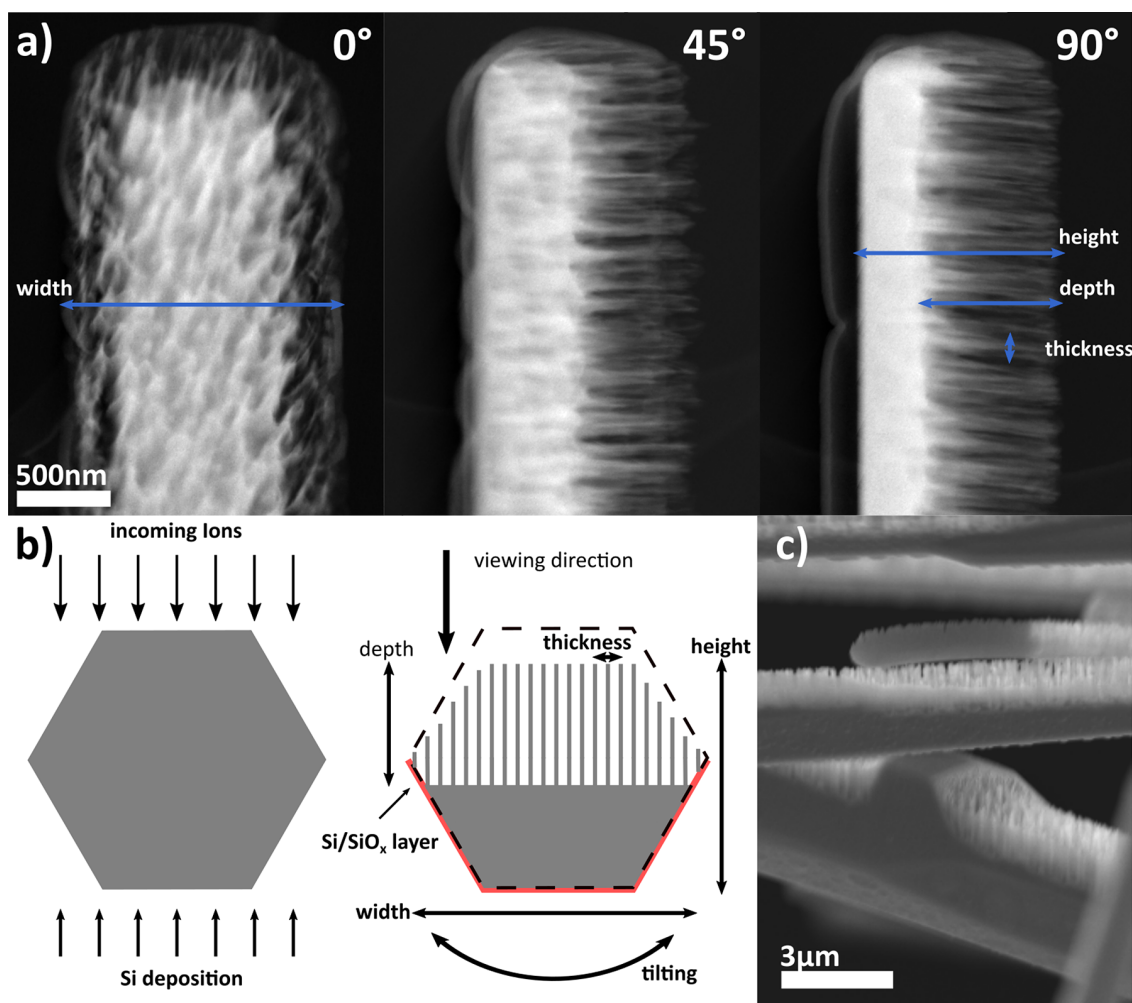


Figure 5. (a) HAADF-STEM micrographs of a tetrapod arm etched for 80 min at 50 W, 30 Pa, and 1% C₂H₂. Different relative tilt angles are given. The angles represent top, intermediate, and side view of a tetrapod arm. (b) Sketch of untreated and plasma-etched tetrapod arm in cross-sectional view. Relevant geometrical quantities and directions are defined. (c) SEM micrograph of ZnO tetrapods etched under identical parameters as in (a), showing etching of the top of the nanowires by comparison to the pristine portion of the same tetrapod arm due to shadowing.

high Zn content where Zn to O ratio approaches 1:1. Toward the top, where the morphology is given by an array of ZnO nanowires, the Zn content decreases while the C and O contents increase. This trend in the EDX line scan is in agreement with a-C:H being present at the surface of the nanowires (see HRTEM micrograph in Figure 3c). The strongly increased surface area then gives rise to the overall higher content of carbon and oxygen compared to zinc seen in the EDX data.

A more detailed look at the layer deposited at the treated tetrapod arm reveals that it is not uniform but rather textured. In Figures 2e,i, 3a, and 4a bubble-like features can be seen. From the EDX line scan across such a bubble-like feature (Figure 4c), it can be observed that these features can be mainly assigned to a-C:H deposition. The Si/SiO_x layers, on the other hand, are more homogeneous, as can be seen from Figure 4a,b. Additionally, the bubble-like features are not found for all treated samples, whereas Si/SiO_x was always observed.

To investigate the origin of Si/SiO_x the Si wafer substrate itself can be investigated. The surface of the Si wafers is initially flat. However, after prolonged plasma exposure it becomes textured (see Figure S1b). Surface texturing strongly indicates

plasma etching and possibly also sputtering of the silicon wafer, which has been reported previously for H₂ plasmas under similar experimental conditions^{43,44} where similar surface morphologies after silicon etching have been observed. Therefore, it is concluded that Si atoms are provided by etching, thus enabling formation of the Si layer. Oxidation is assumed to occur during follow-up oxygen treatment after the etching process. As shown in Figure 4, a 50 nm thick layer formed during 80 min treatment time, resulting in a deposition rate of <1 nm/min.

To reveal the 3D morphology of plasma-etched ZnO tetrapod arms a tilt series from −70 to 70 °C absolute tilt angle is acquired in HAADF-STEM mode. Figure 5a shows HAADF-STEM micrographs at 0°, 45°, and 90° relative tilt, where 0° is defined as top view and 90° as side view. The full tilt series compiled as a video can be found in the Supporting Information.

The tetrapod arm investigated was subject to C₂H₂ plasma etching for 80 min and, thus, shows similar features discussed for the specimen shown in Figures 3 and 4. The HAADF-STEM Z-contrast shows again an array of ZnO nanowires on top of a rigid ZnO basis. The bottom of the arm is coated by a

Table 1. Comparison of Surface Area A , Volume V , and Surface-to-Volume Ratio A/V between Pristine and Plasma-Etched t-ZnO Tetrapod Arms of 1 μm Length and Width with Nanowire Diameters of 50 ± 5 nm; Ratio of A , V , and A/V between Pristine and Two Exemplary Nanowire (NW) Lengths; and Porosity Calculated as a Fraction of Void to Enclosing Volume^a

condition	V (μm^3)	A (μm^2)	$A_{\text{pristine}}/A_{\text{etched}}$	$V_{\text{pristine}}/V_{\text{etched}}$	A/V (μm^{-1})	$(A/V)_{\text{pristine}}/(A/V)_{\text{etched}}$	porosity (%)
pristine	0.65	3.65			5.62		0
etched, 500 nm NW length	0.46	12.05	3.30	0.71	26.30	4.66	29
etched, 900 nm NW length	0.30	21.70	5.95	0.46	72.33	12.87	54

^aThe uncertainty of the given values is determined by the spread in nanowire diameters to be ca. 10%.

Si/SiO_x as well as an a-C:H layer. A cross-sectional sketch of the resulting structure is given in Figure 5b.

The depth of the trenches or length of the nanowires accordingly reaches more than 800 nm for etching times of 80 min, as can be seen from the side view in Figures 3a and 4a. The thickness of ZnO nanowires is found to be roughly 50 ± 5 nm independent of treatment duration. Consistent nanowire thicknesses are found from the top (Figure 2e) as well as side view (Figure 3a). The combination of wire lengths of 800 nm and thicknesses of 50 nm results in an aspect ratio of ~ 16 .

To estimate the increased surface area due to etching the resulting nanowires can be assumed to have a cylindrical shape. From the plane view (e.g., Figure 2g) the area covered by the wires in relation to the area of the etched trenches can then be estimated. The ratio of trench to wire area works out to be roughly 0.4. The volume of a ZnO nanobrush is then derived by combining this ratio of wires to trenches assuming of evenly spaced nanowires with a mean thickness of 50 nm and a known etch depth. Combining this with the cross-sectional geometry shown in Figure 5b both the surface area and the volume can be calculated. Table 1 shows a comparison of surface area as well as surface-to-volume ratio between pristine and etched cases with different nanowire lengths for a tetrapod arm of 1 μm diameter and 1 μm length. It can be seen that both surface area and especially surface to volume ratios can be strongly enhanced by plasma etching.

The porosities of single nanobrushes are estimated by using a similar approach, where the porosity is given by the fraction of the volume of the voids to the total volume enclosed by the arm. For the case of fully etched nanobrushes porosities exceed 50% (Table 1) for a single nanobrush. Furthermore, three-dimensional networks consisting of treated tetrapods would achieve even higher porosities due to the combination of micro- and nanoscale porosities. Single nanobrushes as well as networks of nanobrushes thus show high porosities alongside an enhanced surface area with a roughly 3–5-fold increase as well as strong increase in the surface-to-volume ratios of more than 10 times when compared to pristine ZnO tetrapods (see Table 1).

Hence, the presented plasma etching treatment offers a unique combination of highly directional etching and deposition processes. By use of C₂H₂ as an etchant, the enhanced a-C:H deposition compared to the usage of CH₄ enables the formation of high aspect ratio ZnO nanowires. Amorphous hydrocarbons form a protective coating at the sidewalls of the nanowires during etching and thus protecting the sidewalls from further etching. The carbon signal found in EDX investigations (Figure 4) as well as amorphous areas found by HRTEM investigations (Figure 3) strongly support the assumption of sidewall protection. Such a protection of the sidewalls by film deposition has been reported previously for plasma etching of silicon⁴⁵ and polymers⁴⁶ enabling etching of

structures aspect ratio by carefully controlling plasma parameters.

The deposited Si layer, on the other hand, prevents the tetrapod arms from being fully etched trough when using long treatment times. In this way arrays of ZnO nanowires not connected by a base of ZnO can be fabricated. Such a structure possesses mechanical stability while being flexible, as shown for mechanical deformation in Figure S2d.

3.2. Plasma Etching Characteristics. In the previous section it was shown that zinc oxide tetrapods as well as single tetrapod arms can be efficiently etched in a H₂–C₂H₂ plasma. The formation of nanostructures observed here is in contrast to previous studies on hydrogen–hydrocarbon plasma etching of ZnO, where the resulting surface morphologies showed only minor roughness³⁵ or features of much larger lateral size.²⁷

However, in contrast to previous studies on dry etching of polycrystalline ZnO thin films, we investigate plasma etching of single crystalline ZnO microstructures. Because of the preparation process the ZnO tetrapods are oriented randomly with respect to the surface normal atop the wafer. This means that the crystallographic surfaces of the tetrapods and their arms are also randomly oriented. Etch rates of single crystalline zinc oxide can depend on crystallographic orientation,⁴⁷ so nonhomogeneous etching is expected.

Tilting the SEM stage reveals, however, that the ZnO nanowires formed after the etching process are uniformly oriented across the whole sample (see Figure 2c, Figure 5c, and Figure S2c). Consequently, the orientation of the nanowires is independent of the spatial orientation of the tetrapods and, thus, also of their crystallographic orientation. The uniform orientation of the ZnO nanowires can also be seen from SEM top view images (Figure 2b,g) where only the tips of the wires are visible.

To understand the origin of the uniform nanowire orientation, the conditions during plasma etching need to be taken into account. All etched samples were positioned atop the rf-powered electrode during treatment and, consequently, located in the plasma sheath accordingly. Thus, they are subject to bombardment by directional, high-energy ions.^{48,49} The relation between nanowire orientation and ion influx is sketched in Figure 5b which shows that ion bombardment and SEM top view direction are parallel. From this relation it becomes apparent that the nanowire orientation is parallel to the ion influx.

The dependence of the nanowire orientation on the direction of the ion flux strongly suggests an important role of the ions in the etching mechanism. Etch rates in H₂–CH₄ plasmas are strongly dependent on ion energies,^{36,50} and further enhancement of the etching process due to H⁺ irradiation of ZnO has been proposed.⁵¹ In the plasma sheath ions are continuously accelerated toward the electrode; thus, for samples positioned directly on the electrode maximum ion energy is expected. Accordingly, the highest etch rates are

expected for positioning directly on the electrode as well. On the other hand, no etching was observed for samples located in the bulk plasma, where no high-energy ions are present. The absence of etching in the plasma bulk strongly suggests that there is a minimal ion energy necessary for an efficient etching process. Together the findings confirm the importance of high-energy ions for the plasma etching process of ZnO in H_2 – C_2H_2 plasmas similar to H_2 – CH_4 plasma chemistries.

It was found that the width of tetrapod arms is unaffected by the etching process. The width is assumed to be unchanged due to the formation of a Si/SiO_x layer at the bottom of the tetrapod arm. This layer is unaffected by the etching process and, thus, preserves the original contour (see sketch in Figure 5b). The effect of the Si/SiO_x layer on the width of the tetrapod arms can be seen in Figure 2e,f where the outer contour of the bottom part is preserved. Especially Figure 2f demonstrates this phenomenon where the thin, semitransparent film is visible in the SEM micrograph. The full 3D structure of the etched tetrapods can be observed by looking at a tilt series of HAADF-STEM micrographs (see the video in the Supporting Information as well as Figure 5a). A sketch of the resulting cross-sectional morphology is given in Figure 5b.

The knowledge of the morphology can be used to determine the etch rates for both the trenches and the tips of the nanowires, which themselves are also subject to etching (Figure 5c) by systematic investigations using TEM. To determine both etch rates, the initial height, the trench depth, and the total height (for definition see Figure 5b) after plasma treatment need to be measured. Thereby, the original height needs to be inferred from the measured width in combination with the hexagonal geometry of the tetrapod arms. The relation of width and height depends on the orientation of the cross section with respect to the incoming ions, which can be determined from SAED. A zone axis of $[110]$ coincides with viewing the direction onto one of the six faces, whereas a ZA of $[210]$ means viewing the tetrapod arm edge-on. By combining these considerations and systematically tilting in the TEM, etch rates for trenches and top parts can be determined just from a single data set.

By analysis of samples with the given method, constant etch rates are found for treatment times of 30–80 min. The mean etch rates are determined to 8.00 ± 0.75 nm/min top and 19.0 ± 1.5 nm/min for the trenches. This results in a growth rate of ≈ 11 nm/min for the nanowires as well as a ratio of 2.4 for preferential etching.

Similarly to the sidewall protection effect, the lower etch rates of the tops of the nanowires might also be induced by a-C:H film deposition. In contrast to the sidewalls, however, the a-C:H film at the top is constantly removed by bombardment of the high-energy ions present in the plasma sheath which leads to etching not being completely disabled. Although this consideration is also valid for the trenches, it can be assumed that the deposition of a-C:H is less efficient in the trenches, thus leading to the difference between trench and top etch rates. Definite conclusions about the detailed nature of the etching process are, however, only possible by investigations of the kinetics during plasma operation.

Common plasma etching of ZnO thin films has been performed by using specialized reactive ion etching devices where high plasma densities are created by using an inductively coupled plasma (ICP) and high-energy ions are accelerated toward the specimen by using a bias voltage.^{26,35,50} The use of high plasma densities and ion energies results in large etch

rates of about 100 nm/min, which is much higher than etch rates determined in this work. On the other hand, the etch rates are in good agreement compared to experiments performed by using a capacitively coupled plasma reactor under plasma parameters closer to this study.²⁰ Additionally most previous observations of plasma etching of ZnO have been performed by using polycrystalline, two-dimensional thin films in contrast to the single crystalline tetrapod networks investigated in this work.

The etch rates of ZnO tetrapods observed in this work indicate a very efficient etching process using acetylene and hydrogen when taking into account the significantly higher discharge powers used in most studies on reactive ion etching of ZnO both for ICP and CCP setups. Guo et al. studied the influence of different powers, pressures, and methane admixtures on the resulting etch rates.³⁷ The authors found the etch process to be most efficient very close to the experimental parameters used in this study at a pressure of 25 Pa and 4.4% CH_4 . Additionally, a linear increase of etch rates with rf power was found. Extrapolating the linear relation to 50 W rf power leads to roughly 20 nm/min, which is very close to the rate for preferential etching of 19 nm/min found in this study. However, we found the etching process to be most effective at 1% C_2H_2 content in contrast to 4.4% for the case of methane. When going to higher C_2H_2 content, a-C:H film formation quickly becomes dominant over etching. At 5% C_2H_2 content continuous films and no etching is observed. Instead, formation of continuous a-C:H films around ZnO tetrapods (Figure S2) is found.

The differences observed between etching of ZnO using CH_4 or C_2H_2 strongly indicate that different optimal process parameters exist when using different hydrocarbon precursors. For the case of C_2H_6 even higher etch rates were reported at identical parameters when comparing to CH_4 .⁵² Using C_2H_2 instead of CH_4 should result in lower etch rates due to fewer CH_n species forming, as explained in section 2.2. However, we observe comparable or even higher etch rates using C_2H_2 in contrast.

Surface interactions are a main factor introducing species like CH_3 in a C_2H_2 plasma.³⁸ Thus, a feedback mechanism from a-C:H material deposited on the Si wafer substrate and the electrode is assumed to effectively provide the species needed for efficient etching. In the experiment it was found that after thorough cleaning of the plasma chamber the etching process reached a stable output only after few treatment cycles, where an a-C:H layer formed atop the electrode accordingly. Similar findings of feedback from previous treatment cycles due to film deposition have also been reported for nanoparticle generation.⁵³

No additional treatment of the ZnO tetrapods to facilitate their nanostructuring has been performed previously to plasma etching. Thus, the formation of nanowire arrays by patterned preferential etching must be the result of the plasma etching process and pristine ZnO crystal properties only. By looking at SEM micrographs of tetrapods with short treatment times (see Figure S1), one can see that a structuring of the tetrapod surface sets in gradually. It is thus expected that the process is self-reinforcing where initial surface features and/or crystallographic defects such as oxygen vacancies are being enhanced by preferential etching. The fact that similar self-patterning behavior of single crystalline, wurtzite type ZnO microrods was found for a different etching mechanism³⁰ further points to the

ZnO crystals themselves as the source for the observed patterning.

Formation of nano-on-micro nanowire arrays via a self-patterning process enhanced by sidewall protection has previously not been reported for plasma etching of ZnO. Previously fabrication of ZnO nanostructures using plasma etching has been performed by using lithography^{18,20} or particles as masks.¹⁹ Additionally, wet chemical etching of ZnO using different techniques, for example, via oleic acid or acetic acid can increase the surface area of ZnO microstructure^{54,55} albeit to a much lesser degree. Thus, the process presented in this study allows for both ease of fabrication by eliminating the necessity for a patterning step as well as offering unique increase in surface area via the formation of nanowire arrays.

In comparison with surface modification by plasma treatment where no chemically enhanced etching takes place, the resulting morphologies differ strongly.⁵⁶ This emphasizes the necessity of careful control plasma treatment parameters to achieve the desired results.

3.3. Sensing Properties and Mechanism. The increased surface areas and large surface-to-volume ratios (see Table 1) of ZnO nanobrushes fabricated by plasma etching as described in the previous sections makes them ideal for gas sensing applications. We present a H₂ sensor based on a single nanobrush, e.g., for leak detection in energy applications.^{57,58}

Figure 6 shows a top view SEM micrograph of a ZnO tetrapod arm after plasma treatment and integrated in a single

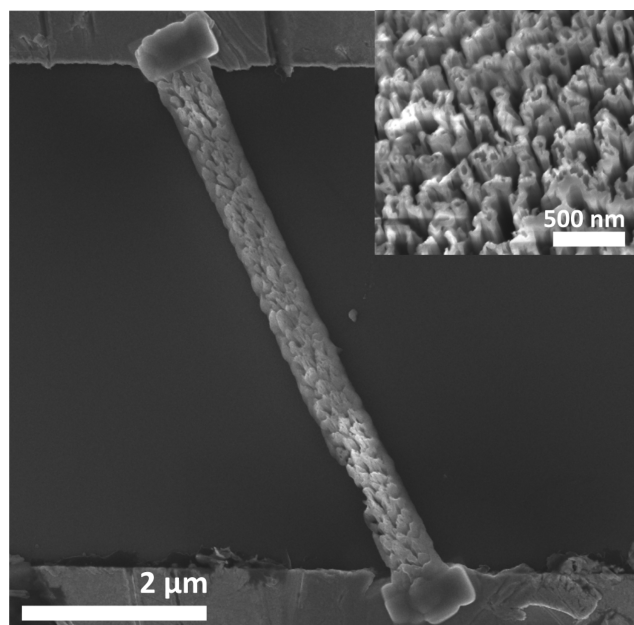


Figure 6. SEM image of a ZnO tetrapod arm after plasma treatment and integrated in a single nanobrush microsensor. The inset shows a magnified view of the surface with formed nanotrenches/wires.

nanobrush microsensor by an approach developed by Lupan et al.⁴¹ The ZnO nanobrush is 11 μm in length with a width of 1 μm. The surface of the ZnO rod is fully covered with trenches/wires formed after plasma etching treatment, as described in the previous sections.

The gas response was calculated as the ratio of current measured during H₂ gas exposure to current measured in air as $S = I_{\text{gas}}/I_{\text{air}}$. The relevant sensing parameters for this as well as for other studies using ZnO nanostructures are given in Table

2. Gas sensing tests were performed at 10% relative humidity. For ease of comparison then gas response values are also given as a percentage increase of the measured quantity. At room temperature no significant gas response to hydrogen exposure was observed. When increasing operating temperatures, however, a gas response of $S = 25\text{--}100$ ppm of H₂ was observed starting from an operation temperature of 100 °C (Figure 7b). A further increase of the operation temperature to 150 °C leads to a strongly enhanced gas response accordingly with a maximum response of ~ 150 being a 6-fold increase compared to 100 °C operating temperature. An upper limit of operating temperatures of 175–180 °C is found above which degradation of the nanosensors due to high currents begins. Therefore, the operation temperature has been limited to a maximum of 150 °C. When exposing a sensor to different concentrations of H₂, a roughly linear increase in gas response is observed (see Figure 7c). It can be seen that the setup presented here offers good sensitivity even to small quantities of hydrogen gas as low as 8 ppm at elevated operating temperatures.

Response times t_{resp} and recovery times t_{recov} are calculated as the rise times to 90% of the maximum gas response after gas exposure and decay time to 10% above $S = 1$ after H₂ shutoff, respectively (Figure 7a)). The values t_{resp} and t_{recov} are on the order of a few seconds and given in Table 2. Contrary to the gas response S t_{resp} and t_{recov} show no strong dependency on the operating temperature with $T_{\text{op}} = 125$ °C indicating faster response as well as recovery times.

The selectivity was determined by comparison of the gas response between hydrogen and methane and ammonia as well as the volatile organic compounds (VOCs) acetone, *n*-butanol, ethanol, and 2-propanol. The sensor device shows a highly selective gas response to hydrogen only across all operation temperatures where no change in current and, thus, no response to the tested compounds other than H₂ were observed.

Both improved gas responses S and response as well as recovery times were found when comparing to various studies using pristine, single ZnO nanorods^{42,59–62} or nanorod arrays^{33,63} (see Table 2). Comparing across all parameters and studies an increase in the gas response S by at least a factor of 10 is found. Additionally, the response and recovery times are likewise enhanced with the response being at least 4 times faster and the recovery 30% faster. However, in comparison to the study reporting the highest gas response³³ our setup shows a 16-fold decrease in t_{resp} and 20-fold decrease in t_{recov} , respectively. From this comparison it becomes evident that the fabricated devices show highly promising performance as a selective, sensitive, and very fast hydrogen sensor.

The sensing of hydrogen using ZnO is based on variation of the surface electron depletion region (SEDR) due to interactions with oxygen (air) and hydrogen, respectively. Under air exposure, oxygen molecules are adsorbed on the surface and consequently enlarging the depletion region and in turn increasing the electrical resistance.⁶⁴ Subsequent exposure to hydrogen enables desorption of oxygen by H₂O formation, in turn reducing the thickness of the depletion layer. Consequently, the resistance of the wire decreases, leading to an increase in measured current. The process of oxygen desorption is reversible when the sensor is exposed to air. Thus, a repeated change in current is observed for subsequent hydrogen and air exposure of single ZnO nanobrush sensor devices (see Figure 7). The formation of a SEDR implies the

Table 2. Comparison of Response for Different Studies on H₂ Sensing Using ZnO Nanostructures, with the Gas Response *S*, Operating Temperature *T*_{op}, the Response Time *t*_{resp}, and the Recovery Time *t*_{recov}^a

study	structure	H ₂ concn (ppm)	<i>T</i> _{op}	<i>S</i>	<i>t</i> _{resp} (s)	<i>t</i> _{recov} (s)
this work	nanobrush	100	100 °C	25/2252%	14	6
this work	nanobrush	100	125 °C	62/7150%	6	3
this work	nanobrush	100	150 °C	148/19276%	16	6
Rout et al. ⁶⁰	nanorod	100	RT	3/–		
Rout et al. ⁶⁰	nanorod	500	RT	5/–		
Lupan et al. ⁶¹	nanorod	150	RT	–/2%	60	300
Lupan et al. ⁶²	nanorod	100	RT	–/6%		
Lupan et al. ⁴²	nanorod	100	RT	–/34%	64	11
Hassan et al. ³³	nanorod array	1000	RT	–/500%	176	116
Hassan et al. ³³	nanorod array	1000	100 °C	–/900%	200	124
Hassan et al. ³³	nanorod array	1000	150 °C	–/1400%	188	118
Chu et al. ⁶³	nanorod array	100	150 °C	–/225%	100	200
Khan et al. ⁵⁹	nanorod	100	200 °C	2.5/–	45	120
Khan et al. ⁵⁹	nanorod array	100	200 °C	5.5/–	45	120

^aThe gas response is either given by $I_{\text{gas}}/I_{\text{air}}$ or $(R_{\text{gas}} - R_{\text{air}})/R_{\text{air}} \times 100\%$. For ref 59 the response is given by $R_{\text{gas}}/R_{\text{air}}$. The uncertainty of the gas response determined in this work is 5% while the response and recovery times have an error of ± 0.5 s at most.

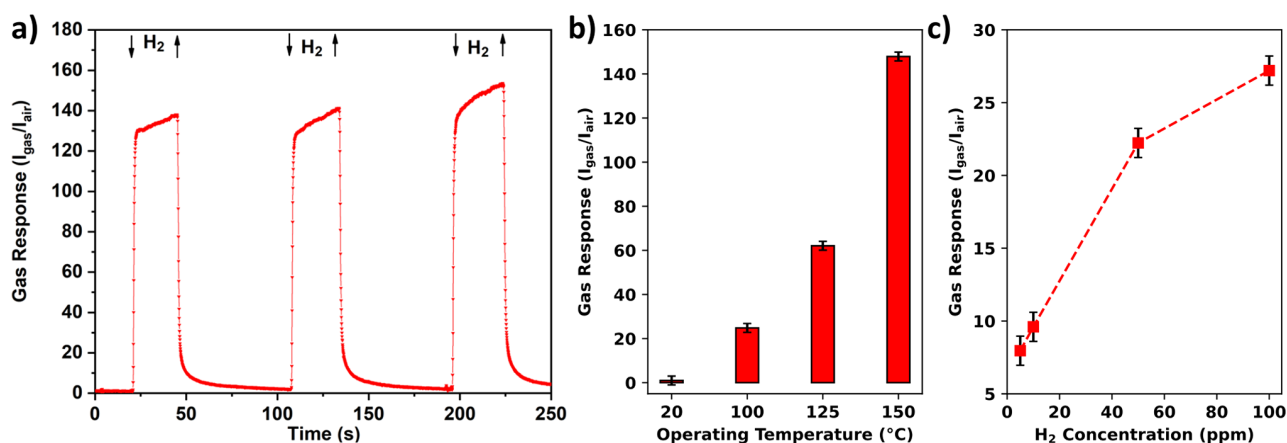


Figure 7. (a) Dynamic response to 100 ppm hydrogen at 150 °C operating temperature of the single nanobrush microsensor shown in Figure 6 for multiple response cycles. (b) Gas response of the identical sensor to 100 ppm of H₂ at different operating temperatures. (c) Gas response of the identical sensor to different concentrations of H₂ at an operating temperature of 100 °C.

formation of a conduction channel within the ZnO nanowire/microwire. It has been shown previously that the relative size of the conduction channel to the size of the wire strongly affects the change in electrical properties due to gas exposure.⁴² Thus, smaller wire diameters lead to an overall increased gas response to hydrogen. Additionally, it was found that smaller wire diameters also promote a higher selectivity toward hydrogen.⁴²

As revealed by detailed structural investigations, the ZnO nanobrushes consist of an array of ZnO nanowires with very small diameters of ≈ 50 nm. Thus, the diameters of the individual nanowires have to be considered when looking at the gas response to hydrogen. As discussed, smaller diameters lead to a higher sensitivity as well as selectivity. Consequently, the strong increase in gas response as well as the excellent selectivity of single nanobrush sensors can be attributed to the small diameters of the ZnO nanowire arrays. The significantly increased surface-to-volume ratio of up to ≈ 13 times compared to a pristine rod of identical diameter (see Table 1) when using a ZnO nanobrush instead of a pristine microrod contributes to an overall higher surface area available for interactions with the ambient gas, thus enhancing the sensing performance further.

Using nanobrushes with different outer diameters and, thus, surface-to-volume ratios as sensors showed no significant influence of the surface-to-volume ratio on the gas response. This strongly suggests that the effect of nanowire formation as discussed above dominates the influence of the additional surface area in the parameter space of this study.

Similar improvements in gas response, although less pronounced, have been found when varying the aspect ratio of ZnO nanorod arrays⁹ or by fabricating cactus-like ZnO nanostructures.³⁰

The influence of the Si/SiO_x layer formed during plasma etching has been investigated by fabrication of a turned over sensor device showing that the surface of the nanobrush covered by SiO_x does not contribute to the measured gas response. Thus, the ZnO nanowire arrays are solely responsible for the functionality of the sensors. The overall behavior of the sensors can be described by assuming nonmodified, crystalline ZnO as the active material. It can thus be safely assumed that the residual a-C:H has no detrimental influence on the surface reactions. On the contrary, the very high selectivity might in part be facilitated by the presence of the thin a-C:H layer atop

the nanowires which could impede the interaction with the ZnO surface for all gases and VOCs except hydrogen.

The long-term stability of the sensors has been studied by performing repeated measurements using an identical sensor at different elapsed times since fabrication. No decrease in sensitivity has been observed within a time frame of 6 months under ambient conditions. Additionally, repeated measurements of the structure of single nanobrushes using TEM showed no changes in chemical composition and morphology. Consequently, excellent long-term stability of single nanobrush sensors as well as the nanostructures themselves is reported.

4. CONCLUSIONS

Novel ZnO nano-on-micro structures (nanobrushes) were manufactured by etching ZnO tetrapods using $\text{H}_2\text{--C}_2\text{H}_2$ plasma treatment. The morphology and structure resulting from plasma etching were studied in detail by using TEM and SEM. The structural analysis showed a brush-like structure in which arrays of ZnO nanowires are located on a tetrapod/tetrapod arm basis. The nanobrushes and nanobrush networks are highly porous on the micro- and nanoscale alike and, thus, possess high surface-to-volume ratios.

The strongly increased surface-to-volume ratio due to the formation of nanowire arrays with small diameters after plasma etching enabled the fabrication of highly sensitive and fast H_2 gas sensors using single nanobrushes. Enhanced gas response as well as recovery and response times could be reached when comparing to the use of pristine ZnO nanostructures. The improved sensitivity as well as response times make single nanobrush sensors ideal candidates to detect hydrogen leaks in energy applications where fast and sensitive detection is highly important due to the dangers of even small quantities of escaped hydrogen gas.^{57,58} Further increased sensing performance could be achieved by using nanobrushes with maximum nanowire length in relation to the tetrapod arm diameter or by using a network of nanobrushes instead of a single one further increasing the available surface area. Potentially the plasma parameters during etching could be altered to reduce the diameters of the formed ZnO nanowires and, thus, further enhance the sensitivity as well as selectivity.

The plasma etching process in which the described ZnO nanobrushes are formed has been investigated, and results are compared to existing studies. The usage of a $\text{H}_2\text{--C}_2\text{H}_2$ plasma is identified as an effective way of etching ZnO tetrapods. The formation of nanowire arrays, so far not observed for plasma etching of ZnO, is linked to a self-patterning process enhanced by sidewall protection due to a-C:H deposition. When compared to other etching methods, e.g., wet chemistry, plasma etching offers superior increase in surface areas. Additionally, the top-down etching process using ZnO micro-tetrapods as base material offers ZnO nanowires with small diameters atop a convenient basis in contrast to ZnO nanowires, e.g., grown via a vapor–liquid–solid process.⁶⁵

The unique combination of etching and Si/SiO_x deposition as two simultaneous, directional processes is found. The inherently created ZnO/Si junctions find use, for example, in solar cell application,⁶⁶ which presents another possible application for the nanobrushes described in this work. Furthermore, the deposition of SiO_x provides enhanced mechanical stability allowing for almost free-standing nanowire arrays that would otherwise be infeasible to achieve.

By using different substrate materials, we can alter the simultaneous deposition process to achieve tailored ZnO

nanowire arrays with a coated base. In this way, built-in heterojunctions can be created. By using a conductive material, e.g., copper, we could create electrically contacted nanowire arrays.

Furthermore, fabrication of highly porous so-called aeromaterials⁶⁷ could be performed by using ZnO template material nano textured via the presented method. This approach would further increase the porosity and strongly enhance the available surface area in comparison to the usage of pristine ZnO tetrapods as template material.

The large surface area of the presented nanobrushes combined with the ease of fabrication as well as the versatility of ZnO as a material makes them ideal candidates for many applications beyond sensing. Possible applications include catalysis,⁶⁸ energy generation,^{10,31} field emission,⁶⁹ and cathodoluminescence.⁷⁰ The plasma treatment process in principle allows for large quantities of ZnO tetrapods being treated at the same time limited only by plasma chamber size. Together with the capability to produce sufficient amounts of ZnO tetrapod source material upscaling of the process can readily be achieved. A first impression of the envisaged upscaling can be found in Figure 2b where a network of porous ZnO nanobrushes is shown.

Therefore, the presented fabrication of ZnO nanobrushes/nanobrush networks via $\text{H}_2\text{--C}_2\text{H}_2$ plasma etching is a highly valuable tool for scientific and possibly industrial applications where high specific surface areas are needed.

■ ASSOCIATED CONTENT

Supporting Information

The Supporting Information is available free of charge at <https://pubs.acs.org/doi/10.1021/acsami.1c18679>.

Additional SEM and TEM micrographs (PDF)

Video of a tilt series in HAADF STEM (MP4)

■ AUTHOR INFORMATION

Corresponding Author

Lorenz Kienle – Institute for Materials Science, Kiel University, 24143 Kiel, Germany; Email: lk@tf.uni-kiel.de

Authors

Niklas Kohlmann – Institute for Materials Science, Kiel University, 24143 Kiel, Germany; orcid.org/0000-0001-8494-118X

Luka Hansen – Institute of Experimental and Applied Physics, Kiel University, 24118 Kiel, Germany; orcid.org/0000-0003-2656-4069

Cristian Lupan – Center for Nanotechnology and Nanosensors, Department of Microelectronics and Biomedical Engineering, Technical University of Moldova, Chişinău 2004, Moldova

Ulrich Schürmann – Institute for Materials Science, Kiel University, 24143 Kiel, Germany

Armin Reimers – Institute for Materials Science, Kiel University, 24143 Kiel, Germany

Fabian Schütt – Institute for Materials Science, Kiel University, 24143 Kiel, Germany; orcid.org/0000-0003-2942-503X

Rainer Adelung – Institute for Materials Science, Kiel University, 24143 Kiel, Germany

Holger Kersten – Institute of Experimental and Applied Physics, Kiel University, 24118 Kiel, Germany; orcid.org/0000-0003-1798-7588

Complete contact information is available at:
<https://pubs.acs.org/10.1021/acsami.1c18679>

Notes

The authors declare no competing financial interest.

ACKNOWLEDGMENTS

The authors thank the DFG for funding under Grants KI 1263/17-1, KE 574/8-1, and AD 183/27-1. The research results are obtained in part with the support of Swedish Radiation Safety Authority (Contract SSM2020-7534).

REFERENCES

- (1) Klingshirm, C. ZnO: Material, Physics and Applications. *ChemPhysChem* **2007**, *8*, 782–803.
- (2) Özgür, Ü.; Hofstetter, D.; Morkoc, H. ZnO Devices and Applications: A Review of Current Status and Future Prospects. *Proc. IEEE* **2010**, *98*, 1255–1268.
- (3) Kołodziejczak-Radzimska, A.; Jesionowski, T. Zinc Oxide - From Synthesis to Application: A Review. *Materials* **2014**, *7*, 2833–2881.
- (4) Theerthagiri, J.; Salla, S.; Senthil, R. A.; Nithyadharseni, P.; Madankumar, A.; Arunachalam, P.; Maiyalagan, T.; Kim, H.-S. A Review on ZnO Nanostructured Materials: Energy, Environmental and Biological Applications. *Nanotechnology* **2019**, *30*, 392001–392001.
- (5) Zhang, Y.; Ram, M. K.; Stefanakos, E. K.; Goswami, D. Y. Synthesis, Characterization, and Applications of ZnO Nanowires. *J. Nanomater.* **2012**, *2012*, 1–22.
- (6) Ong, C. B.; Ng, L. Y.; Mohammad, A. W. A Review of ZnO Nanoparticles as Solar Photocatalysts: Synthesis, Mechanisms and Applications. *Renewable Sustainable Energy Rev.* **2018**, *81*, 536–551.
- (7) Cho, S.; Jung, S.-H.; Lee, K.-H. Morphology-Controlled Growth of ZnO Nanostructures Using Microwave Irradiation: From Basic to Complex Structures. *J. Phys. Chem. C* **2008**, *112*, 12769–12776.
- (8) Mishra, Y. K.; Adelung, R. ZnO Tetrapod Materials for Functional Applications. *Mater. Today* **2018**, *21*, 631–651.
- (9) Gurav, K. V.; Gang, M. G.; Shin, S. W.; Patil, U. M.; Deshmukh, P. R.; Agawane, G. L.; Suryawanshi, M. P.; Pawar, S. M.; Patil, P. S.; Lokhande, C. D.; Kim, J. H. Gas Sensing Properties of Hydrothermally Grown ZnO Nanorods with Different Aspect Ratios. *Sens. Actuators, B* **2014**, *190*, 439–445.
- (10) Sun, X.; Li, Q.; Jiang, J.; Mao, Y. Morphology-Tunable Synthesis of ZnO Nanoforest and Its Photoelectrochemical Performance. *Nanoscale* **2014**, *6*, 8769–8780.
- (11) Flores, N. M.; Pal, U.; Galeazzi, R.; Sandoval, A. Effects of Morphology, Surface Area, and Defect Content on the Photocatalytic Dye Degradation Performance of ZnO Nanostructures. *RSC Adv.* **2014**, *4*, 41099–41110.
- (12) Norton, D. P.; Heo, Y. W.; Ivill, M. P.; Ip, K.; Pearton, S. J.; Chisholm, M. F.; Steiner, T. ZnO: Growth, Doping & Processing. *Mater. Today* **2004**, *7*, 34–40.
- (13) Cooper, J. K.; Ling, Y.; Longo, C.; Li, Y.; Zhang, J. Z. Effects of Hydrogen Treatment and Air Annealing on Ultrafast Charge Carrier Dynamics in ZnO Nanowires Under in Situ Photoelectrochemical Conditions. *J. Phys. Chem. C* **2012**, *116*, 17360–17368.
- (14) Hewlett, R. M.; McLachlan, M. A. Surface Structure Modification of ZnO and the Impact on Electronic Properties. *Adv. Mater.* **2016**, *28*, 3893–3921.
- (15) Liu, Q.; Gong, M.; Cook, B.; Thapa, P.; Ewing, D.; Casper, M.; Stramel, A.; Wu, J. Oxygen Plasma Surface Activation of Electron-Depleted ZnO Nanoparticle Films for Performance-Enhanced Ultraviolet Photodetectors. *Phys. Status Solidi A* **2017**, *214*, 1700176–1700176.
- (16) Cao, P.; Zhao, D. X.; Zhang, J. Y.; Shen, D. Z.; Lu, Y. M.; Yao, B.; Li, B. H.; Bai, Y.; Fan, X. W. Optical and Electrical Properties of P-Type ZnO Fabricated by NH₃ Plasma Post-Treated ZnO Thin Films. *Appl. Surf. Sci.* **2008**, *254*, 2900–2904.
- (17) Yang, F.; Guo, J.; Zhao, L.; Shang, W.; Gao, Y.; Zhang, S.; Gu, G.; Zhang, B.; Cui, P.; Cheng, G.; Du, Z. Tuning Oxygen Vacancies and Improving UV Sensing of ZnO Nanowire by Micro-Plasma Powered by a Triboelectric Nanogenerator. *Nano Energy* **2020**, *67*, 104210–104210.
- (18) Gruber, D.; Kraus, F.; Müller, J. A Novel Gas Sensor Design Based on CH₄/H₂/H₂O Plasma Etched ZnO Thin Films. *Sens. Actuators, B* **2003**, *92*, 81–89.
- (19) Chen, S.-J.; Chang, C.-M.; Kao, J.-S.; Chen, F.-R.; Tsai, C.-H. Fabrication of ZnO Photonic Crystals by Nanosphere Lithography Using Inductively Coupled-Plasma Reactive Ion Etching with CH₄/H₂/Ar Plasma on the ZnO/GaN Heterojunction Light Emitting Diodes. *J. Vac. Sci. Technol., A* **2010**, *28*, 745–749.
- (20) Lee, K. K.; Luo, Y.; Lu, X.; Bao, P.; Song, A. M. Development of Reactive-Ion Etching for ZnO-Based Nanodevices. *IEEE Trans. Nanotechnol.* **2011**, *10*, 839–843.
- (21) Wang, L.; Zhang, X.; Zhao, Y.; Yamada, T.; Naito, Y. Investigation of H₂/CH₄Mixed Gas Plasma Post-Etching Process for ZnO:B Front Contacts Grown by LP-MOCVD Method in Silicon-Based Thin-Film Solar Cells. *Appl. Surf. Sci.* **2014**, *316*, 508–514.
- (22) Das, G.; Bose, S.; Sharma, J. R.; Mukhopadhyay, S.; Barua, A. K. Texturization of ZnO:Al Surface by Reactive Ion Etching in SF₆/Ar, CHF₃/Ar Plasma for Application in Thin Film Silicon Solar Cells. *J. Mater. Sci.: Mater. Electron.* **2018**, *29*, 6206–6214.
- (23) Woo, J.-C.; Ha, T.-K.; Li, C.; Kim, S.-H.; Park, J.-S.; Heo, K.-M.; Kim, C.-I. Dry Etching Characteristics of Zinc Oxide Thin Films in Cl₂-Based Plasma. *Transactions on electrical and electronic materials* **2011**, *12*, 60–63.
- (24) Min, S. R.; Cho, H. N.; Li, Y. L.; Chung, C. W. Inductively Coupled Plasma Reactive Ion Etching of ZnO Films in HBr/Ar Plasma. *Thin Solid Films* **2008**, *516*, 3521–3529.
- (25) Lee, G.-K.; Moon, J.-H.; Lee, B.-T. Inductively Coupled Plasma Reactive Ion Etching of ZnO Using C₂F₆ and NF₃-Based Gas Mixtures. *Semicond. Sci. Technol.* **2006**, *21*, 971–974.
- (26) Lee, J.-M.; Chang, K.-M.; Kim, K.-K.; Choi, W.-K.; Park, S.-J. Dry Etching of ZnO Using an Inductively Coupled Plasma. *J. Electrochem. Soc.* **2001**, *148*, G1–G1.
- (27) Hsueh, K.-P. Elucidating Surface Properties of Dry-Etched ZnO Using H₂/CH₄ and H₂/CH₄/Ar Plasma. *Appl. Surf. Sci.* **2010**, *257*, 969–973.
- (28) He, Y.; Jiang, C.; Yin, H.; Chen, J.; Yuan, W. Superhydrophobic Silicon Surfaces with Micro–Nano Hierarchical Structures via Deep Reactive Ion Etching and Galvanic Etching. *J. Colloid Interface Sci.* **2011**, *364*, 219–229.
- (29) Lupan, O.; Ababii, N.; Mishra, A. K.; Gronenberg, O.; Vahl, A.; Schürmann, U.; Duppel, V.; Krüger, H.; Chow, L.; Kienle, L.; Faupel, F.; Adelung, R.; de Leeuw, N. H.; Hansen, S. Single CuO/Cu₂O/Cu Microwire Covered by a Nanowire Network as a Gas Sensor for the Detection of Battery Hazards. *ACS Appl. Mater. Interfaces* **2020**, *12*, 42248–42263.
- (30) Ryong Ryu, S.; Ram, S. D. G.; Cho, H.-d.; Lee, D. J.; Won Kang, T.; Woo, Y. Single ZnO Nanocactus Gas Sensor Formed by Etching of ZnO Nanorod. *Nanoscale* **2015**, *7*, 11115–11122.
- (31) Ko, S. H.; Lee, D.; Kang, H. W.; Nam, K. H.; Yeo, J. Y.; Hong, S. J.; Grigoropoulos, C. P.; Sung, H. J. Nanoforest of Hydrothermally Grown Hierarchical ZnO Nanowires for a High Efficiency Dye-Sensitized Solar Cell. *Nano Lett.* **2011**, *11*, 666–671.
- (32) Lupan, O.; Emelchenko, G.; Ursaki, V.; Chai, G.; Redkin, A.; Gruzintsev, A.; Tiginyanu, I.; Chow, L.; Ono, L.; Roldan Cuenya, B.; Heinrich, H.; Yakimov, E. Synthesis and Characterization of ZnO Nanowires for Nanosensor Applications. *Mater. Res. Bull.* **2010**, *45*, 1026–1032.
- (33) Hassan, J.; Mahdi, M.; Chin, C.; Abu-Hassan, H.; Hassan, Z. A High-Sensitivity Room-Temperature Hydrogen Gas Sensor Based on

Oblique and Vertical ZnO Nanorod Arrays. *Sens. Actuators, B* **2013**, 176, 360–367.

(34) Mishra, Y. K.; Modi, G.; Cretu, V.; Postica, V.; Lupan, O.; Reimer, T.; Paulowicz, I.; Hrkac, V.; Benecke, W.; Kienle, L.; Adelung, R. Direct Growth of Freestanding ZnO Tetrapod Networks for Multifunctional Applications in Photocatalysis, UV Photo-detection, and Gas Sensing. *ACS Appl. Mater. Interfaces* **2015**, 7, 14303–14316.

(35) Park, J. S.; Park, H. J.; Hahn, Y. B.; Yi, G.-C.; Yoshikawa, A. Dry Etching of ZnO Films and Plasma-Induced Damage to Optical Properties. *J. Vac. Sci. Technol., B: Microelectron. Process. Phenom.* **2003**, 21, 800–803.

(36) Ip, K.; Baik, K. H.; Overberg, M. E.; Lambers, E. S.; Heo, Y. W.; Norton, D. P.; Pearton, S. J.; Ren, F.; Zavada, J. M. Effect of High-Density Plasma Etching on the Optical Properties and Surface Stoichiometry of ZnO. *Appl. Phys. Lett.* **2002**, 81, 3546–3548.

(37) Guo, Q.; Uesugi, N.; Tanaka, T.; Nishio, M.; Ogawa, H. Reactive Ion Etching of Zinc Oxide Using Methane and Hydrogen. *Jpn. J. Appl. Phys.* **2006**, 45, 8597–8599.

(38) Benedikt, J. Plasma-Chemical Reactions: Low Pressure Acetylene Plasmas. *J. Phys. D: Appl. Phys.* **2010**, 43, 043001.

(39) Jacob, W. Surface Reactions during Growth and Erosion of Hydrocarbon Films. *Thin Solid Films* **1998**, 326, 1–42.

(40) Marvi, Z.; von Wahl, E.; Trottenberg, T.; Kersten, H. Spatiotemporal Sampling of Growing Nanoparticles in an Acetylene Plasma. *J. Appl. Phys.* **2020**, 127, 173301–173301.

(41) Lupan, O.; Chai, G.; Chow, L. Novel Hydrogen Gas Sensor Based on Single ZnO Nanorod. *Microelectron. Eng.* **2008**, 85, 2220–2225.

(42) Lupan, O.; Ursaki, V.; Chai, G.; Chow, L.; Emelchenko, G.; Tiginyanu, I.; Gruzintsev, A.; Redkin, A. Selective Hydrogen Gas Nanosensor Using Individual ZnO Nanowire with Fast Response at Room Temperature. *Sens. Actuators, B* **2010**, 144, 56–66.

(43) Vepřek, S.; Sarott, F. A. Electron-Impact-Induced Anisotropic Etching of Silicon by Hydrogen. *Plasma Chem. Plasma Process.* **1982**, 2, 233–246.

(44) Vepřek, S.; Wang, C.; Ratz, G. Control of Isotropic and Anisotropic Etching and Surface Cleaning of Silicon and Silicon Dioxide in a Hydrogen Plasma. *MRS Proc.* **1992**, 282, 511.

(45) Oehrlein, G. S.; Hamaguchi, S. Foundations of Low-Temperature Plasma Enhanced Materials Synthesis and Etching. *Plasma Sources Sci. Technol.* **2018**, 27, 023001.

(46) Oehrlein, G. S.; Phaneuf, R. J.; Graves, D. B. Plasma-Polymer Interactions: A Review of Progress in Understanding Polymer Resist Mask Durability during Plasma Etching for Nanoscale Fabrication. *J. Vac. Sci. Technol., B: Nanotechnol. Microelectron.: Mater., Process., Meas., Phenom.* **2011**, 29, 010801.

(47) Jo, W.; Kim, S.-J.; Kim, D.-Y. Analysis of the Etching Behavior of ZnO Ceramics. *Acta Mater.* **2005**, 53, 4185–4188.

(48) Langmuir, I. Positive Ion Currents from the Positive Column of Mercury Arcs. *Science* **1923**, 58, 290–291.

(49) Lieberman, M. A.; Lichtenberg, A. J. *Principles of Plasma Discharges and Materials Processing: Lieberman/Plasma*, 2nd ed.; John Wiley & Sons, Inc.: Hoboken, NJ, 2005.

(50) Mehta, M.; Ruth, M.; Piegdon, K. A.; Krix, D.; Nienhaus, H.; Meier, C. Inductively Coupled Plasma Reactive Ion Etching of Bulk ZnO Single Crystal and Molecular Beam Epitaxy Grown ZnO Films. *Journal of Vacuum Science & Technology B: Microelectronics and Nanometer Structures Processing, Measurement, and Phenomena* **2009**, 27, 2097–2101.

(51) Li, H.; Karahashi, K.; Friederich, P.; Fink, K.; Fukasawa, M.; Hirata, A.; Nagahata, K.; Tatsumi, T.; Wenzel, W.; Hamaguchi, S. Effects of Hydrogen Ion Irradiation on Zinc Oxide Etching. *J. Vac. Sci. Technol., A* **2017**, 35, 05C303–05C303.

(52) Lim, W.; Voss, L.; Khanna, R.; Gila, B. P.; Norton, D. P.; Pearton, S. J.; Ren, F. Comparison of CH₄/H₂ and C₂H₆/H₂ Inductively Coupled Plasma Etching of ZnO. *Appl. Surf. Sci.* **2006**, 253, 1269–1273.

(53) Geraud-Grenier, I.; Mikikian, M.; Faubert, F.; Massereau-Guilbaud, V. Massereau-Guilbaud, V. Plasma Chemistry and Dust-Particle Generation in Pure Methane Plasma: Influence of the RF Electrode Cleanliness. *J. Appl. Phys.* **2019**, 126, 063301–063301.

(54) Han, X.; Zhou, X.; Jiang, Y.; Xie, Z. The Preparation of Spiral ZnO Nanostructures by Top-down Wet-Chemical Etching and Their Related Properties. *J. Mater. Chem.* **2012**, 22, 10924.

(55) Meng, L.; Xu, Q.; Sun, Z.; Li, G.; Bai, S.; Wang, Z.; Qin, Y. Enhancing the Performance of Room Temperature ZnO Microwire Gas Sensor through a Combined Technology of Surface Etching and UV Illumination. *Mater. Lett.* **2018**, 212, 296–298.

(56) Daria, S.; Sindu, S.; Mathias, H.; Luka, H.; Janik, M.; Jannes, D.; Zaho, K.; Bodo, F.; Holger, K.; Rainer, A. Surface Modification of Highly Porous 3D Networks via Atmospheric Plasma Treatment. *Contrib. Plasma Phys.* **2018**, 58, 384–393.

(57) Lavanya, N.; Sekar, C.; Fazio, E.; Neri, F.; Leonardi, S.; Neri, G. Development of a Selective Hydrogen Leak Sensor Based on Chemically Doped SnO₂ for Automotive Applications. *Int. J. Hydrogen Energy* **2017**, 42, 10645–10655.

(58) Ndaya, C. C.; Javahiraly, N.; Brioude, A. Recent Advances in Palladium Nanoparticles-Based Hydrogen Sensors for Leak Detection. *Sensors* **2019**, 19, 4478.

(59) Khan, R.; Ra, H.-W.; Kim, J.; Jang, W.; Sharma, D.; Im, Y. Nanojunction Effects in Multiple ZnO Nanowire Gas Sensor. *Sens. Actuators, B* **2010**, 150, 389–393.

(60) Rout, C. S.; Kulkarni, G. U.; Rao, C. N. R. Room Temperature Hydrogen and Hydrocarbon Sensors Based on Single Nanowires of Metal Oxides. *J. Phys. D: Appl. Phys.* **2007**, 40, 2777–2782.

(61) Lupan, O.; Chai, G.; Chow, L. Fabrication of ZnO Nanorod-Based Hydrogen Gas Nanosensor. *Microelectron. J.* **2007**, 38, 1211–1216.

(62) Lupan, O.; Chow, L.; Chai, G. A Single ZnO Tetrapod-Based Sensor. *Sens. Actuators, B* **2009**, 141, 511–517.

(63) Chu, J.; Peng, X.; Sajjad, M.; Yang, B.; Feng, P. X. Nanostructures and Sensing Properties of ZnO Prepared Using Normal and Oblique Angle Deposition Techniques. *Thin Solid Films* **2012**, 520, 3493–3498.

(64) Gu, H.; Wang, Z.; Hu, Y. Hydrogen Gas Sensors Based on Semiconductor Oxide Nanostructures. *Sensors* **2012**, 12, 5517–5550.

(65) Greyson, E. C.; Babayan, Y.; Odom, T. W. Directed Growth of Ordered Arrays of Small-Diameter ZnO Nanowires. *Adv. Mater.* **2004**, 16, 1348–1352.

(66) Fallahazad, P.; Naderi, N.; Eshraghi, M. J.; Massoudi, A. Combination of Surface Texturing and Nanostructure Coating for Reduction of Light Reflection in ZnO/Si Heterojunction Thin Film Solar Cell. *J. Mater. Sci.: Mater. Electron.* **2018**, 29, 6289–6296.

(67) Schutt, F.; Zapf, M.; Signetti, S.; Strobel, J.; Kruger, H.; Roder, R.; Carstensen, J.; Wolff, N.; Marx, J.; Carey, T.; Schweichel, M.; Terasa, M.-I.; Siebert, L.; Hong, H.-K.; Kaps, S.; Fiedler, B.; Mishra, Y. K.; Lee, Z.; Pugno, N. M.; Kienle, L.; Ferrari, A. C.; Torrisi, F.; Ronning, C.; Adelung, R. Conversionless Efficient and Broadband Laser Light Diffusers for High Brightness Illumination Applications. *Nat. Commun.* **2020**, 11, 1437.

(68) Liu, F.; Leung, Y. H.; Djurišić, A. B.; Ng, A. M. C.; Chan, W. K.; Ng, K. L.; Wong, K. S.; Liao, C.; Shih, K.; Surya, C. Effect of Plasma Treatment on Native Defects and Photocatalytic Activities of Zinc Oxide Tetrapods. *J. Phys. Chem. C* **2014**, 118, 22760–22767.

(69) Deo, M.; Shinde, D.; Yengantiwar, A.; Jog, J.; Hannoyer, B.; Sauvage, X.; More, M.; Ogale, S. Cu₂O/ZnO Hetero-Nanobrush: Hierarchical Assembly, Field Emission and Photocatalytic Properties. *J. Mater. Chem.* **2012**, 22, 17055.

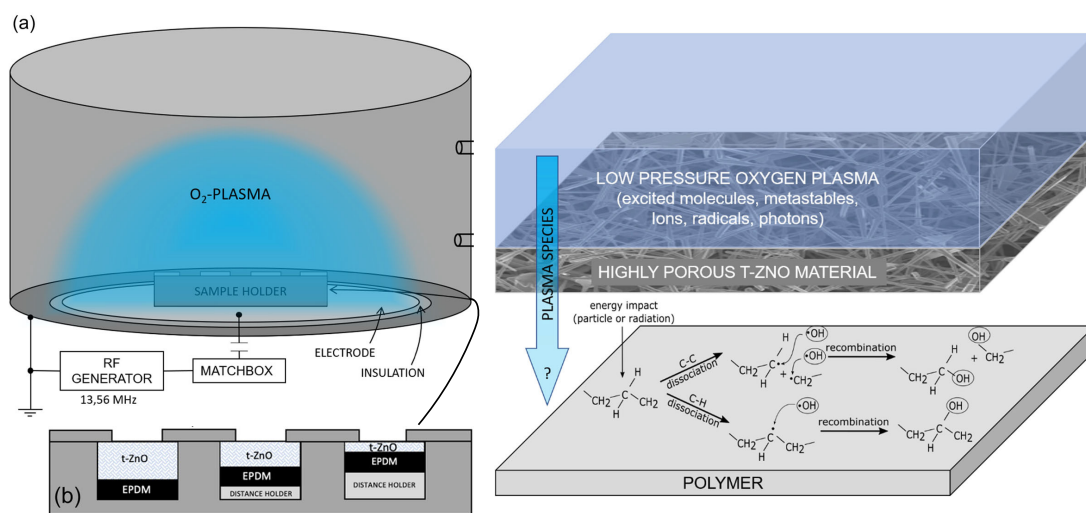
(70) Pal, S.; Maiti, S.; Maiti, U. N.; Chattopadhyay, K. K. Spontaneous Hyper-Branching in ZnO Nanostructures: Morphology Dependent Electron Emission and Light Detection. *RSC Adv.* **2015**, 5, 81176–81187.

Publication V

On the plasma permeability of highly porous ceramic framework materials using polymers as marker materials

Authors	M. L. Marxen, L. Hansen, A. Reimers, T. Tjardts, L. M. Saure, E. Greve, J. Drewes, F. Schütt, R. Adelung, and H. Kersten
Journal	Plasma Processes and Polymers [326]
Technique	Novel technique utilizing a polymers surface activation
Utilized diagnostics	Power, pressure and DC bias monitoring, WCA measurements, XPS analysis, SEM, and EDX imaging
Own contribution	Approx. 30 %

Experimental Setup:



Reprinted (adapted) from [326].

Reprinted (adapted) from [326].

Motivation:

A fundamental question in the context of highly porous materials is the permeation of plasma species into or through the highly porous material. These highly porous materials excel through their high surface-to-volume ratio as already mentioned in context of the previous presented etching process. Tetrapodal ZnO is used as example material for highly porous ceramic framework materials. Knowledge about the penetration depth is key for the production of large quantities of etched t-ZnO, as well as more generalized plasma modifications of highly porous materials or the effective design of plasma catalysis reactors using highly porous materials as catalysts. A novel approach using polymers as marker materials was considered, as the plasma polymer interaction is well studied and can be analyzed with rather simple techniques like WCA measurements.

Main Results:










The proof of principle for the method of using a polymer as marker material to study the plasma permeability of highly porous framework materials was successful. Plasma species produced in an O₂ low-pressure CCP could permeate through the t-ZnO up

to a thickness of 1.6 mm, or up to 4 mm, depending on the sample holder material, and activate the polymer surface. The origin of the surface activation was an increase in the O/C ratio from 11 % to 26 % determined via XPS measurements for a t-ZnO thickness of 1.6 mm and a density of 0.3 g cm^{-3} . Increasing thickness or density of the t-ZnO resulted in less or no surface activation as expected. Placing the samples in the plasma bulk instead of on top of the electrode in the plasma sheath resulted in less surface activation. This fact in combination with the dependence on the conductivity of the sample holder hints towards ions being the dominant species for the permeation of the porous framework materials.

RESEARCH ARTICLE

PLASMA PROCESSES
AND POLYMERS

On the plasma permeability of highly porous ceramic framework materials using polymers as marker materials

M. Leander Marxen¹  | Luka Hansen¹  | Armin Reimers²  |
Tim Tjardts³  | Lena M. Saure²  | Erik Greve² | Jonas Drewes³  |
Fabian Schütt²  | Rainer Adelung²  | Holger Kersten¹ 

¹Plasma Technology, Institute of Experimental and Applied Physics, Kiel University (CAU), Kiel, Germany

²Functional Nanomaterials, Faculty of Engineering, Institute of Material Science, Kiel University (CAU), Kiel, Germany

³Multicomponent Materials, Faculty of Engineering, Institute of Material Science, Kiel University (CAU), Kiel, Germany

Correspondence

M. Leander Marxen, Plasma Technology, Institute of Experimental and Applied Physics, Kiel University, Kiel 24118, Germany.

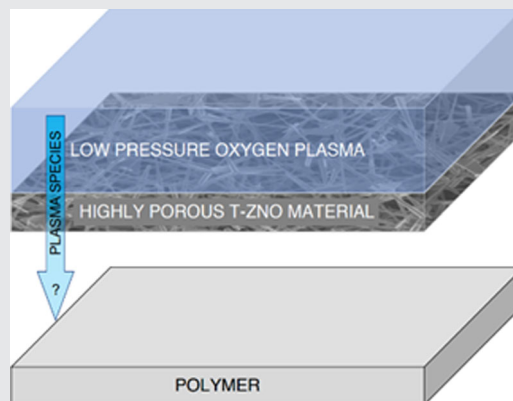
Email: marxen@physik.uni-kiel.de

Funding information

Deutsche Forschungsgemeinschaft, Grant/Award Numbers: Project Number 413664940, Grant Number KE 574/8-1

Abstract

Highly porous framework materials are of large interest due to their broad potential for application, for example, as sensors or catalysts. A new approach is presented to investigate, how deep plasma species can penetrate such materials. For this purpose, a polymer (ethylene propylene diene monomere rubber) is used as marker material and covered with the porous material during plasma exposure. Water contact-angle and X-ray photoelectron spectroscopy measurements are used to identify changes in the polymer surface, originating from the interaction of plasma species with the polymer. The method is demonstrated by studying the plasma permeability of tetrapodal zinc oxide framework materials with a porosity of about 90% in an oxygen low-pressure capacitively coupled plasma. Significant differences in the penetration depth ranging from roughly 1.6–4 mm are found for different densities of the material and different treatment conditions.



KEYWORDS

low-pressure discharges, plasma permeability, polymer activation, porous materials, tetrapodal zinc oxide

Abbreviations: CCP, capacitively coupled plasma; EPDM, ethylene propylene diene monomere rubber; HR, high resolution; rf, radio frequency; SEM, scanning electron microscope; t-ZnO, tetrapodal zinc oxide; UHV, ultra high vacuum; WCA, water contact-angle; XPS, X-ray photoelectron spectroscopy.

This is an open access article under the terms of the Creative Commons Attribution License, which permits use, distribution and reproduction in any medium, provided the original work is properly cited.

© 2022 The Authors. *Plasma Processes and Polymers* published by Wiley-VCH GmbH.

1 | INTRODUCTION

The properties of zinc oxide (ZnO) such as for example, being a high band gap semiconductor, chemically stable, and biocompatible resulted in extensive research and a wide range of applications such as gas sensing or catalysis.^[1–5] Tetrapodal zinc oxide (t-ZnO) became a focus of research as individual tetrapod-shaped ZnO crystals can interconnect and form a network of interconnected tetrapods.^[6] This results in a 3D structured, highly porous framework material with a large surface-to-volume ratio.

Controlling the crystal morphology and defect structure of the t-ZnO enables adaptation to the different applications. Plasma treatment of ZnO showed promising results in modifying ZnO by, for example, plasma etching^[7–15], to improve its properties^[16–18], such as p-type conductivity^[17]. To combine the advantages of the 3D highly porous t-ZnO with modifications gained by plasma treatment, plasma penetration into the 3D structure is necessary.

Further, the plasma itself can be strongly affected by plasma-surface-interactions like secondary electron emission.^[19–24] Thus, usage of the large surface-to-volume ratio of t-ZnO as electrode material could enhance plasma properties, especially, for microplasmas, where the surface-to-volume ratio is already quite large.^[25–27]

Other examples, like plasma catalysis^[28–31], also showcase applications where the penetration of plasma species into the highly porous t-ZnO material is favorable if not necessary. Thus, in this study, we present a simple and convenient approach to determine the plasma

permeability of highly porous materials using the example of t-ZnO framework materials.

In the past, investigations were made to study, for example, the transmission of N-atoms in the afterglow of a microwave discharge through porous materials like sterilization pouches (2D structured materials).^[32,33] Canal et al. used hydrophobic textiles as indicator material behind the porous sheet. For those textiles, the wetting time was measured after plasma exposure.^[33] The t-ZnO framework materials, which were studied in this work, feature a truly 3-dimensional porous structure.^[6] The hydrophobic textile was replaced with a suitable polymer as marker material, which offers an even easier method to determine the plasma permeability of porous materials. Figure 1 shows the idea schematically.

The interaction of plasma with polymer surfaces has been described in many publications and textbooks.^[34–40] Oversimplified summarizing, high energy plasma particles and UV-radiation lead to dissociations of the C–C- and C–H-bonds. Thus, other atoms or groups can be attached to the C-radical sites, depending on the reactive species in the plasma. Exposing a polymer to an oxygen plasma leads to functionalization of the polymer surface by the attachment of oxygen-containing polar groups, as sketched with OH-groups as an example in Figure 1. One expects to detect C–O–C, C–O–H, C–O–O–H, and C=O bonds within the C 1s-Peak of an XPS high-resolution (HR) scan of the surface.

This functionalization leads to a decreased water contact angle (WCA) and a higher oxygen ratio on the surface of the polymer. Depending on the chosen

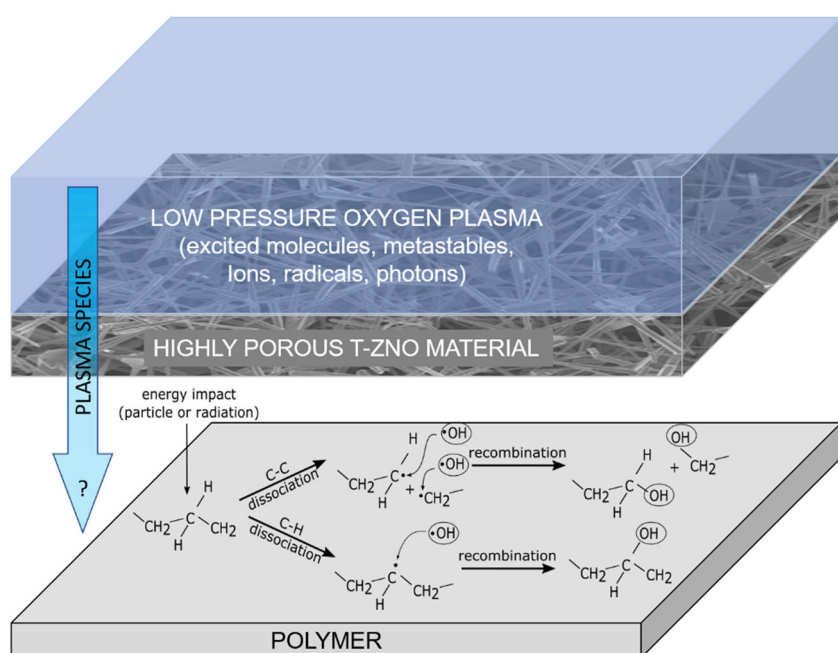


FIGURE 1 Schematic illustration of the indirect approach. If plasma species permeate the highly porous tetrapodal zinc oxide (t-ZnO) framework material, they will modify the surface of the polymer marker material. In the real setup, the gap between the t-ZnO and the polymer does not exist (see Figure 2b).

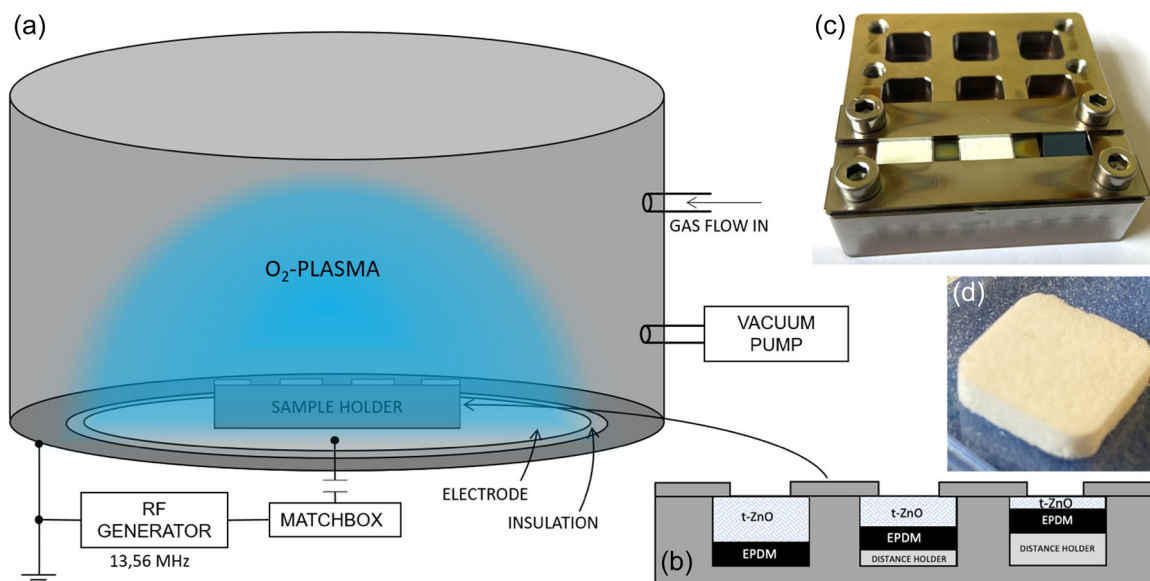


FIGURE 2 (a) Setup for the plasma chamber. (b) Schematic of the sample holder for ethylene propylene diene monomere rubber (EPDM) test polymer covered by tetrapodal zinc oxide (t-ZnO). There is no possibility for the plasma species to reach the EPDM surface directly without permeating the t-ZnO sample. (c) Photograph of the filled stainless-steel sample holder with t-ZnO covers on two samples (left and middle) and pristine EPDM on the right. (d) Photograph of a 2.5 mm thick t-ZnO sample.

polymer and plasma parameters, significant differences in surface modification can easily be measured. Thus, a suitable polymer can be used as an indicator material to study, if plasma can permeate through highly porous 3D structures, which are placed on top of it.

2 | EXPERIMENTAL SECTION

The experiments were performed in an oxygen (Air Liquide, 99.9999% purity) low-pressure CCP.^[41–43] This comes with the advantage of low mechanical impact on the studied material samples compared to strong gas flows using atmospheric pressure plasma jets.^[44] The walls of the plasma chamber are used as the grounded electrode, which results in a large geometric asymmetry (Figure 2a). Hence, a negative self-bias occurs, which has been described elsewhere.^[41,45]

The change of the WCA of the EPDM surface due to oxygen plasma treatment was found to be high in comparison to other for us available polymers (e.g., polyethylene or polypropylene) in former, unpublished measurements of our group. Hence, it was chosen as suitable marker material. Untreated EPDM has a WCA of about 130°. A parameter study was performed to determine the pressure p , rf-plasma power P_{RF} , and treatment time t , for which the maximum change in WCA is observed. The smallest WCA (30°) was found for $p = 10$ Pa, $P_{\text{RF}} = 80$ W and $t = 6$ min. The selfbias is

roughly -700 V. These conditions were realized for all further experiments.

To guarantee the same plasma conditions for t-ZnO samples of varying thicknesses, a sample holder was constructed, which is schematically shown in Figure 2b. A photograph of the holder when typically filled for the experiment is shown in Figure 2c. The whole setup with the sample holder in the plasma chamber is sketched in Figure 2a.

To gain insight into the penetrating species (ions or neutral components like atomic oxygen, molecular oxygen or ozone), different holder potentials were realized. One holder was made out of stainless steel, one was made out of Teflon. The positioning inside the chamber was varied between in the plasma sheath (directly on the rf-electrode, Figure 3a,b) and in the plasma bulk. To lift the holder into the bulk, glass cylinders (height about 4 cm, Figure 3c) were used. In the bulk, the holder acts as a floating body with a floating potential of approximately -10 V. On the rf-electrode, the stainless-steel holder will adopt the negative self-bias potential. In contrast, the Teflon holder will be like a dielectric barrier in front of the electrode. The changes in the sheath configuration are even visible the naked eye (Figure 3).

It was also investigated, if any change in the behavior of the t-ZnO samples is obtained, when they are exposed to the plasma multiple times. For this, the stainless-steel holder was placed in the sheath and in the bulk.

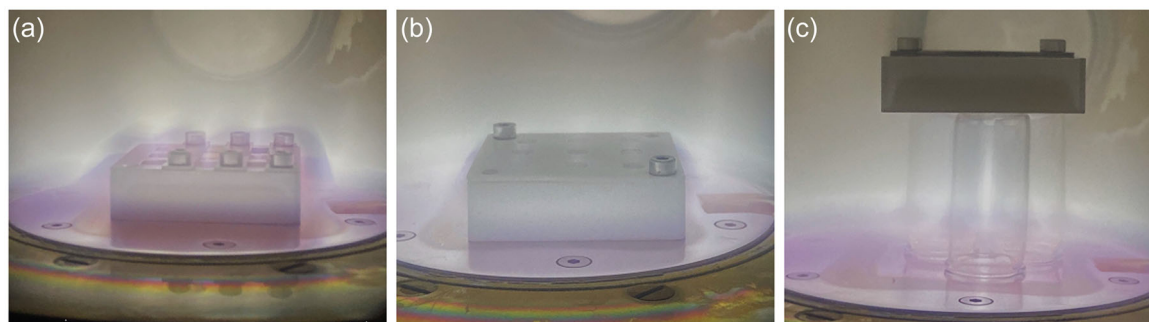


FIGURE 3 Different materials of the sample holders and different positions in the plasma chamber lead to different sheath configurations in front of the tetrapodal zinc oxide (t-ZnO)/ethylene propylene diene monomere rubber (EPDM) substrate. (a) Stainless steel holder on the rf-electrode/in the sheath. (b) Teflon holder on the rf-electrode/in the sheath. (c) Stainless steel holder on glass cylinders and, thus, lifted into the plasma bulk. There is no visible sheath for this configuration.

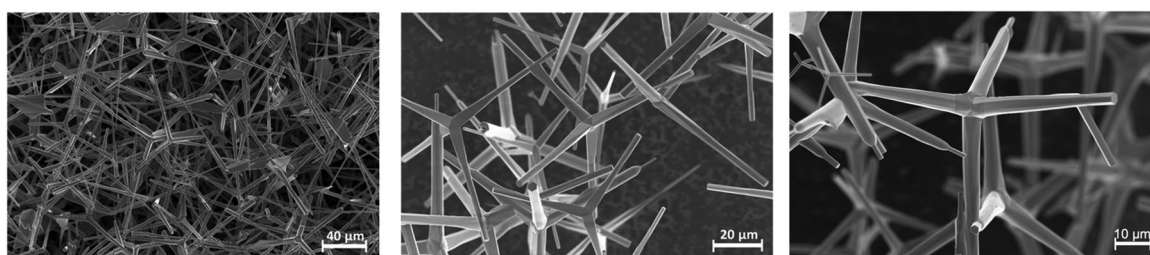


FIGURE 4 Scanning electron microscope pictures of the investigated tetrapodal zinc oxide (t-ZnO) samples with a mass density of 0.3 g cm^{-3} at different scales

WCA measurements were used as a fast and easy method to determine changes in the surface tension due to plasma species that have permeated the t-ZnO material.^[46–48] The sessile-drop method^[46] was conducted via a custom-built setup. More precise information was obtained by XPS.^[46] It was performed for samples in both holders for placement in the sheath. The goal was to prove that the reduced WCA arises from oxygen-containing polar groups, which were formed on the EPDM surface underneath the covering highly porous 3D structures during the plasma exposure. The XPS measurements were conducted with an XPS UHV system (PREVAC Sp. z o. o.) at a pressure of 10^{-9} mbar. An Aluminum anode X-ray tube operated at 300 W (15 kV, 20 mA) was utilized as an X-ray source. Survey scans were conducted at three iterations and a pass energy of 200 eV, while HR scans were performed at 20 iterations and a pass energy of 50 eV. The charge correction was done with the C 1 s main peak at 284.8 eV.

The production of the t-ZnO (Flame Transport Synthesis) was described by Gedamu et al. elsewhere.^[49] It was pressed into $10 \times 10 \text{ mm}$ samples of varying thickness, which were then sintered for 5 h at 1150°C (Figure 2d contains a 2.5 mm thick sample as an

example). Figure 4 shows pictures of a 0.3 g cm^{-3} density t-ZnO framework in different scales, obtained by scanning electron microscopy (SEM). The randomly distributed arms of the ZnO tetrapods form an interconnected network, creating a completely open porous framework material. The porosity of this framework material in % can be calculated by comparing the network's density with the bulk density of ZnO ($\rho_{\text{ZnO}} = 5.61 \text{ g cm}^{-3}$) using the formula $\phi = \left(1 - \frac{\rho_{\text{network}}}{\rho_{\text{ZnO}}}\right) * 100$.^[44]

Most of the investigated t-ZnO framework material samples have mass densities of 0.3 g cm^{-3} , which corresponds to a porosity of $\phi = 94.7\%$. For the stainless-steel holder in the sheath, t-ZnO samples of thicknesses between 1.0 and 2.5 mm were investigated. For the Teflon holder in the sheath, the t-ZnO samples had thicknesses from 1.0 to 5.0 mm. Measurements for multiple usages of the same t-ZnO samples in the sheath and in the bulk were made for t-ZnO with a thickness of 1.6 mm. For 1.3 mm thick t-ZnO samples, densities of 0.45 g cm^{-3} ($\phi = 92.0\%$) and 0.6 g cm^{-3} ($\phi = 89.3\%$) were studied. They were placed in the sheath using the stainless-steel holder.

3 | RESULTS AND DISCUSSION

For placing the stainless-steel holder directly on the rf-electrode, the thickness of the covering material is varied between 1.0 and 2.5 mm. The samples have a mass density of 0.3 g cm^{-3} . In Figure 5, the results for the EPDM examination after the plasma exposure are shown. All depicted results for the performed WCA measurements include error bars originating from repetitions of the experiments. The WCA and XPS values for uncovered (dark green in Figure 5, WCA of $[24 \pm 6]^\circ$) and untreated (red, WCA of $[136 \pm 5]^\circ$) EPDM markers can be considered as references. Figure 5a illustrates the increasing WCA if thicker t-ZnO samples cover the EPDM during the plasma exposure. Starting at $(24 \pm 6)^\circ$ for the uncovered EPDM, the WCA increases to $(56 \pm 16)^\circ$ for 1.0 mm, to $(70 \pm 19)^\circ$ for 1.3 mm, and to

$(84 \pm 25)^\circ$ for 1.6 mm, until it reaches values between 130° and 140° for covering thicknesses of 1.9 mm and thicker. A WCA in this region means no significant change in the surface tension of the marker polymer. These results are very intuitive, as they reveal a better permeability for thinner covers. There are large error bars when a treatment effect underneath the cover occurs (1.0–1.6 mm). The reason for this is probably that the treatment effect on the covered EPDM changes dramatically for little inhomogeneities of the porous material samples. Nevertheless, there is a nonneglectable increasing trend of the WCA in the data for thicker covers.

It is yet to validate that this effect truly is due to oxygen-containing functional groups generated at the EPDM surface and, thus, it is a plasma treatment effect. The XPS measurement (Figure 5b) delivers this

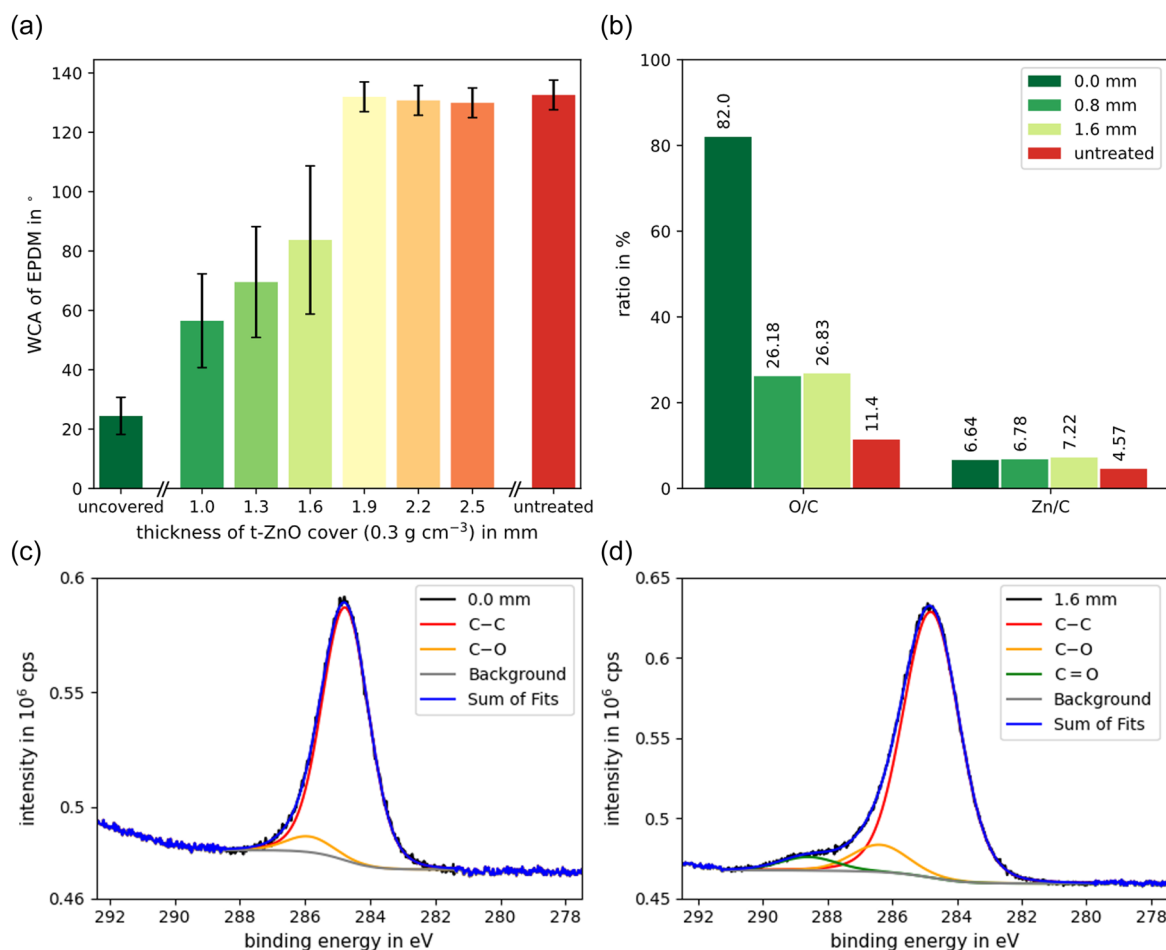


FIGURE 5 Results for different thicknesses of tetrapodal zinc oxide (t-ZnO) covers. The mass density of the t-ZnO is 0.3 g cm^{-3} , the stainless-steel holder was used and placed directly on the rf-electrode. (a) Water contact-angle (WCA) and (b) X-ray photoelectron spectroscopy (XPS) data for the ethylene propylene diene monomere rubber (EPDM) surface after the plasma exposure. (a, b) Include data for untreated EPDM (red bars) and uncovered EPDM (dark green bars), which can be regarded as reference values. (c) High resolution (HR) scan of the C 1s-peak for uncovered EPDM after the plasma exposure. (d) HR scan of the C 1s-peak for EPDM, which was covered with 1.6 mm t-ZnO during the plasma exposure.

information. Data were acquired for pristine EPDM before (untreated) and after plasma exposure (uncovered) as well as for EPDM that was covered with t-ZnO samples. The samples had thicknesses of 0.8 mm and 1.6 mm and a mass density of 0.3 g cm^{-3} . The results show an extreme increase in the O/C ratio for the uncovered EPDM from 11.4%–82.0%. For the covered EPDM, there is still a significant increase in the O/C ratio. A value of more than 26% was observed for both t-ZnO thicknesses. The Zn/C ratio is in the same range (4.5%–7%) for all EPDM samples. This reveals only a small ZnO contamination of the EPDM surface. HR XPS scans of the C 1s-peak (Figure 5c,d) show that C–O ($\sim 286 \text{ eV}$ ^[40]) and C=O ($\sim 289 \text{ eV}$ ^[40]) bonds were formed at the EPDM surface. Hence, the large increase in the O/C ratio will originate from oxygen-containing functional groups (and not from ZnO contamination). These results allow concluding that plasma species can permeate through the highly porous t-ZnO networks.

Summarizing the above, the larger wettability of the EPDM surface, measured by WCA, can be attributed to functionalization of the polymer and does not originate from ZnO leftovers on the surface. Furthermore, the penetration depth of plasma species into the t-ZnO framework material of 0.3 g cm^{-3} can be estimated as approximately 1.6 mm under these conditions.

Considering that plasma species (in particular: oxygen radicals/ions) can permeate the porous framework material, parameters and experimental conditions were varied. The t-ZnO density, the material of the sample holder, and the position in the plasma chamber are changed to investigate their influence on the permeability.

A higher mass density of the t-ZnO cover should lead to a weaker plasma treatment effect on the EPDM surface. Figure 6 confirms at least the trend for this expectation. Taking the large error for frameworks of 0.3 g cm^{-3} density into account ($70 \pm 19^\circ$), it can be concluded that the assumption should be right. The highest studied mass density of a t-ZnO sample is 0.6 g cm^{-3} , which hardly leads to any effect on the EPDM surface ($127 \pm 6^\circ$).

Figure 7 shows that the holder material plays a major role in the permeation through the t-ZnO samples. The Teflon holder was used in the sheath to gain insight into the influence of the holder's potential. The different sheath configurations for the two holders are visible by the naked eye (Figure 3a,b). The WCA for a thickness variation of the t-ZnO samples is depicted in Figure 7a. The blue bars show the values for the Teflon holder. A much better treatment effect on the EPDM surface for all thicknesses (including uncovered EPDM treatment) relative to the stainless-steel holder is observed. For the

t-ZnO in the stainless-steel holder, there is no change in the WCA compared to the untreated EPDM for covering thicknesses larger than 1.9 mm. In contrast, there is just a relatively small change between uncovered treated EPDM ($8 \pm 5^\circ$) and a cover thickness of 1.9 mm ($24 \pm 5^\circ$) in the Teflon holder. Even for a thickness of 4 mm, there is still a small effect in the contact angle of the EPDM ($126 \pm 7^\circ$) if using the Teflon holder.

The XPS measurements in Figure 7b confirm the WCA results. The O/C ratio of the EPDM, which was covered with 1.6 mm thick t-ZnO in the Teflon holder, is 32.55%. This is about 6% higher than in the stainless steel holder. Another important result of the XPS measurement is the fluorine ratio F/C. Since Teflon is not inert to plasma^[50], fluorine compounds could also be responsible for the smaller WCA values. However, there is no significant F/C ratio for the EPDM that was covered with the t-ZnO. Figure 7c shows an HR XPS scan for binding energies, at which fluorine would be detected.^[51,52] A clear peak is found only for the uncovered EPDM sample in the Teflon holder. In Figure 7d, C–O and C=O bonds can be found as subpeaks in the C 1s-peak of the EPDM, which was covered with 1.6 mm t-ZnO during the plasma exposure. C–Fx bonds would have been detected at binding energy between 293 and 294 eV.^[51] They are not found in these measurements. Hence, the smaller WCA originates from the higher oxygen ratio and not from fluorine compounds. Additional EDX (energy dispersive X-ray spectroscopy)^[53] measurements also showed no significant fluorine concentration in the t-ZnO samples, which were used in the Teflon holder. Thus, released fluorine will not be responsible for the enhanced plasma permeability in the Teflon holder.

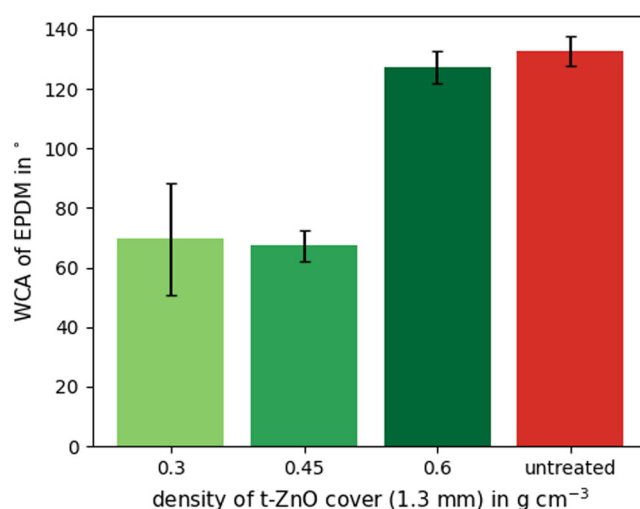


FIGURE 6 Variation of the mass density of the tetrapodal zinc oxide (t-ZnO) samples. The samples were used in the stainless-steel holder in the sheath

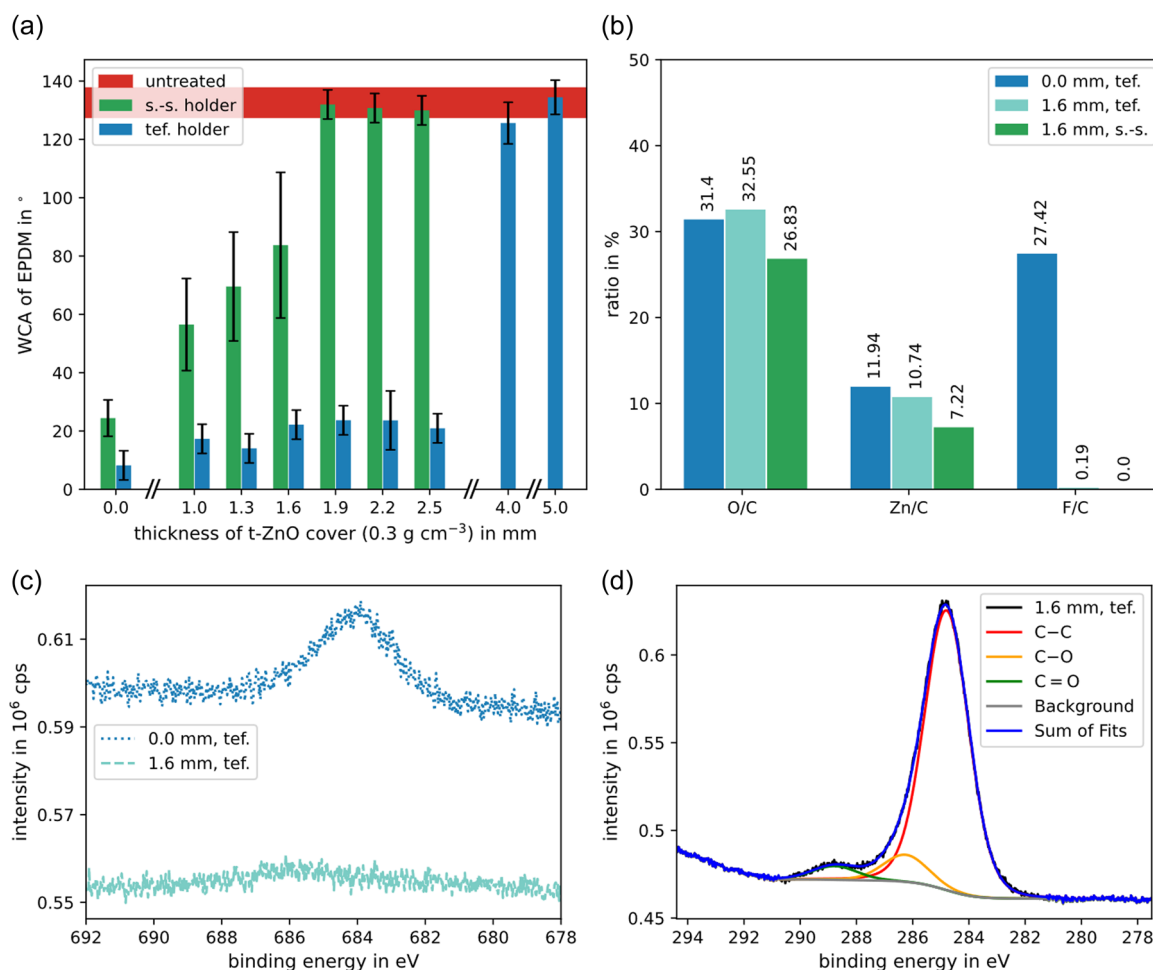


FIGURE 7 Comparison of the Teflon (tef.) holder (blue bars) and the stainless-steel (s.s.) holder (green bars). Both holders were placed in the sheath. (a) Water contact-angle results. For values $\leq 15^\circ$, the water drop was covering almost the complete ethylene propylene diene monomere rubber (EPDM) surface. (b) X-ray photoelectron spectroscopy (XPS) examined surface composition. (c) High resolution (HR) scan of the F 1s-peak. (d) HR scan of the C 1s-peak for EPDM which was covered with 1.6 mm t-ZnO during the plasma exposure in the Teflon holder.

A possible explanation for better surface activation in the Teflon holder compared to the stainless-steel holder could be the following. The stainless-steel holder on the rf-electrode adopts the self-bias potential of roughly -700 V. The t-ZnO samples, instead, will not adopt this potential and will be less negatively charged. Thus, positive ions are deflected in their trajectories and attracted toward the stainless-steel of the holder. This could work similar as a defocusing ion lens. It would result in fewer ions arriving at the top t-ZnO and permeating it towards the bottom EPDM. The Teflon holder instead works like a dielectric barrier in front of the electrode and will not influence the trajectories of the arriving species as much.

To investigate changes in the plasma permeability of the t-ZnO for multiple plasma exposures, four samples of 1.6 mm thickness were used three times each. An unused EPDM sample was placed underneath the t-ZnO for

every run. Figure 8a shows the WCA results. It holds values for positioning in the sheath (light green) and in the bulk (darker green). The different positions result in different sheath configurations (Figure 3). The uncovered EPDM has a WCA of $(79 \pm 5)^\circ$ after being treated in the bulk. In the bulk, the ions, which arrive at the samples, have smaller kinetic energy compared to sample placement in the sheath. This explains, why the overall WCA values are higher for treatment in the bulk. The covered EPDM showed a WCA of about 120° for all three usages of the t-ZnO in the bulk. In contrast, for treatment in the sheath, the WCA decreases with every usage of the t-ZnO samples. (Note: The value for the first use in the sheath differs from the value for 1.6 mm in Figure 5a. That is, because only those samples were considered here, which were truly used multiple times). For the first use, the WCA of the EPDM underneath is $(76 \pm 8)^\circ$, for the second use $(57 \pm 12)^\circ$ and for the third use $(44 \pm 9)^\circ$.

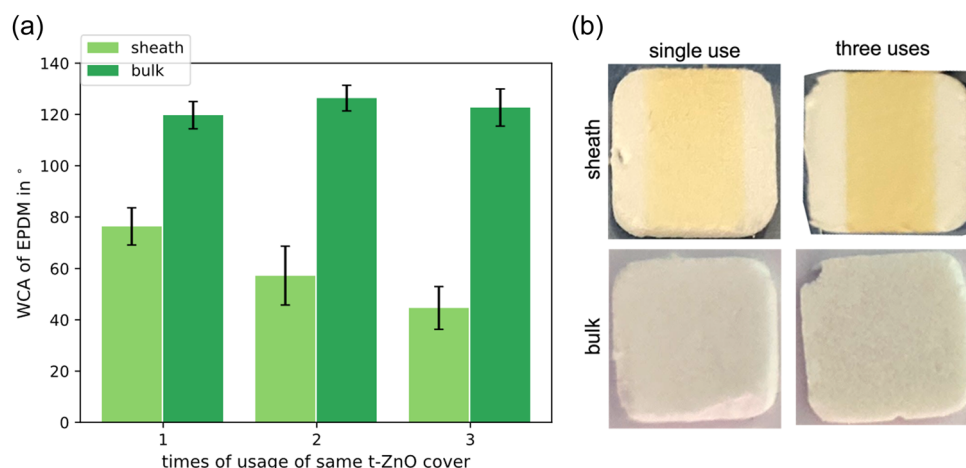


FIGURE 8 Multiple usage of the same tetrapodal zinc oxide (t-ZnO) samples. The samples had a thickness of 1.6 mm and a mass density of 0.3 g cm^{-3} . The stainless steel holder was used. (a) Water contact-angle results. A comparison is made for plasma exposure in the sheath/directly on the rf-electrode (light green) versus in the bulk (darker green). (b) Photos of the t-ZnO samples after the plasma exposure.

Thus, plasma exposure of the t-ZnO in the sheath enhances its plasma permeability.

This also hints toward the species that play a major role in the functionalization of the polymer surface underneath the t-ZnO. In the bulk, the ions are not accelerated to the samples as much as in the sheath (the potential of the holder is roughly -10 to -20 V in comparison to -700 V). On the other hand, neutral species like atomic and molecular oxygen or ozone are barely affected by the different electrical configurations in the bulk. They will even be present at higher densities. Thus, one can assume that ions from the discharge are the major species permeating the porous t-ZnO material. Further, the role of UV-photons will be negligible for the same reason and EPDM was found to be resistant to UV radiation within the short treatment times used in this study.^[54]

In Figure 8b, photos of the t-ZnO samples are shown. The samples in the upper row were exposed to the plasma in the sheath, in the lower row in the bulk. The left photos were taken after the first use and the right photos after the third use of the samples. For positioning in the sheath, an increasing yellowish color change is visible. In contrast, the samples in the bulk do not change in color. A yellowish color change indicates an increase in excess zinc ions in the t-ZnO crystal structure.^[55] The enrichment in zinc ions can occur due to oxygen radicals and ions in the plasma, which are binding oxygen atoms from the zinc oxide. The resulting change in conductivity of the t-ZnO could also influence the permeability of the material. Proving this hypothesis could be a subject of future experiments.

One could also imagine a sputtering effect for the position in the sheath, which would lead to an increase

in porosity. This would enhance the plasma permeability as well. However, SEM of the used samples did not reveal any mechanical changes to the network structure.

4 | CONCLUSION

Summarizing the performed experiments, this study can be regarded as a proof of principle for the method of using polymers as marker materials to study the plasma permeability of highly porous framework materials. The results by WCA and XPS measurements emphasize that porous framework materials produced from t-ZnO possess a plasma permeability in an oxygen low-pressure CCP. The permeability decreases with increasing sample thickness and mass density of the t-ZnO framework. XPS examination validates that oxygen ions and/or radicals modify the covered polymer. The O/C ratio increases from roughly 11% for untreated EPDM to more than 26% for EPDM, which was covered with 1.6 mm thick t-ZnO during the plasma exposure. C–O and C=O bonds on the EPDM surface were detected in HR XPS scans. It was found that the treatment conditions, such as positioning in the plasma chamber and material of the sample holder, play a significant role. The penetration depth was found to be approximately 1.6 mm for t-ZnO (mass density 0.3 g cm^{-3}) when placed in a stainless steel holder directly on the rf-electrode. Using a Teflon holder instead, showed a much larger penetration depth between 2.5 and 4 mm. Exposing t-ZnO samples to the plasma directly on the rf-electrode multiple times enhances the permeability. This was observed by a decreasing WCA from $(76 \pm 8)^\circ$ (first use) to $(44 \pm 9)^\circ$ (third use). This effect was not

obtained for positioning in the plasma bulk. The smaller effects on the covered EPDM in the bulk in general hint toward the ions as being the dominant species for the permeation of the porous network structures. Further understanding of the plasma permeability could be gathered, for example, by covering a mass spectrometer instead an EPDM marker with the porous framework materials to quantify the permeating species.

AUTHOR CONTRIBUTIONS

M. Leander Marxen was involved in conceptualization, performing the experiments, examining the results, and writing – the original draft. Luka Hansen was involved in conceptualization, examining the results, and writing – the original draft. Armin Reimers, Lena M. Saure, and Erik Greve were involved in producing the t-ZnO samples and writing – reviewing, and editing. Tim Tjardts and Jonas Drewes were involved in performing and examining the XPS results and writing – reviewing and editing. Fabian Schütt was involved in writing – reviewing and editing. Rainer Adelung was involved in conceptualization. Holger Kersten was involved in conceptualization, examining the results, and writing – reviewing, and editing.

ACKNOWLEDGMENTS

We would like to thank Margarethe Hauck for helping with the production of t-ZnO samples. Further, we would like to thank Frank Bach and Volker Rohwer for their technical assistance. Funding from the German Research Foundation (DFG, Project Number 413664940, Grant Number KE 574/8-1) is gratefully acknowledged. Open access funding enabled and organized by Projekt DEAL.

CONFLICT OF INTEREST

The authors declare no conflict of interest.

DATA AVAILABILITY STATEMENT

The data that support the findings of this study are available from the corresponding author upon reasonable request.

ORCID

M. Leander Marxen  <http://orcid.org/0000-0002-6457-5888>

Luka Hansen  <http://orcid.org/0000-0003-2656-4069>

Armin Reimers  <http://orcid.org/0000-0001-5225-6815>

Tim Tjardts  <http://orcid.org/0000-0002-0474-3165>

Lena M. Saure  <http://orcid.org/0000-0001-7714-5222>

Jonas Drewes  <http://orcid.org/0000-0002-8539-1543>

Fabian Schütt  <http://orcid.org/0000-0003-2942-503X>

Rainer Adelung  <http://orcid.org/0000-0002-2617-678X>

Holger Kersten  <http://orcid.org/0000-0003-1798-7588>

REFERENCES

- [1] C. Klingshirn, *ChemPhysChem* **2007**, *8*, 782.
- [2] A. Kołodziejczak-Radzimska, T. Jesionowski, *Materials* **2014**, *7*, 2833.
- [3] J. Theerthagiri, S. Salla, R. A. Senthil, P. Nithyadharseni, A. Madankumar, P. Arunachalam, T. Maiyalagan, H.-S. Kim, *Nanotechnology* **2019**, *30*, 392001.
- [4] Ü. Özgür, D. Hofstetter, H. Morkoc, *IEEE* **2010**, *98*, 1255.
- [5] K. V. Gurav, M. G. Gang, S. W. Shin, U. M. Patil, P. R. Deshmukh, G. L. Agawane, M. P. Suryawanshi, S. M. Pawar, P. S. Patil, C. D. Lokhande, J. H. Kim, *Sensor Actuat. B Chem.* **2014**, *190*, 439.
- [6] Y. Mishra, R. Adelung, *Mater. Today* **2018**, *21*, 631.
- [7] D. Gruber, F. Kraus, J. Müller, *Sensor Actuat. B Chem.* **2003**, *92*, 81.
- [8] S.-J. Chen, C.-M. Chang, J.-S. Kao, F.-R. Chen, C.-H. Tsai, *Sci. Technol. A* **2010**, *28*, 745.
- [9] K. K. Lee, Y. Luo, X. Lu, P. Bao, A. M. Song, *IEEE Nanotechnol.* **2011**, *10*, 839.
- [10] L. Wang, X. Zhang, Y. Zhao, T. Yamada, Y. Naito, *Appl. Surf. Sci.* **2014**, *316*, 508.
- [11] G. Das, S. Bose, J. R. Sharma, S. Mukhopadhyay, A. K. Barua, J. Mater, *Sci. Mater. Elect.* **2018**, *29*, 6206.
- [12] J.-C. Woo, T.-K. Ha, C. Li, S.-H. Kim, J.-S. Park, K.-M. Heo, C.-I. Kim, *Trans. Elect. Electron. Mater.* **2011**, *12*, 60.
- [13] S. R. Min, H. N. Cho, Y. L. Li, C. W. Chung, *Thin Solid Films* **2008**, *516*, 3521.
- [14] G.-K. Lee, J.-H. Moon, B.-T. Lee, *Semiconduct. Sci. Technol.* **2006**, *21*, 971.
- [15] N. Kohlmann, L. Hansen, C. Lupan, U. Schürmann, A. Reimers, F. Schütt, R. Adelung, H. Kersten, L. Kienle, *ACS. Appl. Mater. Inter.* **2021**, *13*, 61758.
- [16] Q. Liu, M. Gong, B. Cook, P. Thapa, D. Ewing, M. Casper, A. Stramel, J. Wu, *Phys. Status Solid.* **2017**, *214*, 1700176.
- [17] P. Cao, D. X. Zhao, J. Y. Zhang, D. Z. Shen, Y. M. Lu, B. Yao, B. H. Li, Y. Bai, X. W. Fan, *Appl. Surf. Sci.* **2008**, *254*, 2900.
- [18] F. Yang, J. Guo, L. Zhao, W. Shang, Y. Gao, S. Zhang, G. Gu, B. Zhang, P. Cui, G. Cheng, Z. Du, *Nano Energy* **2020**, *67*, 104210.
- [19] A. V. Phelps, Z. L. Petrovic, *Plasma Sources Sci.* **1999**, *8*, R21.
- [20] A. V. Phelps, L. C. Pitchford, C. Pedoussat, Z. Donko, *Plasma Sources Sci.* **1999**, *8*, B1.
- [21] M. Daksha, A. Derzsi, Z. Mujahid, D. Schulenberg, B. Berger, Z. Donko, J. Schulze, *Plasma Sources Sci.* **2019**, *28*, 034002.
- [22] R. Hippler, H. Kersten, M. Schmidt, K. Schoenbach, *Low Temperature Plasmas: Fundamentals, Technologies and Techniques*, Wiley-VCH, **2008**.
- [23] M. A. Lieberman, A. J. Lichtenberg, *Principles of Plasma Discharges and Materials Processing*, John Wiley and Sons, **2005**.
- [24] Y. P. Raizer, *Gas Discharge Physics*, Springer Berlin Heidelberg, **2011**.
- [25] K. H. Becker, K. H. Schoenbach, J. G. Eden, *J. Phys. D. Appl. Phys.* **2006**, *39*, R55.
- [26] F. Iza, G. J. Kim, S. M. Lee, J. K. Lee, L. Walsh, Y. T. Zhang, M. G. Kong, *Plasma. Process. Polym.* **2008**, *5*, 322.
- [27] L. Hansen, N. Kohlmann, U. Schürmann, L. Kienle, H. Kersten, *Plasma Sources Sci.* **2022**, *31*, 035013.

- [28] A. Bogaerts, X. Tu, J. C. Whitehead, *J. Phys. D. Appl. Phys.* **2020**, 53, 3001.
- [29] E. C. Neyts, A. Bogaerts, *J. Phys. D. Appl. Phys.* **2014**, 47, 224010.
- [30] E. C. Neyts, K. Ostrikov, K. S. Mehandra, A. Bogaerts, *Chem. Rev.* **2015**, 115, 13408.
- [31] X. Feng, H. Liu, C. He, Z. Shen, T. Wang, *Catal. Sci. Technol.* **2018**, 8, 936.
- [32] A. Ricard, C. Canal, S. Villeger, J. Durand, *Plasma. Process. Polym.* **2008**, 5, 867.
- [33] C. Canal, S. Villeger, A. Ricard, *Plasma. Process. Polym.* **2011**, 8, 505.
- [34] C. M. Chan, T. M. Ko, H. Hiraoka, *Surf. Sci. Rep.* **1996**, 24, 1.
- [35] A. Vesel, M. Mozetic, *J. Phys. D. Appl. Phys.* **2017**, 50, 293001.
- [36] J. M. Grace, L. J. Gerenser, *J. Disper. Sci. Technol.* **2003**, 24, 305.
- [37] L. J. Gerenser, *J. Adhes. Sci. Technol.* **1987**, 1, 303.
- [38] A. Vesel, M. Mozetic, *Vacuum* **2012**, 86, 634.
- [39] J. F. Friedrich, R. Mix, R. D. Schulze, A. Meyer-Plath, R. Joshi, S. Wettmarshausen, *Plasma. Process. Polym.* **2008**, 5, 407.
- [40] J. Friedrich, *The Plasma Chemistry of Polymer Surfaces*, WILEY-VCH, **2012**.
- [41] A. M. Hinz, E. von Wahl, F. Faupel, T. Strunskus, H. Kersten, *J. Phys. D. Appl. Phys.* **2015**, 48, 055203.
- [42] Y. A. Ussenov, E. von Wahl, Z. Marvi, T. S. Ramazanov, H. Kersten, *Vacuum* **2019**, 166, 15.
- [43] T. Wegner, A. M. Hinz, F. Faupel, T. Strunskus, H. Kersten, J. Meichsner, *Appl. Phys. Lett.* **2016**, 108, 063108.
- [44] S. Daria, S. Sindu, M. Hoppe, L. Hansen, J. Marx, J. Dittman, Z. Karez, B. Fiedler, H. Kersten, R. Adelung, *Contrib. Plasma Phys.* **2018**, 58, 384.
- [45] M. A. Lieberman, *J. Appl. Phys.* **1989**, 65, 4186.
- [46] M. Stamm, *Polymer Surfaces and Interfaces. Characterization, Modification and Applications*, Springer, **2008**.
- [47] A. W. Adamson, *Physical Chemistry of Surfaces*, 5th edition., Wiley Interscience, **1990**.
- [48] C. J. van Oss, R. J. Good, M. Chaudhury, *Langmuir* **1988**, 4, 884.
- [49] D. Gedamu, I. Paulowicz, S. Kaps, O. Lupan, S. Wille, G. Haidarschin, Y. K. Mishra, R. Adelung, *Adv. Mater.* **2013**, 26, 1541.
- [50] M. K. Shi, L. Martinu, E. Sacher, A. Selmani, M. R. Wertheimer, A. Yelon, *Surf. Interface Anal.* **1995**, 23, 99.
- [51] C. Girardeaux, J.-J. Pireaux, *Surf. Sci. Spectra* **1996**, 4, 138.
- [52] S. W. Gaarenstroom, N. Winograd, *J. Chem. Phys.* **1977**, 67, 3500.
- [53] D. Shindo, T. Oikawa, *Analytical Electron Microscopy for Material Science*, Springer, **2002**, pp. 81.
- [54] B.-H. Youn, C.-S. Huh, *IEEE Dielect. El.* **2005**, 12, 1015.
- [55] F. van Craeynest, W. Maenhout-van der Vorst, W. Dekeyser, *Phys. Status Solid. B* **1965**, 8, 841.

How to cite this article: M. L. Marxen, L. Hansen, A. Reimers, T. Tjardts, L. M. Saure, E. Greve, J. Drewes, F. Schütt, R. Adelung, H. Kersten, *Plasma. Process. Polym.* **2022**, e2200118.
<https://doi.org/10.1002/ppap.202200118>

Chapter 7

In situ Microplasma Cell Development

The main goal of this thesis is the development of a vacuum-proof microplasma cell suited for TEM integration. Most of the previously shown results were highly motivated by this goal and focused on the plasma itself and its interaction with the electrode surface. The electrode setup and, thus, the plasma geometry was already chosen based on the design considerations given in this following chapter. Nevertheless, the obtained results go far beyond the plasma stability tests that are mandatory for the *in situ* microplasma cell. They provided a lot of new insights into the plasma surface interaction under atmospheric pressure conditions, despite being performed *ex situ*. In particular, the determination of effective secondary electron coefficients under atmospheric pressure conditions resulted in follow up works refining the experimental conditions and extending the material and parameter space. Furthermore, the *ex situ* treatment of thin films coated directly onto TEM grids was already refined within a master's thesis [327] as it enables identical location TEM (IL-TEM) by comparing the same sample areas before and after plasma treatment. Utilizing this technique also for nanomaterials placed on top of an electrode film is planned within a follow-up project. The main restrictions are given by the TEM optics, as the pole pieces of the objective lens limit the available space for the *in situ* microplasma cell. The size limitations also resulted in the choice of a microplasma as mentioned in the introduction. Hence, atmospheric pressure is needed inside of the *in situ* cell and a vacuum-proof encapsulation is necessary. Finally, the *in situ* cell has to be electron transparent. The electrodes have to be built up from conductive thin films sputtered on top of the SiN_x TEM grids as introduced in chapter 5. At least, if the electron beam is planned to propagate parallel to the electric field and, thus, the plasma discharge, to observe the plasma effect on the electrodes and to not disturb the TEM optics by the additional electric field.

7.1 Restrictions given by the TEM

The JEOL JEM-2100 microscope is intended to be used for the *in situ* experiments. It can be operated in TEM or STEM mode and is equipped with an EDX detector. Its electron gun consists of a LaB₆ thermionic source operated at 200 kV. The objective lens is built up from a split pole piece (JEOL HR) with a distance of 4.5 mm (illustrated in Fig. 7.1a), which sets the absolute maximum for the height of the *in situ* cell. It would be more preferable to restrict the cell height to 4 mm to minimize the risk of touching and dealigning the pole pieces, as well as enabling small tilts of the cell and the holder to improve the image contrast. The diameter of the sample/holder port is approx. 10 mm. The holder itself also needs space, thus, the maximum outer cell

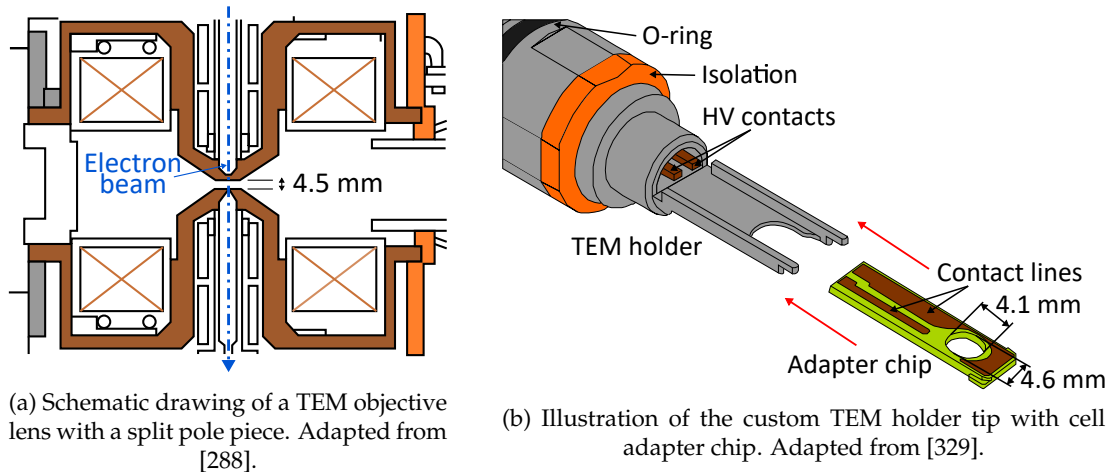


FIGURE 7.1: Illustrations of the split pole piece and the custom TEM holder for a better understanding of the given requirements.

Requirement	Value	Origin
Vacuum sealing	1×10^5 Pa vs. 1×10^{-5} Pa	TEM
Ignition voltage	≤ 1 kV	Holder
Cell height	≤ 4.5 mm	TEM
Cell width	≤ 4 mm	Holder
Cell length	≤ 4 mm	Holder ¹
Gas column height	$\lesssim 100$ μ m	TEM ²
SiN _x thickness	$\lesssim 100$ nm	TEM ²
Electrode thickness	$\lesssim 50$ nm	TEM ²

¹ Given by the hole in the cell adapter chip, could be altered.

² Estimations based on the electron mean free path, see chapter 3.2.1 and [236].

TABLE 7.1: Summary of the requirements on the *in situ* microplasma cell.

diameter is restricted through the holder. For the experiments a custom electrical biasing holder by Hummingbird Scientific based on their 1600 electrical biasing holder (spring contact, type III) [328] was designed, offering 4 mm space for the outer diameter of the cell. An adapter chip is mounted in the tip of the holder as shown in Fig. 7.1b to contact and hold the cell. In addition, the holder is equipped with two high voltage cables (26 AWG Teflon coated micro-flex cable, 3 kV rated) to apply the high voltage to the *in situ* cell and offer an isolated ground. The complete holder with the inserted cell adapter chip is 1 kV rated by Hummingbird Scientific. Along the insertion direction of the holder the TEM would limit the available space to 30 mm, which for obvious reasons is not the critical dimension. Table 7.1 summarizes the requirements on the *in situ* microplasma cell either given by the TEM or the holder.

7.2 Microplasma Setup and Geometry

The plasma geometry also sets boundaries for the cell, especially for the height. It was introduced and successfully tested in the chapters 4 and 5. Due to the restrictions given in table 7.1, the electrodes are based on framed SiN_x TEM grids (Pelco® Prod.

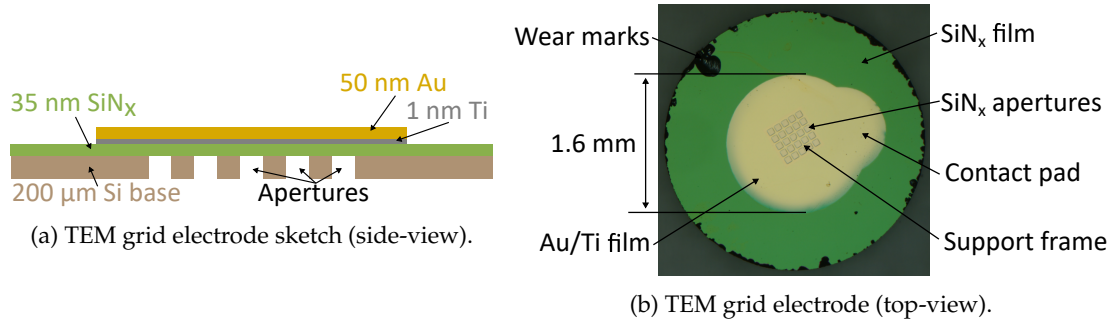


FIGURE 7.2: a) Sketch of a cut through the TEM grid electrode to illustrate the thin film layers. b) Light microscope image of a TEM grid electrode. The 1 nm Ti film is below the 50 nm Au film.

No. 21515-10 [330]) with an outer diameter of 3 mm. In the center of the TEM grid a 500 μm x 500 μm large window with 25 70 μm x 70 μm small electron beam transparent apertures with a film thickness of 35 nm is used for imaging. The frame, as well as the Si base layer, is 200 μm thick and stabilizes the window to withstand the forces due to the pressure gradient. Simplified simulations showed that a 250 μm x 250 μm large, 50 nm thick SiN_x film, partly coated with 50 nm Cu, should not rupture due to the forces created by the comparable pressure gradient [331]. As the force F scales with area A times pressure p ($F = p * A$), the decision was made to reduce the free standing SiN_x thin film area by a factor of nearly 13 to reduce the force for safety reasons and also to be able to use a thinner SiN_x film for better image quality.

On top of the SiN_x layer, a 1 nm thick Ti layer is sputtered as adhesion layer prior to the roughly 50 nm thick Au layer used as electrode. In addition to an improved adhesion, the ultra-thin Ti layer also improves the thermal stability of the electrode [332], which might become important in case plasma instabilities like small arcs form. The thin film layers are illustrated in Fig. 7.2a. The electrode layers are only sputtered onto the center of the TEM grid via a shadow mask to reduce the risk of short circuits between the electrodes via the vacuum encapsulation or unintentional plasma ignition at the sides of the dielectric spacers (introduced in the next paragraph). Further, a small contact pad is also sputtered via the shadow mask visible in Fig. 7.2b for the electrical connection. Isolated Ag wires (Goodfellow AG00-SW-000118 [333], also Cu wires were used for the first experiments CU00-SW-000126 [334]) with a conductor diameter of 25 μm and a 5 μm thick isolating polyimide layer were connected utilizing silver conductive paint (SCP, Electrolube SCP03B [335]). The wire ends were stripped by carefully heating over an open flame.

The interelectrode distance as well as the actual discharge region is set by two 50 μm polyimide foils (so called Kapton spacer, DuPont™ Kapton® HN, Goodfellow IM30-FM-000200 [336]) to 100 μm. These foils are shown in Fig. 7.3 and were either stamped in shape by a custom build punch or laser cut by an external company (Abitsch Präzisionsnormteile GmbH [337]). Laser cutting turned out to be the more reliable and flexible option, as signs of abrasion on the punch led to the expansion of the outer diameter.

The inner diameter of the Kapton spacer sets the boundaries for the discharge channel as observed in chapter 4. It was reduced from 1 mm to 0.45 mm to center the discharge channel above the SiN_x apertures. The reduced diameter was calculated based on the measured current densities and tested in the already mentioned master's thesis [327]. The notch in the outer diameter is necessary to provide space for the wire connection.

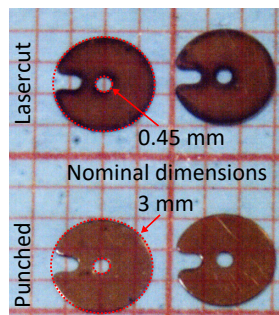


FIGURE 7.3: Long distance microscope pictures of the Kapton spacer either produced by laser cutting or via stamping. The nominal dimensions are illustrated to showcase both manufacturing methods produce a well-suited spacer.

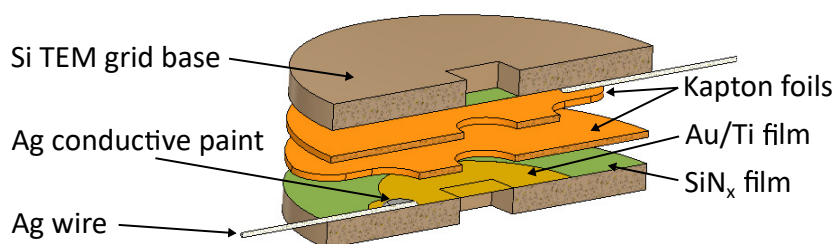


FIGURE 7.4: Half section view of the microplasma electrode setup.

Further, the stack of two foils is essential to avoid short circuits or unwanted plasma ignition at inappropriate locations. The second foil is placed 180° rotated to the first one, resulting in the notch being present at the opposite side of the inner hole. Thus, a dielectric barrier is present anywhere except for the inner hole.

The second electrode is also rotated by 180° and placed on top of the Kapton spacers. A half section view of the assembly is shown in Fig. 7.4. Neglecting the nm thin films the total height of the microplasma geometry adds up to $500\text{ }\mu\text{m}$ which sets another boundary condition for the design of the vacuum encapsulation. Furthermore, the 3 mm outer diameter of the TEM grids would set another boundary condition, which will be addressed in the next section.

7.3 3 mm Cell

Non-custom built TEM holders usually offer only 3.05 mm radial space for the samples, as the TEM grids are standardized to an outer diameter of 3 mm. The first cell design was designated for a standard TEM holder as a custom holder was not available in the beginning of the project. Despite not pushing this design until actual plasma ignition or TEM integration, a prototype of the cell was successfully built. The small 3 mm outer diameter cell could become useful in the future due to its universal fit into nearly every TEM holder.

7.3.1 Dimensions

The outer diameter of the cell was fixed to 3.05 mm to fit into the TEM holder. Another restriction was given by the TEM grids in the center of the cell. Their outer diameter had to be reduced, as the standard diameter of 3 mm obviously did not fit.

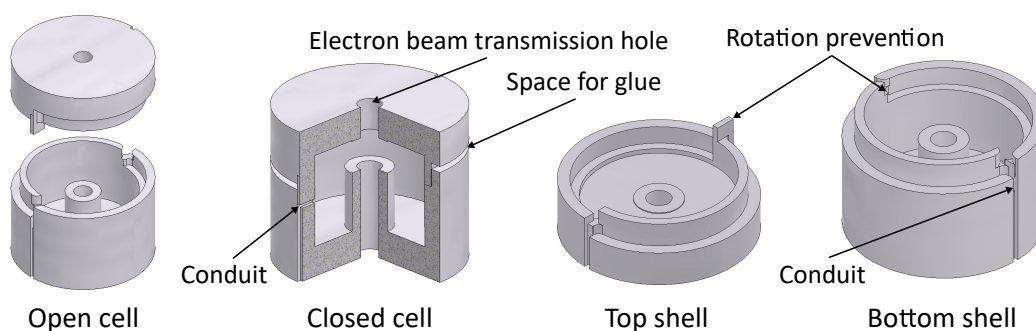


FIGURE 7.5: CAD drawing of the 3 mm *in situ* microplasma cell shells. Technical drawings with dimensions can be found in the appendix A.

TEM grids with smaller outer diameters could only be ordered as custom designs in large quantities. For prototype development these quantities resulted in a too large investment, thus, a technique for the reduction of the outer diameter of standard TEM grids had to be found. Ultrasonic cutting of 2.3 mm circular slides was and still is a TEM sample preparation technique to cut TEM sized sample pieces from, e.g., metallic thin films. The SiN_x TEM grids consists mainly of Si and with ultrasonic cutting nowadays also being used to cut and machine ceramics, the inner diameter of the cell was set to 2.3 mm assuming that the ultrasonic cutting will work.

Based on the set inner and outer diameter, a first design was developed as shown in Fig. 7.5. A technical drawing with all dimensions can be found in the appendix A. The decision was made to manufacture the cell from two shells which are stacked and glued with vacuum compatible epoxy (Torr Seal ® Low Vapor Pressure Epoxy [338]). Ideas utilizing a screw connection or similar instead of glue had to be discarded based on the small dimensions.

So-called micrOrings (micro O-rings, Apple Rubber [339]) with an inner diameter of 0.81 mm and a cross section of 0.69 mm made from fluorocarbon (Viton®) were chosen to seal the microplasma atmosphere versus the holes in the shells necessary for the TEM electron beam transmission. The O-ring glands were calculated based on the typical 25 % height compression [340]. The centered TEM electron beam transmission hole had to be chosen with a diameter of 0.4 mm to provide sufficient wall thickness. The walls at the bottom and the top were chosen with a thickness of 0.5 mm resulting in a total height of the *in situ* microplasma cell of approx. 2.5 mm, fulfilling the requirements.

The shells are designed asymmetric in height to enable stacking of the components in the bottom shell prior to sealing the cell. More details on the assembly of the cell are given in section 7.3.3. The small gap between the shells on the outside should be filled with epoxy, as a certain volume is required for good adhesion. The wires leave the cell through small conduits, which are also sealed during the gluing of the shells. A rotation prevention is constructed by machining inner and outer half circles interlocking with each other during the assembly. This is necessary to protect the small wires and to ensure that the conduits are not closing due to rotation. The long slit on the outside is another conduit to lead the cables in the TEM holder out of the diameter limiting plane.

The shells were machined from aluminum (EN AW-6061) by the physics workshop of the Kiel University.

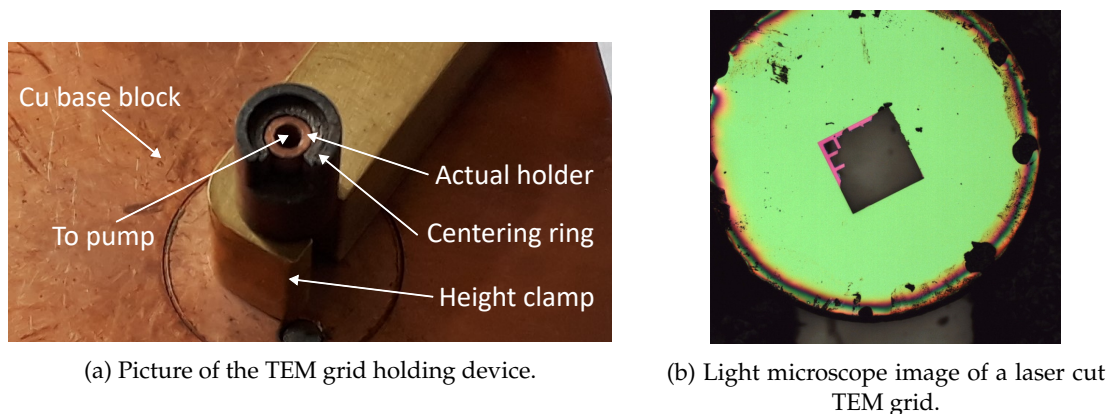


FIGURE 7.6: a) The TEM grid holder designed for the laser cut process. The centering ring is slid down after the vacuum is created and the height clamp is removed. b) The outer diameter of the TEM grid was successfully reduced with a clear edge. The heat introduced to the TEM grid during the cutting resulted in modifications of the SiN_x film at the edge visible in the reflection pattern. The window in the center was destroyed during the process.

7.3.2 Reducing the TEM Grid Size

For the 3 mm cell, the outer diameter of the TEM grids had to be reduced to 2.3 mm. Machining Si is a non-trivial task, made even more difficult by its small dimensions and the free-standing membrane in the center. The various methods for reducing the diameter are listed.

Ultrasonic Cutting

The ultrasonic cutting did reduce the outer diameter of the TEM grids but the free standing SiN_x membrane ruptured due to the vibration as soon as the tool touched the TEM grid. The same happened with other mechanical processing, such as experiments with the wafer saw or by means of CNC milling. Thus, mechanical processing does not work for the reduction of the diameter.

Laser Cutting

Reduction of the diameter without mechanical stress could be achieved via laser cutting. With Si being transparent in the infrared region not all laser cutting devices can be used for the processing. In consultation with RJ Lasertechnik GmbH [341], a TEM grid holding device based on a vacuum pump was developed and built in the physics workshop to hold the TEM grids in their center to cut off the edges. Fig. 7.6a shows the device after several uses. The TEM grids are centered on top of a small Cu tube. Cu was used as material, as it reflects the laser during the cutting process and quickly dissipates any heat input.

After the first quite successful tests, 60 TEM grids with various window sizes and SiN_x film thicknesses were laser cut with mixed results. Only 17 of them were cut without damaging the window. Fig. 7.6b shows a laser cut TEM grid with a damaged window. It is unclear how the window was damaged, as the cutting edge looks good and no ruptures or other signs of thermal induced stress are visible near the center of the TEM grid. It is assumed, that handling issues led to the destruction of the window as already the smallest touch can result in fatal damage. Overall, laser cutting turned

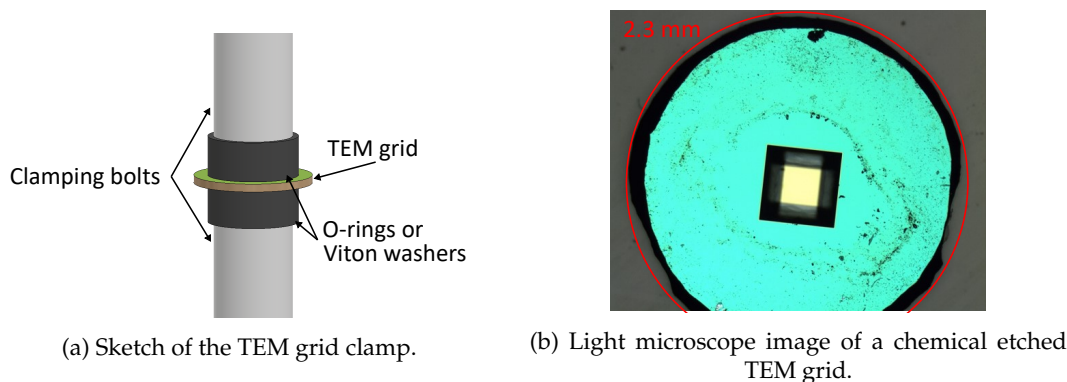


FIGURE 7.7: a) Sketch of the TEM grid clamp made from PTFE for the chemical etching process. The diameter of the O-rings or Viton® washers can control the area to be etched. b) A chemical etched TEM grid with an intact window. The red circle indicates the target diameter of 2.3 mm. The edge got thinned due to the etching.

out to work for the size reduction, but the large scrap rate was intolerable. With direct access to a suited laser cutting machine this method could prove to work fine.

Chemical Etching

The wet chemical etching process of Si is already known since the 1950s [342–345] and offers another method of diameter reduction without introducing mechanical stress to the TEM grid. A clamping device from PTFE was built to clamp the TEM grid in between two O-rings or Viton® washers. A sketch is shown in Fig. 7.7a. The outer diameter of the O-rings or Viton® washers in combination with the clamping pressure is used to influence the area to be etched. The clamping device was inserted into a 13 wt% hydrofluoric acid solution. The solution was set up from 60 ml hydrofluoric acid (48 % aq. solution), 100 ml nitric acid (65 % aq. solution) and 60 ml acetic acid (96 % aq. solution).

The etching time was varied with best results after 80 min. Fig. 7.7b shows an etched TEM grid. Viton® residues are visible on the surface and the edge is not perfectly sharp, but the window is intact. The red circle indicates the target diameter of 2.3 mm which was hit nearly perfectly. The non-uniformity of the TEM grid, as well as etching to a slightly smaller diameter should not be a problem for the assembly of the cell. Thus, the chemical etching of the TEM grids works fine to reduce the diameter.

7.3.3 Assembly of the 3 mm Microplasma Cell

A custom 30x30x30 cm³ glove box utilizing thin laboratory gloves (LLG Labware, nitrile gloves standard) equipped with a load lock was constructed from poly(methyl methacrylate) (PMMA) and silicone rubber. The thin laboratory gloves are necessary to carefully handle the small parts with tweezers. Further, a long-distance microscope (see section 3.1.3) was mounted above the glove box in order to display the working area magnified on a monitor.

Fig. 7.8 shows a photograph of the custom-built glove box setup. In the glove box, the centering tool is visible. It enables clamping of the cell shells centered to each other in a way that they fit into each other if the top shell is lowered onto the bottom one. The long distance microscope is focused onto the bottom shell in which the components of the microplasma cell are assembled. The assembly procedure is as follows:

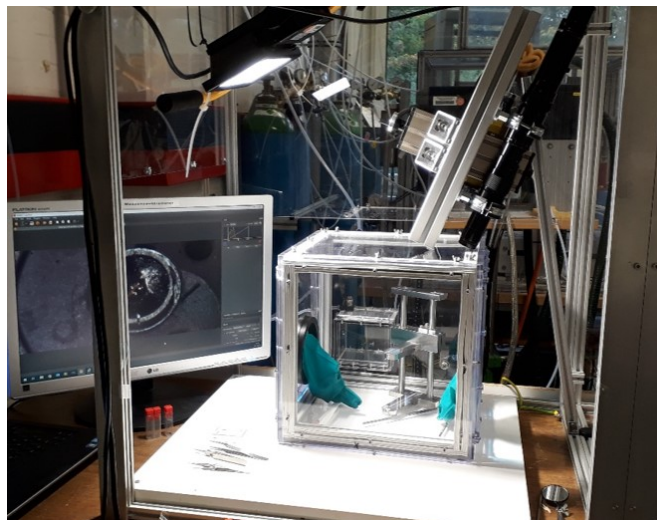


FIGURE 7.8: Photograph of the custom-built glove box setup. The long distance microscope images are displayed on the monitor on the left and enable a closer look during the cell assembly.

First, the electrodes are wired. The insulating wires are cut to a length of approx. 3 cm and the cable ends are carefully stripped using a small flame. Stripping can be avoided, if one ensures that in the following connection, the SCP is touching the cut wire end. The (stripped) wire is connected to the contact pad via the SCP. Here, a fine art brush size 0 (Rico Design [346]) proved to work best for the application of small amounts of the SCP. It is important that the SCP is only applied on the contact pad, as it would modify the microplasma electrode if applied too close to the center, or could result in short circuits, if applied too close to the edge of the TEM grid. After the successful wiring the SCP should dry for at least 30 min.

While the glove box is unsealed and open, the shells are clamped into the centering tool. First, the shells are stacked into each other and placed into the bottom clamp without the clamp being closed. The centering tool is closed slowly and the upper shell should nearly disappear in the top clamping device. The top clamp is closed first while the shells are still joined to ensure both shells rotate evenly in case the pressure from the clamp results in a small rotation. The bottom clamp is closed afterwards and the clamping device is opened and closed again to double check the right orientation from the shells towards each other.

The O-rings are pressed into both shells and stick in their position. The bottom electrode is placed on top of the O-ring with the cable being fitted into the conduit of the bottom shell. The first Kapton spacer is placed on top of the bottom electrode with notch fitting the contacted wire. This step is shown in Fig. 7.9 a). Laser cut TEM grids were used for this prototype. Kapton tape is stuck around the cell to avoid epoxy sticking to the centering tool.

The second Kapton spacer is placed with its notch aligned to the second conduit. The top electrode is placed with the gold film facing downwards and the wire orientated to the second conduit as shown in Fig. 7.9 b). The wires are barely visible due to their small size and the poor contrast on the Kapton tape. Fig. 7.9 c) shows the height of the electrode stack and its instability. The final interelectrode distance, as well as stability to the electrode stack, is given by the connection of both shells.

The glove box is sealed and flushed with 3 slm He for 30 min followed by 1 slm for 2.5 h. The He flux is increased to 3 slm during the gluing of the shells.

The two parts of the epoxy are prepared separately from each other in a small petri

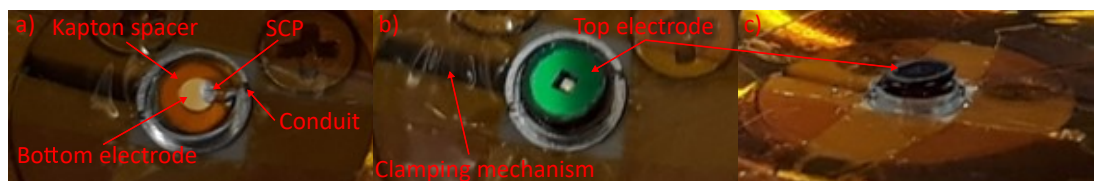


FIGURE 7.9: Photographs during the assembly of the 3 mm cell. a) The bottom O-ring, electrode and Kapton spacer are already placed inside of the bottom shell. The silver conductive paint (SCP) for this prototype was applied too close to the center of the electrode. b) The second Kapton spacer and top electrode were placed to complete the electrode stack. c) Side-view onto the electrode stack.

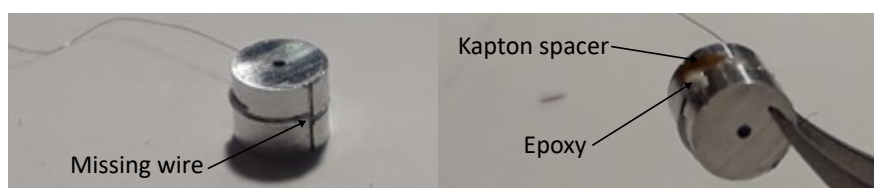


FIGURE 7.10: Photographs of the assembled 3 mm cell prototype. Obvious imperfections are visible as a result of errors during the assembly.

dish and placed in the load lock. The load lock is flushed for 3 min with 3 slm. Afterwards, the two components of the epoxy are mixed inside of the glove box. The epoxy is applied to the outer edges of the shells with the tip of an insulin cannula. If some parts of the electrode stack misaligned it has to be corrected prior to closing the centering tool.

The centering tool is slowly closed and the shells stacked into each other. The closing should be done slowly to avoid a sudden overpressure on the TEM grid windows. The shells are pressed together to squeeze the O-rings. The centering tool keeps the pressure during the hardening process. The He influx is reduced to 1 slm for another 2 h during the first hardening, and, thus, sealing of the cell.

After 48 h the clamps are opened and the *in situ* microplasma cell is carefully removed. If epoxy sticks to the tape stuck around the bottom shell, the cell is removed together with the tape and afterwards the tape can be peeled off the epoxy.

7.3.4 State of the Art

Fig. 7.10 shows photographs of the first and only assembled prototype of the 3 mm cell. A wire was ripped off during the removal from the centering tool as it was accidentally glued to the tape. Further, a part of one Kapton spacer is visible on the outside, indicating that the Kapton spacer slipped out of the electrode stack shortly before the closing of the centering tool. Some epoxy is also visible on the outside, which can be carefully removed if necessary. Apart from these obvious errors, the cell looks good and the epoxy resulted in a strong connection between the shells despite being applied to quite small areas. Overall, the design for the 3 mm cell works out well and can be refined for future experiments.

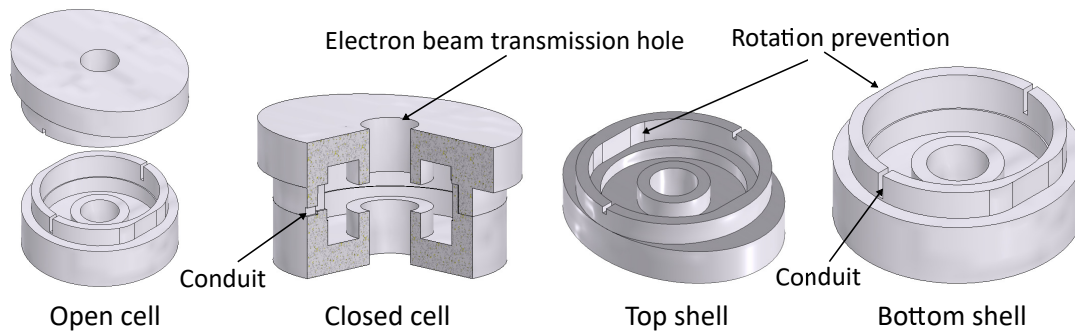


FIGURE 7.11: CAD drawing of the 4 mm *in situ* microplasma shells. Technical drawings with dimensions can be found in the appendix A.

7.4 4 mm Cell

During the project the opportunity arose to buy a custom Hummingbird Scientific electrical biasing holder which enabled to increase the outer diameter of the *in situ* microplasma cell to 4 mm and, thus, avoid the necessity of reducing the outer diameter of the TEM grids. The larger dimensions of the 4 mm cell also simplified the manufacturing and assembly of the shells, especially the wire connection via SCP. Therefore, efforts were concentrated on building an operating prototype of the 4 mm cell.

7.4.1 Dimensions

The 4 mm cell is fixed to an outer diameter of 4 mm and an inner diameter of 3.05 mm. The O-ring size obviously also increased to an inner diameter of 1.5 mm with a cross section of 0.6 mm made from fluorocarbon (FPM micro O-ring, Sealware® [347]). The O-ring glands have been adapted to the new O-rings. Again, the choice was made to set up the cell from two shells which are glued together by the vacuum compatible epoxy. Fig. 7.11 shows the updated cell design, which was again machined from aluminum (EN AW-6061) by the physics workshop. The technical drawings are again given in the appendix A.

The cell is again designed asymmetrically to stack the components mainly into the bottom shell. The central hole for the electron beam could be increased. In contrast to the previously shown 3 mm cell, the inner circle of the locking and centering mechanism is placed fully on the bottom shell. This change allows for easier application of the epoxy, as a wall is constantly present between the surface area covered with epoxy and the electrode stack in the center. The rotation prevention is realized via two plane areas interrupting the circle. Further, the top part of the top shell is designed elliptically instead of circular. The elliptical parts surpassing the rest of the cell are setting the mounting height of the cell in the adapter chip (chip shown in Fig. 7.1b). The cell will be inserted in the hole in the chip until the elliptical part touches the chip. If necessary, the elliptical part can be fixed on the chip with vacuum compatible carbon tape. The mounting height results in centering of the microplasma cell in the focus plane of the TEM.

The microplasma electrode setup is identical to the previously discussed setup as illustrated in Fig. 7.4 with the only difference being the outer diameter. A three quarter section view of the designed 4 mm *in situ* microplasma cell is shown in Fig. 7.12. In the closed state, the height of the cell should be 2.39 mm and, thus, easily fit between the pole pieces of the TEM.

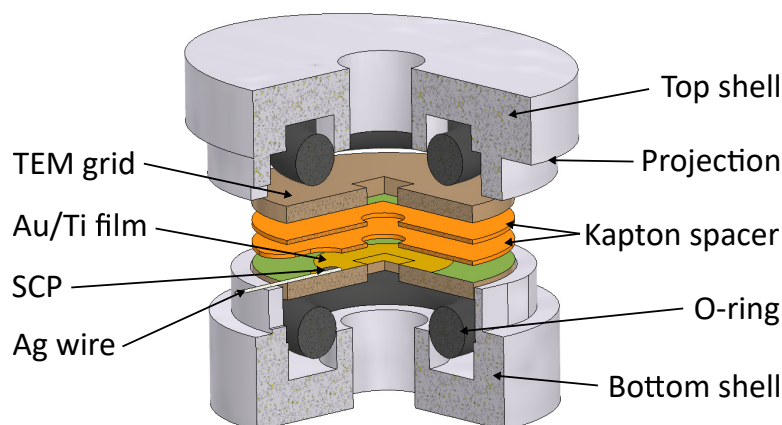


FIGURE 7.12: Three quarter section view of the designed 4 mm *in situ* microplasma cell.

7.4.2 Assembly of the 4 mm Microplasma Cell

The assembly procedure is similar to the one for the 3 mm cell as described before. The clamping mechanism of the centering tool was adapted to fit the bigger shells. Tape is placed around the bottom clamp to shield it from the epoxy. The shells are clamped into the centering device. With the elliptical top shell, the order of closing the clamps (first top clamp, then bottom clamp) is important to avoid damage to the rotation prevention. The O-rings are pressed into the shells and the contacted bottom electrode is placed with its wire fitted in the conduit. The two Kapton spacers are placed on top of the bottom electrode and the top electrode is placed upside down next to the bottom shell. The glove box is sealed and flushed with 3 slm He for 30 min followed by 1 slm for 2.5 h.

The He influx is increased again to 3 slm with the start of the gluing process. Fig. 7.13 shows different steps of the gluing process. The components should be arranged as shown in Fig. 7.13 a) prior to sealing and flushing the glove box. The two components of the epoxy are introduced through the airlock and mixed thoroughly. The epoxy is applied to the small edge with the cannula tip as demonstrated in Fig. 7.13 b). Some epoxy overhangs the edge of the shell and runs onto the tape. The second conduit for the wire of the top electrode should be omitted from epoxy to fit the electrode wire into the conduit. This step is shown in Fig. 7.13 c) followed by Fig. 7.13 d), the placement of the top electrode. The placement of the top electrode is not trivial, as it should not touch one of the edges covered with epoxy. Further, the wire has to be fitted in the conduit as it would get ripped off during the closing otherwise. The conduit has to be sealed with epoxy as shown in Fig. 7.13 e). Letting the epoxy slowly slide off the cannula tip allows to seal the conduit without directly touching the wire. Otherwise, misalignment of the electrode stack is quite probable. Fig. 7.13 f) Shows the final state before closing the centering tool. Both wires are in their respective conduits and the epoxy is applied all around the bottom shell.

The centering tool is slowly closed and the shells are pressed together. The centering tool is locked to keep the pressure up during the hardening. The He influx is reduced to 1 slm for the next 2 h. After these 2 h, the epoxy should be capable of sealing the He atmosphere inside of the cell. The He influx is switched off and the cell is left inside of the glove box for at least 48 h to fully harden.

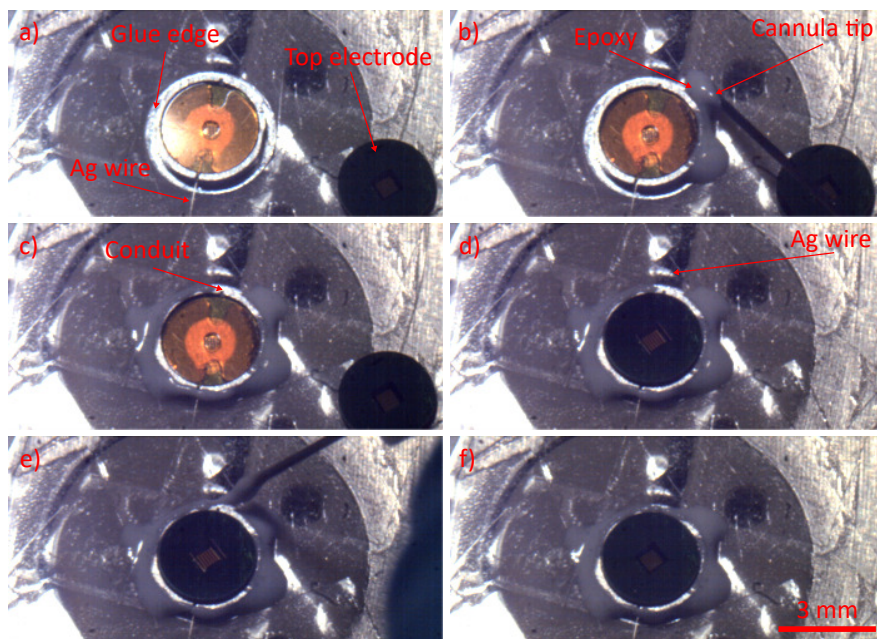


FIGURE 7.13: Long distance microscope images during the assembly of the 4 mm cell. The scale is valid for all images. a) Prepared for gluing. b) Application of epoxy. c) Conduit omitted from epoxy. d) Placement of top electrode with wire in conduit. e) Sealing the conduit with epoxy. g) Ready for closing the centering tool.

Movies of the full assembly are available on the Plasma Technology Group data storage and may be shared upon reasonable request. After the cell is hardened the *in situ* microplasma cell can be removed. One has to be careful with the wires, as these can easily be ripped off due to mishandling. If excess epoxy prevents an easy removal of the cell, the cell has to be removed together with the tape applied to the bottom clamp. The tape can be removed from the bottom clamp by carefully scratching underneath the tape with the tip of a pair of tweezers. After the tape and cell have been removed from the bottom clamp, the tape can be carefully peeled off the epoxy.

Fig. 7.14 shows a successfully assembled 4 mm *in situ* microplasma cell. The long distance microscope image in Fig. 7.14 a) was taken directly after opening the centering tool. The TEM window in the center of the cell is not fully visible due to the viewing angle of the microscope. Fig. 7.14 b) shows the cell upside down after it was removed from the centering tool. The TEM window is intact and was not damaged during the

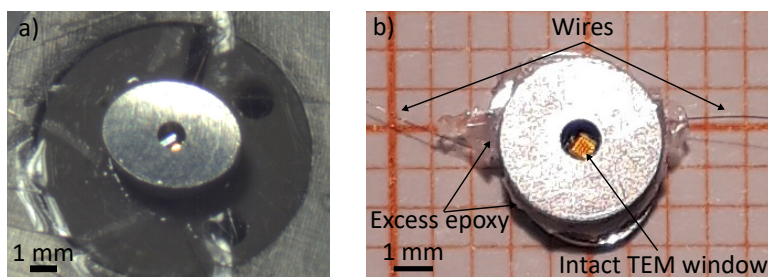


FIGURE 7.14: Pictures of the 4 mm *in situ* microplasma cell. a) Taken with the long distance microscope while still clamped in the centering tool. b) Upside down on mm paper with focus on the intact TEM window.

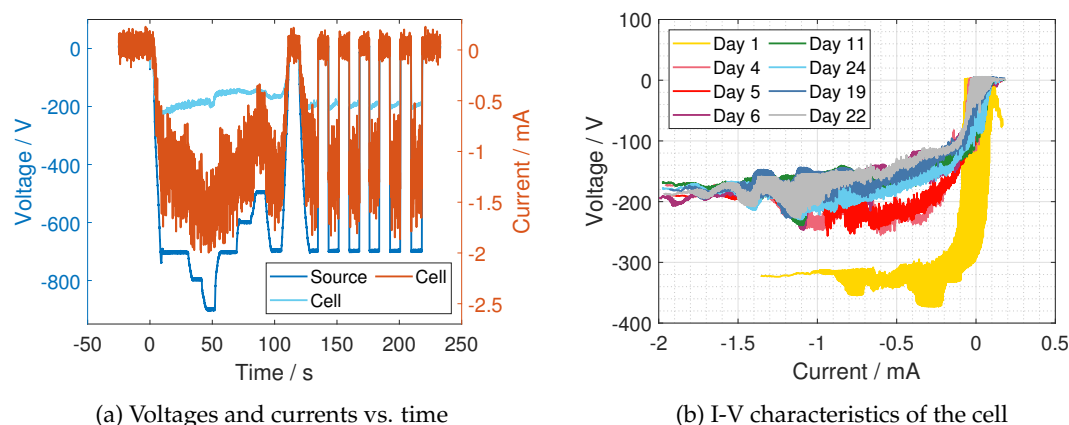


FIGURE 7.15: a) The applied voltage (source), the voltage present at the electrodes (cell), and the current through the microplasma (cell, red, right y-axis) over time of a glued microplasma cell. b) I-V characteristics of a glued microplasma cell ignited on several days.

assembly process. Excess epoxy is visible on the sides. Close to the wires the epoxy will not be removed, as the risk of accidentally ripping off the wires is too high and it does not influence the fitting of the cell into the adapter chip as the hole in the adapter chip was chosen elliptically anyway to provide space for the wires to exit the cell.

7.4.3 Electrical Testing

The functionality of the *in situ* microplasma cell has to be ensured prior to introducing it into the TEM, since every insertion into the TEM is always associated with the risk of damaging the TEM. Electrical measurements are applied first, to check successful ignition of the microplasma, as well as its I-V characteristics. The electrical circuit that is shown in Fig. 3.1 and is used for nearly all experiments, was connected to the microplasma cell.

Fig. 7.15a shows a typical test procedure performed at a glued microplasma cell. The first cells were tested more intense as it is shown here with multiple ignitions and a variation of the discharge current via the external applied voltage. Cells intended for actual use in the TEM were only ignited once shortly (<1 s) to avoid degradation and modification of the electrodes.

The cell shows a behavior as expected from the *ex situ* studies on the microplasma (cf. chapter 4). The voltage measured at the electrodes is in the range of -200 V and does not change significant and instantly with a change in the external applied voltage and discharge current. A drift is visible in the cell voltage, which was also seen in *ex situ* studies. Especially during the optical imaging experiments utilizing ITO coated glass as electrodes, these drifts or even jumps were visible and correlate with the discharge channel moving across the electrodes. Arcing or other instabilities are most likely to happen during the switch on of the plasma, thus, multiple ignitions were performed as visible in Fig. 7.15a. The current in the range of approx. 1 mA to 1.5 mA also fits the expectations from the *ex situ* experiments. The noise level is higher which might hint to a not perfect gas purity as a result of the outgassing epoxy during the hardening. The test procedure was performed on several days over 3 weeks and the I-V characteristics are plotted in Fig. 7.15b. The typical behavior of a minimum current being necessary for a successful operation as well as a nearly constant voltage with increasing current is visible for all days. For the first day (Day 1) higher voltages at the

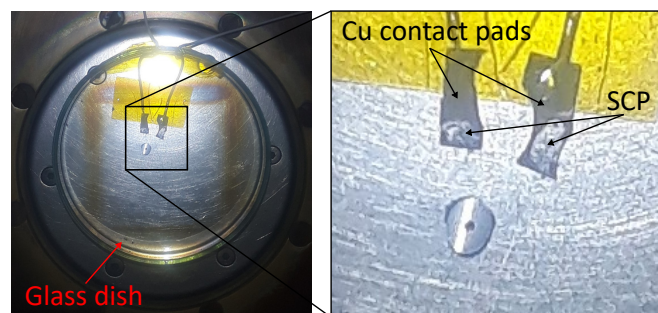


FIGURE 7.16: View onto the microplasma cell inside of a low-pressure chamber connected via two contact pads on an isolating glass dish for electrical testing.

electrodes are visible which can be explained by electrode contamination, which was also seen in *ex situ* experiments. The first ignition removes the contamination which results in better discharge conditions for the following days. Here, it is assumed that the contamination was on the electrodes and was brought into the gas phase due to the plasma surface interaction. While the plasma was burning it was present in the gas phase, thus, altering the I-V characteristics. After the switch off it preferably adsorbed on colder surfaces like the edges of the Kapton spacer or the non-central region of the electrodes. Thus, the central electrode regions are clean for the next ignition.

The microplasma cell was tested over 3 weeks to check its sealing properties. Leaks would lead to a contamination of the gas atmosphere and alter the I-V characteristics or even prevent the plasma ignition at voltages below 1 kV. The electrical testing showed no hints towards leaking and overall expected results, thus, the design and assembly of the *in situ* microplasma cell seems promising.

7.4.4 Vacuum Testing

The second step of the testing procedure prior to TEM introduction was the ignition of the microplasma cell in a low-pressure environment. The low-pressure plasma chamber described and used in chapter 6 was equipped with an electrical feedthrough. The microplasma cell was placed inside a glass dish and electrically contacted via two Cu contact pads as shown in Fig. 7.16. SCP was used to glue the small wires onto the contact pads. The contact pads are placed with a distance to each other, that no breakdown between them happens at atmospheric pressure and also under low-pressure conditions. The glass dish ensured electrical isolation to the chamber to achieve the same conditions present in the TEM. Outside of the chamber the same electrical circuit as before (see Fig. 3.1) was set up and connected to the cell via the electrical feedthrough.

The microplasma cell was ignited for approx. 1 s prior to reducing the chamber pressure to check all electrical connections. The pressure was reduced to <1 Pa and the cell ignited again for approx. 1 s. The cell was left in the low-pressure environment for 60 min with a <1 s ignition every 15 min. Exemplary test data of a single cell is shown in the appendix B. A leak would result in a pressure reduction inside of the microplasma cell, and, thus, alter the I-V characteristics or prevent an ignition, if the pressure is too low according to the Paschen law (cf. section 2.2.2).

The pressure inside of the TEM is with 1×10^{-5} Pa five orders of magnitude lower compared to the pressure inside of the test chamber. Still, pressures <1 Pa are sufficient, as already a pressure gradient of five orders of magnitude is present. Thus, the force changes on the TEM windows would be in the fifth decimal place and below if

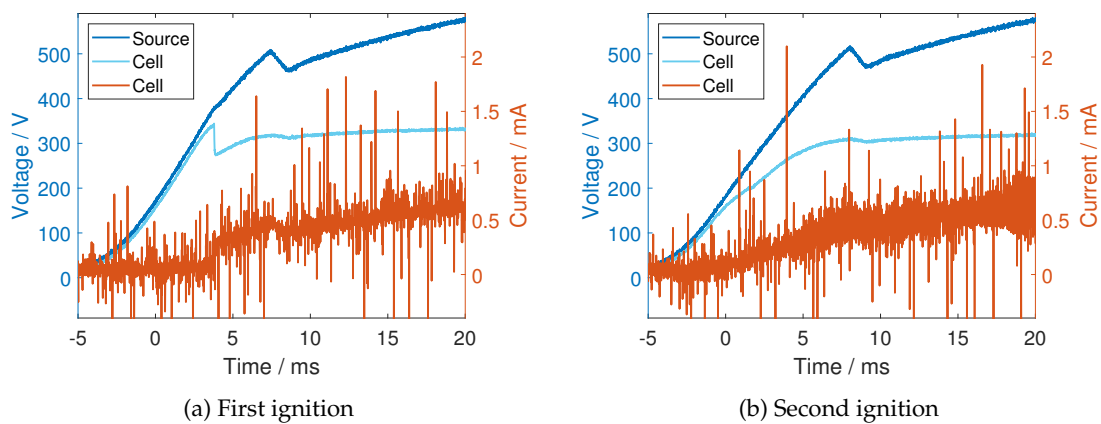


FIGURE 7.17: The applied voltage (source), the voltage present at the electrodes (cell), and the current through the microplasma (cell, red, right y-axis) over time of an *in situ* microplasma cell for the first ignition a) or the second ignition b).

the additional five orders of magnitude of pressure were present.

After the low-pressure ignitions, the chamber is slowly ventilated to avoid fast pressure, and, thus, force changes onto the TEM windows. If all tests were successful, the microplasma cell was fitted into and connected to the adapter chip. If also an ignition in the TEM holder was possible, the microplasma cell was ready for TEM integration.

7.4.5 State of the Art

Multiple 4 mm *in situ* microplasma cells were successfully introduced into the TEM, but no microplasma could be ignited till today. TEM images of these experiments are shown and discussed in chapter 8. Here, the reasons and proposed solutions for the until today unsuccessful proof of principle will be discussed.

The previously introduced testing procedure prior to TEM integration fully relies onto electrical measurements, which are convenient, as they are easy to apply, seemingly reliable, and also available if the cell is inside of the TEM. The plasma-typical I-V characteristics should only be measured if everything works out, as every leak, short-circuit, or not connected wire should result in completely different I-V characteristics. Thus, they were not questioned until an damaged cell was introduced into the TEM. The membranes were obviously damaged and could not hold a He atmosphere. Still, the I-V characteristics looked fine, similar to the ones shown in Fig. 7.15.

A closer look at electrical measurements, especially the ignition phase, of such a cell is given in Fig. 7.17. For the first ignition shown in Fig. 7.17a, the expected behavior is visible. The external applied voltage (source) increases in the same way as the voltage at the electrodes (cell, blue) and no current is measured (cell, red) until a breakdown event (at approx. 4 ms) is observable. After the breakdown, current is flowing through the cell which slowly ramps up similarly to the external applied voltage. The voltage at the electrodes stays constant.

For the second ignition shown in Fig. 7.17b, however, a different behavior is visible. No breakdown event is observable, instead a steady ramp up in the measured electrode voltage is found with a difference to the external applied voltage starting at approx. 0 ms and 150 V. Further, the current is also increasing slowly and does not start flowing instantly, as one would expect from a gas breakdown. Significant current starts to flow at the same time the measured voltages start to differ, thus, at a

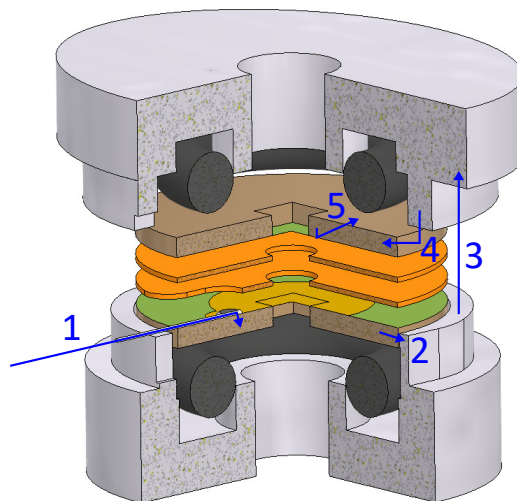


FIGURE 7.18: Three quarter section view of the designed 4 mm *in situ* microplasma cell to illustrate the current path through the avalanche diode. 1) Incoming current via the wire, breakthrough of the 35 nm SiN_x insulation layer to enter the doped Si wafer. 2) Direct contact to the aluminum cell housing. 3) In the closed state a direct contact between the shells is present. 4) Again, a direct contact between the aluminum cell and the doped Si wafer is present. 5) Breakthrough of the second isolating SiN_x layer to establish contact to the second electrode, and, thus leave the cell via the second wire.

voltage of approx. 150 V, which is way below the breakdown voltage predicted by the Paschen law and determined experimentally in the *ex situ* studies.

The detailed investigation of the I-V characteristics led to the conclusion that instead of a microplasma cell an avalanche diode [348, 349] was built. An avalanche breakdown can occur in (doped) Si [350] as free charge carriers, electrons and holes, are present at room temperature. The free charge carriers can get accelerated by an external applied electric field to energies that are high enough to knock out bound electrons, creating a new pair of charge carriers, similar to the α -process described in section 2.2.1. The I-V characteristics are therefore similar to the I-V characteristics of a DC plasma, since the physical processes, simply speaking, are similar to each other, just once in the solid phase and once in the gas phase. The fact that the breakdown voltage, the voltage at the electrodes during operation, and the current through the cell was close to the *ex situ* measured values for the given assembly of the avalanche diode complicated the understanding that electrical measurements alone are not enough to test the *in situ* microplasma cells.

The breakdown event observable during the first "ignition" of the microplasma cell is explained by the assumed current pathway through the cell illustrated in Fig. 7.18. The external voltage is applied via the two wires creating an electric potential difference between the Au coated electrodes. This potential difference should result in gas breakdown inside of the cell, allowing the current to flow through the created plasma from one electrode to the other. But, instead of the gas breakdown, the 35 nm thin isolating SiN_x films break down allowing the charge carriers to enter the doped Si base of the TEM grids. The electrons enter the cell through the first wire and breakthrough the SiN_x film to enter the doped Si (1) in Fig. 7.18. A direct contact to the aluminum shell is present (2) as all parts are stacked tightly and the electrode stack is centered

by the shell. In the closed state both shells are connected (3), thus, the shells enable a contact between both TEM grids (4). The second SiN_x film breaks down and the electrons leave the cell via the second wire (5). The electrical circuit of the avalanche diode is complete. The cell is non-conductive with no external voltage, as it is the case for two parallel plate electrodes in a microplasma setup. Thus, checking the cells for short circuits did not reveal problems.

The necessary breakdowns of the SiN_x films to enable the current flow explain the breakdown event during the first "ignition" of the cell. Once the isolation is broken, the I-V characteristics fit to an avalanche diode with a smooth transition into the constant operation voltage as shown in Fig. 7.17b.

A thicker SiN_x film on the TEM grid could resolve this issue, but deteriorate the TEM imaging quality. Further, it is unclear how thick the film has to be and how defects within the thin film would influence the isolation properties. Therefore, the current pathway has to be interrupted differently.

The development of a process to apply a uniform isolation layer on the sides of the TEM grids without damaging or coating the window in the center was too challenging in the limited time left within the project. Instead, it was tried to isolate the inner parts of the shells via an SiO_x coating applied by a PECVD process, anodizing the shells, or an isolating silicone resin conformal coating aerosol (Red Conformal Coating, RS Pro [351]). None of these approaches worked, as the TEM grids are sharp-edged and scratched through the insulating film when inserted into the shell. Optimization of the PECVD process might result in a working coating, but was beyond the scope of the current work. Instead, options were explored to manufacture the shells from a ceramic material.

7.5 Ceramic Cell

The design of the ceramic cell is essentially identical with the 4 mm design introduced in the previous section. Additive manufacturing is used to 3D print the shells from Al_2O_3 (FormAlox 998) in cooperation with an external company (Steinbach AG [352]). The dimensions of the shells had to be slightly altered to be printable with existing ceramic 3D printing devices. Further, the shrinkage of the printed parts had to be accounted. The iterative process of altering the dimensions, print prototypes, and measurement of the real dimensions of the printed part is still ongoing. In addition to measuring the dimensions, promising prototype shells are also tested via an assembly of a *in situ* microplasma cell. This extra step prolongs the iteration time, but ensures to find the right dimensions for future cell assemblies. The latest technical drawings of the ceramic cell are given in the appendix A.

Fig. 7.19 shows long distance microscope images of the most recent prototype. The 3D printed ceramic shells are placed on mm paper in Fig. 7.19 a). The outer diameters are slightly larger than the 4 mm, or 5 mm for the long side of the elliptical mounting mechanism, respectively, initially aimed for. The conduit slit size had to be increased to be printable, as the minimal dimension of the ceramic 3D printer is limited to about 20 μm to 30 μm . Further, the interconnecting cell walls, especially the outer wall, are fringing and do not reach the designed height. The fringing is a result of tapering these walls to increase the thickness at the base and, thus, ensure that the walls are formed by the 3D printer. First prototypes were printed without the tapering using the dimensions of the 4 mm cell resulting in missing walls at the location of the thinned wall for the rotation prevention in the bottom shell. Therefore, the tapering was intended to resolve this issue while keeping the rotation prevention. But the rotation prevention is

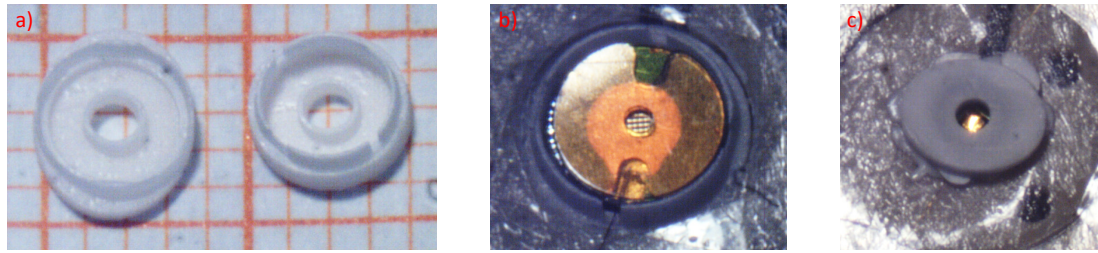


FIGURE 7.19: Long distance microscope images of the current ceramic cell design. a) The 3D printed ceramic shells on mm paper. b) The bottom electrode and both Kapton spacers stacked into the bottom cell prepared for gluing. c) Glued ceramic *in situ* microplasma cell.

not functional anymore, probably as a result of the tapered and fringed walls. The next iteration, and, thus, the latest technical drawings given in the appendix, renounces the tapered walls and realizes the rotation prevention via small noses surpassing the inner walls and fitting recesses in the outer walls.

Despite the slightly too large outer dimensions, the shells could be clamped in the centering tool and a complete assembly was performed. Fig. 7.19 b) shows the bottom ceramic shell prior to the epoxy application. The O-ring, bottom electrode, and both Kapton spacers could successfully be stacked inside. A closer look reveals the inner diameter being slightly too large as the parts are not perfectly centered above each other. At the bottom left edge, a region of the TEM grid not covered by the Kapton spacers is visible. Further, a slight misalignment in the central holes of the Kapton spacers is visible. For the next iteration, the inner diameter was chosen slightly smaller.

The result of the assembly process is shown in Fig. 7.19 c). During the closing of the centering tool cracking noises could be heard, probably as a result of the fringing wall partly cracking. Increasing the wall strength in the upper regions by the removal of the tapering hopefully prevents potential cracking in the next iteration. No hints towards cracking could be observed, as the epoxy covers most of the outer walls. For this prototype a large amount of epoxy was applied to ensure proper sealing despite the larger conduits and the not perfectly fitting, fringing walls.

Unfortunately, no microplasma ignition was possible with the prototype, instead the same avalanche diode behavior described in section 7.4.5 was found. The first breakdown happened at approx. -800 V^1 and no further breakdown events were measured in subsequent "ignitions", as it can be seen in the appendix B. It is assumed, that the ceramic cell was leaking, as the He microplasma could usually be reliably ignited at voltages in the range of 600 V to 700 V. Further, the educated guess is made, that the small misalignment in the electrode stack resulted in a direct contact of the SiN_x films of the upper and lower TEM grid at the edges. Therefore, the diode circuit was closed by electrons breaking through the first SiN_x film below the Au coating entering the doped Si. At the edge with the direct contact, the electrons had to break through two SiN_x films to enter the doped Si of the second TEM grid, followed by another SiN_x film breakthrough to reach the second Au coating. Overall, four instead of two SiN_x films had to breakdown to close the diode circuit, explaining the roughly twice as high breakdown voltage for the first breakdown.

A better alignment and, thus, centering, of the electrode stack components should resolve this issue. Further, microplasma ignition should be possible with voltages below the breakdown voltage of the four SiN_x films, if a pure He atmosphere is achieved.

¹The polarity switch does not matter in the current context (cf. chapter 4) and will be explained in chapter 8.

Thus, successful sealing is the major problem which will be tackled with the next prototypes.

Chapter 8

In situ Microplasma Cell TEM Imaging

The proof of principle experiment of successfully igniting a microplasma inside of the TEM to observe the plasma-induced surface modifications could not be performed yet, as already spoiled in the previous chapter. The unforeseen and hard to identify problems with the aluminum shell-based cells prevented the microplasma ignition. Still, some aluminum-based 4 mm *in situ* microplasma cells have been introduced into the TEM to check the image quality, the sealing properties, and proof the overall compatibility of the cell design with the TEM.

8.1 Mounting of the Cell into the Custom Holder

The cell is placed in an elliptical hole of the adapter chip. The ellipse has a major axis (perpendicular to the insertion direction of the holder) of 4.6 mm and a minor axis (parallel to the insertion direction of the holder) of 4.1 mm. The extra space along the major axis is intended for the wires. Thus, the cell is placed in the hole with the cables along the major axis.

The slight extra space along the minor axis should prevent canting during the insertion of the cell. If excess epoxy enlarges the diameter of the cell and cannot be removed due to the risk of damaging the cell, the hole in the adapter chip can be enlarged by carefully filing it out. The contact lines on top of the adapter chip should not touch the edges of the hole after the filing, which limits the maximum enlargement of the hole. After the cell is placed in the hole it has to be grounded either by contact pressure of the surrounding adapter chip, if the cell fits exactly the hole, or by, e.g., SCP, which also electrically connects the shells to the ground contact to avoid charging of the shells due to the electron beam of the TEM. The wires of the cell are connected to the contact lines on top of the adapter chip via SCP. Afterwards, the adapter chip is mounted into the custom TEM holder and it has to be double checked, that the cell stayed in place and that the wires neither contact the metallic parts of the holder, nor surpass the height of the cell. Otherwise, short circuits or touching of the TEM optics could be possible. Fig. 8.1 a) shows the 4 mm *in situ* microplasma cell mounted into the custom TEM holder. The cell was placed in the hole of the adapter chip with its major axis of the elliptical top shell in the insertion direction of the TEM holder as described before. The wires leave the cell perpendicular to the insertion direction of the TEM holder and are connected to the contact pads of the adapter chip via SCP. The large contact pad is grounded to derive the current of the TEM electron beam and, thus, avoid charging of the adapter chip. The microplasma cell is also connected to the grounded contact pad via SCP for the same reason and to be mechanically fixed to the chip. This charging current is assumed to be small compared to the plasma current, but could influence

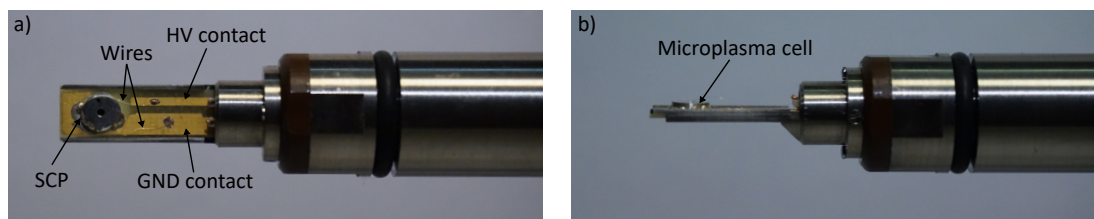


FIGURE 8.1: a) Top view of the *in situ* microplasma cell connected to the adapter chip and mounted into the custom TEM holder. b) Side view of the custom TEM holder with the mounted *in situ* microplasma cell.

the plasma current measurements. Thus, the current has to be monitored also while the plasma is switched off, to measure a possibly occurring current offset.

The side view of the mounted cell is shown in Fig. 8.1 b). The mounting device of the adapter chip is slightly off center in height of the holder by design, to center the microplasma cell between the pole pieces. Further, Fig. 8.1 b) shows, that the total height of the assembly inserted into the TEM column is not only given by the height of the microplasma cell. The mounting device of the adapter chip adds height at the bottom to the total assembly. Still, the total height is below 3 mm and, thus, should be easily fit between the pole pieces and even allow tilting of the holder.

8.2 Image Quality and Accessible Imaging Modes

The first proof of principle experiments reported on a sub-100 nm spatial resolution using the TEM bright field imaging mode [62]. Their supplementary material shows that the images were recorded during operation of the microplasma. Therefore, a direct comparison is not appropriate, as the influence of the microplasma itself is missing in the images of the cell presented here in this work.

Furthermore, without a successful microplasma ignition inside of the TEM, the presence of the He atmosphere, and therefore, successful sealing, is not trivial to proof. The exception is when the sealing of the cell fails or a TEM window ruptures inside of the TEM and the pressure gradient is measurable. For this reason, it will be stated, whether the measurements were performed on a cell with a guaranteed He atmosphere, despite the fact, that the He atmosphere is not the most critical parameter in terms of image quality (cf. section 3.2.1).

The measurements were performed using the JEOL JEM-2100 equipped with an Oxford Instruments EDX detector. More details regarding the image conditions and TEM parameters are given in the thesis of Niklas Kohlmann [236].

8.2.1 Bright Field Imaging

Bright field images of two different *in situ* microplasma cells are shown in Fig. 8.2. The cell used for Fig. 8.2 a)-c) was filled with a He atmosphere. For the cell used for Fig. 8.2 d)-f), the He atmosphere could not be guaranteed, as it did not rupture within the TEM. The brighter, more intense spot in the center of Fig. 8.2 d) could indicate only one TEM window (SiN_x aperture) in the center was intact and the second one was damaged. On the other hand, the intensity profile does not look purely limited onto the middle aperture and this intensity gradient was not visible for all imaging conditions. Thus, the intensity gradient could also be a result of a not further investigated focusing effect caused by an interaction of the TEM electron beam and the shells of the cell.

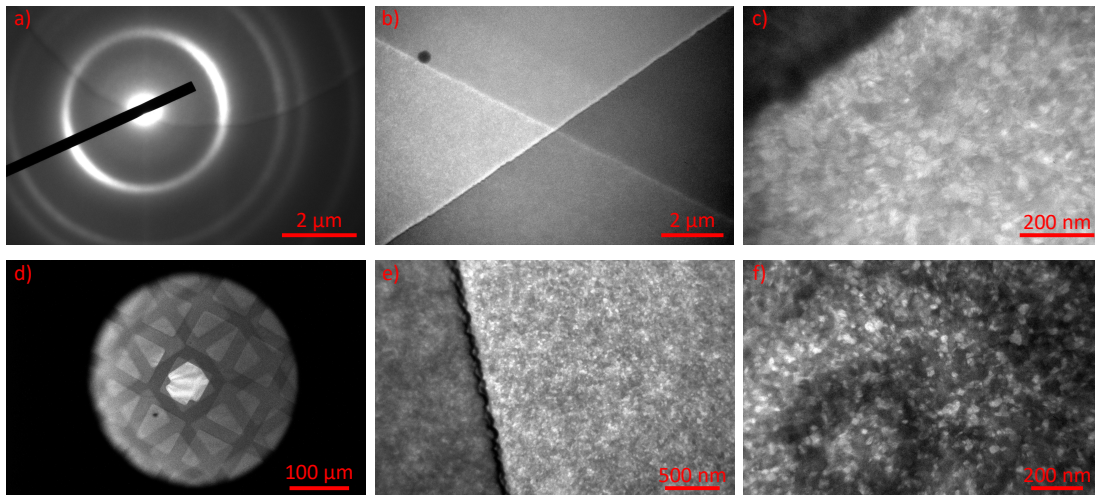


FIGURE 8.2: Different TEM bright field images partly overshadowed by diffraction patterns (a, f)) of two *in situ* microplasma cells. In a)-c) images of a He filled cell is shown. For the cell used for the images d)-f) the He atmosphere is expected, but could not be guaranteed.

Fig. 8.2 a) shows a mixed bright field, diffraction pattern image. The electrodes of the microplasma cell are far enough apart that one creates the bright field image and the other one the diffraction patterns. The practical use of these kind of images is limited, as better resolution and signal to noise levels are achieved by focusing onto one of the electrodes and deciding for one imaging mode. Nevertheless, it nicely shows effects caused by imaging through two TEM grids and once again proves the electron beam transmits both electrodes.

The bright field image shows the edge of a single aperture window. The darker region corresponds to the frame structure, while the brighter area towards the top represents the free standing 35 nm SiN_x film. Of course, the 1 nm Ti, 50 nm Au film is present in both regions on both TEM grids. The concentric ring structure of the diffraction pattern results from the polycrystalline Au film and was expected from the *ex situ* obtained results. A comparison to the *ex situ* results is given in the next section.

A second example of effects caused by imaging through two TEM windows is shown in Fig. 8.2 b). The brightest quadrant on the left corresponds to an area where the TEM electron beam passes through two 35 nm SiN_x apertures. In the quadrants towards the top and the bottom, the TEM electron beam passes through one 35 nm SiN_x aperture and through the frame structure on the other TEM grid. The dark quadrant on the right represents the intensity after passing through the frame structure of both TEM grids. Again, in all regions, the Ti/Au films are also present.

Fig. 8.2 c) demonstrates the image quality achieved by focusing onto one of the electrodes and imaging through two 35 nm SiN_x apertures. The Au grains are visible and features with spatial dimensions in the range of approx. 30 nm can be identified. From the *ex situ* experiments it is known, that the grain size will increase due to the plasma treatment (cf. chapter 5). The capability of resolving the grains prior to plasma treatment raises expectations to image the grain growths in real time.

The already addressed image of the second cell introduced into the TEM is shown in Fig. 8.2 d) and illustrates the centering of the electrodes above each other. The little nib of the frame structure is a marker for the central aperture, thus, the TEM grids are nearly perfectly centered. The asymmetric shell design with the intention of stacking all components into the bottom shell as explained in section 7.4, seems to work well.

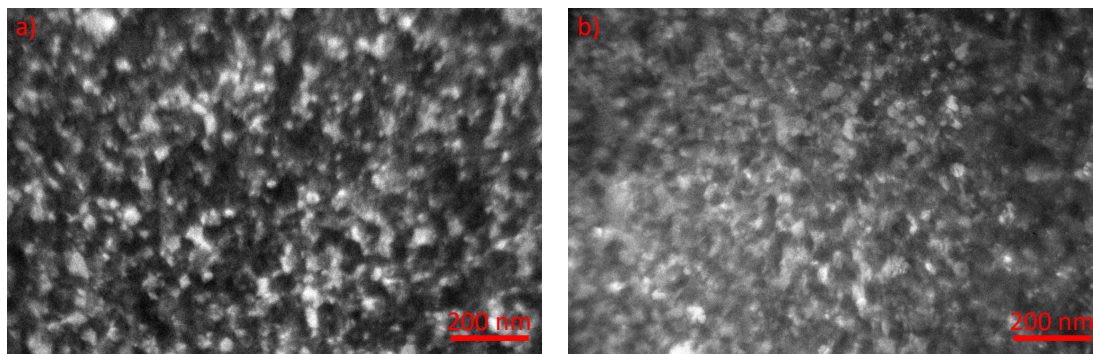


FIGURE 8.3: Comparison of the achieved resolution at the entrance (a) and exit (b) window of the *in situ* microplasma cell. Please note, that no He atmosphere was present inside of the cell.

Further, some bending of one of the central apertures is visible, which indicates stress in the thin film. The internal stress is either probably originating from the Ti/Au deposition process or the stress caused by the pressure gradient. If the origin is internal stress, the deposition process should be refined or the coated TEM grids should be annealed in the future, to reduce the risk of aperture rapture.

Fig. 8.2 e) and f) are again examples of the achievable image quality. Fig. 8.2 e) shows the edge of one of the frames used to focus the image. Again, the Au grains are visible in both pictures. Especially, in some regions of Fig. 8.2 f), the roughly 30 nm large structures can be visualized with an increased contrast compared to Fig. 8.2 c). The ring structure in the intensity in Fig. 8.2 f) is a result of the diffraction on the other electrode. The image quality is therefore heavily influenced by the transmission through two Au/Ti thin films and could be improved by small holes in one of the electrode films similar to the holes used during the first proof of principle experiments [62].

Another important aspect to achieve the best possible imaging quality is the choice of focusing onto the right electrode. In the field of environmental or *in situ* TEM, usually one differentiates between the entrance and the exit window [305, 306]. The entrance window is passed first by the TEM electron beam and the exit window is passed second. For a TEM operating in the bright field imaging mode, the best image quality should be achieved by focusing on the exit window [353]. Fig. 8.3 compares images taken while focusing on the entrance (a) or exit (b) window of an *in situ* microplasma cell without He atmosphere. The image quality obtained at the exit window is indeed better. Therefore, the electrode of interest should be the one at the exit window. In most cases this is the cathode, as it receives a higher energy flux which results in larger surface modifications (cf. chapter 4 and 5). The switchable polarity of the setup enables free choice whether the exit window is used as anode or cathode.

8.2.2 Selected Area Electron Diffraction (SAED)

Diffraction pattern obtained from the microplasma cell electrodes were already shown overshadowed by or overshadowing a bright field image. Half of a pure SAED image is shown in Fig. 8.4 a) and compared to the SAED pattern of a single electrode. The signal to noise ratio of the cells pattern is more blurred compared to a single electrode, which was expected as electrons are also scattered by the second electrode and the He atmosphere. Inelastic scattering events result in an overall decreased intensity, which can be resolved by longer exposure times. Elastic scattering on the other hand, increases the background noise and broadens the circular patterns, which becomes more

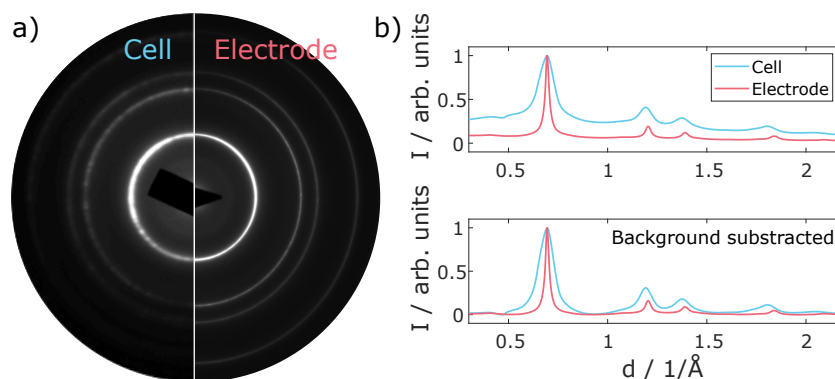


FIGURE 8.4: Comparison of SAED patterns of the with He filled *in situ* microplasma cell and a single electrode.

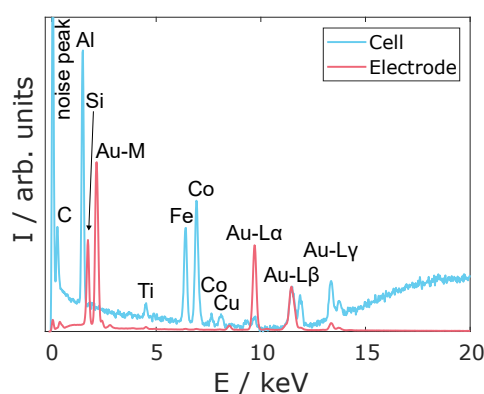


FIGURE 8.5: Comparison of EDX spectra obtained either measuring an He filled *in situ* microplasma cell or a single electrode.

obvious when building the rotational averages shown in Fig. 8.4 b). The upper graph compares the obtained data, while the background of the cell data was subtracted in the bottom graph. Therefore, the decreased signal to noise ratio is visualized in the upper graph and the broadening of the peaks, also due to the elastic scattering events, is demonstrated by the bottom graph. Still, it is possible to obtain SAED pattern with the *in situ* microplasma cell and the plasma-induced increasing texture of the electrode film (cf. chapter 5) should be observable.

8.2.3 Energy Dispersive X-ray Spectroscopy (EDX)

Access of the chemical elements present in the *in situ* microplasma cell would be a huge benefit for future applications to investigate, e.g., plasma catalytic processes, thin film growth or plasma etching processes. This access could be granted in the TEM by EDX spectroscopy, if the generated X-rays can leave through the small center hole of the cell and reach the detector.

Fig. 8.5 shows an EDX spectrum obtained using a He filled *in situ* microplasma cell and compares it to an EDX spectrum of a single electrode. The used microplasma cell during these measurements was slightly modified by placing a piece of Kapton adhesive tape, followed by a piece of conductive metal tape on top of the cell. The Kapton tape should serve as an isolation layer between the conductive metal tape and the cell. The metal tape was grounded via the TEM holder. The idea behind these modifications was to obtain electrically floating cell shells to prevent breakdown between the

high voltage wire and the grounded cell shells. The conductive metal tape should prevent any charging of the cell caused by the TEM electron beam. Of course, a hole was stamped into the adhesive tapes to enable the electron beam transmission. Even though the adhesive tape modification did not alter the image quality, it influenced the EDX spectrum shown in Fig. 8.5.

Firstly, both spectra were normalized to the Au-L β -peak for a better comparison. Further, both spectra were obtained without tilting the sample. The integration time had to be chosen significantly longer for the microplasma cell, still, the absolute count numbers obtained using only a single electrode are larger. This was expected, as the small and deep holes for TEM electron beam transmission in the cell shells strictly limit the angular window for the created X-rays to leave the cell.

The elements corresponding to the EDX peaks of the cell spectrum are C, Al, Ti, Fe, Co, Cu and Au from different excitation energies. Au should originate from the electrode thin film. For Ti, the origin could be the same, but the signal seems quite strong for a 1 nm layer. Thus, a different source for the Ti signal is more probable.

The Al signal originates from the cell shells and was therefore expected. Al, or more specific 6061 aluminum alloy, contains next to Al the following constituent elements with below 1.2 % (by weight): Mg, Si, Fe, Cu, Cr, Zn, Ti and Mn [354]. Theoretically, the Ti signal, as well as Fe and Cu could originate from the shells, but with the other elements missing in the spectrum, the admixture seems to be too small to show up. Therefore, it is assumed, that the Ti, Fe, Co, Cu signals originate from the conductive tape on top of the shell. Unfortunately, no further information regarding the conductive tape is available, therefore an EDX scan of the solely conductive tape in the future would be necessary to answer the origin of the signal with certainty.

The C peak probably originates from the Kapton tape used as isolation layer, which was not perfectly covered by the conductive tape.

The single electrode spectrum only shows expected elements: Si from the TEM grid and Au from the electrode. It is noticeable that different Au excitation states dominate the spectrum compared to the cell spectrum. In the cell spectrum the lowest energy state (Au-M) is missing and the second lowest (Au-L β) only slightly pronounced. The relative intensity of the highest energy excitation state (Au-L γ) is significantly larger compared to the electrode signal. These differences probably are the result of two effects. First, higher energy X-rays have larger mean free path lengths [302, 309], thus, less interaction with the cell shells are expected. Second, no elements with transition energies close to the Au-L β - and Au-L γ -transitions are present in the shell material. The same two effects are probably also responsible for the missing Si peak in the cell spectrum.

The current *in situ* microplasma cell design in principle allows EDX analysis, but has a few drawbacks. The signals from the cell shells are significantly larger compared to the signal generated from the actual sample. Further, low energy X-rays generated from the sample are absorbed and do not reach the detector. Therefore, an upgraded version of the cell design could try to include a free line of sight to the EDX detector.

Chapter 9

Summary and Outlook

The present thesis was dedicated to the development of a microplasma discharge suitable for TEM integration. The combination of microplasma and TEM imaging promises to visualize plasma surface processes with spatial resolution in the nm range in real time. A proof of principle experiment in the past showed basic possibility of introducing a microplasma into a TEM [62], but could not be reproduced or extend until today. Successfully introducing a microplasma into a TEM is linked to high technical requirements, mainly given by the very limited space in the TEM combined with the necessity of the microplasma being electron transparent.

The first step was to design a stable atmospheric pressure DC normal glow microplasma discharge and extensively analyze it using several conventional and non-conventional plasma diagnostics. The second step was to investigate its interaction with the electrode surface, especially with TEM electron beam transparent electrodes, to set a kind of benchmark for the *in situ* experiments. Simultaneously, a vacuum-proof housing for the microplasma was designed and a plasma etch process for t-ZnO was developed, as these highly porous materials are of great interest and showed significant structural changes that are probably well observable *in situ*.

These different steps will be summarized in more detail, followed by a conclusion concerning the whole project before an outlook on still pending experiments and possibilities for adaptations of the current *in situ* microplasma cell is given.

Stability was a major concern during the design of the microplasma, as the electrodes had to be sufficiently thin to be TEM electron beam transparent. Therefore, a DC normal glow discharge was aimed for, as any kind of arcing or other instabilities could break the thin electrodes. These instabilities are most probable to appear during the breakdown process, thus, pulsed or high-frequency discharges were excluded for the first proof of principle experiments. These kinds of discharges could further result in high electromagnetic noise, which would surely disturb the TEM optics. Electrical and optical diagnostics have been applied to proof operation in the normal glow regime and ensure the stability of the discharge.

The I-V characteristics showed glow-like behavior as soon as a minimum current of approx. ± 0.8 mA was surpassed. The voltage at the electrodes was nearly constant in the range of ± 190 V to 200 V using Ar as working gas, or ± 130 V to 170 V for He, respectively, if Au, Cu, or ITO was used as electrode material. For Mg the voltage was in the range of ± 80 V to 100 V and only operation utilizing He as working gas was possible. Also, the electrode distance showed differences in the voltage measured at the electrode. For He as working gas, a significant increase in electrode voltage with increasing electrode distance was measured. Therefore, changes in electrode distance of the *in situ* microplasma cell due to bending of the electrodes caused by the pressure gradient could be determined by the electrical measurements.

Optical diagnostics confirmed the glow-like behavior. Optical emission spectroscopy

revealed broadened Ar I, or He I, respectively, lines with temporal constant intensities. Further, O I and Au I lines were found, indicating a strong plasma surface interaction, as these excited atoms had to originate from the electrode surface. Spatially resolved optical imaging parallel to the discharge channel through transparent ITO coated electrodes enabled to determine the area of the discharge footprints. In combination with the electrical diagnostics, the current densities could be calculated, which were constant with increasing currents, again, a strong indicator of a normal glow discharge. Side view imaging of the discharge allowed an approximate determination of the sheath thickness, which correlated well with the sheath thickness calculated by the collision-dominated Child-Langmuir law.

Non-conventional calorimetric diagnostics were applied to investigate the plasma surface interaction in more detail. The energy flux from the plasma to the electrodes was measured utilizing two PTPs as electrodes. The measurements revealed an asymmetric, cathode-favored energy flux probably caused by ions. Furthermore, the measured power transfer to the cathode was not constant in time due to different contributions to the measured integral energy flux changing over time. The determined energy flux values were in the range of 10 W cm^{-2} to 30 W cm^{-2} if normalized to the full accessible electrode area or up to 275 W cm^{-2} if normalized to the actually measured discharge area. The quite large energy fluxes, compared to other atmospheric pressure discharges, should result in observable surface modifications. The efficiency for surface modifications with the presented discharge was found in the range of 70 % to 90 %, only depending on the electrode distance, as power losses are mainly due to radiation leaving the discharge volume through the Kapton spacer. Furthermore, the combination of the addressed diagnostics allowed the determination of effective SEE coefficients under atmospheric pressure conditions. These were with 1.1 to 1.6 significantly larger than their purely ion-induced counterparts or values determined under low-pressure conditions, as non-ionic species and radiation play a crucial role for the generation of secondary electrons.

The measured integral energy fluxes were connected with the surface modifications of polycrystalline Au thin films used as electrodes in the designed microplasma discharge. An *ex situ* experiment was set up, imitating the actual *in situ* microplasma cell, only missing the vacuum encapsulation, to verify the electrode stability and benchmark the surface modifications for *in situ* measurements. Therefore, SiN_x based TEM grids were coated with 50 nm Au and plasma treated with Ar or He as working gas. The observed surface modifications were correlated with the measured energy fluxes and confirmed expectations given by structure zone diagrams [225] that a higher energy flux results in more textured films with larger crystal grains. The modified Au thin films showed significantly different changes, depending on the working gas and whether they had been used as anode or cathode. Correlating the surface modifications with the measured integral energy flux showed the importance of the different contributions to the integral energy flux. The ion component was identified as the most important component in regards to surface modifications. Under the assumption, that the ion contribution is mainly responsible for the difference in energy flux towards the anode or cathode, the ion contribution can be directly calculated. It is significantly larger using Ar as working gas compared to He, as He tends to form metastables and therefore input power is rather used for the production of metastables.

Furthermore, the power transfer mechanism to the cathode also was found to be different depending on the working gas. Utilizing Ar as working gas results in the main power transfer being given by the kinetic energy of Ar ions and fast neutrals, despite

their low individual kinetic energy due to the large number of collisions. Therefore, the power is transferred in many small doses, resulting in a more uniform surface modification. For He as working gas, the main power transfer mechanism was found to be the recombination on the cathode surface. Thus, the power is transferred in fewer, but larger doses, resulting in a less uniform surface modification.

The less uniform surface modification was visible in the TEM imaging represented by local thinning of the Au thin film. If a He ion recombines on the surface, the recombination energy results in localized heating of the thin film and surface desorption of Au atoms is strongly enhanced, resulting in desorption hot spots, creating the observed localized thinning of the Au film. The desorption processes were accounted for in a postulated energy balance at the cathode and fit well to the measured values, demonstrating the plausibility of the suggested desorption hot spots as a result of the different power transfer mechanisms.

Observing the modification of the Au electrodes inside of the TEM would be the most simple case for the intended proof of principle *in situ* experiments. But for application of the *in situ* microplasma cell afterwards it could be filled with materials of today's research and observe structural changes caused by plasma treatment. T-ZnO was chosen as model material, as it has multiple applications and can be modified by plasma processing. A plasma etch process was developed to produce novel ZnO nano-on-micro structure, also called nanobrushes, by etching t-ZnO in an H₂-C₂H₂ low-pressure CCP plasma. The etch process resulted in strong structural changes of the t-ZnO well observable in the TEM and, thus, well-suited for *in situ* observations.

But also without the context of the *in situ* microplasma cell, the created t-ZnO nanobrushes are of great interest, as they have high surface-to-volume ratios. The created nano-on-micro t-ZnO structures were used as highly sensitive and fast H₂ gas sensors. The gas response, as well as the recovery and response times, are greatly enhanced compared towards pristine t-ZnO nano structures. The self-patterning, single step etching process also allows control over the achieved nanowire length and, therefore, the nanobrushes can be tuned towards different applications. In the near future, these t-ZnO nanobrushes could be used as foundation for the production of so-called aeromaterials [355, 356] instead of pristine t-ZnO to increase the porosity and enhance the available surface area.

The production of larger quantities of the t-ZnO nanobrushes is closely connected to the more fundamental question of plasma permeability of highly porous framework materials. Regardless of whether it is a plasma etching process or more generalized a plasma surface interaction effect as, e.g., during plasma catalysis, it is important to know how deep plasma can penetrate into such highly porous structures. Knowledge about the penetration depth allows to optimize the thickness of the highly porous material in a way to achieve the largest plasma touching surface area.

A novel method was developed to determine the penetration depth of plasma species through highly porous ceramic framework materials using polymers as marker materials. The polymer EPDM was placed in a low-pressure oxygen CCP discharge underneath porous t-ZnO framework materials with different mass densities and thicknesses. The surface activation of the polymer by plasma species permeating through the framework material was measured via WCA and XPS analysis.

The XPS analysis showed that plasma created oxygen ions and/or radicals modify the covered polymer. The O/C ratio increased from 11 % to 26 % due to the plasma treatment, despite the fact, that the polymer was covered by a 1.6 mm t-ZnO framework

material. For a mass density of 0.3 g cm^{-3} , 1.6 mm was also found to be the maximum penetration depth, if the polymer was placed directly on the CCP electrode in a stainless-steel holder. Using a Teflon holder instead resulted in a larger penetration depth from up to 4 mm. If the samples were placed in the plasma bulk instead of the sheath region on top of the electrode, smaller treatment effects were observed. In combination with the holder material playing a significant role for the penetration depth, the conclusion was made, that ions are the plasma species mainly permeating through the highly porous ceramic framework material.

The TEM electron beam transparent microplasma was successfully tested and characterized using various conventional and non-conventional diagnostics. The surface modifications of the TEM electron beam transparent Au electrodes were studied *ex situ* and even a plasma etch process in principle suited to be investigated *in situ* was developed. Only the assembly of the microplasma into the vacuum-encapsulation is missing at this point, to fulfill all goals set within this project.

Two different designs for the *in situ* microplasma cell were developed differing in their outer diameter. The smaller one with an outer diameter of 3 mm promises more versatile usage in nearly all TEMs if an electrical feedthrough holder is available, as TEM substrates usually have an outer diameter of 3 mm. But this is also a drawback, as the TEM grids used as foundation for the electrodes of the microplasma have to be reduced in diameter from 3 mm to 2.3 mm. A solution for this non-trivial task was found by the development of a chemical wet etching process. Still, the assembly of the 3 mm cell is more difficult compared to the slightly larger 4 mm cell. With the acquisition of a custom TEM holder capable of mounting a cell with 4 mm outer diameter the focus was set onto the larger cell. However, the design of the 3 mm cell was successfully assembled and might be pursued further in the future.

Multiple prototypes of the 4 mm cell have been built and successfully introduced into the TEM. The vacuum and general TEM compatibility of the design could be proofed and first images, without microplasma ignition, were taken. Bright field imaging revealed spatial resolution in the 30 nm range. Effects of imaging through two electrodes, or rather two Au/Ti thin films, were visible and were also the main reason for the low spatial resolution. Broadened SEAD patterns could be visualized and also EDX spectra could be taken. The quality of the EDX spectra is limited as the X-rays from the electrodes are partly absorbed by the shells and additionally superimposed by X-rays from the shells with significantly higher intensities compared to the electrode signals. Overall, both TEM analysis techniques were successfully applied to the *in situ* microplasma cell.

Unfortunately, no microplasma could be ignited, yet, most probably as a result of setting up an avalanche diode by connecting both TEM grids used as electrodes via the aluminum shell housing. Ceramic shells are in production via additive manufacturing and should solve the current issues, finally enabling microplasma ignition inside of the TEM.

The limited project duration does not allow to wait for the optimized ceramic shells prior to finalizing the doctoral theses. Therefore, the aimed for proof of principle experiments are missing in the doctoral theses, but will be performed as soon as the additive manufacturing process has been optimized. The plans for a follow-up project are already being developed. After the successful proof of principle experiments, one can imagine countless applications for the developed *in situ* microplasma cell. Observing the surface modifications of the electrode material is just the first step. Filling the cell with micro- or nanostructured materials such as the t-ZnO allows to observe

plasma modifications of multiple materials in real time. The same could be possible for plasma etching processes relevant for the MEMS industry. Furthermore, catalysts could be observed during catalytic processes, revealing that structural changes of the catalytic material in contact with plasma may be present. Even in the field of plasma medicine observations of bacteria or viruses during their contact with the physical plasma could help to understand the actual antibacterial and antiviral effects of the plasma.

Some of these proposed experiments could directly be performed with the current design of the *in situ* microplasma cell. For other experiments, the cell should be adapted to better fulfill the needs of the respective goal of the experiment. A major improvement would be the introduction of small "windows" into the metallic electrode film, similarly to the first proof of principle experiments [62]. Small holes in the metallic film would eliminate effects caused by imaging through two electrodes, and, thus, would enable spatial resolution close to the obtained resolution in the *ex situ* experiments. A lithographic process for the production of windowed Au electrodes was already developed within the current project and is described in the thesis of Niklas Kohlmann [236]. The usage of these windowed electrodes would enhance the resolution and allow a better focus on material treatment inside of the cell.

Shifting the research focus towards material treatment inside of the microplasma cell and away from the electrode material modification would also require a more stable electrode material to avoid electrode degradation prior to plasma modifications of the material of interest. TiN as conductive ceramic was investigated with the result of it being more stable compared to the Au thin films [327] and could replace these in the future.

Another approach to connect the *in situ* microplasma cell closer to various applications would be to change the plasma generation mechanism from a DC plasma to either a pulsed plasma or an AC plasma. Both, pulsed and AC plasma, would allow to modify the microplasma geometry to a dielectric barrier discharge to mimic most microplasmas used under atmospheric pressure conditions for catalysis or surface activation. Furthermore, operation using ns pulses could be used for a stroboscopic method, resulting in an *in operando* approach, avoiding interference between the plasma and the TEM optics, while drastically improving the temporal resolution.

Of course there are many more ideas to improve or apply the *in situ* microplasma cell, but first the proof of principle experiments in the most basic version of the cell have to be done. Within this thesis it was not possible to ignite the microplasma inside of the TEM, but all the necessary foundations to do so were obtained.

A microplasma geometry suited for the TEM integration was designed and extensively diagnosed to ensure its stability. The plasma diagnostics have been connected with investigations on the surface modifications to reveal more insight on the fundamentals of the power transfer mechanisms from the plasma to the surface under atmospheric pressure conditions. The microplasma geometry was successfully assembled in a vacuum-proof housing, completing the *in situ* microplasma cell. The cell was successfully introduced into the TEM and it could be proofed, that bright field imaging with a resolution of approx. 30 nm, as well as SAED and EDX measurements are possible.

Bibliography

- ¹I. Langmuir, "Oscillations in Ionized Gases", *Proceedings of the National Academy of Sciences* **14**, 627–637 (1928).
- ²H. M. Mott-Smith, "History of "Plasmas"", *Nature* **233**, 219–219 (1971).
- ³J. Cipo and H. Kersten, "Die Geschichte der Gasentladungsphysik", *Vakuum in Forschung und Praxis* **30**, 34–42 (2018).
- ⁴W. Crookes, "On radiant matter a lecture delivered to the British Association for the Advancement of Science, at Sheffield, Friday, August 22, 1879.", *American Journal of Science and Arts* **18**, 241 (1879).
- ⁵A. Fridman et al., *Plasma Physics and Engineering* (CRC Press, 2004).
- ⁶M. D. Smith, "Plasma Technology", *Kirk-Othmer Encyclopedia of Chemical Technology*, (2000).
- ⁷H. Falck-Ytter, *Aurora: The Northern Lights in Mythology, History, and Science* (Steiner-Books, 1999).
- ⁸F. Chen, *Introduction to Plasma Physics and Controlled Fusion* (Springer-Verlag GmbH, Dec. 2015).
- ⁹M. A. Lieberman and A. J. Lichtenberg, *Principles of Plasma Discharges and Materials Processing* (John Wiley & Sons, Inc., 2005).
- ¹⁰P. M. Bellan, *Fundamentals of Plasma Physics* (Cambridge University Press, 2006).
- ¹¹A. Piel, *Plasma Physics* (Springer Berlin Heidelberg, 2010).
- ¹²J. Meichsner et al., eds., *Nonthermal Plasma Chemistry and Physics* (CRC Press, 2012).
- ¹³G. Fridman et al., "Applied Plasma Medicine", *Plasma Processes and Polymers* **5**, 503–533 (2008).
- ¹⁴I. Adamovich et al., "The 2017 Plasma Roadmap: Low temperature plasma science and technology", *Journal of Physics D: Applied Physics* **50**, 323001 (2017).
- ¹⁵P. J. Bruggeman, F. Iza, and R. Brandenburg, "Foundations of atmospheric pressure non-equilibrium plasmas", *Plasma Sources Science and Technology* **26**, 123002 (2017).
- ¹⁶M. Laroussi et al., "Low-Temperature Plasma for Biology, Hygiene, and Medicine: Perspective and Roadmap", *IEEE Transactions on Radiation and Plasma Medical Sciences* **6**, 127–157 (2022).
- ¹⁷I. Adamovich et al., "The 2022 Plasma Roadmap: low temperature plasma science and technology", *Journal of Physics D: Applied Physics* **55**, 373001 (2022).
- ¹⁸D. B. Graves, "Plasma processing in microelectronics manufacturing", *AIChE Journal* **35**, 1–29 (1989).
- ¹⁹K.-D. Weltmann et al., "The future for plasma science and technology", *Plasma Processes and Polymers* **16**, 1800118 (2018).

- ²⁰M. Shearn et al., *Advanced plasma processing: etching, deposition, and wafer bonding techniques for semiconductor applications* (InTech New York, 2010).
- ²¹R. W. Johnson, A. Hultqvist, and S. F. Bent, "A brief review of atomic layer deposition: from fundamentals to applications", *Materials Today* **17**, 236–246 (2014).
- ²²H. Kim and I.-K. Oh, "Review of plasma-enhanced atomic layer deposition: Technical enabler of nanoscale device fabrication", *Japanese Journal of Applied Physics* **53**, 03DA01 (2014).
- ²³G. E. Moore, "Cramming More Components Onto Integrated Circuits", *Electronics* **38**, 19 (1965).
- ²⁴M. Lundstrom, "Moore's Law Forever?", *Science* **299**, 210–211 (2003).
- ²⁵*Semiconductor industry factbook* (Semiconductor Industry Association, 2018).
- ²⁶R. Henderson, *Industry employment and output projections to 2024*, 2015.
- ²⁷H. Hernández et al., *EU R&D scoreboard: the 2014 EU industrial R&D investment scoreboard*. (Publications Office, 2016).
- ²⁸R. d'Agostino et al., "Low-Temperature Plasma Processing of Materials: Past, Present, and Future", *Plasma Processes and Polymers* **2**, 7–15 (2005).
- ²⁹P. M. Martin, *Handbook of Deposition Technologies for Films and Coatings: Science, Applications and Technology* (William Andrew, 2009).
- ³⁰B. P. Jelle et al., "Fenestration of today and tomorrow: A state-of-the-art review and future research opportunities", *Solar Energy Materials and Solar Cells* **96**, 1–28 (2012).
- ³¹K. Allen et al., "Smart windows—Dynamic control of building energy performance", *Energy and Buildings* **139**, 535–546 (2017).
- ³²C. Tendero et al., "Atmospheric pressure plasmas: A review", *Spectrochimica Acta Part B: Atomic Spectroscopy* **61**, 2–30 (2006).
- ³³J. Winter, R. Brandenburg, and K.-D. Weltmann, "Atmospheric pressure plasma jets: an overview of devices and new directions", *Plasma Sources Science and Technology* **24**, 064001 (2015).
- ³⁴U. Kogelschatz, "Dielectric-Barrier Discharges: Their History, Discharge Physics, and Industrial Applications", *Plasma Chemistry and Plasma Processing* **23**, 1–46 (2003).
- ³⁵A. Zille, F. R. Oliveira, and A. P. Souto, "Plasma Treatment in Textile Industry", *Plasma Processes and Polymers* **12**, 98–131 (2014).
- ³⁶Y. Kusano, "Atmospheric Pressure Plasma Processing for Polymer Adhesion: A Review", *The Journal of Adhesion* **90**, 755–777 (2014).
- ³⁷O. V. Penkov et al., "A review of recent applications of atmospheric pressure plasma jets for materials processing", *Journal of Coatings Technology and Research* **12**, 225–235 (2015).
- ³⁸J. Friedrich, *The Plasma Chemistry of Polymer Surfaces: Advanced Techniques for Surface Design* (John Wiley & Sons, 2012).
- ³⁹Plasmatreteat, *Testimonials from Industry and Science*, Last accessed: 20.04.2022.
- ⁴⁰T. von Woedtke et al., "Plasmas for medicine", *Physics Reports* **530**, 291–320 (2013).
- ⁴¹V. Scholtz et al., "Nonthermal plasma — A tool for decontamination and disinfection", *Biotechnology Advances* **33**, 1108–1119 (2015).

- ⁴²G. Isbary et al., "Cold atmospheric argon plasma treatment may accelerate wound healing in chronic wounds: results of an open retrospective randomized controlled study in vivo", *Clinical Plasma Medicine* **1**, 25–30 (2013).
- ⁴³M. Keidar et al., "Cold atmospheric plasma in cancer therapy", *Physics of Plasmas* **20**, 057101 (2013).
- ⁴⁴D. B. Graves, "Reactive Species from Cold Atmospheric Plasma: Implications for Cancer Therapy", *Plasma Processes and Polymers* **11**, 1120–1127 (2014).
- ⁴⁵M. Keidar, "Plasma for cancer treatment", *Plasma Sources Science and Technology* **24**, 033001 (2015).
- ⁴⁶H. Tanaka et al., "New Hopes for Plasma-Based Cancer Treatment", *Plasma* **1**, 150–155 (2018).
- ⁴⁷S. E. Hunt, *Fission, Fusion and the Energy Crisis* (Elsevier Science, 2013).
- ⁴⁸C. L. Smith, "The need for fusion", *Fusion Engineering and Design* **74**, 3–8 (2005).
- ⁴⁹A. J. H. Donné, "The European roadmap towards fusion electricity", *Philosophical Transactions of the Royal Society A: Mathematical, Physical and Engineering Sciences* **377**, 20170432 (2019).
- ⁵⁰D. Meade, "50 years of fusion research", *Nuclear Fusion* **50**, 014004 (2009).
- ⁵¹J. Nuckolls et al., "Laser Compression of Matter to Super-High Densities: Thermonuclear (CTR) Applications", *Nature* **239**, 139–142 (1972).
- ⁵²R. S. Craxton et al., "Direct-drive inertial confinement fusion: A review", *Physics of Plasmas* **22**, 110501 (2015).
- ⁵³J. Nührenberg et al., "Overview on Wendelstein 7-X Theory", *Fusion Technology* **27**, 71–78 (1995).
- ⁵⁴T. Klinger et al., "Overview of first Wendelstein 7-X high-performance operation", *Nuclear Fusion* **59**, 112004 (2019).
- ⁵⁵L. J. Spitzer et al., "Problems of the Stellarator as a useful Power Source", (1954).
- ⁵⁶R. Aymar, "The ITER project", *IEEE Transactions on Plasma Science* **25**, 1187–1195 (1997).
- ⁵⁷ITER Physics Basis Editors et al., "Chapter 1: Overview and summary", *Nuclear Fusion* **39**, 2137–2174 (1999).
- ⁵⁸P.-H. Rebut, "From JET to the reactor", *Plasma Physics and Controlled Fusion* **48**, B1–B13 (2006).
- ⁵⁹R. Hawryluk et al., "Principal physics developments evaluated in the ITER design review", *Nuclear Fusion* **49**, 065012 (2009).
- ⁶⁰M. Seeger, "Perspectives on Research on High Voltage Gas Circuit Breakers", *Plasma Chemistry and Plasma Processing* **35**, 527–541 (2014).
- ⁶¹C. M. Franck, "HVDC Circuit Breakers: A Review Identifying Future Research Needs", *IEEE Transactions on Power Delivery* **26**, 998–1007 (2011).
- ⁶²K. Tai et al., "Integration of microplasma with transmission electron microscopy: Real-time observation of gold sputtering and island formation", *Scientific Reports* **3**, (2013).
- ⁶³J. G. Eden and S.-J. Park, "Microcavity plasma devices and arrays: a new realm of plasma physics and photonic applications", *Plasma Physics and Controlled Fusion* **47**, B83–B92 (2005).

- ⁶⁴K. H. Becker, K. H. Schoenbach, and J. G. Eden, "Microplasmas and applications", *Journal of Physics D: Applied Physics* **39**, R55–R70 (2006).
- ⁶⁵J. Franzke et al., "Microdischarges for Analytical Atomic Spectrometry: Design Considerations and Applications", *Encyclopedia of Analytical Chemistry: Applications, Theory and Instrumentation*, (2011).
- ⁶⁶L. Lin and Q. Wang, "Microplasma: A New Generation of Technology for Functional Nanomaterial Synthesis", *Plasma Chemistry and Plasma Processing* **35**, 925–962 (2015).
- ⁶⁷C. Chapman, *Glow Discharge Processes* (John Wiley & Sons, Sept. 1980).
- ⁶⁸J. Roth, *Industrial plasma engineering* (Institute of Physics Pub., Bristol Philadelphia, 1995).
- ⁶⁹R. Hippler et al., *Low Temperature Plasmas, Fundamentals, Technologies and Techniques* (Wiley-VCH, 2008).
- ⁷⁰A. Fridman, *Plasma Chemistry* (Cambridge University Press, 2008).
- ⁷¹Y. P. Raizer, *Gas Discharge Physics* (Springer Berlin Heidelberg, Sept. 2011).
- ⁷²A. von Keudell and V. Schulz-von der Gathen, "Foundations of low-temperature plasma physics—an introduction", *Plasma Sources Science and Technology* **26**, 113001 (2017).
- ⁷³P. Bruggeman and R. Brandenburg, "Atmospheric pressure discharge filaments and microplasmas: physics, chemistry and diagnostics", *Journal of Physics D: Applied Physics* **46**, 464001 (2013).
- ⁷⁴D. Mariotti and R. M. Sankaran, "Microplasmas for nanomaterials synthesis", *Journal of Physics D: Applied Physics* **43**, 323001 (2010).
- ⁷⁵P. Debye and E. Hückel, "Zur Theorie der Elektrolyte I. Gefrierpunktserniedrigung und verwandte Erscheinungen", *Phys. Zeitschrift* **24**, 185 (1923).
- ⁷⁶J. S. Townsend, *Electricity in Gases* (Clarendon Press, Oxford, 1915).
- ⁷⁷P. Tolias, "On secondary electron emission and its semi-empirical description", *Plasma Physics and Controlled Fusion* **56**, 123002 (2014).
- ⁷⁸S. Arumugam, P. Alex, and S. K. Sinha, "Effective secondary electron emission coefficient in DC abnormal glow discharge plasmas", *Physics of Plasmas* **24**, 112106 (2017).
- ⁷⁹M. Pamperin, F. X. Bronold, and H. Fehske, "Ion-induced secondary electron emission from metal surfaces", *Plasma Sources Science and Technology* **27**, 084003 (2018).
- ⁸⁰L. Hansen et al., "Conventional and non-conventional diagnostics of a stable atmospheric pressure DC normal glow microplasma discharge intended for in situ TEM studies", *Plasma Sources Science and Technology* **31**, 035013 (2022).
- ⁸¹W. de la Rue and H. W. Muller, "Experimental researches on the electric discharge with the chloride of silver battery", *Philosophical Transactions of the Royal Society of London* **171**, 65–116 (1880).
- ⁸²F. Paschen, "Über die zum Funkenuebergang in Luft, Wasserstoff und Kohlensäure bei verschiedenen Drücken erforderliche Potentialdifferenz", *Annalen der Physik* **273**, 69–96 (1889).
- ⁸³J. Lehr and P. Ron, *Foundations of Pulsed Power Technology* (Wiley & Sons, Limited, John, 2017).

- ⁸⁴J.-M. Torres and R. S. Dhariwal, "Electric field breakdown at micrometre separations in air and vacuum", *Microsystem Technologies* **6**, 6–10 (1999).
- ⁸⁵J.-M. Torres and R. S. Dhariwal, "Electric field breakdown at micrometre separations", *Nanotechnology* **10**, 102–107 (1999).
- ⁸⁶D. B. Go and A. Venkattraman, "Microscale gas breakdown: ion-enhanced field emission and the modified paschen's curve", *Journal of Physics D: Applied Physics* **47**, 503001 (2014).
- ⁸⁷L. H. Germer and F. E. Haworth, "A Low Voltage Discharge between Very Close Electrodes", *Physical Review* **73**, 1121–1121 (1948).
- ⁸⁸P. Chabert and N. Braithwaite, *Physics of radio-frequency plasmas* (Cambridge University Press, 2011).
- ⁸⁹M. Lieberman, "Dynamics of a collisional, capacitive RF sheath", *IEEE Transactions on Plasma Science* **17**, 338–341 (1989).
- ⁹⁰C. D. Child, "Discharge From Hot CaO", *Physical Review (Series I)* **32**, 492–511 (1911).
- ⁹¹I. Langmuir, "The Effect of Space Charge and Residual Gases on Thermionic Currents in High Vacuum", *Physical Review* **2**, 450–486 (1913).
- ⁹²D. Bohm, "The characteristics of electrical discharges in magnetic fields", *Qualitative Description of the Arc Plasma in a Magnetic Field* (1949).
- ⁹³R. N. Franklin, "Where is the sheath edge?", *Journal of Physics D: Applied Physics* **37**, 1342–1345 (2004).
- ⁹⁴K.-U. Riemann, "The Bohm criterion and sheath formation", *Journal of Physics D: Applied Physics* **24**, 493–518 (1991).
- ⁹⁵K.-U. Riemann, "The influence of collisions on the plasma sheath transition", *Physics of Plasmas* **4**, 4158–4166 (1997).
- ⁹⁶J. L. Blank, "Collision-Dominated Positive Column of a Weakly Ionized Gas", *Physics of Fluids* **11**, 1686 (1968).
- ⁹⁷R. N. Franklin and J. Snell, "The transition from collisionless to collisional active plasma in the fluid model and the relevance of the Bohm criterion to sheath formation", *Physics of Plasmas* **7**, 3077–3083 (2000).
- ⁹⁸R. N. Franklin, "What significance does the Bohm criterion have in an active collisional plasma sheath?", *Journal of Physics D: Applied Physics* **35**, 2270–2273 (2002).
- ⁹⁹R. P. Brinkmann, "From electron depletion to quasi-neutrality: the sheath–bulk transition in RF modulated discharges", *Journal of Physics D: Applied Physics* **42**, 194009 (2009).
- ¹⁰⁰H. R. Koenig and L. I. Maissel, "Application of RF Discharges to Sputtering", *IBM Journal of Research and Development* **14**, 168–171 (1970).
- ¹⁰¹P. S. Kothnur, X. Yuan, and L. L. Raja, "Structure of direct-current microdischarge plasmas in helium", *Applied Physics Letters* **82**, 529–531 (2003).
- ¹⁰²M. J. Kushner, "Modeling of microdischarge devices: Pyramidal structures", *Journal of Applied Physics* **95**, 846–859 (2004).
- ¹⁰³M. J. Kushner, "Modelling of microdischarge devices: plasma and gas dynamics", *Journal of Physics D: Applied Physics* **38**, 1633–1643 (2005).

- ¹⁰⁴P. G. C. Almeida, M. S. Benilov, and M. J. Faria, "Three-Dimensional Modeling of Self-Organization in DC Glow Microdischarges", *IEEE Transactions on Plasma Science* **39**, 2190–2191 (2011).
- ¹⁰⁵Y. Fu, P. Zhang, and J. P. Verboncoeur, "Paschen's curve in microgaps with an electrode surface protrusion", *Applied Physics Letters* **113**, 054102 (2018).
- ¹⁰⁶A. D. White, "New Hollow Cathode Glow Discharge", *Journal of Applied Physics* **30**, 711–719 (1959).
- ¹⁰⁷D. J. Sturges and H. J. Oskam, "Studies of the Properties of the Hollow Cathode Glow Discharge in Helium and Neon", *Journal of Applied Physics* **35**, 2887–2894 (1964).
- ¹⁰⁸K. H. Schoenbach et al., "High-pressure hollow cathode discharges", *Plasma Sources Science and Technology* **6**, 468–477 (1997).
- ¹⁰⁹S.-J. Park and J. G. Eden, "13–30 micron diameter microdischarge devices: Atomic ion and molecular emission at above atmospheric pressures", *Applied Physics Letters* **81**, 4127–4129 (2002).
- ¹¹⁰J. W. Frame et al., "Microdischarge devices fabricated in silicon", *Applied Physics Letters* **71**, 1165–1167 (1997).
- ¹¹¹J. P. Boeuf, L. C. Pitchford, and K. H. Schoenbach, "Predicted properties of microhollow cathode discharges in xenon", *Applied Physics Letters* **86**, 071501 (2005).
- ¹¹²E. Badareu and I. Popescu, "Researches on the double cathode effect", *International Journal of Electronics* **4**, 503–514 (1958).
- ¹¹³K. H. Schoenbach et al., "Microhollow cathode discharge excimer lamps", *Physics of Plasmas* **7**, 2186–2191 (2000).
- ¹¹⁴K. Frank et al., in *Conf. Record IEEE Int. Conf. on Plasma Science (Las Vegas, NV, USA)* (2001), p. 381.
- ¹¹⁵M. Moselhy et al., "Excimer emission from microhollow cathode argon discharges", *Journal of Physics D: Applied Physics* **36**, 2922–2927 (2003).
- ¹¹⁶C. Penache et al., "Characterization of a high-pressure microdischarge using diode laser atomic absorption spectroscopy", *Plasma Sources Science and Technology* **11**, 476–483 (2002).
- ¹¹⁷R. Block, O. Toedter, and K. H. Schoenbach, in *Proc. 30th AIAA Plasma Dynamics and Lasers Conf. (Norfolk, VA, USA)* (1999), Paper AIAA-99-3434.
- ¹¹⁸R. Block et al., in *Proc. 14th Int. Symp. on Plasma Chemistry (Prague, CZE)*, Vol. 2 (1999), p. 945.
- ¹¹⁹F. Leipold et al., "Electron density measurements in an atmospheric pressure air plasma by means of infrared heterodyne interferometry", *Journal of Physics D: Applied Physics* **33**, 2268–2273 (2000).
- ¹²⁰P. Kurunczi et al., "Measurement of rotational temperatures in high-pressure microhollow cathode (MHC) and capillary plasma electrode (CPE) discharges", *acta physica slovacica* **54**, 115–124 (2004).
- ¹²¹S. Iseni et al., "On the validity of neutral gas temperature by emission spectroscopy in micro-discharges close to atmospheric pressure", *Plasma Sources Science and Technology* **28**, 065003 (2019).
- ¹²²L. B. Loeb and J. M. Meek, *The mechanism of the electric spark* (Stanford University Press, 1941).

- ¹²³N. Brenning et al., "High-pressure pulsed avalanche discharges: formulas for required preionization density and rate for homogeneity", *IEEE Transactions on Plasma Science* **25**, 83–88 (1997).
- ¹²⁴U. Kogelschatz, B. Eliasson, and W. Egli, "From ozone generators to flat television screens: history and future potential of dielectric-barrier discharges", *Pure and Applied Chemistry* **71**, 1819–1828 (1999).
- ¹²⁵R. Brandenburg, "Dielectric barrier discharges: progress on plasma sources and on the understanding of regimes and single filaments", *Plasma Sources Science and Technology* **26**, 053001 (2017).
- ¹²⁶M. Šimor et al., "Atmospheric-pressure diffuse coplanar surface discharge for surface treatments", *Applied Physics Letters* **81**, 2716–2718 (2002).
- ¹²⁷M. Černák et al., "Diffuse Coplanar Surface Barrier Discharge and its applications for in-line processing of low-added-value materials", *The European Physical Journal Applied Physics* **47**, 22806 (2009).
- ¹²⁸M. Černák et al., "Generation of a high-density highly non-equilibrium air plasma for high-speed large-area flat surface processing", *Plasma Physics and Controlled Fusion* **53**, 124031 (2011).
- ¹²⁹L. Hansen, K. Reck, and H. Kersten, "Energy flux measurements on an atmospheric pressure surface barrier discharge", *Journal of Physics D: Applied Physics* **52**, 325201 (2019).
- ¹³⁰L. Hansen et al., "Understanding the energy balance of a surface barrier discharge for various molecular gases by a multi-diagnostic approach", *Journal of Applied Physics* **129**, 053308 (2021).
- ¹³¹B. Offerhaus et al., "Spatially resolved measurements of the physical plasma parameters and the chemical modifications in a twin surface dielectric barrier discharge for gas flow purification", *Plasma Processes and Polymers* **14**, 1600255 (2017).
- ¹³²F. Kogelheide et al., "Characterisation of volume and surface dielectric barrier discharges in N₂-O₂ mixtures using optical emission spectroscopy", *Plasma Processes and Polymers* **17**, 1900126 (2019).
- ¹³³T. Hoder et al., "Complex interaction of subsequent surface streamers via deposited charge: a high-resolution experimental study", *Plasma Physics and Controlled Fusion* **59**, 074001 (2017).
- ¹³⁴X. Lu et al., *Nonequilibrium Atmospheric Pressure Plasma Jets* (CRC Press, 2019).
- ¹³⁵P. Viegas et al., "Physics of plasma jets and interaction with surfaces: review on modelling and experiments", *Plasma Sources Science and Technology* **31**, 053001 (2022).
- ¹³⁶S. Reuter, T. von Woedtke, and K.-D. Weltmann, "The kINPen—a review on physics and chemistry of the atmospheric pressure plasma jet and its applications", *Journal of Physics D: Applied Physics* **51**, 233001 (2018).
- ¹³⁷J. Golda et al., "Concepts and characteristics of the 'COST reference microplasma jet'", *Journal of Physics D: Applied Physics* **49**, 084003 (2016).
- ¹³⁸J. Choi et al., "Electron and ion kinetics in a DC microplasma at atmospheric pressure", *IEEE Transactions on Plasma Science* **35**, 1274–1278 (2007).
- ¹³⁹D. Mariotti, J. A. McLaughlin, and P. Maguire, "Experimental study of breakdown voltage and effective secondary electron emission coefficient for a micro-plasma device", *Plasma Sources Science and Technology* **13**, 207–212 (2004).

- ¹⁴⁰Y. Fu et al., “Electrical breakdown from macro to micro/nano scales: a tutorial and a review of the state of the art”, *Plasma Research Express* **2**, 013001 (2020).
- ¹⁴¹V. I. Arkhipenko et al., “DC atmospheric pressure glow microdischarges in the current range from microamps up to amperes”, *The European Physical Journal D* **60**, 455–463 (2010).
- ¹⁴²N. Škoro, “Breakdown and discharge regimes in standard and micrometer size dc discharges”, *Journal of Physics: Conference Series* **399**, 012017 (2012).
- ¹⁴³S. Samukawa et al., “The 2012 plasma roadmap”, *Journal of Physics D: Applied Physics* **45**, 253001 (2012).
- ¹⁴⁴G. S. Oehrlein, “Surface processes in low pressure plasmas”, *Surface Science* **386**, 222–230 (1997).
- ¹⁴⁵G. S. Oehrlein et al., “Surface science issues in plasma etching”, *IBM Journal of Research and Development* **43**, 181–197 (1999).
- ¹⁴⁶J. Chang and J. P. Chang, “Achieving atomistic control in materials processing by plasma–surface interactions”, *Journal of Physics D: Applied Physics* **50**, 253001 (2017).
- ¹⁴⁷G. S. Oehrlein and S. Hamaguchi, “Foundations of low-temperature plasma enhanced materials synthesis and etching”, *Plasma Sources Science and Technology* **27**, 023001 (2018).
- ¹⁴⁸D. Hegemann and S. Gaiser, “Plasma surface engineering for manmade soft materials: a review”, *Journal of Physics D: Applied Physics* **55**, 173002 (2021).
- ¹⁴⁹A. Bogaerts et al., “The 2020 plasma catalysis roadmap”, *Journal of Physics D: Applied Physics* **53**, 443001 (2020).
- ¹⁵⁰C. Kittel, *Introduction to solid state physics* (Wiley, 2005).
- ¹⁵¹S. Arumugam, P. Alex, and S. K. Sinha, “Effective Secondary Electron Emission Coefficient of Brass”, *Current Smart Materials* **2**, 44–48 (2017).
- ¹⁵²W. H. Preece, “II. on a peculiar behaviour of glow-lamps when raised to high incandescence”, *Proceedings of the Royal Society of London* **38**, 219–230 (1885).
- ¹⁵³O. W. Richardson, “On the negative radiation from hot platinum”, *Philosophical of the Cambridge Philosophical Society* **11**, 286–295 (1901).
- ¹⁵⁴C. Crowell, “The Richardson constant for thermionic emission in Schottky barrier diodes”, *Solid-State Electronics* **8**, 395–399 (1965).
- ¹⁵⁵N. W. Ashcroft, *Solid state physics* (Holt, Rinehart and Winston, 1976).
- ¹⁵⁶M. Planck, “Über das Gesetz der Energieverteilung im Normalspectrum”, *Annalen der Physik* **309**, 553–563 (1901).
- ¹⁵⁷S. Dushman, “Electron Emission from Metals as a Function of Temperature”, *Physical Review* **21**, 623–636 (1923).
- ¹⁵⁸E. L. Murphy and R. H. Good, “Thermionic Emission, Field Emission, and the Transition Region”, *Physical Review* **102**, 1464–1473 (1956).
- ¹⁵⁹J. Orloff, *Handbook of Charged Particle Optics* (CRC Press, 2008).
- ¹⁶⁰M. Komm et al., “On thermionic emission from plasma-facing components in tokamak-relevant conditions”, *Plasma Physics and Controlled Fusion* **59**, 094002 (2017).
- ¹⁶¹L. S. Volkov, N. Y. Babaeva, and N. N. Antonov, “Role of thermionic emission in the formation of negative electric potential and oscillations in low pressure discharges”, *Journal of Physics D: Applied Physics* **54**, 105202 (2020).

- ¹⁶²X. Tang et al., "Enhanced thermionic emission of mayenite electride composites in an Ar glow discharge plasma", *Ceramics International* **47**, 16614–16631 (2021).
- ¹⁶³A. V. Phelps and Z. L. Petrovic, "Cold-cathode discharges and breakdown in argon: surface and gas phase production of secondary electrons", *Plasma Sources Science and Technology* **8**, R21–R44 (1999).
- ¹⁶⁴R. Buschhaus, M. Prenzel, and A. von Keudell, "Ion-induced secondary electron emission of oxidized nickel and copper studied in beam experiments", *Plasma Sources Science and Technology* **31**, 025017 (2022).
- ¹⁶⁵A. Marcak et al., "Note: Ion-induced secondary electron emission from oxidized metal surfaces measured in a particle beam reactor", *Review of Scientific Instruments* **86**, 106102 (2015).
- ¹⁶⁶F. Haase et al., "Dynamic determination of secondary electron emission using a calorimetric probe in a plasma immersion ion implantation experiment", *Plasma Sources Science and Technology* **27**, 044003 (2018).
- ¹⁶⁷C. Böhm and J. Perrin, "Retarding-field analyzer for measurements of ion energy distributions and secondary electron emission coefficients in low-pressure radio frequency discharges", *Review of Scientific Instruments* **64**, 31–44 (1993).
- ¹⁶⁸M. Daksha et al., "A computationally assisted spectroscopic technique to measure secondary electron emission coefficients in radio frequency plasmas", *Journal of Physics D: Applied Physics* **49**, 234001 (2016).
- ¹⁶⁹M. Daksha et al., "Material dependent modeling of secondary electron emission coefficients and its effects on PIC/MCC simulation results of capacitive RF plasmas", *Plasma Sources Science and Technology* **28**, 034002 (2019).
- ¹⁷⁰F. X. Bronold and H. Fehske, "Invariant embedding approach to secondary electron emission from metals", *Journal of Applied Physics* **131**, 113302 (2022).
- ¹⁷¹A. W. Adamson, *Physical chemistry of surfaces* (Wiley, 1997).
- ¹⁷²A. A. Abrikosov et al., *Methods of quantum field theory in statistical physics* (Dover Publications, 1975).
- ¹⁷³P. Kisliuk, "The sticking probabilities of gases chemisorbed on the surfaces of solids", *Journal of Physics and Chemistry of Solids* **3**, 95–101 (1957).
- ¹⁷⁴D. D. Koleske, S. M. Gates, and J. A. Schultz, "Facile abstraction of chemisorbed D on Si(100) by atomic H", *The Journal of Chemical Physics* **99**, 5619–5622 (1993).
- ¹⁷⁵D. D. Koleske, S. M. Gates, and B. Jackson, "Atomic H abstraction of surface H on Si: An Eley–Rideal mechanism?", *The Journal of Chemical Physics* **101**, 3301–3309 (1994).
- ¹⁷⁶P. Atkins and J. de Paula, *Physical Chemistry* (W. H. Freeman, 2006).
- ¹⁷⁷I. Langmuir, "The Adsorption Of Gases on Plane Surfaces of Glass, Mica and Platinum.", *Journal of the American Chemical Society* **40**, 1361–1403 (1918).
- ¹⁷⁸R. G. Compton, C. H. Bamford, and C. F. H. Tipper, *Simple Processes at the Gas-Solid Interface* (Elsevier Science & Technology Books, 1984).
- ¹⁷⁹Z. Zhang and M. G. Lagally, "Atomistic Processes in the Early Stages of Thin-Film Growth", *Science* **276**, 377–383 (1997).
- ¹⁸⁰C. Ratsch and J. A. Venables, "Nucleation theory and the early stages of thin film growth", *Journal of Vacuum Science & Technology A: Vacuum, Surfaces, and Films* **21**, S96–S109 (2003).

- ¹⁸¹F. C. Frank and J. H. van der Merwe, "One-dimensional dislocations. i. Static theory", *Proceedings of the Royal Society of London. Series A. Mathematical and Physical Sciences* **198**, 205–216 (1949).
- ¹⁸²F. C. Frank and J. H. van der Merwe, "One-dimensional dislocations. II. Misfitting monolayers and oriented overgrowth", *Proceedings of the Royal Society of London. Series A. Mathematical and Physical Sciences* **198**, 216–225 (1949).
- ¹⁸³F. C. Frank and J. H. van der Merwe, "One-dimensional dislocations - III. Influence of the second harmonic term in the potential representation, on the properties of the model", *Proceedings of the Royal Society of London. Series A. Mathematical and Physical Sciences* **200**, 125–134 (1949).
- ¹⁸⁴I. N. Stranski and L. Krastanow, "Zur Theorie der orientierten Ausscheidung von Ionenkristallen aufeinander", *Monatshefte für Chemie* **71**, 351–364 (1937).
- ¹⁸⁵M. Volmer and A. Weber, "Keimbildung in übersättigten Gebilden", *Zeitschrift für Physikalische Chemie* **119U**, 277–301 (1926).
- ¹⁸⁶A. von Keudell, "Surface processes during thin-film growth", *Plasma Sources Science and Technology* **9**, 455–467 (2000).
- ¹⁸⁷A. Zangwill, *Physics at surfaces* (Cambridge University Press, 1988), p. 454.
- ¹⁸⁸M. Cacciatore and M. Rutigliano, "Dynamics of plasma–surface processes: E–R and L–H atom recombination reactions", *Plasma Sources Science and Technology* **18**, 023002 (2009).
- ¹⁸⁹D. D. Eley and E. K. Rideal, "Parahydrogen Conversion on Tungsten", *Nature* **146**, 401–402 (1940).
- ¹⁹⁰M. Barbato, V. Bellucci, and C. Bruno, "Effects of catalytic boundary conditions accounting for incomplete chemical energy accommodation", in 7th AIAA/ASME joint thermophysics and heat transfer conference (1998).
- ¹⁹¹J. Küppers, "The hydrogen surface chemistry of carbon as a plasma facing material", *Surface Science Reports* **22**, 249–321 (1995).
- ¹⁹²A. Petukhov, "Effect of molecular mobility on kinetics of an electrochemical langmuir-hinshelwood reaction", *Chemical Physics Letters* **277**, 539–544 (1997).
- ¹⁹³B. Pignataro, *New Strategies in Chemical Synthesis and Catalysis* (Wiley-VCH Verlag GmbH, 2012).
- ¹⁹⁴A. Rousseau, G. Cartry, and X. Duten, "Surface recombination of hydrogen atoms studied by a pulsed plasma excitation technique", *Journal of Applied Physics* **89**, 2074–2078 (2001).
- ¹⁹⁵P. Sigmund, "Sputtering by ion bombardment theoretical concepts", in *Topics in Applied Physics* (Springer Berlin Heidelberg, 1981), pp. 9–71.
- ¹⁹⁶D. L. Smith, *Thin-film deposition, Principles and Practice* (McGraw-Hill, 1995).
- ¹⁹⁷K. Wasa, *Handbook of Sputter Deposition Technology, Fundamentals and Applications for Functional Thin Films, Nano-Materials and MEMS* (Elsevier Science & Technology Books, 2012).
- ¹⁹⁸D. Depla and S. Mahieu, eds., *Reactive Sputter Deposition* (Springer Berlin Heidelberg, 2008).
- ¹⁹⁹P. C. Zalm, "Some useful yield estimates for ion beam sputtering and ion plating at low bombarding energies", *Journal of Vacuum Science & Technology B: Microelectronics and Nanometer Structures* **2**, 151 (1984).

- ²⁰⁰J. Bohdansky, J. Roth, and H. L. Bay, "An analytical formula and important parameters for low-energy ion sputtering", *Journal of Applied Physics* **51**, 2861 (1980).
- ²⁰¹J. F. Ziegler, M. Ziegler, and J. Biersack, "SRIM – the stopping and range of ions in matter (2010)", *Nuclear Instruments and Methods in Physics Research Section B: Beam Interactions with Materials and Atoms* **268**, 1818–1823 (2010).
- ²⁰²T. Trottenberg, A. Spethmann, and H. Kersten, "An interferometric force probe for beam diagnostics and the study of sputtering", *EPJ Techniques and Instrumentation* **5**, (2018).
- ²⁰³M. Klette et al., "Directionally resolved measurements of momentum transport in sputter plumes as a critical test for simulations", *Journal of Vacuum Science & Technology A* **38**, 033013 (2020).
- ²⁰⁴R. Stephens, "Observation of sputtering at atmospheric pressure", *Journal of Analytical Atomic Spectrometry* **3**, 1137 (1988).
- ²⁰⁵H.-R. Lee, D.-J. Kim, and K.-H. Lee, "Anti-reflective coating for the deep coloring of PET fabrics using an atmospheric pressure plasma technique", *Surface and Coatings Technology* **142-144**, 468–473 (2001).
- ²⁰⁶K. Fricke et al., "High Rate Etching of Polymers by Means of an Atmospheric Pressure Plasma Jet", *Plasma Processes and Polymers* **8**, 51–58 (2010).
- ²⁰⁷N. Y. Babaeva et al., "Ion activation energy delivered to wounds by atmospheric pressure dielectric-barrier discharges: sputtering of lipid-like surfaces", *Journal of Physics D: Applied Physics* **45**, 115203 (2012).
- ²⁰⁸M. T. Jamil et al., "Atmospheric pressure glow discharge (APGD) plasma generation and surface modification of aluminum and silicon Si (100)", *Digest Journal of Nanomaterials and Biostructures* **12**, 595–604 (2017).
- ²⁰⁹J. Peran and S. E. Ražić, "Application of atmospheric pressure plasma technology for textile surface modification", *Textile Research Journal* **90**, 1174–1197 (2019).
- ²¹⁰J. M. Jasinski, B. S. Meyerson, and B. A. Scott, "Mechanistic Studies of Chemical Vapor Deposition", *Annual Review of Physical Chemistry* **38**, 109–140 (1987).
- ²¹¹L. Martinu and D. Poitras, "Plasma deposition of optical films and coatings: A review", *Journal of Vacuum Science & Technology A: Vacuum, Surfaces, and Films* **18**, 2619–2645 (2000).
- ²¹²P. D. Davidse, "Theory and practice of RF sputtering", *Vacuum* **17**, 139–145 (1967).
- ²¹³S. Rossnagel, "Directional and preferential sputtering-based physical vapor deposition", *Thin Solid Films* **263**, 1–12 (1995).
- ²¹⁴S. Sriraman et al., "Mechanism of hydrogen-induced crystallization of amorphous silicon", *Nature* **418**, 62–65 (2002).
- ²¹⁵L. Guo et al., "High Rate Deposition of Microcrystalline Silicon Using Conventional Plasma-Enhanced Chemical Vapor Deposition", *Japanese Journal of Applied Physics* **37**, L1116–L1118 (1998).
- ²¹⁶K. Tachibana et al., "Diagnostics and modelling of a methane plasma used in the chemical vapour deposition of amorphous carbon films", *Journal of Physics D: Applied Physics* **17**, 1727–1742 (1984).
- ²¹⁷K. Bewilogua and D. Hofmann, "History of diamond-like carbon films — From first experiments to worldwide applications", *Surface and Coatings Technology* **242**, 214–225 (2014).

- ²¹⁸J. Vetter, "60 years of DLC coatings: Historical highlights and technical review of cathodic arc processes to synthesize various DLC types, and their evolution for industrial applications", *Surface and Coatings Technology* **257**, 213–240 (2014).
- ²¹⁹M. Kamo et al., "Diamond synthesis from gas phase in microwave plasma", *Journal of Crystal Growth* **62**, 642–644 (1983).
- ²²⁰N. Marchack and J. P. Chang, "Chemical Processing of Materials on Silicon: More Functionality, Smaller Features, and Larger Wafers", *Annual Review of Chemical and Biomolecular Engineering* **3**, 235–262 (2012).
- ²²¹H. B. Profijt et al., "Plasma-Assisted Atomic Layer Deposition: Basics, Opportunities, and Challenges", *Journal of Vacuum Science & Technology A* **29**, 050801 (2011).
- ²²²B. A. Movchan and A. V. Demchishin, "Structure and Properties of Thick Condensates of Nickel, Titanium, Tungsten, Aluminum Oxides, and Zirconium Dioxide in Vacuum.", *Fizika Metallov I Metallovedenie* **28**, 653–60 (1969).
- ²²³J. A. Thornton, "Influence of apparatus geometry and deposition conditions on the structure and topography of thick sputtered coatings", *Journal of Vacuum Science and Technology* **11**, 666–670 (1974).
- ²²⁴P. B. Barna and M. Adamik, "Fundamental structure forming phenomena of polycrystalline films and the structure zone models", *Thin Solid Films* **317**, 27–33 (1998).
- ²²⁵A. Anders, "A structure zone diagram including plasma-based deposition and ion etching", *Thin Solid Films* **518**, 4087–4090 (2010).
- ²²⁶R. F. Bunshah, *Handbook of Deposition Technologies for Films and Coatings: Science, Applications and Technology* (William Andrew, 1994).
- ²²⁷D. M. Mattox, *Handbook of Physical Vapor Deposition (PVD) Processing* (William Andrew, 2010).
- ²²⁸A. Anders, *Cathodic Arcs: From Fractal Spots to Energetic Condensation*, Vol. 50 (Springer, 2008).
- ²²⁹H. Kersten et al., "The energy balance at substrate surfaces during plasma processing", *Vacuum* **63**, 385–431 (2001).
- ²³⁰J. W. Coburn and H. F. Winters, "Ion- and electron-assisted gas-surface chemistry—An important effect in plasma etching", *Journal of Applied Physics* **50**, 3189–3196 (1979).
- ²³¹H. F. Winters and J. Coburn, "Surface science aspects of etching reactions", *Surface Science Reports* **14**, 162–269 (1992).
- ²³²V. M. Donnelly and A. Kornblit, "Plasma etching: Yesterday, today, and tomorrow", *Journal of Vacuum Science & Technology A: Vacuum, Surfaces, and Films* **31**, 050825 (2013).
- ²³³M. Stahl, T. Trottenberg, and H. Kersten, "A calorimetric probe for plasma diagnostics", *Review of Scientific Instruments* **81**, 023504 (2010).
- ²³⁴S. Bornholdt, M. Fröhlich, and H. Kersten, "Calorimetric Probes for Energy Flux Measurements in Process Plasmas", in *Complex Plasmas* (Springer International Publishing, 2014), pp. 197–234.
- ²³⁵L. Rosenfeldt, L. Hansen, and H. Kersten, "The Use of Passive Thermal Probes for the Determination of Energy Fluxes in Atmospheric Pressure Plasmas", *IEEE Transactions on Plasma Science* **49**, 3325–3335 (2021).
- ²³⁶N. Kohlmann, "(Plasma) Modification of nano scale materials studied by TEM", PhD thesis (Kiel University, (Submitted)).

- ²³⁷M. Pelgrom, *Analog-to-Digital Conversion* (Springer-Verlag GmbH, Sept. 2016).
- ²³⁸W. Demtröder, *Experimentalphysik 2* (Springer Berlin Heidelberg, 2013).
- ²³⁹U. Fantz, “Basics of plasma spectroscopy”, *Plasma Sources Science and Technology* **15**, S137–S147 (2006).
- ²⁴⁰V. N. Ochkin, *Spectroscopy of Low Temperature Plasma* (Wiley, 2009).
- ²⁴¹G. Dilecce, “Optical spectroscopy diagnostics of discharges at atmospheric pressure”, *Plasma Sources Science and Technology* **23**, 015011 (2014).
- ²⁴²D. M. Devia, L. V. Rodriguez-Restrepo, and E. Restrepo-Parra, “Methods Employed in Optical Emission Spectroscopy Analysis: a review”, *Ingeniería y Ciencia* **11**, 239–267 (2015).
- ²⁴³R. Engeln, B. Klarenaar, and O. Guaitella, “Foundations of optical diagnostics in low-temperature plasmas”, *Plasma Sources Science and Technology* **29**, 063001 (2020).
- ²⁴⁴R. Payling et al., *Glow Discharge Optical Emission Spectroscopy, A Practical Guide* (The Royal Society of Chemistry, 2007).
- ²⁴⁵C. O. Laux et al., “Optical diagnostics of atmospheric pressure air plasmas”, *Plasma Sources Science and Technology* **12**, 125–138 (2003).
- ²⁴⁶M. Šimek, “Optical diagnostics of streamer discharges in atmospheric gases”, *Journal of Physics D: Applied Physics* **47**, 463001 (2014).
- ²⁴⁷V. M. Donnelly, “Plasma electron temperatures and electron energy distributions measured by trace rare gases optical emission spectroscopy”, *Journal of Physics D: Applied Physics* **37**, R217–R236 (2004).
- ²⁴⁸D. L. Crintea et al., “Plasma diagnostics by optical emission spectroscopy on argon and comparison with Thomson scattering”, *Journal of Physics D: Applied Physics* **42**, 045208 (2009).
- ²⁴⁹X.-M. Zhu and Y.-K. Pu, “Optical emission spectroscopy in low-temperature plasmas containing argon and nitrogen: determination of the electron temperature and density by the line-ratio method”, *Journal of Physics D: Applied Physics* **43**, 403001 (2010).
- ²⁵⁰X.-M. Zhu et al., “Measurement of the temporal evolution of electron density in a nanosecond pulsed argon microplasma: using both stark broadening and an OES line-ratio method”, *Journal of Physics D: Applied Physics* **45**, 295201 (2012).
- ²⁵¹A. Y. Nikiforov et al., “Electron density measurement in atmospheric pressure plasma jets: Stark broadening of hydrogenated and non-hydrogenated lines”, *Plasma Sources Science and Technology* **24**, 034001 (2015).
- ²⁵²S. S. Ivković et al., “On the use of the intensity ratio of the lines for electric field measurements in atmospheric pressure dielectric barrier discharge”, *Journal of Physics D: Applied Physics* **47**, 055204 (2014).
- ²⁵³Z. Navrátil et al., “Electric field development in γ -mode radiofrequency atmospheric pressure glow discharge in helium”, *Plasma Sources Science and Technology* **25**, 03LT01 (2016).
- ²⁵⁴P. J. Bruggeman et al., “Gas temperature determination from rotational lines in non-equilibrium plasmas: a review”, *Plasma Sources Science and Technology* **23**, 023001 (2014).
- ²⁵⁵A. Kramida and Y. Ralchenko, *NIST Atomic Spectra Database, NIST Standard Reference Database* 78, 1999.

- ²⁵⁶*Specair*, <http://www.specair-radiation.net/index.php> - Last accessed: 02.11.2022.
- ²⁵⁷J. Luque and D. R. Crosley, "Lifbase: Database and Spectral Simulation Program (Version 1.5)", SRI International Report MP 99, <https://www.sri.com/engage/products-solutions/lifbase> - Last accessed: 02.11.2022 (1999).
- ²⁵⁸C. M. Western, "PGOPHER: A program for simulating rotational, vibrational and electronic spectra", *Journal of Quantitative Spectroscopy and Radiative Transfer* **186**, 221–242 (2017).
- ²⁵⁹J. Voráč and P. Synek, *MassiveOES software package*, https://bitbucket.org/OES_muni/massiveoes/ - Last accessed: 02.11.2022, 2016.
- ²⁶⁰S. Reuter et al., "Review on VUV to MIR absorption spectroscopy of atmospheric pressure plasma jets", *Plasma Sources Science and Technology* **24**, 054001 (2015).
- ²⁶¹G. D. Stancu, "Spectroscopy and Spectroscopic: measurement techniques for aerospace flows", in, edited by D. Giordano and Y. Babou (VKI, 2014) Chap. Laser based spectroscopic diagnostics from UV to Mid-IR applied to the study of atmospheric pressure discharges.
- ²⁶²H. R. Griem, *Plasma spectroscopy* (McGraw-Hill, 1964).
- ²⁶³R. C. Hilborn, "Einstein coefficients, cross sections, f values, dipole moments, and all that", *American Journal of Physics* **50**, 982–986 (1982).
- ²⁶⁴N. Sadeghi, "Practical Aspects of Molecular Spectroscopy in Plasmas 6. Molecular Spectroscopy Techniques Applied for Processing Plasma Diagnostics", *Journal of Plasma and Fusion Research* **80**, 767–776 (2004).
- ²⁶⁵W. Demtröder, *Laser Spectroscopy* (Springer Berlin Heidelberg, 2008).
- ²⁶⁶H.-J. Kunze, *Introduction to Plasma Spectroscopy* (Springer Berlin Heidelberg, 2009).
- ²⁶⁷OceanOptics, *HR2000+ Spectrometer Installation and Operation Manual*, <https://www.oceaninsight.com/globalassets/catalog-blocks-and-images/manuals-instruction-old-logo/spectrometer/hr2000-.pdf> - Last accessed: 02.11.2022, 2010.
- ²⁶⁸C. H. Thomas and O. S. Duffendack, "Anode Spots and their Relations to the Absorption and Emission of Gases by the Electrodes of a Geissler Discharge", *Physical Review* **35**, 72–91 (1930).
- ²⁶⁹Y. A. Astrov and H.-G. Purwins, "Plasma spots in a gas discharge system: birth, scattering and formation of molecules", *Physics Letters A* **283**, 349–354 (2001).
- ²⁷⁰T. Verreycken, P. Bruggeman, and C. Leys, "Anode pattern formation in atmospheric pressure air glow discharges with water anode", *Journal of Applied Physics* **105**, 083312 (2009).
- ²⁷¹N. Shirai, S. Ibuka, and S. Ishii, "Self-Organization Pattern in the Anode Spot of an Atmospheric Glow Microdischarge using an Electrolyte Anode and Axial Miniature Helium Flow", *Applied Physics Express* **2**, 036001 (2009).
- ²⁷²H. Grosch et al., "Spatio-temporal development of microdischarges in a surface barrier discharge arrangement in air at atmospheric pressure", *The European Physical Journal D* **60**, 547–553 (2010).
- ²⁷³Y. E. Kovach, M. C. Garcia, and J. E. Foster, "The variation in self-organized anode plasma pattern structure with solution electrolyte type in 1 atm DC glow discharge", *Plasma Sources Science and Technology* **30**, 015007 (2021).
- ²⁷⁴J. Smith et al., "Intensified CCD camera system for plasma diagnostics (abstract)", *Review of Scientific Instruments* **56**, 871–871 (1985).

- ²⁷⁵V. A. Shuvalov, A. E. Churilov, and M. G. Bystritskii, "Diagnostics of Flows of Pulsed Plasma by Probe, Microwave, and Photometric Methods", *High Temperature* **38**, 843–847 (2000).
- ²⁷⁶H. Kersten et al., "Energy influx from an rf plasma to a substrate during plasma processing", *Journal of Applied Physics* **87**, 3637–3645 (2000).
- ²⁷⁷H. Kersten et al., "Plasma and ion beam characterization by non-conventional methods", *Surface and Coatings Technology* **200**, 809–813 (2005).
- ²⁷⁸Z. Wang and C. M. Ticos, "Dust as a versatile matter for high-temperature plasma diagnostic", *Review of Scientific Instruments* **79**, 10F333 (2008).
- ²⁷⁹Navitar[®], *12x Zoom Lense System*, <https://navitar.com/products/imaging-optics/high-magnification-imaging/12x-zoom/> - Last accessed: 02.11.2022.
- ²⁸⁰Navitar[®], *12x Xtender*, <https://navitar.com/products/imaging-optics/high-magnification-imaging/12x-zoom/12x-xtender/> - Last accessed: 02.11.2022.
- ²⁸¹Ximea, *MQ042CG-CM*, <https://www.ximea.com/products/usb3-vision-cameras-xiq-line/mq042cg-cm> - Last accessed: 02.11.2022.
- ²⁸²© 2021 IEEE. Reprinted, with permission, from Lukas Rosenfeldt, Luka Hansen and Holger Kersten, *The Use of Passive Thermal Probes for the Determination of Energy Fluxes in Atmospheric Pressure Plasmas*, *IEEE Transactions on Plasma Science*, November 2021.
- ²⁸³M. Born, *Principles of Optics, Electromagnetic Theory of Propagation, Interference and Diffraction of Light* (Cambridge University Press, 1999).
- ²⁸⁴E. Abbe, "VII.-On the Estimation of Aperture in the Microscope.", *Journal of the Royal Microscopical Society* **1**, 388–423 (1881).
- ²⁸⁵E. Abbe, "XV.-The Relation of Aperture and Power in the Microscope (continued)", *Journal of the Royal Microscopical Society* **3**, 790–812 (1883).
- ²⁸⁶S. G. Lipson, *Optical Physics* (Cambridge University Press, 1995).
- ²⁸⁷L. De Broglie, "Waves and Quanta", *Nature* **112**, 540–540 (1923).
- ²⁸⁸D. B. Williams, *Transmission Electron Microscopy, A Textbook for Materials Science : Imaging* (Plenum Press, 2009).
- ²⁸⁹Gringer, By Gringer (talk) - Commons: Scheme TEM en.png, CC BY-SA 3.0, <https://commons.wikimedia.org/w/index.php?curid=5624170>.
- ²⁹⁰Steff, By File:Schema MEB (it).svg: User:Steff, modified by User:ARTEderivative work MarcoTolo - File:Schema MEB (it).svg, CC BY-SA 3.0, <https://commons.wikimedia.org/w/index.php?curid=9643934>.
- ²⁹¹P. W. Hawkes, "Ernst Ruska", *Physics Today* **43**, 84–85 (1990).
- ²⁹²R. Erni et al., "Atomic-Resolution Imaging with a Sub-50-pm Electron Probe", *Physical Review Letters* **102**, 096101 (2009).
- ²⁹³B. Fultz and J. M. Howe, *Transmission Electron Microscopy and Diffractometry of Materials 3rd Edition* (Springer, 2008).
- ²⁹⁴J. Thomas and T. Gemming, *Analytical Transmission Electron Microscopy, An Introduction for Operators* (Springer London, Limited, 2014).
- ²⁹⁵A. Fleming, "On the history and development of the thermionic valve", *Journal of Scientific Instruments* **11**, 44–49 (1934).
- ²⁹⁶P. Buseck, J. M. Cowley, and L. Eyring, *High-Resolution Transmission Electron Microscopy, And Associated Techniques* (Oxford University Press, USA, 1989).

- ²⁹⁷P. Geuens and D. Van Dyck, "The S-state model: a work horse for HRTEM", *Ultra-microscopy* **93**, 179–198 (2002).
- ²⁹⁸A. J. D'Alfonso et al., "Atomic-resolution chemical mapping using energy-dispersive x-ray spectroscopy", *Physical Review B* **81**, 100101(R) (2010).
- ²⁹⁹L. J. Allen et al., "Chemical mapping at atomic resolution using energy-dispersive x-ray spectroscopy", *MRS Bulletin* **37**, 47–52 (2012).
- ³⁰⁰R. F. Egerton, "Electron energy-loss spectroscopy in the TEM", *Reports on Progress in Physics* **72**, 016502 (2008).
- ³⁰¹F. Hofer et al., "Fundamentals of electron energy-loss spectroscopy", *IOP Conference Series: Materials Science and Engineering* **109**, 012007 (2016).
- ³⁰²C. E. Lyman, *Scanning Electron Microscopy, X-Ray Microanalysis, and Analytical Electron Microscopy, A Laboratory Workbook* (Springer US, 1990).
- ³⁰³Y. Leng, *Materials Characterization, Introduction to Microscopic and Spectroscopic Methods* (Wiley & Sons, Incorporated, 2013).
- ³⁰⁴R. F. Egerton, *Physical Principles of Electron Microscopy, An Introduction to TEM, SEM, and AEM* (Springer London, Limited, 2016).
- ³⁰⁵G. Dehm, J. M. Howe, and J. Zweck, *In-Situ Electron Microscopy, Applications in Physics, Chemistry and Materials Science* (Wiley & Sons, Incorporated, 2012).
- ³⁰⁶F. M. Ross and A. M. Minor, *In Situ Transmission Electron Microscopy*, edited by P. Hawkes and J. C. H. Spence, *Springer Handbook of Microscopy* (Springer-Verlag GmbH, Nov. 2019).
- ³⁰⁷M. von Ardenne, "Das Elektronen-Rastermikroskop", *Zeitschrift für Physik* **109**, 553–572 (1938).
- ³⁰⁸D. McMullan, "Scanning electron microscopy 1928–1965", *Scanning* **17**, 175–185 (2006).
- ³⁰⁹J. I. Goldstein et al., *Scanning Electron Microscopy and X-Ray Microanalysis* (Springer New York, 2018).
- ³¹⁰H. G. J. Moseley, "The high-frequency spectra of the elements", *The London, Edinburgh and Dublin Philosophical Magazine and Journal of Science* **26**, 1024–1034 (1913).
- ³¹¹H. G. J. Moseley, "The High-Frequency Spectra of the Elements. Part II", *The London, Edinburgh and Dublin Philosophical Magazine and Journal of Science* **27**, 703–713 (1914).
- ³¹²M. Stamm, ed., *Polymer Surfaces and Interfaces Characterization, Modification and Applications* (Springer Berlin Heidelberg, 2008).
- ³¹³M. P. Seah, "The quantitative analysis of surfaces by XPS: A review", *Surface and Interface Analysis* **2**, 222–239 (1980).
- ³¹⁴J. D. Andrade, "X-ray Photoelectron Spectroscopy (XPS)", in *Surface and Interfacial Aspects of Biomedical Polymers* (Springer US, 1985), pp. 105–195.
- ³¹⁵G. Greczynski and L. Hultman, "X-ray photoelectron spectroscopy: Towards reliable binding energy referencing", *Progress in Materials Science* **107**, 100591 (2020).
- ³¹⁶C. J. V. Oss, R. J. Good, and M. K. Chaudhury, "Additive and nonadditive surface tension components and the interpretation of contact angles", *Langmuir* **4**, 884–891 (1988).
- ³¹⁷R. J. Good, "Contact angle, wetting, and adhesion: a critical review", *Journal of Adhesion Science and Technology* **6**, 1269–1302 (1992).

- ³¹⁸H. B. Eral, D. J. C. M. 't Mannetje, and J. M. Oh, "Contact angle hysteresis: a review of fundamentals and applications", *Colloid and Polymer Science* **291**, 247–260 (2012).
- ³¹⁹M. A. Q. Siddiqui et al., "Current understanding of shale wettability: A review on contact angle measurements", *Earth-Science Reviews* **181**, 1–11 (2018).
- ³²⁰T. Huhtamäki et al., "Surface-wetting characterization using contact-angle measurements", *Nature Protocols* **13**, 1521–1538 (2018).
- ³²¹R. Akbari and C. Antonini, "Contact angle measurements: From existing methods to an open-source tool", *Advances in Colloid and Interface Science* **294**, 102470 (2021).
- ³²²T. Young, "III. An essay on the cohesion of fluids", *Philosophical Transactions of the Royal Society of London* **95**, 65–87 (1805).
- ³²³L. Hansen et al., "Conventional and non-conventional diagnostics of a stable atmospheric pressure DC normal glow microplasma discharge intended for in situ TEM studies", *Plasma Sources Science and Technology* **31**, © IOP Publishing. Reproduced with permission. All rights reserved., 035013 (2022).
- ³²⁴L. Hansen et al., "Correlations between energy flux and thin film modifications in an atmospheric pressure direct current microplasma", *Thin Solid Films* **765**, 139633 (2023).
- ³²⁵N. Kohlmann et al., "Fabrication of ZnO nanobrushes by H₂–C₂H₂ plasma etching for H₂ sensing applications", *ACS Applied Materials & Interfaces* **13**, 61758–61769 (2021).
- ³²⁶M. L. Marxen et al., "On the plasma permeability of highly porous ceramic framework materials using polymers as marker materials", *Plasma Processes and Polymers*, (2022).
- ³²⁷Y. Ekici, "Development and characterisation of suitable electrode materials for a tem integrable microplasma cell", MA thesis (Insitute for Materials Science, Faculty of Engineering, Kiel University, 2022).
- ³²⁸Hummingbird Scientific, *Electrical biasing*, <https://hummingbirdscientific.-com/wp-content/uploads/Biasing-Brochure-WEB.pdf> - Last accessed: 02.11.2022, 2014.
- ³²⁹D. H. Alsem, *High Voltage Biasing Holder Design JOEL HR Objective Pole Piece*, (Confidential) Hummingbird Scientific Design Review, 2022.
- ³³⁰Pelco®, *Silicon Nitride Support Film, 35nm, 70x70µm Aperture (25) on 0.5 x 0.5mm Window*, Product No. 21515-10 https://www.tedpella.com/grids_html/silicon-nitride.aspx - Last accessed: 02.11.2022.
- ³³¹X. Cui, "In-Situ TEM Plasma Chip Nanofabrication and Characterization", MA thesis (Department of Mechanical Engineering - Michigan Technological University, 2014).
- ³³²W. M. Abbott et al., "Less is More: Improved Thermal Stability and Plasmonic Response in Au Films via the Use of SubNanometer Ti Adhesion Layers", *ACS Applied Materials & Interfaces* **11**, 7607–7614 (2019).
- ³³³Goodfellow, *Silver - Insulated Wire*, Product Code: AG00-SW-000118 - <https://www.goodfellow.com/de/en-us/displayitemdetails/p/ag00-sw-000118/silver-insulated-wire> - Last accessed: 02.11.2022.
- ³³⁴Goodfellow, *Copper - Insulated Wire*, Product Code: CU00-SW-000126 - <https://www.goodfellow.com/de/en-us/displayitemdetails/p/cu00-sw-000126/copper-insulated-wire> - Last accessed: 02.11.2022.

- ³³⁵Electrolube, *Silver Conductive Paint*, Product Code: SCP03B - <https://www.macdermidalpha.com/sites/default/files/2022-07/SCP-Maintenance-and-Service-Aids-EN-01Apr22-TB.pdf> - Last accessed: 02.11.2022.
- ³³⁶Goodfellow, *Polyimide - Film, Grade: DuPont™ Kapton® HN*, Product Code: IM30-FM-000200 - <https://www.goodfellow.com/de/en-us/displayitemdetails/p/im30-fm-000200/polyimide-film> - Last accessed: 02.11.2022.
- ³³⁷Abitzsch, *Präzisionsnormteile GmbH*, Contact Person: Maik Kreuzau - <https://www.abitzsch-gmbh.de/> - Last accessed: 02.11.2022.
- ³³⁸Kurt J. Lesker Company, *Torr Seal® Low Vapour Pressure Epoxy*, <https://www.lesker.com/newweb/fluids/sealants-epoxy/torrseal/> - Last accessed: 02.11.2022.
- ³³⁹Apple Rubber, *MicrOring*, APPLE P/N: R00032-027-75VTB - <https://www.applerrubber.com/src/pdf/microrings.pdf> - Last accessed: 02.11.2022.
- ³⁴⁰Pfeiffer Vacuum GmbH, *The Vacuum Technology Book - Volume II - Part 2* (Pfeiffer Vacuum GmbH, 2013).
- ³⁴¹RJ Lasertechnik GmbH, <https://www.rjlasertechnik.de/> - Last accessed: 02.11.2022.
- ³⁴²H. Robbins and B. Schwartz, "Chemical Etching of Silicon", *Journal of The Electrochemical Society* **106**, 505 (1959).
- ³⁴³H. Robbins and B. Schwartz, "Chemical Etching of Silicon", *Journal of The Electrochemical Society* **107**, 108 (1960).
- ³⁴⁴B. Schwartz and H. Robbins, "Chemical Etching of Silicon", *Journal of The Electrochemical Society* **108**, 365 (1961).
- ³⁴⁵B. Schwartz and H. Robbins, "Chemical Etching of Silicon: IV . Etching Technology", *Journal of The Electrochemical Society* **123**, 1903–1909 (1976).
- ³⁴⁶Rico Design, *Art School Aquarell Synthetic rund grauer stiel Gr. 0*, Product No.: 7329.000, Size: 0 - <https://www.rico-design.com/rico-design-pinsel-art-school-aquarell-synthetic-rund-grauer-stiel?number=2649986> - Last accessed: 02.11.2022.
- ³⁴⁷Sealware®- Internationale Dichtungstechnik GmbH, *Micro O-ring Design VIOR 1.50 x 0.60 FPM 70*, Order No.: 10171038 - <https://sealware.de/sealingtechnology/O-Rings-Micro-O-Rings-DIN-3770-3771-ISO-3601/seals/VIOR+1,50x0,60+FPM+10171038> - Last accessed: 02.11.2022.
- ³⁴⁸R. C. Jaeger, *Microelectronic Circuit Design* (McGraw-Hill, 2011).
- ³⁴⁹P. Horowitz and W. Hill, *The Art of Electronics* (Cambridge University Press, 2016).
- ³⁵⁰K. G. McKay, "Avalanche Breakdown in Silicon", *Physical Review* **94**, 877–884 (1954).
- ³⁵¹RS PRO, *Red Silicone Resin Conformal Coating*, RS Stock No.: 831-141 - <https://ie.rs-online.com/web/p/conformal-coatings/0831141> - Last accessed: 02.11.2022.
- ³⁵²Steinbach AG, Contact Person: Viktoria Lieder - <https://www.steinbach-ag.de/> - Last accessed: 02.11.2022.
- ³⁵³N. de Jonge et al., "Resolution and aberration correction in liquid cell transmission electron microscopy", *Nature Reviews Materials* **4**, 61–78 (2018).
- ³⁵⁴B07 Committee, *Specification for Aluminum and Aluminum-Alloy Sheet and Plate (Metric)*, DOI: 10.1520%2Fb0209m-14 - Last accessed: 02.11.2022.
- ³⁵⁵F. Rasch et al., "Wet-Chemical Assembly of 2D Nanomaterials into Lightweight, Microtube-Shaped, and Macroscopic 3D Networks", *ACS Applied Materials & Interfaces* **11**, 44652–44663 (2019).

- ³⁵⁶F. Schütt et al., “Conversionless efficient and broadband laser light diffusers for high brightness illumination applications”, *Nature Communications* **11**, (2020).

Acknowledgements

It has been nearly a decade since I started my physics studies at Kiel University and after a rough start it has been an amazing time. Needless to say, that this was thanks to my friends, family, (former) colleagues and collaboration partners. Without them my journey could have ended way too early.

Prof. Dr. Holger Kersten recruited me as student during my second semester, allowed me to gain lab experience and to find my passion for the field of plasma physics. Without experiencing the lab environment and witnessing the perfect mix of fundamental and applied research, I might could have ended up with an engineering degree. He helped me to integrate an internship at the INP in Greifswald into the busy physics curriculum which resulted in contacts allowing me to write my Master thesis at Princeton University. His help during the application at Princeton and organization of the paperwork from the examination office in Kiel enabled me to leave the continent for the first time. The visit of Prof. Dr. Gary Edens group following my time in Princeton helped to gain a smooth start into the DFG project resulting in the present thesis. The honest joy in Prof. Dr. Holger Kerstens eyes when he told me about the DFG approval for this project and therefore the possibility for me to do my PhD in his group, is not forgotten till today. The same is true for countless other moments, especially at international conferences, which visits can not be taken for granted. His leadership, characterized by trust, enabled independent work and a lot of freedom, but also the possibility to discuss results or further procedures with him at any time. For me, these were the perfect working conditions. The overall family atmosphere within the working group as a result of him leading by example is what every workplace wishes for. In the end, I would like to express my special thanks to him for the time he gave me during a difficult period and for the words he found.

The development of the microplasma cell, especially the vacuum-proof housing, required a lot of technical knowledge on the possibilities and current limits of fine machining. Without the help and constant discussions with Frank Brach the design of the shells would have been way harder. Further, I would like to thank the workshop of the physics institute for actually machining the shells. Michael Poser helped with the design of the electric circuit and constantly reminded me, that the high voltage components have to be secured in grounded or dielectric boxes. Volker Rohwer basically did everything else related to the laboratories infrastructure. Thank you for always reacting instantly if any problems appeared.

I have been part of the Plasma Technology Group for over 8 years. Starting under the supervision of Dr. Sven Bornholdt on a low pressure magnetron sputtering device, before switching in the atmospheric pressure lab to work with Dr. Thorben Kewitz and Johannes von Frieling. The office was shared with Dr. Sven Gauter and Dr. Fabian Haase. The atmosphere was incredibly casual and both of them always took their time to answer questions and help out with programming issues. Further, I would like to thank my office colleague Dr. Viktor Schneider, our so-called "AG Mutti", for countless (non) scientific discussions, for his help with all kinds of organizational work and a lot of extraordinary memories from different conferences or joint evenings in Kiel. Felix Schlichting and Mathis Klette also contribute to this memories. Felix always found the best hotels or AirBnBs and even more importantly the best bars in town. Despite working in a different field of plasma physics Dr. Thomas Trottenberg always came up with good questions and ideas if any problems occurred. Tobias Hahn is slowly taking over the atmospheric pressure plasma lab, thank you for everything you did in the lab while I was busy and could not contribute to such things as updating the safety sheets. The position "AG Mutti Jr." is filled more and more by Jessica Schleitzer, who

organized already a lot of different events and always offers healthy refreshments in small glasses. Another thank you goes to all the students I have had the privilege of mentoring over the years. Special mention should be made of Kristian Reck, Lukas Rosenfeldt and Leander Marxen, it was always a pleasure to work with you and learn from every question you asked.

The cooperation with the Synthesis and Real Structure Group from the Faculty of Engineering was pretty fruitful and mandatory to connect plasma properties with surface modifications. I would like to thank Prof. Dr. Lorenz Kienle for his trust in the prototypes of the *in situ* microplasma cells so that we could introduce them into the TEM. Further, for his input during the discussions on the material modifications and his positive attitude through the whole project. Thank you to Niklas Kohlmann for the countless hours spent in front of the TEM and SEM, as well as the fruitful discussion and explanations. Also for all the effort you put into the preparation of the samples and the deposition of the thin films. Further, thank you to Dr. Ulrich Schürmann for his input during the project meetings.

Another big thank you goes to Prof. Dr. Gary Eden and his co-workers of the University of Illinois Urbana-Champaign for hosting me prior to the start of the project. Your comments on the proof of principle experiments and microplasmas in general made it much easier to get started on this project.

Further, I would like to thank Prof. Dr. Jan Benedikt for his support during the last phase of this thesis.

Thank you to Jana Scharbeutz for proofreading this thesis on short notice. Her fast responses and comments were again perfectly helpful.

Funding of the German Research Foundation (DFG, Project No. 413664940, Grant Nos. KE574/8-1 and KI 1263/17-1) and Kiel Nano, Surface and Interface Science (KINSIS) is gratefully acknowledged.

Being surrounded by people who care about one, always stand behind one, understand one, but also criticize one if its necessary is the greatest gift one can obtain. Life got me this gift and I am thankful every day. I found my perfect match and will never let her go. I will never be able to tell you how thankful I am for all the time we already spent together. Dear Kerstin, thank you for everything you have done for me, for all the time you were patient with me and for every time you cheered me up when I was not in a good mood. Words can not describe what you mean to me, but I hope I show it to you every day.

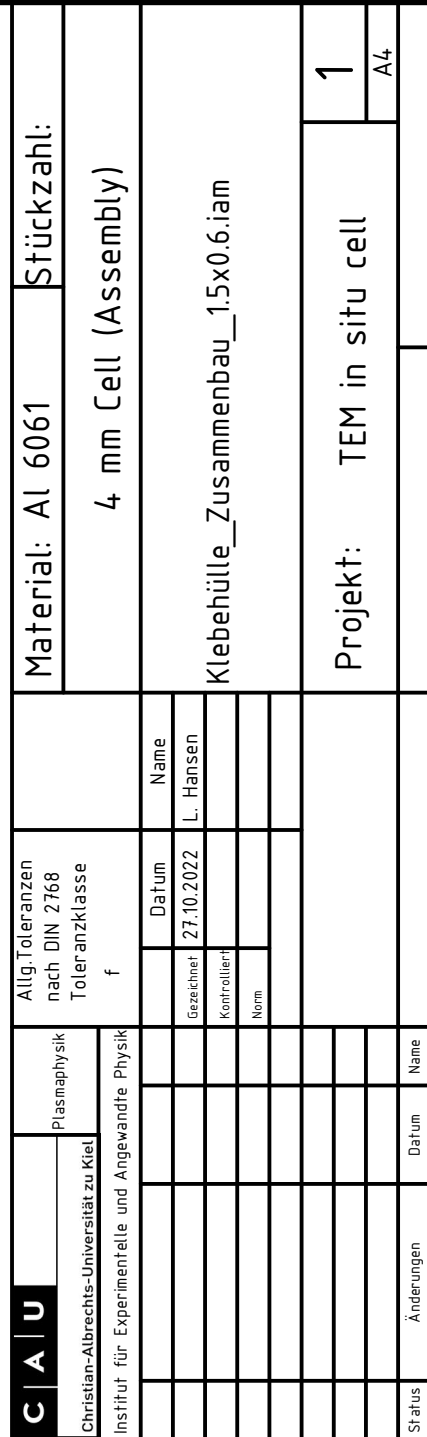
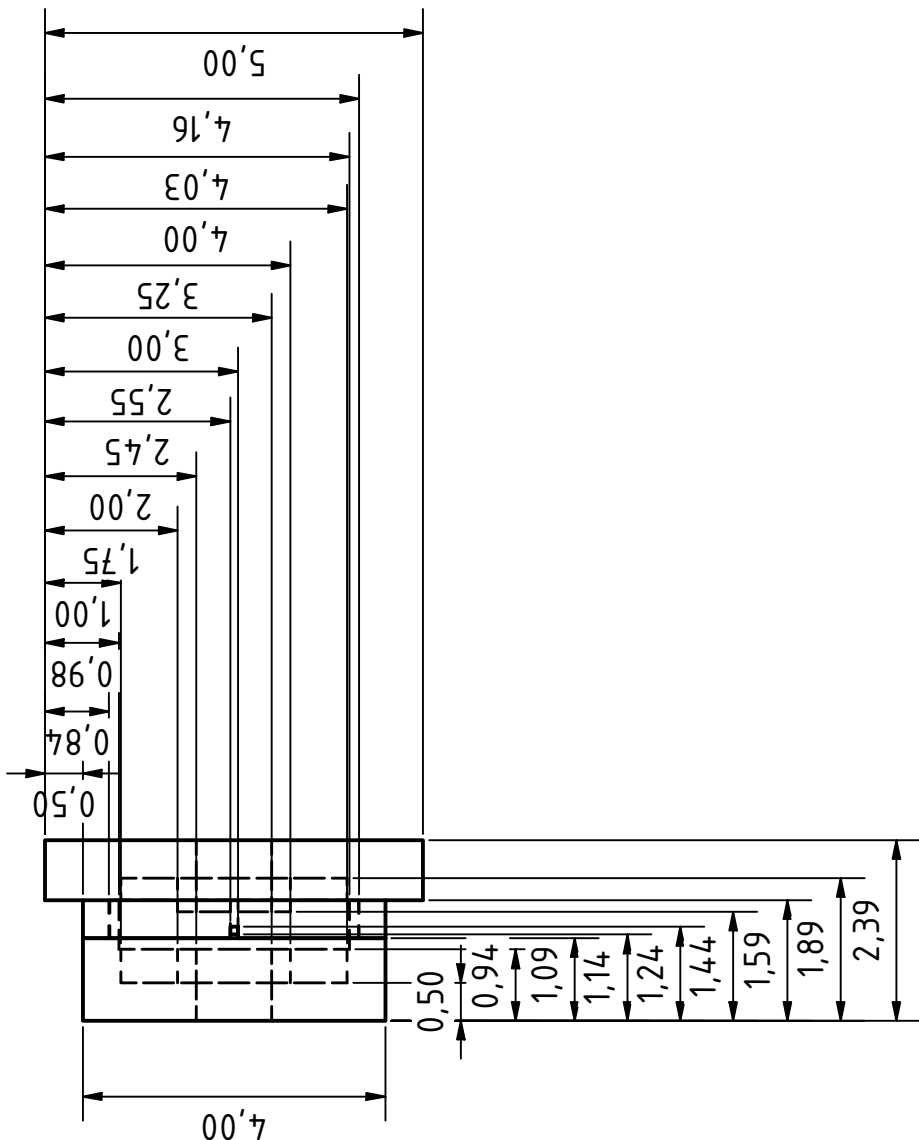
Another thank you goes to my big family. I would like to mention my grandmother Elke for always being interested and supportive since I can remember. My aunt Bine and uncle Karsten who are always there if one asks them. The beer Karsten and I had in the evening of the 8th of May in 2016 will always stick to my memories. My cousin Alex who is part of some of the best evenings I spent in Kiel, Nils and Chantal who were always up for a board game evening and of course my sister Lina, on whom I can always rely.

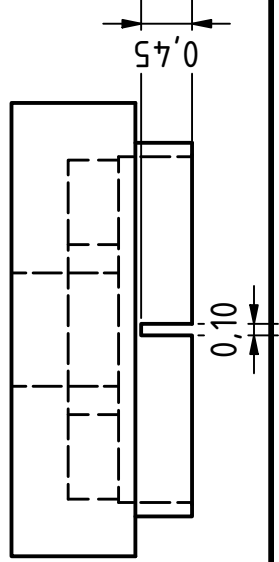
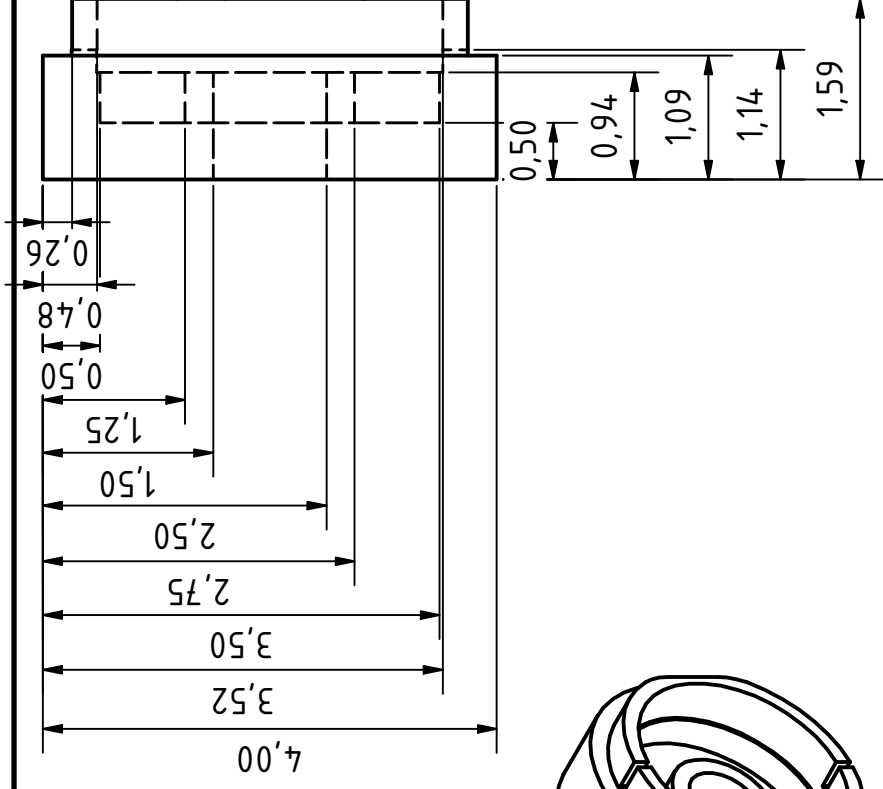
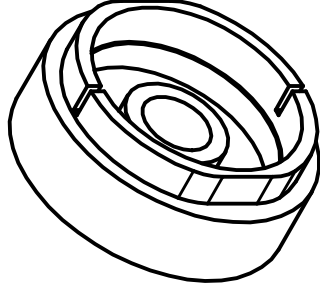
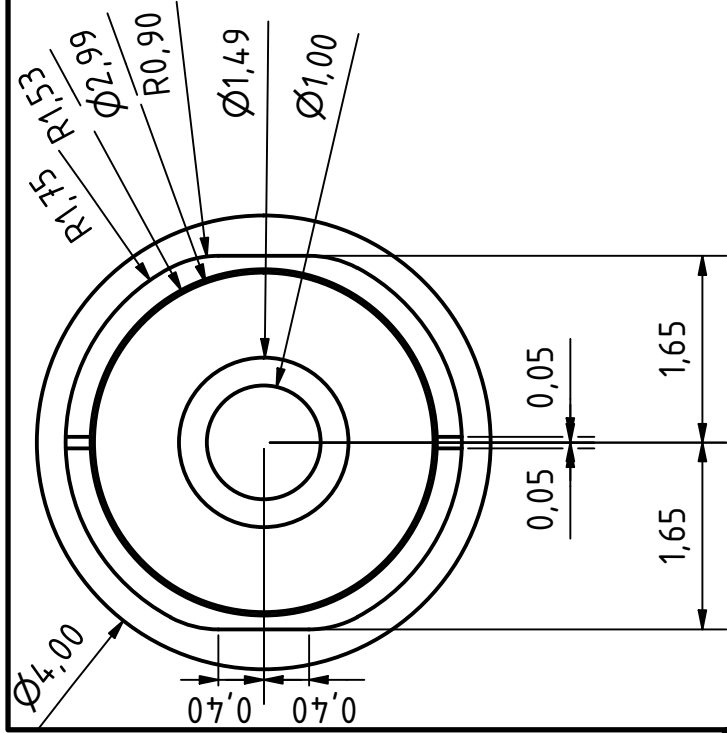
I dedicated this thesis to my parents and also the last big thank you is dedicated to them. My father Michael called me "Herr Doktor" (Mr. Dr.) since I was a child. Even if it was because of my heady and nerdy personality, he probably already knew what was coming. While my father motivated me to always do my best, my mother made sure I was feeling well while pursuing my goals. Your never ending support enabled me to achieve everything I have done till today. As a working-class child I never took it for granted to not worry about money and fully focus on my studies. The efforts my parents, especially my mother Kirsten, have taken over the years are unmatched. I will always be grateful to them.

Appendix A

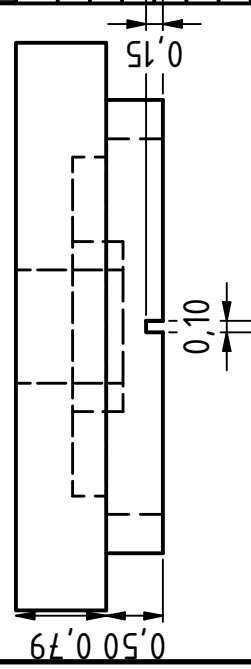
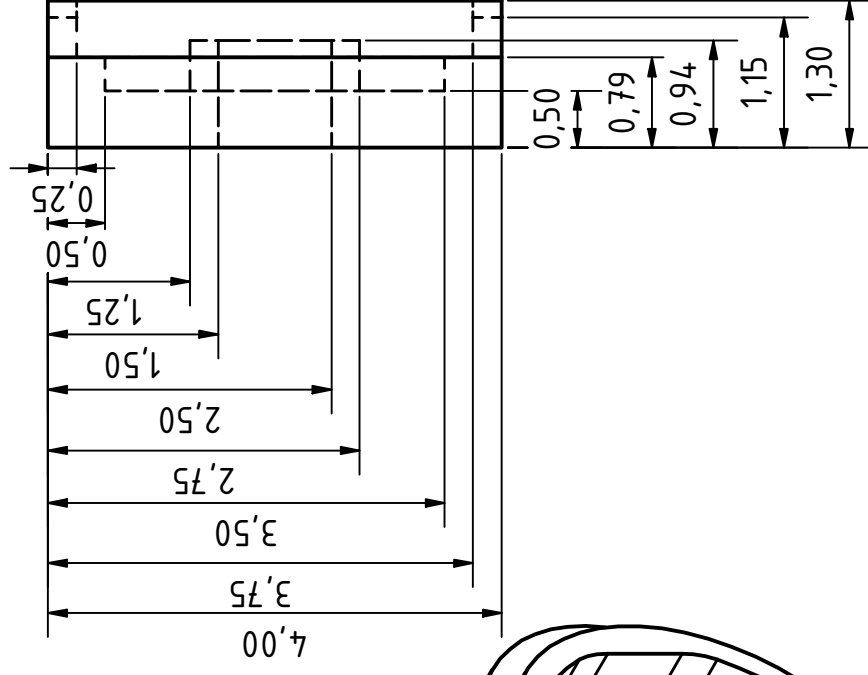
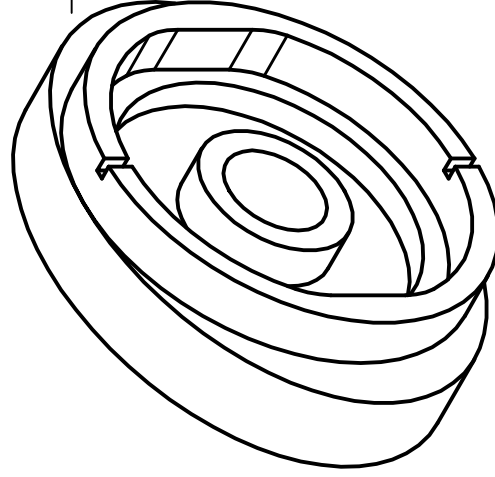
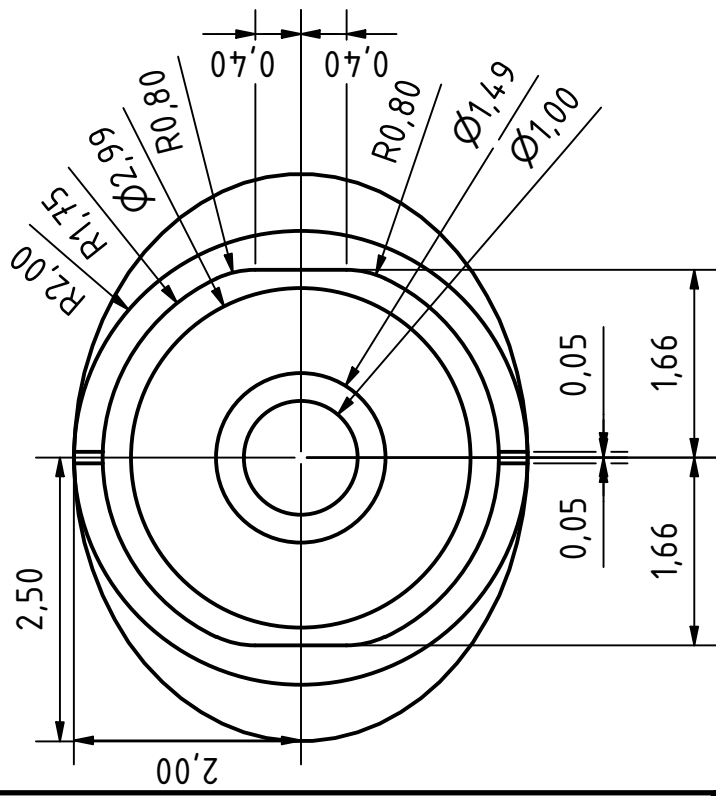
Technical Drawings

The technical drawings of the shells for the different *in situ* microplasma cells are given on the following pages. The respective computer-aided design (CAD) files can be found in the Autodesk Inventor Vault of the Plasma Technology Group and may be shared upon reasonable request.

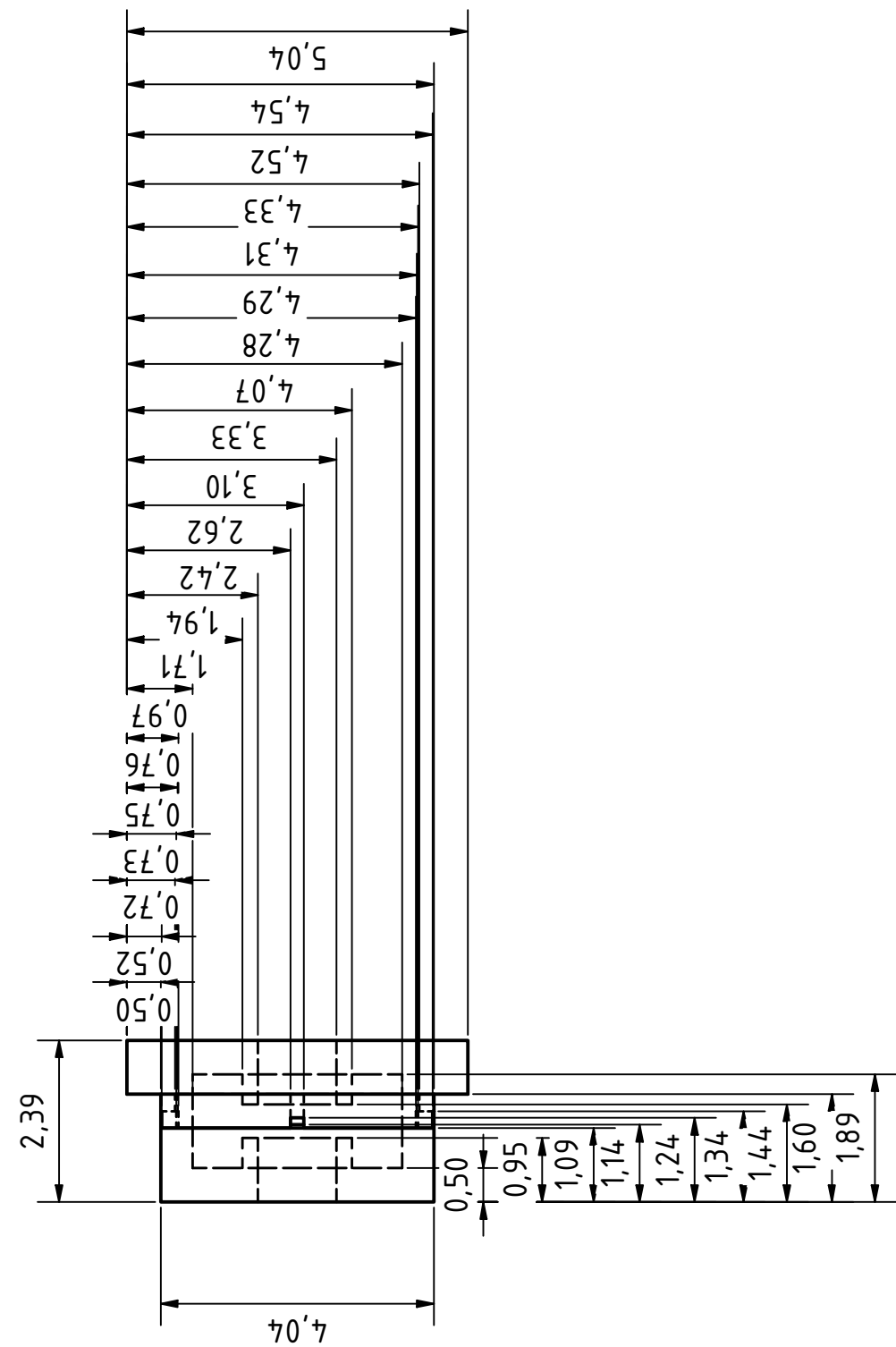




C A U		Material: AL 6061		Stückzahl: 1	
Christian-Albrechts-Universität zu Kiel		4 mm Cell (Bottom Shell)			
Institut für Experimentelle und Angewandte Physik		Klebehülle_unten_1.5x0.6.ipt			
		Allg.Toleranzen nach DIN 2768	Projekt: TEM in situ cell		
		Toleranzklasse f			
		Gezeichnet	Datum	Name	2
		27.10.2022		L. Hansen	
		Kontrolliert			
		Norm			
					A4
Status	Änderungen	Datum	Name		

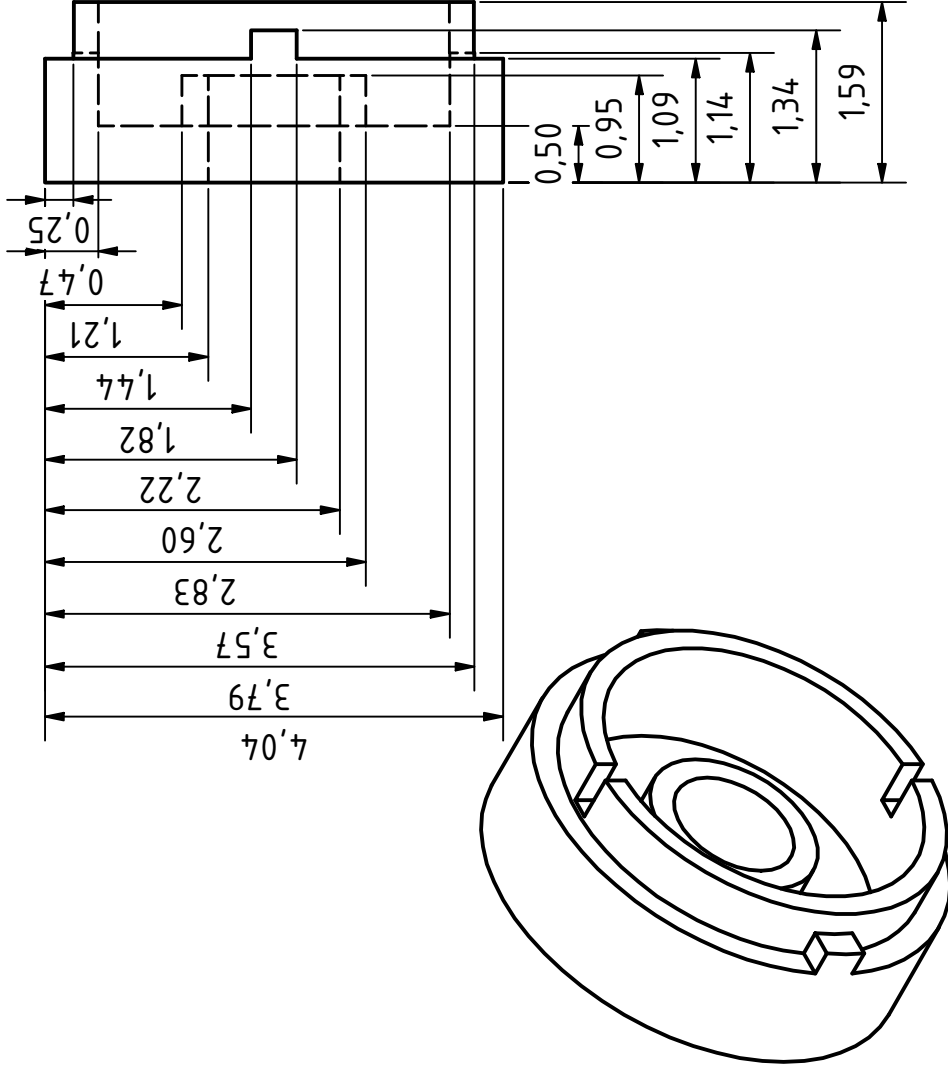


C A U	Plasmaphysik		Allg.Toleranzen nach DIN 2768 Toleranzklasse f	Material: AL 6061	Stückzahl: 1
	Christian-Albrechts-Universität zu Kiel				
				4 mm Cell (Top Shell)	
				Klebehülle_oben_1.5x0.6.ipf	
				Projekt: TEM in situ cell	3
				A4	
Status	Änderungen	Datum	Name		

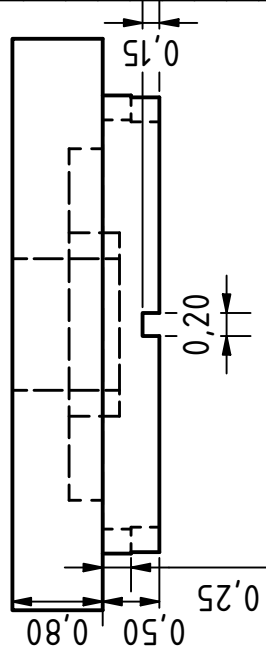
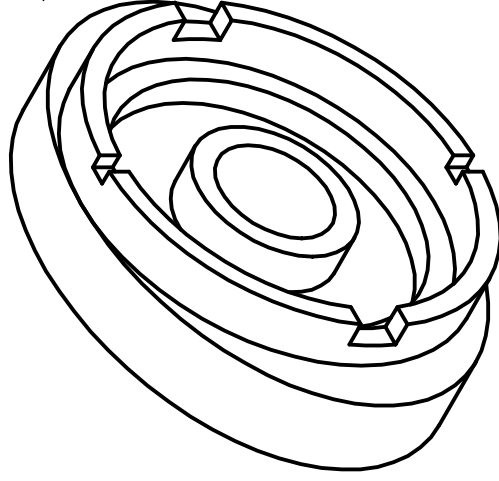


(FormAlox 998)

C A U		Plasmaphysik				Material: Al2O3		Stückzahl:	
Christian-Albrechts-Universität zu Kiel									
Institut für Experimentelle und Angewandte Physik						Allg.Toleranzen nach DIN 2768 Toleranzklasse f			
							Datum	Name	
							27.10.2022	L. Hansen	
Status	Änderungen	Datum	Name	Projekt: TEM in situ cell					
				1					
				A4					



C A U			Plasmaphysik		Allg.Toleranzen nach DIN 2768 Toleranzklasse f		Material: Al203		Stückzahl: 1			
Christian-Albrechts-Universität zu Kiel							Ceramic Cell (Bottom Shell)					
Institut für Experimentelle und Angewandte Physik												
							Gezeichnet		Datum		Name	
							27.10.2022		L. Hansen			
							Kontrolliert					
							Norm					



<div> <div>C A U</div> <div> Christian-Albrechts-Universität zu Kiel Institut für Experimentelle und Angewandte Physik </div> </div>		Plasmaphysik	Allg.Toleranzen nach DIN 2768 Toleranzklasse f		(FormAlox 998)	
					Material: AL203	Stückzahl: 1
					Ceramic Cell (Top Shell)	
					Klebehülle_oben_Steinbach.ipt	
					Projekt: TEM in situ cell	
					3	
					A4	
Status	Änderungen	Datum	Name			

Appendix B

Additional Electrical Data from *in situ* Cell Testing

B.1 Vacuum Testing

Exemplary electrical data of a 4 mm *in situ* microplasma cell is presented in Fig. B.1 to demonstrate not changing currents and electrode voltages despite being placed in a low-pressure environment. Strong current fluctuations are visible during the beginning of the first ignition, but stabilize and do not appear again in the following ignitions.

B.2 Ceramic Cell Testing

Fig. B.2 shows the voltages and currents of the ceramic cell during the first and second "ignition". As explained in the main text, a "plasma-like" breakdown only occurs during the first "ignition".

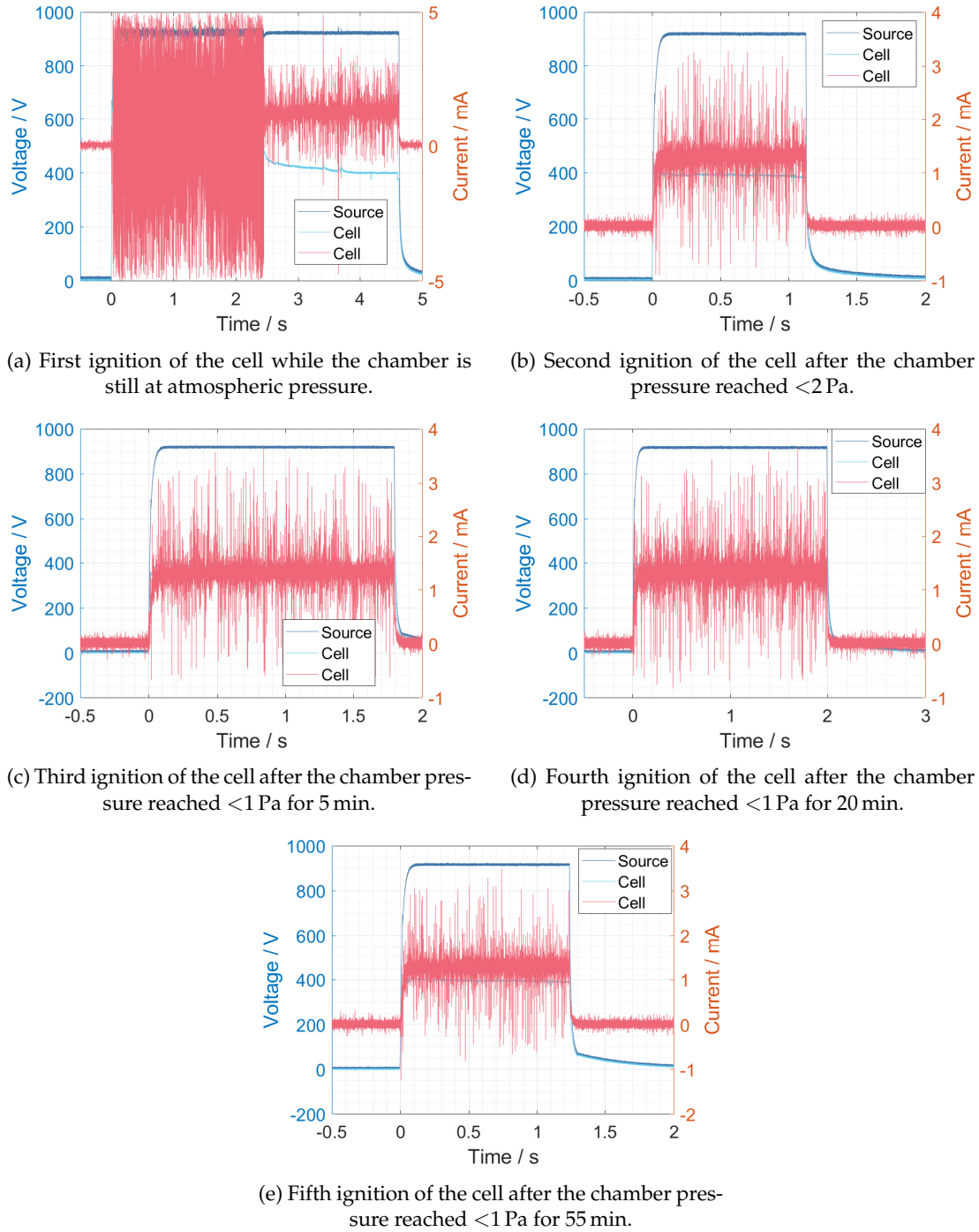


FIGURE B.1: Voltages and currents of a 4 mm *in situ* microplasma cell placed inside of a vacuum chamber at different pressures and time steps.

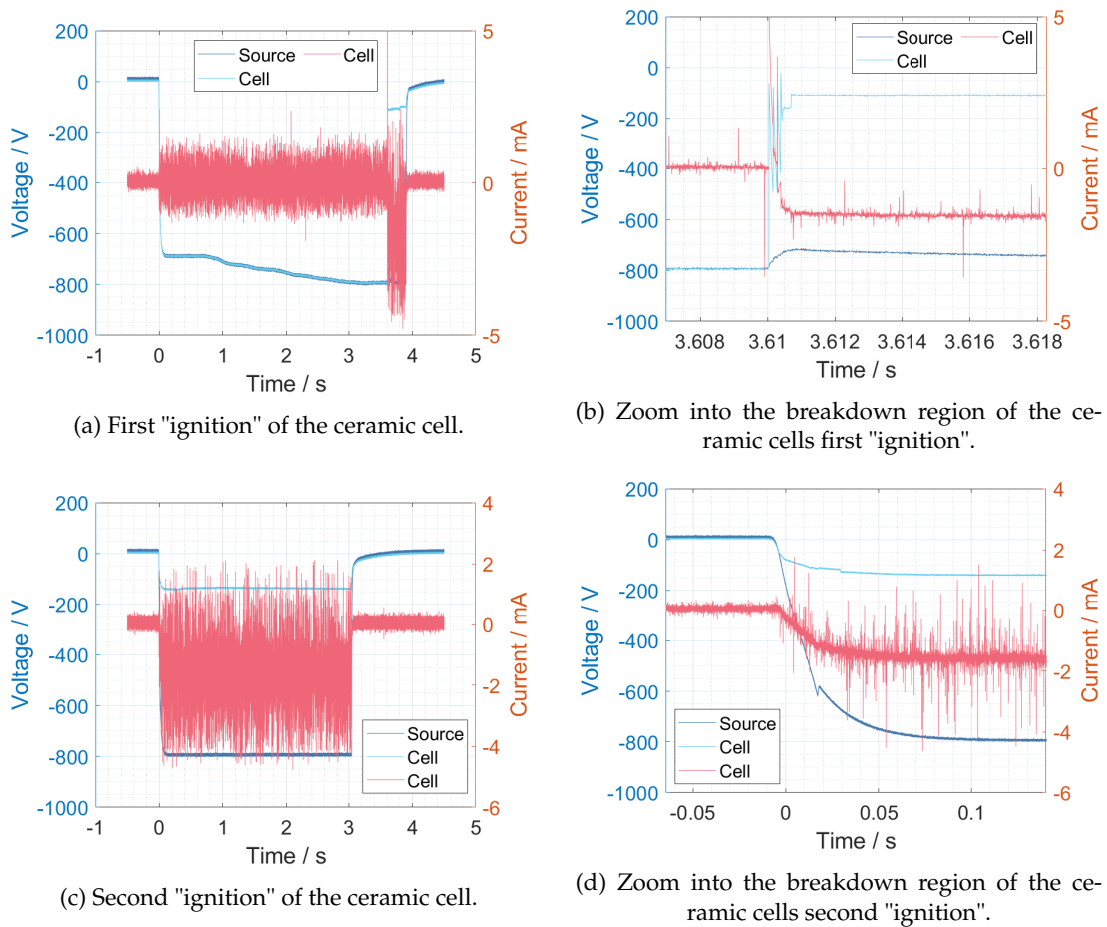


FIGURE B.2: Voltages and currents of the ceramic cell to demonstrate the avalanche diode like behavior with a higher breakdown voltage compared to the cells assembled with aluminum shells.

Appendix C

Peer-reviewed Publications and selected Conference Contributions

C.1 List of Peer-reviewed Publications

A list of all (co-)authored peer-reviewed publications written during my scientific career chronologically sorted. Some were part of this thesis, others were pursued in side projects with cooperation partners or during the supervision of students.

- D. Smazna, S. Shree, M. Hoppe, **L. Hansen**, J. Marx, J. Dittman, Z. Kareh, B. Fiedler, H. Kersten, and R. Adelung, "Surface modifications of highly porous 3D networks via atmospheric plasma treatment", *Contributions to Plasma Physics* **58**, 384-393 (2018)
- **L. Hansen**, A. Schmidt-Bleker, R. Bansemer, H. Kersten, K.-D. Weltmann, and S. Reuter, "Influence of a liquid surface on the NO_x production of a cold atmospheric pressure plasma jet", *Journal of Physics D: Applied Physics* **51**, 474002 (2018)
- **L. Hansen**, K. Reck, and H. Kersten, "Energy flux measurements on an atmospheric pressure surface barrier discharge", *Journal of Physics D: Applied Physics* **52**, 325201 (2019)
- M. Becker, S. Quabius, T. Kewitz, **L. Hansen**, G. Becker, M. Kern, H. Kersten, and S. Harder, "*In vitro* proinflammatory gene expression changes in human whole blood after contact with plasma-treated implant surfaces", *Journal of Cranio-Maxillofacial Surgery* **47**, 1255-1261 (2019)
- T. Krueger, **L. Hansen**, and H. Kersten, "Deposition of SiO_x thin films using hexamethyldisiloxane in atmospheric pressure plasma enhanced chemical vapor deposition", *Journal of Physics: Conference Series* **1492**, 012023 (2020)
- Y. A. Ussenov, **L. Hansen**, T. Krüger, T. S. Ramazanov, and H. Kersten, "Particle formation during deposition of SiO_x nanostructured thin films by atmospheric pressure plasma jet", *Japanese Journal of Applied Physics* **59**, SHHE06 (2020)
- K. S. Mews, M. M. Alhubail, **L. Hansen**, H. B. Motra, F. Wuttke, Q. Ye, A. Misra, and R. Barati Ghahfarokhi, "From Peak Force Quantitative Nanomechanical Mapping Measurements to Triaxial Testing: A Comparative Study of Geomechanical Properties of Clay-Rich Carbonates", *Proceedings of the ASME 2020 39th International Conference on Ocean, Offshore and Arctic Engineering* **11**, V011T11A009 (2020)

- **L. Hansen**, L. Rosenfeldt, K. A. Reck, and H. Kersten, "Understanding the energy balance of a surface barrier discharge for various molecular gases by a multi-diagnostic approach", *Journal of Applied Physics* **129**, 053308 (2021)
- V. Postica, O. Lupan, A. Gapeeva, **L. Hansen**, R. Khaledialidusti, A. K. Mishra, J. Drewes, H. Kersten, F. Faupel, R. Adelung, and S. Hansen, "Improved Long-Term Stability and Reduced Humidity Effect in Gas Sensing: SiO₂ Ultra-Thin Layered ZnO Columnar Films", *Advanced Materials Technologies* **6**, 2001137 (2021)
- **L. Hansen**, B. M. Goldberg, D. Feng, R. B. Miles, H. Kersten, and S. Reuter, "Energy transfer in interaction of a cold atmospheric pressure plasma jet with substrates", *Plasma Sources Science and Technology* **30**, 045004 (2021)
- L. Rosenfeldt, **L. Hansen**, and H. Kersten, "The Use of Passive Thermal Probes for the Determination of Energy Fluxes in Atmospheric Pressure Plasmas", *IEEE Transactions on Plasma Science* **49**, 3325-3335 (2021)
- N. Kohlmann, **L. Hansen**, C. Lupan, U. Schürmann, A. Reimers, F. Schütt, R. Adelung, H. Kersten and L. Kienle, "Fabrication of ZnO Nanobrushes by H₂-C₂H₂ Plasma Etching for H₂ Sensing Applications", *ACS Applied Materials & Interfaces* **13**, 61758-61769 (2021)
- **L. Hansen**, N. Kohlmann, U. Schürmann, L. Kienle, and H. Kersten, "Conventional and non-conventional diagnostics of a stable atmospheric pressure DC normal glow microplasma discharge intended for *in situ* TEM studies", *Plasma Sources Science and Technology* **31**, 035013 (2022)
- M. L. Marxen, **L. Hansen**, A. Reimers, T. Tjardts, L. M. Saure, E. Greve, J. Drewes, F. Schütt, R. Adelung, and H. Kersten, "On the plasma permeability of highly porous ceramic framework materials using polymers as marker materials", *Plasma Processes and Polymers* e2200118 (2022)
- K. A. Reck, **L. Hansen**, M. Stummer, T. Kewitz, H. Testrich, A. Hinterer, R. Foest, and H. Kersten, "Energy flux characterisation of atmospheric pressure plasma spray torches with passive thermal probes", *Journal of Thermal Spray Technology* (2022)
- **L. Hansen**, N. Kohlmann, L. Kienle, and H. Kersten, "Correlations between energy flux and thin film modifications in an atmospheric pressure direct current microplasma", *Thin Solid Films* **765**, 139633 (2023)
- S. An, **L. Hansen**, R. Foest, T. Kewitz, M. Fröhlich, A. Quade, M. Stankov, and H. Kersten, "Investigation of the energetic characteristics during plasma electrolytic polishing of tungsten carbide", (**in preparation**)

C.2 Selected Conference Contributions

An incomplete chronologically sorted list of contributions presented at international conferences.

- **L. Hansen**, K. Reck, S. Gauter, and H. Kersten, "Measurements of the energy flux on an atmospheric pressure surface barrier discharge", 24th Europhysics Conference on Atomic and Molecular Physics of Ionized Gases (ESCAMPIG), 17.-22.07.2018, Glasgow, Scotland, Poster Presentation

- **L. Hansen**, S. Reuter, K. Reck, B. M. Goldberg, D. Feng, L. Rosenfeldt, R. B. Miles, and H. Kersten, "Energy transfer in interaction of non-equilibrium atmospheric pressure plasmas with substrates", XXXIV International Conference on Phenomena in Ionized Gases (ICPIG) & 10th International Conference on Reactive Plasmas (ICRP), 14.-19.07.2019, Sapporo, Japan, Oral Presentation
- **L. Hansen**, N. Kohlmann, U. Schürmann, L. Kienle, and H. Kersten, "Plasma surface interaction on atomic level - Towards *in situ* TEM studies", 12th Asian-European International Conference on Plasma Surface Engineering (AEPSE), 01.-05.09.2019, Jeju Island, Korea, Oral and Poster Presentation
- **L. Hansen**, N. Kohlmann, U. Schürmann, L. Kienle, and H. Kersten, "Plasma Diagnostics on an Atmospheric Pressure DC Microplasma Discharge Intended for *in situ* TEM Integration", 74th Annual Gaseous Electronics Conference (GEC), 04.-08.10.2021, Huntsville (Alabama), USA, *Virtual Online Conference*, Oral Presentation
- **L. Hansen**, N. Kohlmann, U. Schürmann, L. Kienle, and H. Kersten, "Towards *in situ* plasma surface interaction studies utilizing a microplasma in a TEM", IPLasmaNano-XI, 04.-08.09.2022, Seville, Spain, Oral Presentation